Universidad de Granada

Escuela
Internacional
de Posgrado

UNIVERSIDAD DE GRANADA

PROGRAMA DE DOCTORADO:

FÍSICA Y CIENCIAS DEL ESPACIO

MEMORIA DE TESIS DOCTORAL

MEDIDA Y TRANSPORTE DE GASES DE EFECTO INVERNADERO ATMOSFÉRICOS, MONÓXIDO DE CARBONO Y POLVO SAHARIANO, CON ESPECIAL ÉNFASIS EN LA TROPOSFERA LIBRE DEL ATLÁNTICO NORESTE SUBTROPICAL

ÁNGEL JESÚS GÓMEZ PELÁEZ

Año 2018

Directores de Tesis:

Dr. Emilio Cuevas Agulló

Prof. Dr. Fernando Moreno Insertis

Editor: Universidad de Granada. Tesis Doctorales
Autor: Ángel Jesús Gómez Peláez
ISBN: 978-84-1306-040-8
URI: http://hdl.handle.net/10481/54412

Esta tesis doctoral ha sido realizada con datos y resultados obtenidos en el Centro de Investigación Atmosférica de Izaña de la Agencia Estatal de Meteorología, donde el doctorando desarrolló su trabajo como funcionario de carrera del Cuerpo Superior de Meteorólogos del Estado, y su director principal de tesis trabaja como Director de dicho centro.

AEMet

Agencia Estatal de Meteorología

Resumen

Las concentraciones de los gases de efecto invernadero atmosféricos bien mezclados (CO_2, CH_4 y N_2O, fundamentalmente) se han incrementado sustancialmente desde el comienzo de la revolución industrial debido a emisiones antropogénicas. Esto está cambiando el clima a nivel global de forma lenta (debido a la gran inercia térmica de los océanos) pero inexorable. El CO también influye en este proceso debido a su impacto en el ciclo del CH4. El polvo mineral atmosférico además de influir en el forzamiento radiativo, tiene un gran impacto en la calidad del aire, los ecosistemas y los medios de transporte.

El objetivo fundamental de esta tesis ha sido realizar una contribución científica significativa en la medida y el transporte de gases de efecto invernadero atmosféricos, monóxido de carbono y polvo sahariano, con especial énfasis en la troposfera libre del Atlántico Noreste subtropical. Los resultados presentados en esta tesis han sido previamente publicados por el doctorando en tres artículos científicos de revistas internacionales con árbitro, del primer cuartil (en índice de impacto) del campo "Ciencias Atmosféricas y Meteorología", por lo que se ha optado por presentar esta tesis como compendio de publicaciones.

Se ha desarrollado un procedimiento riguroso para determinar la incertidumbre en las medidas semi-continuas de CO realizadas en la estación VAG global de Izaña. Este método es aplicable a otras estaciones de la red global VAG de la OMM. El error en las medidas ha sido reportado como incertidumbre combinada estándar calculada a partir de cuatro componentes. Se ha cuantificado la incertidumbre en cada una de las medidas de CO realizadas a lo largo de los años 2008-2011. Cuando se calculan medias, aparece un quinto tipo de incertidumbre, que llamamos incertidumbre de representación, cuando algunos de los datos necesarios para calcular una media temporal están ausentes. Se ha desarrollado un procedimiento para calcular la incertidumbre de las medias de CO, propagando la incertidumbre de los datos utilizados para el cálculo de dichas medias teniendo en cuenta el carácter aleatorio o sistemático de cada componente de la incertidumbre. La serie temporal de medias diarias nocturnas en Izaña para el periodo 2008-2011 ha sido analizada, y estudiado el comportamiento de la componente interanual, del ciclo estacional y del ciclo diurno. Se han comparado las medidas in situ de Izaña con medidas de matraces NOAA muestreados en Izaña, introduciendo el concepto de incertidumbre de comparación, que permite determinar cuándo la diferencia es compatible o no con cero.

Se ha utilizado el modelo Oslo CTM3, que es un modelo de transporte que incluye química atmosférica, para estudiar la evolución del CH_4 durante el periodo 1970-2012. Además, se han utilizado 18 trazadores ficticios pasivos, uno por cada sector de emisión de CH_4 considerado. Se ha hecho una comparación exhaustiva de los campos de CH_4 atmosférico simulados con las medidas de estaciones de superficie para todas las regiones del planeta. La variación estacional es reproducida para la mayoría de las estaciones. El modelo también reproduce gran parte de la evolución observada del CH_4 en las escalas interanual y decadal. Las variaciones en las emisiones de los humedales son los mayores forzadores de las variaciones del CH_4 de un año a otro. Nuestros resultados sugieren que el reciente crecimiento de las emisiones antropogénicas en Asia a partir de 2006 está sobreestimado en el inventario EDGAR v4.2. Nos cuestionamos también las tendencias en las emisiones asiáticas en los años noventa y el comienzo de la década del 2000, en el inventario EDGAR v4.2. En nuestras simulaciones, la vida media del CH_4 decrece más de un 8% entre 1970 y 2012, debido al incremento de la capacidad de oxidación de la atmósfera. Nuestro análisis revela que los factores clave que explican esto son los cambios en:

la humedad específica, la proporción de emisión entre NO_x y CO, las emisiones de NO_x debidas a rayos, y la columna total de O_3. Se ha obtenido una ecuación sencilla para predecir la vida media del CH_4 a partir de una combinación de estos parámetros.

Se ha mostrado que NAFDI (Intensidad del Dipolo Norte Africano) modula los flujos de salida de polvo hacia el SNA (Atlántico Norte Subtropical) y el Mediterráneo a escala intra-estacional durante el verano, alternando entre uno y otro. Para NAFDI positivo, las anomalías positivas de AOD (Espesor Óptico de Aerosoles) se observan en el Sahara occidental y el SNA, mientras que para NAFDI negativo, éstas aparecen en el Sahara central-oriental y en el Mediterráneo central-occidental. Por primera vez, se ha demostrado que existe una estrecha relación entre la posición longitudinal de la SHL (Baja Térmica Sahariana) y el índice NAFDI, a escala temporal diaria, yendo el NAFDI un día adelantado respecto a la SHL. El NAFDI conduce a la SHL a través de advección horizontal de temperatura. El NAFDI positivo parece favorecer la emisión de polvo en el Sahara Occidental, norte de Mauritania, y Argelia central. Se ha mostrado que las variaciones intra-estacionales del NAFDI son producidas por aquellas ondas de Rossby de latitudes medias que se propagan sobre el Norte de África y que penetran lo suficiente en la baja troposfera.

Dedicatoria

A mis hijos, Enol y Martín Ángel.

Agradecimientos

Agradezco a la Agencia Estatal de Meteorología y a su Centro de Investigación Atmosférica de Izaña (CIAI), la posibilidad de realizar esta tesis doctoral con resultados del trabajo que desempeñé como funcionario de carrera del Cuerpo Superior de Meteorólogos del Estado en el CIAI. Mi agradecimiento también al programa de doctorado “Física y Ciencias del Espacio” de la Universidad de Granada, que ha servido de marco académico para esta tesis doctoral. Así mismo, agradezco al Instituto de Astrofísica de Canarias (IAC) y al Departamento de Astrofísica de la Universidad de La Laguna, el soporte recibido entre octubre de 1997 y septiembre de 2001, donde me formé y trabajé en magnetohidrodinámica aplicada a la astrofísica, obtuve la Suficiencia Investigadora y publiqué dos estudios científicos (Gomez-Pelaez, 1999; Gomez-Pelaez & Moreno-Insertis, 2002). Allí me dejé la piel enfrentándome a la “infinita” complejidad de esa rama de la astrofísica; pero también me formé sólidamente en campos que trascienden la astrofísica: mecánica de fluidos, ecuaciones en derivadas parciales, métodos numéricos y procesos de transporte.

Doy las gracias también a mis dos directores de tesis: Dr. Emilio Cuevas y Prof. Dr. Fernando Moreno. Al primero, director del CIAI (AEMET), por su gran afán investigador, por su apoyo en la realización de esta tesis doctoral, y por trabajar arduamente mano a mano conmigo en el artículo que él lideró que forma parte del compendio de esta tesis. Al segundo, sobre todo por supervisar/dirigir mi formación y trabajo en el pasado, durante mi estancia en el IAC. Mi agradecimiento también al Prof. Dr. Ángel V. Delgado, director del mencionado programa de doctorado de la Universidad de Granada, sobre todo por su buena disposición a que esta tesis doctoral se desarrollase en dicho programa a pesar de que los dos directores de tesis no eran profesores de plantilla de la Universidad de Granada, y también a mi tutor académico de doctorado, Prof. Dr. Francisco J. Olmo de la Universidad de Granada.

Mi agradecimiento también a todos los coautores de los artículos que conforman el compendio de esta tesis, por su contribución a ellos. Especial mención merecen: Ramón Ramos, por ser mi compañero de fatigas modificando por dentro los instrumentos de medida de gases de efecto invernadero (GEI) e instalando todos los elementos periféricos necesarios para convertirlos en sistemas de medida de gran exactitud, así como reparándolos cuando ha sido necesario; Dr. Stig Dalsoren, por invitarme a participar en el artículo que él lideró y por tener la paciencia y confianza de esperar a que yo convirtiera el punto débil de la versión inicial del manuscrito en uno de sus puntos más fuertes; Dr. Emilio Cuevas, director del CIAI, por pedirme que participara en el estudio que él lideró, asignándome todo lo relativo a la dinámica atmosférica; y por último, al gran científico Prof. Dr. Ivar S. A. Isaksen, fallecido en mayo de 2017 a la edad de 79 años. Descanse en paz.

Doy las gracias a todos los profesores que me enseñaron física y matemáticas a lo largo de mi vida, tanto a aquellos que lo hicieron en las aulas (D. Antonio Toribio, Doña Mercedes Torres, D. Salvador Valibrea, Prof. Dr. Ramón Román, Prof. Dr. Eduardo Battaner, Prof. Dr. Fernando Moreno, Prof. Dr. Javier Trujillo y muchos más), como a aquellos otros que lo hicieron a través de excelentes libros de texto (Lighthill, Courant, Morton, Acheson, Whitham, Braginski, Holton, Peixoto, Iribarne, Morán, Rodgers y muchos más).

Doy las gracias a mis padres, Antonio y Encarna, que me educaron dando gran importancia a “los estudios”, que ellos no pudieron tener. Por último, pero no por ello menos importante, doy las gracias a mi esposa, Silvia, y a mis dos hijos, Enol y Martín Ángel, por su gran paciencia con esta tesis doctoral y por ser maravillosos.

ÍNDICE

Publicaciones

Artículos que forman parte del compendio de la tesis doctoral

Gomez-Pelaez, A. J., Ramos, R., Gomez-Trueba, V., Novelli, P. C., and Campo-Hernandez, R.: A statistical approach to quantify uncertainty in carbon monoxide measurements at the Izaña global GAW station: 2008–2011, Atmos. Meas. Tech., 6, 787-799, doi:10.5194/amt-6-787-2013, 2013.

Dalsøren, S. B., Myhre, C. L., Myhre, G., Gomez-Pelaez, A. J., Søvde, O. A., Isaksen, I. S. A., Weiss, R. F., and Harth, C. M.: Atmospheric methane evolution the last 40 years, Atmos. Chem. Phys., 16, 3099-3126, doi:10.5194/acp-16-3099-2016, 2016.

Cuevas, E.; Gómez-Peláez, A. J.; Rodríguez, S.; Terradellas, E.; Basart, S.; García, R. D.; García, O. E.; Alonso-Pérez, S.: The pulsating nature of large-scale Saharan dust transport as a result of interplays between mid-latitude Rossby waves and the North African Dipole Intensity, Atmospheric Environment, 167, 586-602, doi: 10.1016/j.atmosenv.2017.08.059, 2017.

Los dos primeros artículos (AMT y ACP) tienen licencia CC By 3.0, con lo que pueden incluirse en esta memoria de tesis tal y como fueron publicados. Para el tercer artículo (Atmospheric Environment), AEMET pagó la tasa necesaria para que fuera de libre acceso bajo licencia CC By 4.0, por lo que también se puede usar en esta memoria de tesis tal y como fue publicado. Los indicadores de calidad de estas publicaciones se detallan en las secciones 4.1.1, 4.2.1 y 4.3.1.

Otros artículos en los que ha participado el doctorando durante el periodo de tesis

Belikov, D. A., Maksyutov, S., Yaremchuk, A., Ganshin, A., Kaminski, T., Blessing, S., Sasakawa, M., Gomez-Pelaez, A. J., and Starchenko, A.: Adjoint of the global Eulerian–Lagrangian coupled atmospheric transport model (A-GELCA v1.0): development and validation, Geosci. Model Dev., 9, 749-764, doi:10.5194/gmd-9-749-2016, 2016.

García, O. E., Sepúlveda, E., Schneider, M., Hase, F., August, T., Blumenstock, T., Kühl, S., Munro, R., Gómez-Peláez, Á. J., Hultberg, T., Redondas, A., Barthlott, S., Wiegele, A., González, Y., and Sanromá, E.: Consistency and quality assessment of the Metop-A/IASI and Metop-B/IASI operational trace gas products (O3, CO, N2O, CH4, and CO2) in the subtropical North Atlantic, Atmos. Meas. Tech., 9, 2315-2333, doi:10.5194/amt-9-2315-2016, 2016.

Tsuruta, A., Aalto, T., Backman, L., Hakkarainen, J., van der Laan-Luijkx, I. T., Krol, M. C., Spahni, R., Houweling, S., Laine, M., Dlugokencky, E., Gomez-Pelaez, A. J., van der Schoot, M., Langenfelds, R., Ellul, R., Arduini, J., Apadula, F., Gerbig, C., Feist, D. G., Kivi, R., Yoshida, Y., and Peters, W.: Global methane emission estimates for 2000–2012 from CarbonTracker Europe-CH4 v1.0, Geosci. Model Dev., 10, 1261-1289, doi:10.5194/gmd-10-1261-2017, 2017.

Shirai, T., M. Ishizawa, R. Zhuravlev, A. Ganshin, D. Belikov, M. Saito, T. Oda, V. Valsala, A.J. Gomez-Pelaez, R. Langenfelds, and S. Maksyutov; A decadal inversion of CO2 using the Global

Eulerian–Lagrangian Coupled Atmospheric model (GELCA): sensitivity to the ground-based observation network, Tellus B: Chemical and Physical Meteorology, Vol. 69 , Iss. 1, 2017.

Yuan, Y., Ries, L., Petermeier, H., Steinbacher, M., Gómez-Peláez, A. J., Leuenberger, M. C., Schumacher, M., Trickl, T., Couret, C., Meinhardt, F., and Menzel, A.: Adaptive selection of diurnal minimum variation: a statistical strategy to obtain representative atmospheric CO2 data and its application to European elevated mountain stations, Atmos. Meas. Tech., 11, 1501-1514, https://doi.org/10.5194/amt-11-1501-2018, 2018.

García, R. D., Barreto, A., Cuevas, E., Gröbner, J., García, O. E., Gómez-Peláez, A., Romero-Campos, P. M., Redondas, A., Cachorro, V. E., and Ramos, R.: Comparison of observed and modeled cloud-free longwave downward radiation (2010–2016) at the high mountain BSRN Izaña station, Geosci. Model Dev., 11, 2139-2152, https://doi.org/10.5194/gmd-11-2139-2018, 2018.

García, O. E., Schneider, M., Ertl, B., Sepúlveda, E., Borger, C., Diekmann, C., Wiegele, A., Hase, F., Barthlott, S., Blumenstock, T., Raffalski, U., Gómez-Peláez, A., Steinbacher, M., Ries, L., and de Frutos, A. M.: The MUSICA IASI CH4 and N2O products and their comparison to HIPPO, GAW and NDACC FTIR references, Atmos. Meas. Tech., 11, 4171-4215, https://doi.org/10.5194/amt-11-4171-2018, 2018.

Comunicaciones a congresos

García. O.E., M. Schneider, T. August, F. Hase, T. Blumenstock, E. Sepúlveda, T. Hultberg, M.E. Sanromá, A. Gómez-Peláez, A. Redondas, E. Cuevas, P.M. Romero-Campos, Y. González, Towards a Near Operational Validation of IASI Level 2 trace gas products, ATMOS 2015-ESA, 8-12 June, Heraklion (Crete), 2015.

García. O.E., M. Schneider, T. August, F. Hase, T. Blumenstock, E. Sepúlveda, T. Hultberg, S. Barthlott, A. Wiegele, M.E. Sanromá, A. Gómez-Peláez, A. Redondas, E. Cuevas, P.M. Romero-Campos, Y. González, Quality Assessment of the IASI Operational Trace Gas Products by using ground-based Fourier Transform Spectrometry at the Izaña Atmospheric Observatory, IRWG-NDACC/TCCON Meeting, 8-12 June, Toronto, 2015.

Gomez-Pelaez, A.J., R. Ramos, V. Gomez-Trueba, R. Campo-Hernandez, E. Reyes-Sanchez: "GGMT-2015 Izaña station update: instrumental and processing software developments, scale updates, aircraft campaign, and plumbing design for CRDS" in GAW report (No. 229) of the "18th WMO/IAEA Meeting on Carbon Dioxide, Other Greenhouse Gases, and Related Measurement Techniques (GGMT) (La Jolla, CA, USA, 13-17 September, 2015)", edited by P. Tans and C. Zellweger, World Meteorological Organization, 125-131, 2016

Sepúlveda, E., O. E. García, M. Schneider, T. August, F. Hase, T. Blumenstock, A. Gómez-Peláez, E. Cuevas, T. Hultberg, N. Peinado, X. Calbet, E. López-Baeza, M.E. Sanroma, V. Carreño:Long-term validation of the IASI operational L2 products (total column amounts and vertical profiles) by using ground-based Fourier Transform Spectrometry at the Izaña Atmospheric Observatory, EUMETSAT Conference 2015, 21-25 September, Tolouse, France.

Sepúlveda, E., O.E. García, M. Schneider, T. August, F. Hase, T. Blumenstock, E. Sanroma, A. Gómez-Peláez, T. Hultberg, A. Redondas, P.M. Romero-Campos, V. Carreño, and Y. González, A

Quasi Near-Real Time Operational Validation of IASI Level 2 Trace Gas Products, IASI Conference 2016, 11-15 April, Antibes Juan-les-Pins, France, 2016

Gomez-Pelaez, Ángel J., Emilio Cuevas, Sergio Rodríguez, Enric Terradellas, Sara Basart, Rosa Delia García, Omaira E. García, Silvia Alonso-Pérez: Ondas de Rossby barotrópicas libres como conductoras de las variaciones del NAFDI, la baja térmica sahariana y las intrusiones de polvo hacia el Atlántico y el Mediterráneo, Seminario del Centro de Investigación Atmosférica de Izaña, https://doi.org/10.13140/RG.2.1.3622.2327, May 19, 2016.

Gómez-Peláez, Ángel J., Ramón Ramos, Vanessa Gómez-Trueba, Emilio Cuevas, Enrique Reyes: “CO2, CH4, and CO with CRDS technique at the Izaña Global GAW station: instrumental tests, developments and first measurement results”; 19th WMO/IAEA Meeting on Carbon Dioxide, Other Greenhouse Gases, and Related Measurement Techniques (GGMT-2017), Dubendorf, Switzerland, August 27–31, 2017.

García, O.E., E. Sepúlveda, M. Schneider, A. Wiegele, C. Borger, F. Hase, E. Sanromá, Á.-J. Gómez-Peláez, A. Cansado, M. Aullé, and S. Barthlott, INMENSE: IASI for Surveying Methane and Nitrous Oxide in the Troposphere, EUMETSAT Meteorological Satellite Conference, Roma, 2-6 Octubre, 2017.

García, O.E., M. Schneider, B. Ertl, F. Hase, C. Borger, E. Sepúlveda, T. Blumenstock, Uwe Raffalski and A.J. Gómez-Peláez, IASI for Surveying Methane and Nitrous Oxide in the Troposphere: MUSICA products and its validation, 14th International Workshop on Greenhouse Gas Measurements from Space (IWGGMS-14), Toronto (Canada), 8-10 May, 2018.

García, O.E., E. Sepúlveda, E. Cuevas, A.J. Gómez-Peláez, M. Schneider, F. Hase. T. Blumenstock, A. Redondas, and V. Carreño, Long-term Monitoring of Greenhouse Gases at the Izaña Atmospheric Observatory, 14th International Workshop on Greenhouse Gas Measurements from Space (IWGGMS-14), Toronto (Canada), 8-10 May, 2018.

Reports

Cuevas, E., Milford, C., Bustos, J. J., del Campo-Hernández, R., García, O. E., García, R. D., Gómez-Peláez, A. J., Ramos, R., Redondas, A., Reyes, E., Rodríguez, S., Romero-Campos, P. M., Schneider, M., Belmonte, J., Gil-Ojeda, M., Almansa, F., Alonso-Pérez, S., Barreto, A., González-Morales, Y., Guirado-Fuentes, C., López-Solano, C., Afonso, S., Bayo, C., Berjón, A., Bethencourt, J., Camino, C., Carreño, V., Castro, N. J., Cruz, A. M., Damas, M., De Ory-Ajamil, F., García, M. I., Fernández-de Mesa, C. M., González, Y., Hernández, C., Hernández, Y., Hernández, M. A., Hernández-Cruz, B., Jover, M., Kühl, S. O., López-Fernández, R., López-Solano, J., Peris, A., Rodríguez-Franco, J. J., Sálamo, C., Sepúlveda, E. and Sierra, M. : Izaña Atmospheric Research Center Activity Report 2012-2014 , (Eds. Cuevas, E., Milford, C. and Tarasova, O.), State Meteorological Agency (AEMET), Madrid, Spain and World Meteorological Organization, Geneva, Switzerland, NIPO: 281-15-004-2, WMO/GAW Report No. 219, 2015.

Cuevas, E., Milford, C., Bustos, J. J., del Campo-Hernández, R., García, O. E., García, R. D., Gómez-Peláez, A. J., Guirado-Fuentes, C., Marrero, C., Prats, N., Ramos, R., Redondas, A., Reyes, E., Rodríguez, S., Romero-Campos, P. M., Schneider, M., Belmonte, J., Yela, M., Almansa, F., Barreto, A., López-Solano, C., Basart, S., Terradellas, E., Afonso, S., Bayo, C., Berjón, A., Bethencourt, J., Carreño, V., Castro, N. J., Cruz, A. M., Damas, M., De Ory-Ajamil, F., García, M.I., Gómez-Trueba,

V., González, Y., Hernández, C., Hernández, Y., Hernández-Cruz, B., Jover, M., León-Luís, S. F., López-Fernández, R., López-Solano, J., Rodríguez, E., Rodríguez-Franco, J. J., Rodríguez-Valido, M., Sálamo, C., Sanromá, E., Santana, D., Santo Tomás, F., Sepúlveda, E., Sierra, M. and Sosa, E.: Izaña Atmospheric Research Center Activity Report 2015-2016. (Eds. Cuevas, E., Milford, C. and Tarasova, O.), State Meteorological Agency (AEMET), Madrid, Spain and World Meteorological Organization, Geneva, Switzerland, NIPO: 014-17-012-9, WMO/GAW Report No. 236, 2017.

1. Introducción

1.1. Gases de efecto invernadero atmosféricos y cambio climático

El efecto invernadero atmosférico natural hace que la temperatura junto a la superficie terrestre sea en promedio superior en 33 K a la que tendría dicha superficie en equilibrio radiativo con la radiación solar incidente (Peixoto & Oort, 1992). Las emisiones antropogénicas de gases de efecto invernadero (GEI) a la atmósfera desde el comienzo de la Revolución Industrial están incrementado el efecto invernadero atmosférico natural (Stocker et al., 2013). El aumento de las concentraciones de GEI bien mezclados está provocando un desequilibrio radiativo entre la radiación solar incidente y la radiación infrarroja enviada de vuelta al espacio, que está causando un lento (debido a la gran inercia térmica de los océanos) incremento de la temperatura de los océanos, de la superficie de la corteza continental, y de la atmósfera en las proximidades de la superficie terrestre, el aumento del nivel del mar, y la disminución de la masa de la criosfera (Stocker et al., 2013).

Los gases de efecto invernadero son aquellos constituyentes naturales de la atmósfera, naturales y antropogénicos, que absorben y emiten radiación infrarroja en el rango espectral emitido por la superficie de la Tierra, la propia atmósfera y las nubes. Esta propiedad causa el efecto invernadero. Vapor de agua (H_2O), dióxido de carbono (CO_2), óxido nitroso (N_2O), metano (CH_4) y ozono (O_3) son los GEI primarios en la atmósfera de la Tierra. Además, hay un conjunto de GEI en la atmósfera completamente antropogénicos como los halocarbonos y otros compuestos que contienen cloro y bromo, considerados en el protocolo de Montreal: hexafluoruro de azufre (SF_6), hidrofluorocarbonos (HFCs) y perfluorocarbonos (PFCs). Se llama GEI bien mezclados (CO_2, CH_4, N_2O, halocarbonos y SF_6) a aquellos que se acumulan en la atmósfera en escalas de tiempo de décadas a siglos, y por tanto tienen tiempo para mezclarse bien en la atmósfera (IPCC, 2013a). Se llama GEI de corta vida al O_3 troposférico y estratosférico así como al H_2O estratosférico (Stocker et al., 2013). La concentración del H_2O troposférico viene determinada por factores meteorológicos (no por emisiones), y su efecto como GEI se tiene en cuenta como retroalimentación inducida por los cambios en las concentraciones de los GEI bien mezclados y de corta vida.

Las concentraciones atmosféricas de los gases de efecto invernadero dióxido de carbono (CO_2), metano (CH_4) y óxido nitroso (N_2O) se han incrementado desde 1750 debido a las actividades humanas (Stocker et al., 2013). En 2016 las concentraciones medias globales de estos gases eran 403.3 ppm para CO_2, 1853 ppb para CH_4, y 328.9 ppb para N_2O; y excedían el nivel preindustrial en un 45%, 157% y 22%, respectivamente (WMO, 2017). Son los niveles más altos de GEI de los últimos 800.000 años (Stocker et al., 2013).

Las emisiones antropogénicas de CO_2 a la atmósfera son debidas a: quema de combustibles fósiles, cambio en los usos del suelo (deforestación) y producción de cemento. Aproximadamente la mitad del CO_2 emitido permanece en la atmósfera a largo plazo (siglos) y la otra mitad es absorbida por el océano y la biosfera; por lo que mientras se siga emitiendo CO_2 seguirá aumentando la concentración de CO_2 atmosférico (WDCGG, 2017). El CO_2 no es destruido por reacciones químicas en la atmósfera ni se deposita en la superficie de la Tierra, sino que es redistribuido entre los grandes reservorios de carbono: atmósfera, océano y biosfera terrestre, existiendo múltiples escalas de tiempo para el intercambio entre ellos y para la redistribución del carbono dentro de cada reservorio. El continuo de escalas temporales implicadas se puede aproximar en la práctica por unas pocas de ellas mediante un ajuste numérico, no pudiéndosele asignar a cada una de ellas un significado directo asociado a un proceso. Tras la emisión de un pulso instantáneo de CO_2 a la atmósfera, el 21.7% permanece en la atmósfera indefinidamente, el 22.4% decae exponencialmente con una escala de tiempo de 394 años, el 28.3% decae exponencialmente con una escala de tiempo de 36.5 años, y el 27.6% decae exponencialmente con una escala de tiempo de 4.30 años (Joos et al, 2013; Myhre et al, 2013b).

El CH_4 se destruye en la atmósfera (reacción con el radical OH fundamentalmente). Su vida media es de unos 9 años. Es suficiente con mantener constante (durante unos 10-20 años) la tasa anual de emisión de CH_4 a la atmósfera para que la concentración de CH_4 se mantenga constante. Las emisiones de CH_4 son naturales en un 40%, fundamentalmente procedentes de humedales y termitas, y antropogénicas en un 60%: rumiantes, explotación de combustibles fósiles, vertederos, cultivo de arroz, y quema de biomasa (Ghosh et al., 2015; WDCGG, 2017). La vida media en la atmósfera del N_2O es de 121 años. Se destruye en la estratosfera por fotolisis y por reacción química con O(1D). El 40% de sus emisiones son antropogénicas: agricultura (fertilizantes), combustión de combustibles fósiles y procesos industriales, quema de biomasa y biocombustibles…; mientras que el 60% de sus emisiones son naturales: suelos bajo vegetación natural y océanos (Stocker et al., 2013; WDCGG, 2017).

El forzamiento radiativo (RF) debido al cambio de concentración de un componente atmosférico (respecto al nivel preindustrial) es el cambio en el flujo neto radiativo hacia abajo (onda corta + onda larga; W/m^2) en la tropopausa tras permitir que las temperaturas estratosféricas alcancen el equilibrio radiativo, pero manteniendo las otras variables de estado en su valor no perturbado (preindustrial), como por ejemplo temperaturas troposféricas, vapor de agua y cobertura nubosa (Stocker et al., 2013). Aunque este concepto ha probado ser muy útil, Stocker et al. (2013) introducen un concepto mejor, el forzamiento radiativo efectivo (ERF), que incluye también los ajustes rápidos de la superficie terrestre y la troposfera, pero no los que son mucho más lentos. A la temperatura media global de la atmósfera junto a la superficie terrestre (GMST), la temperatura de los océanos y la cobertura de hielo marino no se les permite ajustarse (al llevar asociadas cambios muy lentos). En particular, son ajustes rápidos los debidos al impacto de los aerosoles en el perfil de temperatura de la atmósfera, en las propiedades de las nubes y en las capas de nieve y hielo (cambian su albedo). Esto hace que RF y ERF sean significativamente diferentes para los aerosoles antropogénicos. Para otros componentes atmosféricos, por ejemplo, los GEI, RF y ERF son muy parecidos, y es útil usar RF ya que su cálculo requiere unos recursos computacionales menores y no es afectado por cambios en las variables meteorológicas y por tanto puede aislar mejor los forzamientos pequeños. Si RF y ERF son significativamente diferentes, ERF ha mostrado ser un mejor indicador de la respuesta en la GMST, y por tanto es el indicador preferido por Stocker et al. (2013).

La figura 1.1.1 muestra ERF y RF en 2011 respecto a 1750 provocados por la variación de los distintos componentes atmosféricos respecto a 1750 (Stocker et al., 2013), e incertidumbres asociadas. En lo que respecta a los GEI bien mezclados, el RF para CO_2 es 1.82 W/m^2, incrementándose en los últimos 15 años a un ritmo ligeramente menor que 0.3 W/m^2 por década. El RF para CH_4 es 0.48 W/m^2. El RF para N_2O es 0.17 W/m_2. El RF para los halocarbonos en conjunto es 0.36 W/m^2. El RF combinado de todos los gases de efecto invernadero bien mezclados es 2.83 W/m^2. La figura 1.1.1 muestra claramente que el forzamiento debido a los gases de efecto invernadero bien mezclados es dominante. El resto de componentes serán considerados en las siguientes subsecciones.

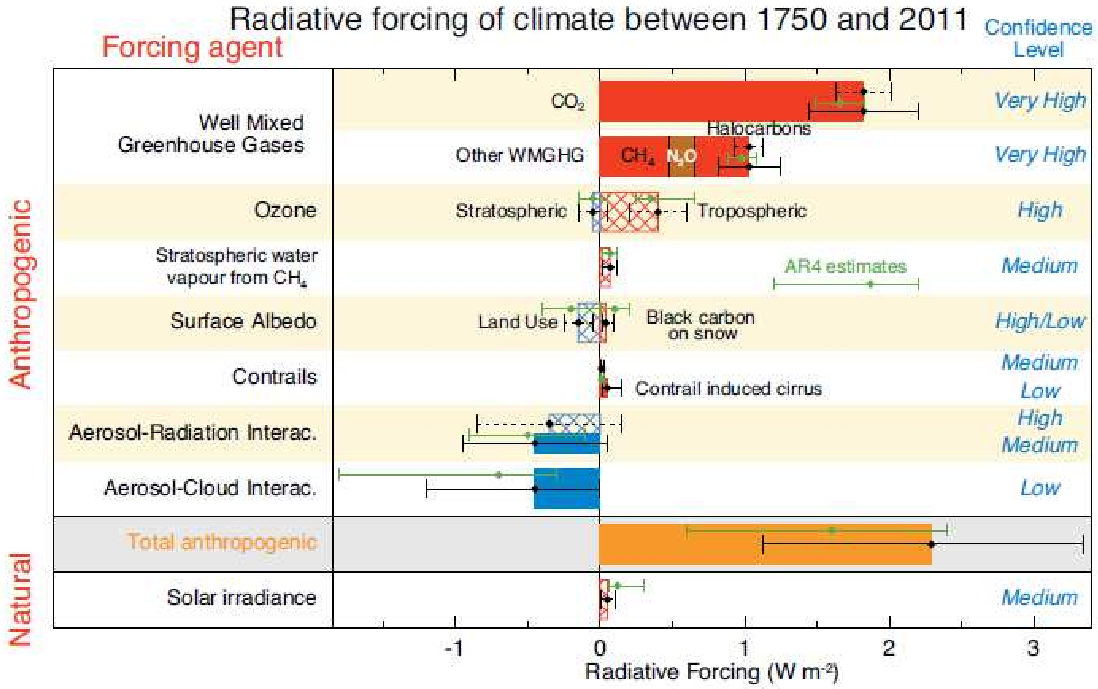

Figura 1.1.1. ERF (barras sólidas) y RF (barras rayadas) en 2011 respecto a 1750 provocados por la variación de los distintos componentes atmosféricos respecto a 1750, e incertidumbres asociadas (Stocker et al., 2013). Los diamantes verdes corresponden al RF obtenido por Solomon et al. (2007). Mitad superior de la Figura TS.6 de Stocker et al. (2013).

La figura 1.1.2 muestra ERF en 2011 respecto a 1750 provocado por la variación de los distintos componentes atmosféricos respecto a 1750 clasificados a partir de los compuestos primarios emitidos que originaron los incrementos de concentración de cada forzador (IPCC, 2013b), e incertidumbres asociadas. En lo que respecta a los GEI bien mezclados, el ERF total para CO_2 es 1.82 W/m^2, procediendo: 1.68 W/m^2 de la emisión directa de CO_2, 0.02 W/m^2 de la oxidación del CH_4 emitido a CO_2, 0.09 W/m^2 de la oxidación del CO emitido a CO_2, y 0.03 W/m^2 de la oxidación de NMVOC (compuestos orgánicos volátiles distintos del CH_4) a CO_2. El RF total para CH_4 es 0.48 W/m^2, procediendo: 0.64 W/m^2 de la emisión directa de CH4, 0.07 W/m^2 de la emisión de CO que compite con el CH4 por el OH, que es un destructor de CH4, 0.03 W/m^2 a la emisión de NMVOC y -0.25 W/m^2 a la emisión de NO_x, que tiende a aumentar la concentración de OH (Stocker et al., 2013).

El forzamiento radiativo positivo, dominado por el incremento de los gases de efecto invernadero, provoca un lento aumento de la GMST debido a la gran inercia térmica de los océanos. Tiempo de respuesta de la capa de mezcla del océano: 8.4 años; tiempo de respuesta del océano profundo: 409.5 años. El tiempo de respuesta se refiere al tiempo que tarda en absorber el 63% de la energía que debe absorber (Myhre et al., 2013b).

Conforme va aumentando la GMST, se producen las dos siguientes retroalimentaciones climáticas, que intensifican la respuesta al forzamiento. El H_2O es un gas de efecto invernadero, el que más contribuye al efecto invernadero. Sin embargo, su presencia en la atmósfera no viene determinada por sus emisiones, sino por las condiciones meteorológicas (básicamente la temperatura). Continuamente está entrando H_2O en la atmósfera por evaporación y saliendo de ella por precipitación. Retroalimentación por vapor de agua: el incremento de temperatura provocado por el aumento de concentración de los gases de efecto invernadero bien mezclados, hace que "quepa" más H_2O en la atmósfera y por tanto se refuerce el incremento del efecto invernadero. Retroalimentación por hielos polares marinos/cobertura nivosa: si el aire está más caliente, se derrite más hielo/nieve, por lo que hay menor superficie con hielo/nieve, esto disminuye el albedo, por lo que se absorbe más radiación solar y por tanto aumenta más la temperatura (Stocker et al., 2013).

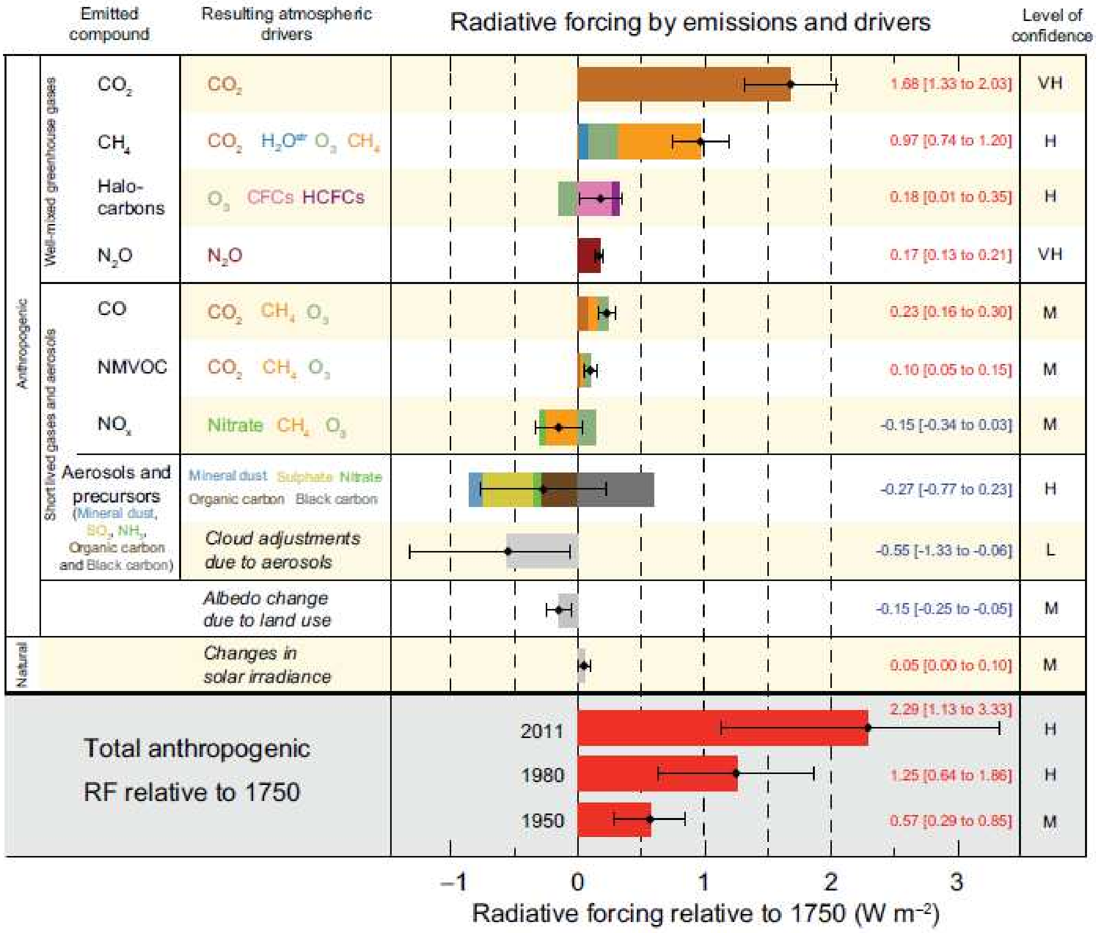

Figura 1.1.2. ERF en 2011 respecto a 1750 provocado por la variación de los distintos componentes atmosféricos respecto a 1750 clasificados a partir de los compuestos primarios emitidos que originaron los incrementos de concentración de cada forzador. Figura SPM.5 de IPCC (2013b).

Efectos fundamentales ya observados en el sistema climático (IPCC, 2013b): 1) aumento de la temperatura global de la atmósfera junto a la superficie entre 1880 y 2012: 0.85 [0.65 a 1.06] °C; 2) más del 90% de la energía debida al forzamiento radiativo durante el periodo 1971-2010 ha sido empleada en calentar los océanos; 3) disminución durante las dos últimas décadas del hielo en Groenlandia, Antártida y glaciares, y de la superficie con nieve y hielos marinos; y 4) en el periodo de 1901 a 2010, el nivel medio del mar ha subido 0.19 [0.17 a 0.21] metros, debido a la expansión térmica del océano por el calentamiento y a la mayor cantidad de agua (procedente del hielo derretido). Atribución del cambio climático: es extremadamente probable que las actividades humanas hayan causado más de la mitad del incremento de temperatura superficial global media observado entre 1951 y 2010 (IPCC, 2013b)

La sensibilidad climática utilizada por Myhre et al. (2013b) en el cálculo de los AGTPs (Potenciales de cambio Absoluto de la Temperatura Global; concepto que escapa a los propósitos de esta breve introducción) es 1.06 $K \cdot m^2/W$. La sensibilidad climática es el aumento de la GMST asociado a un forzamiento radiativo tras alcanzar el equilibrio (después de siglos). Por ejemplo, si el forzamiento radiativo que había en 2011, 2.29 W/m^2, se mantuviese constante los próximos siglos (en lugar de seguir aumentando), el aumento de temperatura tras alcanzar el equilibrio sería de 2.43 °C.

La comprensión de los ciclos de vida de estos gases de efecto invernadero atmosféricos y su interacción con los otros componentes del sistema climático (fundamentalmente la biosfera terrestre y los océanos) es importante para poder predecir escenarios de clima futuro (no basta con saber cuáles serán las emisiones antropogénicas futuras, sino que además es necesario predecir cuánto de estas emisiones permanecerá en la atmósfera). Para estudiar los ciclos de los gases de efecto invernadero, el primer paso es medir con gran exactitud la distribución espacio temporal de dichos gases en la atmósfera y los flujos superficiales de intercambio con la biosfera terrestre y los océanos. Al tener estos gases una vida larga en comparación con los tiempos de dispersión y mezcla en la atmósfera, su concentración en la atmósfera en puntos alejados de fuentes locales es muy homogénea espacialmente (Patra et al., 2014). Por tanto, si además de monitorizar el incremento global de la concentración de dichos gases en la atmósfera, se pretende obtener información sobre la distribución espacio temporal de sus fuentes y sumideros, es necesario medir con altísima exactitud dichas concentraciones atmosféricas (Chevalier et al., 2010).

1.2. Monóxido de carbono atmosférico

El monóxido de carbono (CO) afecta a la capacidad de oxidación de la troposfera, y, en particular, juega un papel importante en los ciclos del radical hidroxilo (OH), radical hidroperoxil (HO_2) y ozono (O_3); véase por ejemplo Logan et al. (1981). La vida media del CO va desde diez días sobre regiones continentales en verano hasta más de un año sobre las regiones polares en su correspondiente invierno (Novelli et al., 1992). Su relativamente corta vida media (comparada con la de los gases de efecto invernadero bien mezclados) y la distribución irregular de sus fuentes, dan lugar a grandes variaciones temporales y espaciales de la fracción molar de CO. Las mayores fuentes de CO son la quema de combustibles fósiles, la quema de biomasa, la oxidación de CH_4, y la oxidación de hidrocarburos distintos del CH_4. El mayor sumidero de CO es la reacción con OH, mientras que la deposición en superficie es un sumidero pequeño (Ehhalt et al., 2001).

El ciclo del ozono es afectado por el CO. El ozono, además de ser un gas muy reactivo que aparece en la atmósfera por reacciones fotoquímicas, es un gas de efecto invernadero. El RF debido al ozono troposférico es 0.40 W/m^2 (Figura 1.1.1); mientras que para el ozono estratosférico el RF es -0.05 W/m^2, debido a la disminución de la concentración de O_3 por la presencia de halocarbonos antropogénicos (Stocker et al., 2013).

El CO no es un gas de efecto invernadero, pero se puede considerar como un gas de efecto invernadero indirecto debido a su efecto sobre las concentraciones de CO_2, CH_4 y O_3, con un ERF neto de 0.23 W/m^2, como se detalla a continuación: 0.09 W/m^2 debidos a la oxidación del CO emitido a CO_2, 0.07 W/m^2 debidos al CH4 atmosférico que no se ha destruido por la emisión de CO que compite con el CH_4 por el OH, que es el principal destructor de CH_4, y 0.08 W/m^2 debidos a que el CO emitido actúa como precursor del O_3 (Stocker et al., 2013).

1.3. Polvo atmosférico y su impacto en: el balance radiativo, calidad del aire, medios de transporte y ecosistemas

El viento levanta polvo mineral de suelos áridos y éste queda suspendido en el aire, siendo su velocidad de sedimentación mayor cuanto mayor es el tamaño de las partículas de polvo. Las principales fuentes de polvo suficientemente fino para poder ser transportado a miles de kilómetros de distancia, se encuentran en lechos secos de antiguos lagos de cuencas endorreicas que se encuentran en zonas áridas. El norte de África, y específicamente el desierto del Sahara, es la fuente de polvo mayor y más activa del mundo (Ginoux et al., 2004, 2012; Huneeus et al., 2011).

Hay numerosos estudios que tratan el transporte de polvo mineral desde el Sahara al Atlántico Norte dentro de la Capa de Aire Sahariano (SAL), y sus impactos en regiones remotas, como el Caribe y Sudamérica (Engelstaedter and Washington, 2007; Prospero and Carlson, 1972; Prospero et al., 2014; Rodríguez et al., 2015); así como hacia el Mediterráneo (Basart et al., 2009; Pérez et al., 2006). El polvo mineral tiene un gran impacto en la calidad del aire (Escudero et al., 2007a; 2007b; Querol et al., 2009; Rodríguez et al., 2001), en la fertilización de los océanos (Ravelo-Pérez et al., 2016), y en los medios de transporte (Baddoc et al., 2013; Goudie, 2009).

El RF producido por la presencia de polvo mineral en suspensión en la atmósfera es -0.10 W/m^2 (Figura 1.1.2), y es debido a la conjunción de dos hechos: el polvo mineral aumenta la fracción de radiación solar que es devuelta al espacio por retrodispersión, y hay más polvo mineral en la atmósfera que antes de la revolución industrial debido al aumento de la desertificación, al aumento de la agricultura en zonas semiáridas, ya que ésta aumenta la cantidad de polvo emitido a la atmósfera, y a la sobre-explotación y/o mala gestión del agua produciendo el desecado de lagos y cuencas hidrográficas. La cantidad de polvo mineral en la atmósfera se ha duplicado aproximadamente durante el siglo XX (Myhre et al., 2013a).

1.4. Modelos de transporte de gases de efecto invernadero e inversión de los flujos de emisión superficiales

En esta sección, se introduce brevemente el marco teórico de la parte atmosférica de los ciclos de los gases de efecto invernadero. El transporte de gases traza en la atmósfera viene descrito por la ecuación (en derivadas parciales -EDP-) de continuidad incluyendo términos de difusión (fundamentalmente turbulenta, por cizalladura del viento y por convección térmica) y términos fuente/sumidero (Seinfeld & Pandis, 1998), actuando normalmente el gas traza como un trazador pasivo que no influye en la dinámica atmosférica (es decir, no influye sobre los campos de velocidad atmosférica -velocidad promedio y velocidad turbulenta-). Hay fundamentalmente dos métodos para calcular la evolución temporal de los gases traza en la atmósfera: el euleriano y el lagrangiano (Seinfeld & Pandis, 1998). El método euleriano resuelve mediante técnicas numéricas (normalmente diferencias finitas) la EDP de continuidad utilizando: condiciones iniciales y de contorno, el campo de velocidad promedio que produce la advección, y las propiedades turbulentas del campo de velocidad en la escala no resuelta explícitamente por el modelo, que determinarán la difusión. Por otra parte, el método lagrangiano calcula multitud de trayectorias de elementos del fluido sujetos a dos componentes de movimiento que se suman: 1) advección debida al campo de velocidad promedio y 2) advección debida a un campo de velocidad turbulento/parcialmente estocástico (cada elemento de fluido en un mismo “punto” del espacio-tiempo sobre el que se definen las magnitudes promedio sufrirá una velocidad turbulenta distinta). Este método calcula posteriormente promedios volumétricos del número de partículas (elementos de fluido); siendo algo así como una simulación de Monte-Carlo (en el sentido que se le da a dicho término en física del plasma). El método utilizado normalmente a escala global es el euleriano, siendo el lagrangiano utilizado en aplicaciones particulares en escalas espaciales locales/regionales.

Sin embargo, en el momento presente, los modelos de transporte eulerianos globales están sujetos a incertidumbres importantes debido a los errores de los campos de velocidad promedio (aunque se usen campos de reanálisis, en lugar de campos previstos) y especialmente a los errores en las parametrizaciones de los procesos de transporte turbulento a la escala no resuelta por el modelo. Desde hace unos años, es relativamente común la aplicación de métodos de inversión globales para el cálculo de flujos superficiales de gases de efecto invernadero. En estos métodos se utilizan: campos de flujos superficiales a priori (obtenidos de inventarios de emisiones y de medidas/modelos de flujos superficiales en ecosistemas terrestres y los océanos) con su correspondiente incertidumbre (normalmente alta), series temporales de observaciones atmosféricas en numerosos puntos del planeta, y un modelo de transporte (advección-difusión). Entonces, se buscan (mediante cálculo iterativo) los flujos superficiales a posteriori que minimizan la discrepancia entre las fracciones molares simuladas por el modelo de transporte y las observaciones reales, pero teniendo en cuenta una penalización proporcional a la discrepancia entre los flujos superficiales a priori y a posteriori, que tiene en cuenta la incertidumbre de dichos flujos (véase, por ejemplo, Chevallier et al., 2010).

Para la modelización del transporte de polvo mineral en la atmósfera, no basta con calcular el campo de concentración (el mapa tridimensional de los valores de la concentración del polvo), sino que es necesario además tener en cuenta el espectro en tamaño de dicho polvo en cada punto del espacio, ya que en su transporte también influye la velocidad de sedimentación, que depende del tamaño de las partículas de polvo (Seinfeld & Pandis, 1998). Muy recientemente, se han comenzado a hacer también inversiones de los flujos superficiales de emisión de polvo mineral utilizando medidas del polvo en suspensión en la atmosfera obtenidas mediante teledetección y un modelo de transporte de polvo mineral (Escribano et al., 2016).

1.5. El Observatorio Atmosférico de Izaña

El Observatorio Atmosférico de Izaña (OAI) alberga una estación global VAG (Vigilancia Atmosférica Global) de la OMM (Organización Meteorológica Mundial) que se encuentra en la cima de una montaña a 2373 metros sobre el nivel del mar en la isla de Tenerife (Canarias). La mayor parte del tiempo se encuentra por encima del nivel de una fuerte inversión térmica subtropical que hace que las condiciones de medida sean de troposfera libre del Atlántico Noreste Subtropical no influenciada por fuentes locales, especialmente durante el periodo nocturno (véase, por ejemplo, Gomez-Pelaez et al., 2013). Es por tanto un lugar óptimo para estudiar la atmósfera de fondo y el transporte de larga distancia de gases traza atmosféricos. Por otro lado, su proximidad a la zona subtropical del norte de África, hace que esta estación también sea ideal para estudiar las intrusiones en la baja troposfera (hasta unos 6 km de altitud) de la SAL hacia el Atlántico durante el verano (Cuevas et al., 2015a; Rodríguez et al., 2015).

Las actividades que se realizan en el Centro de Investigación Atmosférica de Izaña (CIAI) de la AEMET (Agencia Estatal de Meteorología; -AEMET-) están resumidas de forma sistemática y extensa en las publicaciones AEMET/OMM: Cuevas et al. (2015b) y Cuevas et al. (2017). En los siguientes capítulos de esta memoria de tesis doctoral, se expondrán detalles del programa de medida de gases de efecto invernadero del CIAI.

El OAI desempeña un papel destacado en esta tesis doctoral porque, entre otros motivos, el doctorando es funcionario del Cuerpo Superior de Meteorólogos del Estado y estuvo destinado en el CIAI, siendo el responsable científico y técnico del programa de gases de efecto invernadero del CIAI, desde 2005 a 2017. Además, el director principal de esta tesis doctoral, es el director del CIAI.

2. Objetivos

El objetivo general de esta tesis es hacer una contribución científica significativa en la medida y el transporte de gases de efecto invernadero atmosféricos, monóxido de carbono y polvo sahariano, con especial énfasis en la troposfera libre del Atlántico Noreste subtropical. Este objetivo general se ha ido en parte concretando y desarrollando en la medida de las necesidades y oportunidades que han ido surgiendo en el trabajo del doctorando como meteorólogo en el CIAI.

Los objetivos específicos se detallan a continuación:

1) Contribuir a la mejora de: las técnicas de medida in situ de gases de efecto invernadero y trazadores relacionados, la comparación entre medidas coincidentes espacial y temporalmente realizadas con distintos analizadores, el procesado de datos brutos, y/o la cuantificación rigurosa de la incertidumbre de dichas medidas.

2) Análisis y caracterización de las variaciones de gases de efecto invernadero, monóxido de carbono y/o polvo sahariano en el Observatorio Atmosférico de Izaña y la troposfera libre del Atlántico Noreste subtropical, a varias escalas temporales (diaria, sinóptica, estacional e interanual).

3) Estudio del transporte de polvo sahariano en la troposfera libre del Atlántico Norte, y de gases de efecto invernadero a escala mundial, esto último mediante un modelo euleriano de advección-difusión.

3. Metodología

Tras haber presentado aspectos introductorios de los campos de estudio en los que se enmarca el trabajo desarrollado en esta tesis doctoral, y los objetivos brevemente, procede resumir de forma didáctica la metodología utilizada en esta tesis doctoral antes de presentar los resultados. Nótese que al seguir esta memoria de tesis doctoral la modalidad de compendio de publicaciones, hay cierta redundancia entre lo presentado en este capítulo y la sección de metodología de cada uno de los artículos que componen este compendio. Sin embargo, este capítulo, cuya presencia es obligatoria por la normativa de la Universidad de Granada, da una visión integrada de los métodos utilizados directa o indirectamente en los artículos que componen esta memoria de tesis, y explora en detalle algunos aspectos que permitirán a los científicos no expertos en los temas tratados en esta memoria de tesis alcanzar un punto de partida óptimo para proceder a la lectura de los artículos del compendio.

3.1. Medida de gases de efecto invernadero atmosféricos y monóxido de carbono

Esta sección tiene como objetivo presentar una introducción a la metodología que directa o indirectamente se utiliza en el artículo de la sección 4.1, yendo en algunos aspectos más allá de lo estrictamente usado en dicho artículo, por completitud y para permitir al lector obtener una visión más amplia de los métodos utilizados en este campo de estudio.

3.1.1. El programa de medidas VAG

El programa de Vigilancia Atmosférica Global (VAG) de la Organización Meteorológica Mundial (OMM) es un esfuerzo coordinado a nivel mundial para monitorizar la composición química de la atmósfera y magnitudes físicas relacionadas con el equilibrio/forzamiento radiativo de la atmósfera. En esta memoria de tesis doctoral vamos a considerar solo las técnicas de medida de gases de efecto invernadero y de monóxido de carbono, y no las de polvo mineral, que están fuera del propósito de esta tesis. El CO es un gas reactivo, pero también actúa como gas de efecto invernadero indirecto (ver sección 1.2), por lo que también es medido con alta exactitud por la comunidad científica que se dedica a gases de efecto invernadero. El programa de medida VAG de gases de efecto invernadero también engloba las medidas de CO. En el programa VAG hay dos tipos de estaciones: las de categoría global, que han de tener condiciones de medida de fondo global (hay pocas; el OAI es una de ellas), y las de categoría regional, que tienen condiciones de medida de fondo regional (hay muchas más).

La metodología de la medida de gases de efecto invernadero es compleja, tanto en la parte instrumental como en la de procesado numérico, debido a la muy alta exactitud requerida por el programa VAG de la OMM para dichas medidas, por los motivos expuestos al final de la sección 1.1.

El programa VAG de gases de efecto invernadero dispone de Laboratorios Centrales de Calibración (CCL), uno por gas, que se encargan de mantener y propagar las correspondientes escalas de medida hasta gases patrón que se distribuyen entre las estaciones de medida. La primera labor de un CCL es la construcción de estándares primarios en aire natural del gas traza de interés, ya sea mediante la técnica manométrica, como ocurre con el CO_2 (Zhao et al., 1997), o mediante la técnica gravimétrica, como ocurre para el CH_4 (Dlugokencky et al., 2005), N_2O (Hall et al., 2007), SF_6 (hexafluoruro de azufre), y CO (Novelli et al., 1991), con trazabilidad a unidades patrón del Sistema Internacional. Una vez construidos los patrones gaseosos primarios, el siguiente paso es armonizar sus fracciones molares empleando la función respuesta obtenida al medir estos patrones con el instrumento que se va a usar para propagar la escala (Zhao et al., 2006). Las escalas se pueden propagar con mucha mayor precisión que la exactitud absoluta con la que se conocen. Por tanto, al tener todas las estaciones una trazabilidad única a los patrones mundiales de la OMM, la consistencia de las medidas entre las estaciones es muy superior a la que se obtendría si cada estación obtuviese gases patrón de sus correspondientes servicios metrológicos nacionales, obtenidos a partir de magnitudes patrón fundamentales. Nótese que la precisión crece al disminuir la dispersión en las medidas y solo se ve influida por los errores aleatorios, mientras que la exactitud también se ve influida por los errores sistemáticos, es decir, incluye también el sesgo (véase JCGM, 2008, y las referencias que contiene, para una definición precisa de estos conceptos). Los patrones gaseosos primarios, aunque se almacenan en tanques de alta presión hechos de aluminio, el material que ha demostrado ser más adecuado para minimizar la deriva en la fracción molar de los estándares, pueden derivar a lo largo de los años. Por ello, cada pocos años es necesario volver a determinar la fracción molar absoluta de los estándares para tener en cuenta posibles derivas, realizando nuevas medidas manométricas (Zhao et al., 2006) o construyendo estándares gravimétricos nuevos de comparación. En caso de que se detecte una deriva significativa en un patrón primario, dicha deriva se tiene en cuenta (la fracción molar del patrón depende del tiempo), se crea una nueva versión de la escala (revisada), y se vuelven a recalcular todas las asignaciones pasadas a patrones de nivel inferior hasta llegar a recalcular las asignaciones a las medidas ambiente. Se procede de forma análoga cuando se detectan derivas en patrones no primarios, aunque en este caso no conllevan una revisión de la escala (salvo que se trate de patrones secundarios usados por el CCL para propagar la escala). El software de procesado de datos brutos ha de construirse de forma que permita recalcular de forma rápida todas las asignaciones de fracción molar en caso de revisión de la escala de medida por el CCL, en caso de detección de deriva en los patrones de laboratorio (terciarios OMM) o en los patrones de trabajo (cuaternarios OMM).

La compatibilidad entre laboratorios requerida por VAG para la medida de gases de efecto invernadero atmosféricos viene detallada en la sección 3.1.2. Para poder alcanzar tan alto grado de exactitud es necesario: implementar sistemas de medida que funcionen de forma no comercial (los instrumentos comerciales están diseñados para ser operados de forma más sencilla pero producen datos menos exactos), conocerlos perfectamente, calibrarlos con altísima frecuencia manteniendo la cadena de calibraciones desde los estándares primarios de la OMM, y procesar los datos brutos teniendo en cuenta dicha jerarquía de calibraciones para obtener las concentraciones físicas con alta exactitud.

Otros componentes del programa VAG de gases de efecto invernadero son: WCCs (World Calibration Centres; Centros de Calibración Mundiales), congreso de expertos, SAG (Scientific Advisory Group; Grupo de Asesoramiento Científico), WDCGG (World Data Centre for Greenhouse Gases; Centro Mundial de Datos para Gases de Efecto Invernadero), Round Robins (ver más adelante), que se describen a continuación, y para los que existen componentes equivalentes en otros programas VAG. Existe un WCC para cada gas de efecto invernadero, siendo por ejemplo EMPA (Swiss Federal Laboratories for Materials Science and Technology; Laboratorios Federales Suizos para Ciencia de Materiales y Tecnología) el WCC para CO_2, CH4 y CO. Estos WCCs se dedican a realizar auditorías científicas a las estaciones VAG de categoría global fundamentalmente. La auditoría VAG del programa de gases de efecto invernadero más reciente realizada en Izaña viene detallada en Zellweger et al. (2013). En ésta, además de auditar todos los sistemas de medida de gases de efecto invernadero, se realizaron medidas de aire ambiente en paralelo con un instrumento viajero de última generación (para CO_2, CH_4 y CO) del EMPA durante varios meses, y además, un conjunto de patrones viajeros "incógnita" del EMPA fueron medidos como si fueran aire ambiente con los instrumentos de Izaña y se les asignó concentración, para compararlas a posteriori con las asignadas por el EMPA. El SAG del programa está formado por cinco científicos, y cada dos años además se realiza un congreso de expertos en la medida de CO_2, y otros gases de efecto invernadero y traza, en el que se presentan y discuten todos los avances en este campo y se consensuan y aprueban las recomendaciones de dicho grupo de expertos (WMO, 2016). Los datos procesados finales son enviados por las estaciones VAG al WDCGG del programa VAG, donde están públicamente disponibles vía web para cualquier usuario, y en particular para científicos que quieran realizar inversiones de dominio global de los flujos superficiales de gases de efecto invernadero. Otra actividad periódica importante dentro del programa VAG son las Round Robins: se llama así a cada conjunto de estándares incógnita (simultáneamente para CO_2, CH_4, N_2O, SF_6, CO…) preparados por el CCL de la NOAA (National Oceanic and Atmospheric Administration; Agencia Federal de EE.UU. para los Océanos y la Atmósfera), que se hace circular alrededor del mundo por las distintas estaciones VAG y laboratorios participantes para que dichos estándares sean medidos (calibrándolos frente a sus estándares de mayor nivel en la jerarquía VAG) y cada participante les asigne fracción molar. Cada participante envía sus resultados de medida al CCL, y una vez todos lo han hecho, el CCL compara las medidas de todos con las suyas propias y las hace públicas vía web. El propósito es chequear la capacidad de cada estación/laboratorio de propagar las escalas de la OMM. En esta web se puede acceder a los resultados de varias Round Robins, y en particular de la última realizada (la sexta): https://www.esrl.noaa.gov/gmd/ccgg/wmorr/wmorr_results.php .

3.1.2. Técnicas de medida en el Observatorio Atmosférico de Izaña

Los gases de efecto invernadero que se miden en el OAI están detallados en la Tabla 3.1.2.1, así como la instrumentación que se utiliza. Esta tabla también detalla la compatibilidad entre laboratorios requerida por VAG para la medida de gases de efecto invernadero atmosféricos (WMO, 2016). Nótese que son compatibilidades objetivo del programa, lo que no significa que sea posible conseguir dichas compatibilidades actualmente en el mundo (por ejemplo, para el N_2O aún no se ha conseguido). Como se indicó al final de la sección 1.1, estos objetivos de compatibilidad, que son mucho más exigentes de lo necesario para determinar el crecimiento anual de estos GEI en la atmósfera, pretenden que sea posible inferir información sobre la distribución espacial de las fuentes y sumideros de GEI a partir de los pequeños gradientes espaciales medidos en la atmósfera para estos GEI bien mezclados.

La técnica NDIR (Infrarroja no dispersiva) se basa en la emisión de radiación IR en la banda de 4.2 µm del CO_2, la atenuación de ésta por la absorción producida por el CO_2 contenido en el aire que fluye por dos celdas, una de análisis y otra de referencia, y la medida independiente de la radiación infrarroja que llega al final de cada una de estas dos celdas. Por la celda de referencia siempre fluye un mismo gas, a muy bajo flujo, mientras que por la celda de análisis fluye aire ambiente, al que se le ha extraído la humedad mediante una trampa de vidrio a -70^{o}C, salvo durante 9 minutos cada hora durante los cuales fluyen tres patrones de trabajo (3 minutos cada uno) construidos en Izaña. Estos patrones de trabajo son calibrados cada 2 semanas frente a los patrones de laboratorio, adquiridos al CCL de CO_2. La respuesta bruta de los sensores infrarrojos durante la medida de los distintos patrones y del aire ambiente, se utiliza para determinar las fracciones molares de los patrones de trabajo (en las calibraciones cada 2 semanas; ya que pueden sufrir deriva a lo largo de los meses que duran en uso), calcular continuamente la función respuesta del instrumento (que deriva bastante), y asignar fracción molar a las medidas ambiente. Para más detalles sobre esta técnica implementada en Izaña, véanse Gomez-Pelaez & Ramos (2011), Gomez-Pelaez et al. (2014), y Gomez-Pelaez et al. (2016).

Molécula	Desde el año	Valor medio medido en 2016 (OAI)	Compatibilidad entre laboratorios requerida por VAG	Exactitud relativa requerida (suponiendo que no hay interferencias)	Analizador
CO2	1984	404.3 ppm	+-0.1 ppm (Hemis. Norte)	0.025%	NDIR, y CRDS desde 2016
CH4	1984	1880 ppb	+-2 ppb	0.11%	GC-FID, y CRDS desde 2016
N2O	2007	329.7 ppb	+-0.1 ppb	0.030%	GC-ECD
SF6	2007	9.07 ppt	+-0.02 ppt	0.22%	GC-ECD
CO	2008	99.2 ppb	+-2 ppb	2.0%	GC-RGD, y CRDS desde 2016

Tabla 3.1.2.1. Gases de efecto invernadero atmosféricos medidos con analizadores in situ en el OAI e información complementaria sobre dichas medidas; compatibilidad entre laboratorios requerida por el programa VAG de la OMM y exactitud relativa requerida (relativa al promedio medido en el OAI durante el año 2016). El CO no es un gas de efecto invernadero, pero influye en el ciclo del CH4, y se mide en el CIAI siguiendo una metodología semejante a la del resto de gases.

La cromatografía de gases (GC) se basa en la inyección de una muestra de aire, a la que se ha extraído el vapor de agua previamente, en una corriente de gas portador de alta pureza (por ejemplo, nitrógeno), y el paso de dicho flujo por dos columnas cromatográficas rellenas de un material poroso, que están en el interior de un horno cromatográfico para mantenerlas a la temperatura deseada. Los distintos gases traza se desplazan a lo largo de dichas columnas a una velocidad diferente, debido a los diferentes equilibrios que se establecen entre el gas traza en la fase gaseosa y el atrapado en los poros del material empaquetado en las columnas. La constante de equilibrio es distinta para cada gas traza y además depende de la temperatura. En general, cuanto mayor sea la temperatura, más desplazado estará el equilibro hacia la fase gaseosa y más rápido se desplazará el gas traza a lo largo de las columnas. El resultado es que, al final de las columnas, los gases traza de la muestra ambiente salen por separado en distintos instantes de tiempo, a pesar de que entraron mezclados juntos, y su presencia es registrada por un detector emplazado en dicho punto. Lo que registra el detector en función del tiempo es lo que se llama cromatograma, y en él se ven los picos cromatográficos separados, correspondiendo cada uno de ellos a un gas traza. Para más detalles sobre los fundamentos de este proceso de separación, véase Gomez-Pelaez (2009a) y las referencias que contiene. Además, el uso de dos columnas y una válvula de inyección apropiada con suficientes puertos, permite establecer un flujo inverso (back-flush) durante la segunda parte del ciclo cromatográfico, que hace que los compuestos más lentos salgan por donde entraron y así no interfieran en el siguiente ciclo cromatográfico.

En Izaña hay tres cromatógrafos: un GC Dani 3800 con un detector FID (Detector de Ionización de Llama) para la medida del CH_4, un GC Varian 3800 con dos detectores correspondientes a circuitos cromatográficos independientes: un FID (para CH_4) y un ECD (Detector de Captura Electrónica) para la medida de N_2O y SF_6, y un RGA-3 con un detector RGD (Detector de Gas por Reducción) para la medida de CO. Para más detalles sobre estas técnicas de medida en Izaña, véanse Gomez-Pelaez et al. (2006), Gomez-Pelaez et al. (2009b), Gomez-Pelaez & Ramos (2011), Gomez-Pelaez et al. (2012), Gomez-Pelaez et al. (2013), Gomez-Pelaez et al. (2014), y Gomez-Pelaez et al. (2016).

La nueva técnica de medida CRDS, implementada recientemente en Izaña, se detalla en la sección 3.1.4.

3.1.3. Cuantificación de la incertidumbre de las medidas

Se requiere que las medidas de gases de efecto invernadero efectuadas en el seno del programa VAG sean muy exactas y precisas, por los motivos ya mencionados previamente. Esos mismos motivos hacen necesario la implementación de métodos para determinar hasta qué punto se están consiguiendo los objetivos de compatibilidad establecidos por VAG y estimar la incertidumbre de las medidas.

La compatibilidad en las medidas de los distintos laboratorios se puede determinar mediante diversos métodos: las Round Robins (ya mencionadas en la sección 3.1.1), las auditorías de los WCCs (ya mencionadas en la sección 3.1.1), la medida de matraces (aire contenido en matraces estancos) llenados con aire procedente del mismo patrón gaseoso, la comparación entre las medidas continuas realizadas in situ en una estación y las medidas realizadas por otro laboratorio en matraces con aire ambiente muestreado en la misma estación (por ejemplo, en Izaña se muestrean cada semana simultáneamente dos matraces para NOAA-ESRL-GMD-CCGG (Earth System Research Laboratory-Global Monitoring Division-Carbon Cycle and Greenhouse Gases); https://www.esrl.noaa.gov/gmd/ccgg/flask.php), y la comparación de las medidas continuas de dos instrumentos distintos en una misma estación, entre otras.

Los métodos descritos en el párrafo previo permiten determinar la compatibilidad entre laboratorios: bias (sesgo) entre ellos a distintas escalas temporales y precisión de las medidas (dependiendo de la frecuencia de aplicación del método, la frecuencia de medida y la duración del periodo de promediado de medidas o diferencias usado), aunque no la exactitud de éstas; y, por tanto, en cierto modo, pueden dar una estimación muy grosera de la incertidumbre de la medida. La forma más rigurosa (y compleja) de determinar la incertidumbre en las medidas es utilizar técnicas de estadística inferencial para ir propagando la incertidumbre asociada a los diferentes componentes del sistema de medida, incluyendo la de los gases patrón en los sucesivos niveles de propagación de la escala, y la del cálculo de la función respuesta de los instrumentos, siguiendo las recomendaciones generales consensuadas a nivel internacional por las organizaciones metrológicas (JCGM, 2008).

3.1.4. Implementación de la técnica CRDS en Izaña

Como se indicó en la sección 3.1.2, en el Observatorio de Izaña existen varios instrumentos para la medida de GEI basados en las técnicas NDIR y cromatografía de gases, muchos de ellos con más de quince años de antigüedad. A finales del año 2015, se adquirió un nuevo instrumento basado en la técnica CRDS ("Cavity Ring-Down Spectroscopy"), con cargo al proyecto de infraestructuras "Equipamiento para la Monitorización e Investigación de Gases de Efecto Invernadero y Aerosoles en la estación Global VAG (Vigilancia Atmosférica Global) de Izaña (Tenerife)", con referencia: AEDM13-3E-1773, financiado por el Ministerio de Economía y

Competitividad con Fondos F.E.D.E.R. El nuevo analizador permite medir simultáneamente in situ, con altísima exactitud, las fracciones molares atmosféricas de dióxido de carbono (CO_2), monóxido de carbono (CO), metano (CH_4) y vapor de agua (H_2O).

Las partes fundamentales del instrumento son: 1) una cavidad óptica (de volumen interno menor de 35 ml) con espejos de alta reflectividad que permite caminos ópticos efectivos de medida de hasta 20 km; 2) un sistema que controla la temperatura y presión de la cavidad con una precisión de +-0.005 ºC y +-0.0002 atm, respectivamente; 3) tres láseres monocromáticos a los que el sistema de control va cambiando la longitud de onda utilizando un monitor de longitud de onda de alta precisión (+- 2 MHz); y 4) un foto-detector rápido que mide la pequeña intensidad de radiación que escapa de la cavidad a través de uno de los espejos. Los láseres van funcionando cíclicamente de forma que en cada instante de tiempo solo hay uno trabajando. Cada láser trabaja de manera pulsada, y lo que mide el sistema periódicamente es la curva de decaimiento temporal (muestreada con una frecuencia temporal de 25 MHz) de la intensidad que sale de la cavidad cada vez que el láser se apaga. El tiempo de decaimiento depende entre otras variables del coeficiente de absorción de los gases a la longitud de onda seleccionada y de sus concentraciones (este método no se ve afectado por las variaciones temporales de intensidad de la fuente láser). El instrumento va cambiando la longitud de onda del láser en uso, de forma que obtiene un espectro en una pequeña región espectral que incluye una o varias líneas espectrales (de los distintos gases cuya fracción molar se quiere medir). A partir de las alturas de las distintas líneas espectrales, el instrumento calcula las fracciones molares de los gases que producen dichas líneas.

La presencia para cada gas de un valor de referencia fijo (el valor cero: línea espectral con altura cero) y la gran estabilidad temporal de la función respuesta espectral del tiempo de decaimiento, hacen que la respuesta de este instrumento sea mucho más estable en el tiempo que la de los NDIRs y los GCs, por lo que el uso requerido de gases patrón es mucho menos frecuente y por tanto mucho menor su consumo. Además, el espectrómetro no requiere el uso de gases cromatográficos (gases portadores necesarios para los GCs, y H_2 y aire sintético necesarios para el detector FID).

Instalamos el instrumento en Izaña a finales del año 2015 tras realizarle los tests de aceptación. Gomez-Pelaez et al. (2017) describen dichos tests de aceptación, el esquema numérico de procesado de datos brutos implementado, las funciones respuesta usadas, los resultados de calibración, la corrección por vapor de agua implementada (no es estrictamente necesario secar el aire ambiente que se mide, aunque se hace desde finales de noviembre de 2016), la estadística de inyecciones de gases "target", las medidas de aire ambiente realizadas entre diciembre de 2015 y julio de 2017, y su comparación con las otras medidas in situ realizadas en Izaña.

3.1.5. Descomposición de las series temporales de dióxido de carbono, metano y monóxido de carbono de Izaña

Como se mencionó en la sección 1.5, en el Observatorio Atmosférico de Izaña las medidas nocturnas (desde las 20:00 UTC del día previo hasta las 08:00 UTC del día considerado) son las más representativas de la troposfera libre del Atlántico Noreste subtropical. Durante el día, el calentamiento del suelo debido al sol genera una brisa anabática que asciende ladera arriba y es capaz de atravesar la inversión térmica subtropical, transportando por tanto aire procedente de la parte baja de Tenerife hasta Izaña. Sin embargo, durante la noche ocurre el proceso opuesto: el suelo se enfría por emisión infrarroja y se genera una brisa catabática, que transporta aire ladera abajo. Como Izaña está en la cresta de una montaña, este proceso favorece la llegada de aire de la troposfera libre, debido a la divergencia asociada a la brisa en la cresta de la montaña y consiguiente subsidencia sobre la cresta. Por todo lo anterior, se consideran las medidas tomadas en el periodo 20:00 – 08:00 UTC como representativas de condiciones de fondo de troposfera libre, y son las que se utilizan para calcular los valores medios diarios y con ellos los valores medios mensuales.

Las figuras 3.1.5.1, 3.1.5.2 y 3.1.5.3 muestran las series de medias diarias nocturnas (20:00-08:00 UTC) de CO_2, CH_4 y CO atmosféricos medidos en el Observatorio de Izaña (en rojo), y tendencia interanual (en azul) calculada a partir de las medidas como se indica a continuación.

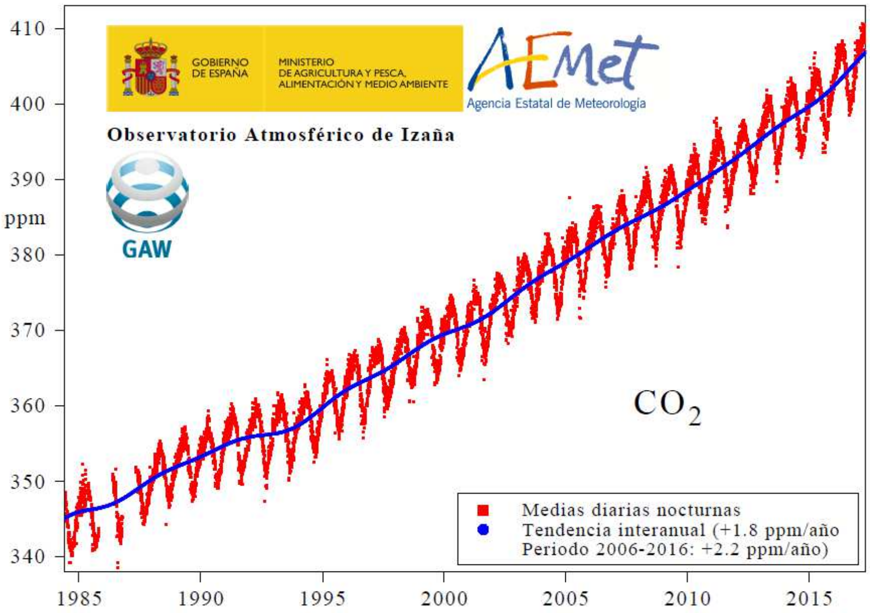

Figura 3.1.5.1. Serie de medias diarias nocturnas (20:00-08:00 UTC) de CO_2 atmosférico medido en el Observatorio de Izaña (en rojo), y tendencia interanual (en azul) calculada a partir de las medidas como se indica en el texto principal de esta memoria.

Descomponemos cada serie de valores nocturnos en tres: tendencia interanual, ciclo anual (con amplitud y fase constante a lo largo de toda la serie) y residuo, siguiendo el método introducido por Gómez-Peláez et al. (2005), Gómez-Peláez et al. (2010), y Cuevas et al. (2013). En concreto, realizamos un ajuste por mínimos cuadrados de los datos diarios a la función:

$$f(t) = a_1 + a_2 t + a_3 t^2 + \sum_{i=1}^{p} \left[b_i \cos(\omega_i t) + c_i \sin(\omega_i t) \right] + \sum_{j=1}^{4} \left[d_j \cos(k_j t) + e_j \sin(k_j t) \right]$$

donde: *t* es el tiempo en días (*t*=1 para el 1 de enero de 1984 para CO_2 y CH_4 en Izaña); a_1, a_2, a_3, b_i y c_i son los parámetros de la tendencia interanual, que han de ser determinados; *p* se elige de forma que el armónico de Fourier de menor periodo esté en el rango 2-3 años y el ajuste sea visualmente bueno; d_j y e_j son los parámetros del ciclo anual (que se supone constante), que han de ser determinados; $\omega_i = 2\pi i / N$ con *N* igual al número de días en el periodo de años considerado; $k_j = 2\pi j / T$ con *T*=365.25 días.

Resumiendo, para la tendencia interanual, se utilizan armónicos de Fourier de periodo mayor de 2-3 años (dependiendo del análisis concreto) y una función cuadrática. Los armónicos sirven para describir los detalles en escalas de tiempo mayores de 2-3 años, pero al ser periódicos, se requiere también usar una función cuadrática. El término cuadrático es importante, ya que una función lineal por sí sola, forzaría que la derivada fuera periódica en los extremos de la serie, y generaría importantes efectos irreales de borde. Para el ciclo anual, se usan los dos armónicos de Fourier de periodo anual, y sus tres primeros sub-armónicos. Para el cálculo de los coeficientes de todos los términos mencionados, se utiliza un ajuste por mínimos cuadrados de los datos nocturnos a la función suma de los términos mencionados. La ventaja de hacerlo así y no mediante una transformada de Fourier después de haber quitado la tendencia cuadrática de la serie, es que en caso de que la serie de medida tenga lagunas, lo que es bastante habitual, no es necesario rellenar dichas lagunas para poder proceder con el análisis. Los residuos del ajuste por mínimos cuadrados son la tercera sub-serie mencionada.

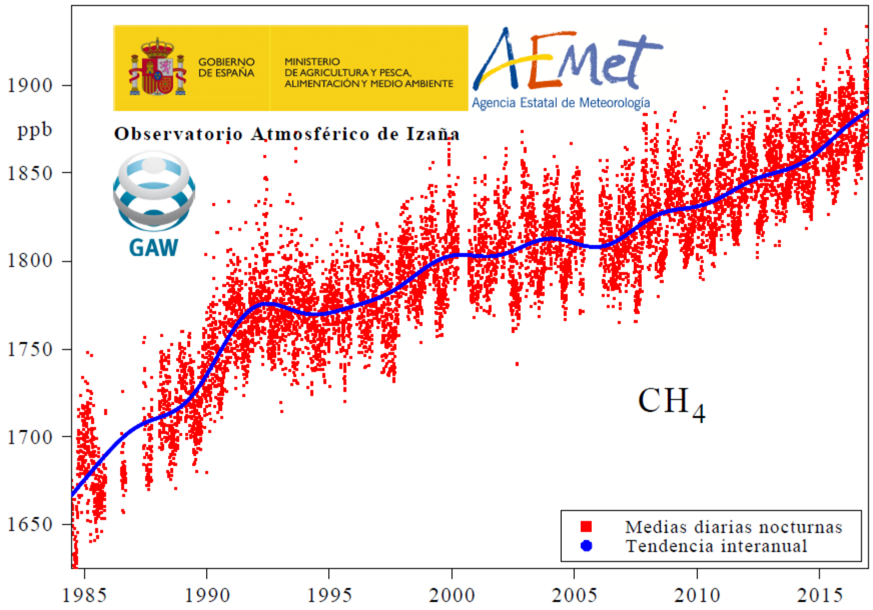

Figura 3.1.5.2. Serie de medias diarias nocturnas (20:00-08:00 UTC) de CH_4 atmosférico medido en el Observatorio de Izaña (en rojo), y tendencia interanual (en azul) calculada a partir de las medidas como se indica en el texto principal de esta memoria.

La figura 3.1.5.4 muestra los ciclos anuales de CO_2, CH_4 y CO en Izaña, obtenidos en la descomposición de las series mencionada previamente. El ciclo anual del CO_2, tiene el máximo a primeros de mayo y el mínimo a mediados de septiembre. El motivo es qué durante el otoño y el invierno del hemisferio norte, las plantas producen una emisión neta de CO_2 a la atmósfera mediante la respiración y la descomposición de material vegetal, mientras que en la primavera y el verano, las plantas, durante la fotosíntesis, absorben CO_2 atmosférico y lo combinan con agua para generar materia vegetal. Los ciclos anuales del CH_4 y del CO vienen fundamentalmente determinados por el ciclo anual del causante de su principal sumidero, el radical hidroxilo, aunque en menor medida también por la estacionalidad de sus fuentes. El radical hidroxilo, para su creación en la atmósfera, depende del flujo de radiación solar ultravioleta, que sufre un ciclo estacional, siendo el máximo en el solsticio de verano, y el mínimo en el solsticio de invierno.

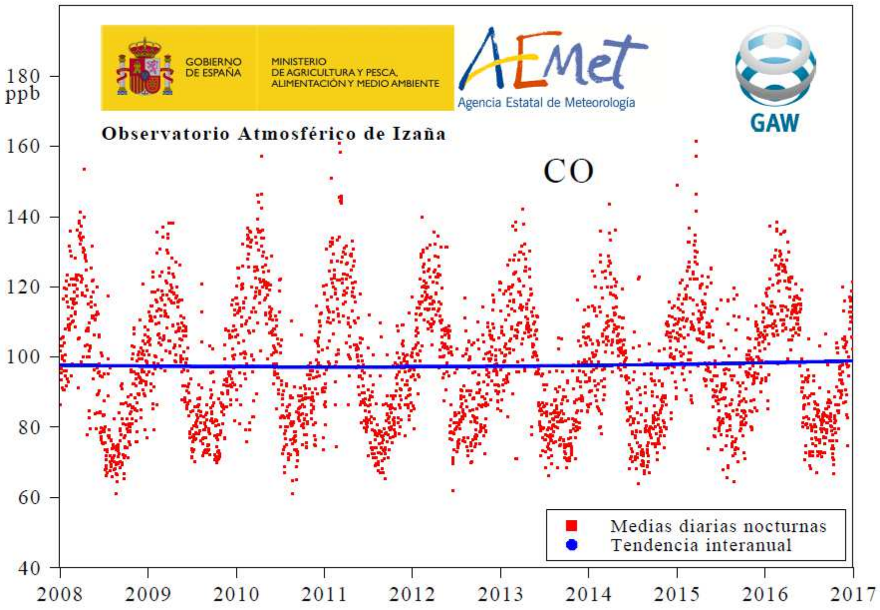

Figura 3.1.5.3. Serie de medias diarias nocturnas (20:00-08:00 UTC) de CO atmosférico medido en el Observatorio de Izaña (en rojo), y tendencia interanual (en azul) calculada a partir de las medidas como se indica en el texto principal de esta memoria.

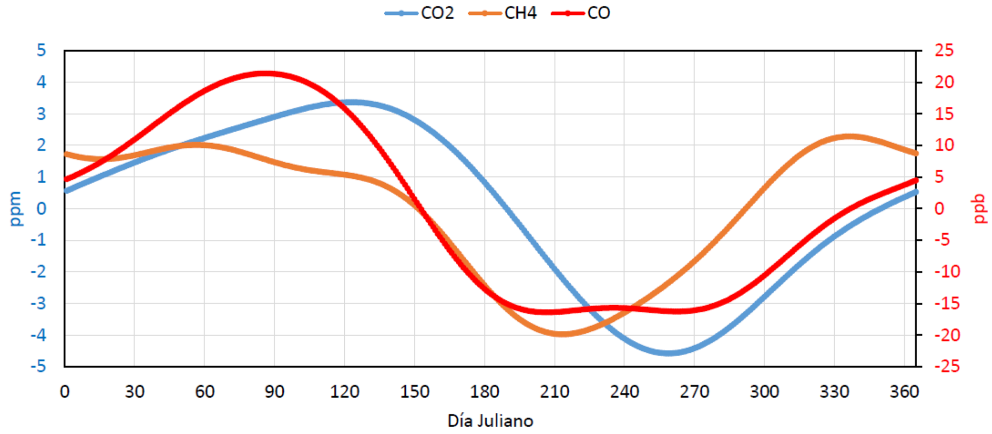

Figura 3.1.5.4. Ciclo anual obtenido en la regresión para cada uno de los gases: CO_2 (en azul y con eje de ordenadas izquierdo), CH_4 (en naranja y con eje de ordenadas derecho) y CO (en rojo y con eje de ordenadas derecho).

3.2. Modelos de transporte de gases de efecto invernadero e inversión de los flujos de emisión superficiales

El método para el estudio del ciclo del CH_4 que se utiliza en uno de los artículos que conforman el compendio de esta memoria de tesis doctoral (sección 4.2) es el siguiente. Se utilizan campos de flujos superficiales a priori obtenidos de inventarios de emisiones y/o de medidas/modelos de flujos superficiales en ecosistemas terrestres y los océanos, y un modelo de transporte (advección-difusión) “hacia adelante en el tiempo” (“forward model”). Los resultados de la simulación se comparan con series temporales de observaciones atmosféricas en numerosos puntos del planeta. En las próximas subsecciones, se mencionan brevemente estos elementos para el caso del CH_4. Además, por completitud (para permitir al lector obtener una visión más amplia de los métodos utilizados en este campo de estudio), también se menciona brevemente el caso en el que además se realiza una inversión de flujos superficiales: modificar los flujos superficiales a priori (dentro de su rango de incertidumbre) de forma que los campos atmosféricos simulados sean más compatibles con las observaciones atmosféricas de dichos gases.

3.2.1. Flujos superficiales e inventarios de emisiones

En el artículo de la sección 4.2, se utiliza el inventario EDGAR v4.2 (EC-JRC/PBL, 2011) para las fuentes antropogénicas de CH_4, mientras que para el CH_4 procedente de la quema de biomasa y de fuentes naturales se usa Bousquet et al. (2011), así como para la absorción de CH_4 por el suelo (debida a bacterias metanotróficas). La combinación de ambos inventarios permite estudiar por separado el impacto de muchos sectores de emisión (18 en total).

EDGAR ("Emissions Database for Global Atmospheric Research") es un proyecto conjunto entre la Comisión Europea-JRC (Joint Research Centre) y la Agencia de Evaluación del Medioambiente de Holanda (PBL). EDGAR calcula las emisiones antropogénicas de los distintos gases de efecto invernadero, precursores de ozono, material particulado… separadamente por tipo de fuente a escala mensual, con un método genérico que se aplica de forma consistente a todos los países del mundo y teniendo en cuenta la distribución geográfica de los lugares de emisión (tamaño de celda 0.1°x0.1° en la rejilla).

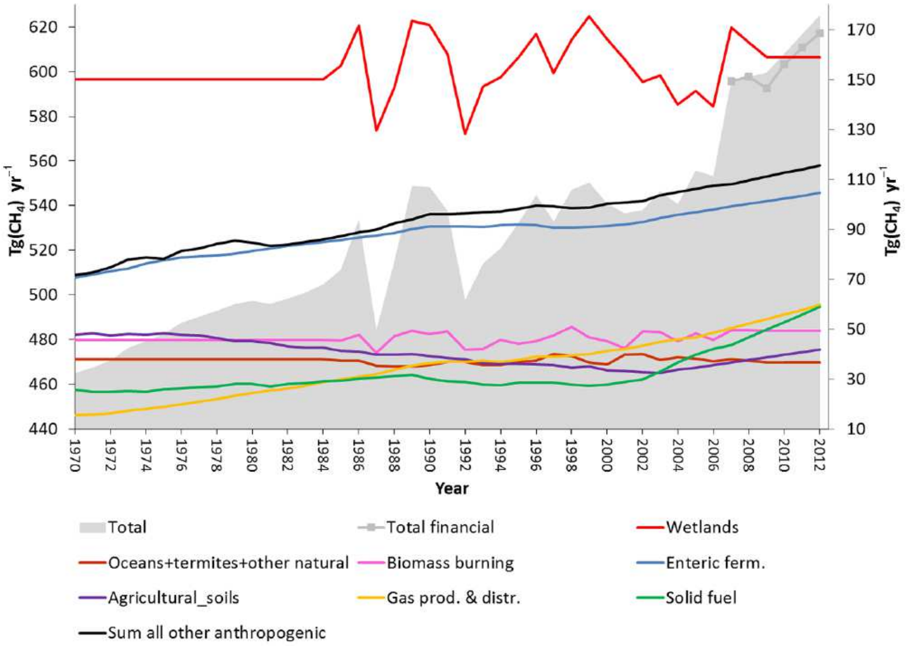

Figura 3.2.1.1. El área gris sombreada muestra la emisión total anual (eje de ordenadas de la izquierda), mientras que las líneas de colores muestran la emisión anual por sectores principales (eje de ordenadas de la derecha). La figura procede de Dalsøren et al. (2016), uno de los artículos que forman el compendio de esta memoria de tesis doctoral (véase sección 4.2).

El inventario EDGAR v4.2 cubre el periodo 1970-2008 mientras que Bousquet et al. (2011) cubre el periodo 1984-2009. Como el artículo de la sección 4.2 cubre el periodo 1970-2012, fue necesario realizar extrapolaciones para los años no cubiertos por estos inventarios (véanse los detalles en el artículo de la sección 4.2). La figura 3.2.1.1 muestra la emisión total anual y por sectores para el periodo considerado. Hay un importante aumento de las emisiones de CH_4 desde 1970 a 2012, sin embargo, en escalas de tiempo de 1-4 años, hay una gran variabilidad, presentándose incluso periodos con decrecimiento en las emisiones. Esto ocurre debido a la gran variabilidad interanual de las emisiones naturales, especialmente las de los humedales, que son los que producen las mayores emisiones.

Las variaciones interanuales de los humedales tienden a estar anti-correlacionadas con el índice MEI (Multivariate ENSO Index) de ENSO (Hodson et al., 2011), El Niño-Southern Oscillation (la teleconexión más importante del sistema climático). Las emisiones en los trópicos constituyen el 44% de las emisiones totales de CH_4 de los humedales. Durante El Niño, hay menos precipitación en los trópicos, se reduce la extensión de los humedales, y también su emisión de CH_4. En los años posteriores a la erupción del Pinatubo en 1991 (Dutton and Christy, 1992), la temperatura global sufrió un descenso momentáneo, y disminuyeron las emisiones naturales de CH_4 (Bândă, 2013) En los noventa, el crecimiento de las emisiones antropogénicas de CH_4 fue pequeño, principalmente debido al colapso de los países sucesores de la antigua Unión Soviética. Entre los años 2000 y 2006, las emisiones totales de CH_4 permanecieron bastante estables, debido al decrecimiento de las emisiones de los humedales provocado por las condiciones secas en los trópicos en combinación con un incremento de las emisiones antropogénicas. Desde 2006, hay un crecimiento fuerte en las emisiones totales de CH_4, debido a la gran emisión de los humedales y al crecimiento continuado de las emisiones antropogénicas. El abrupto incremento de las emisiones en 2007 se explica principalmente por la alta emisión de los humedales, provocada por las altas temperaturas en latitudes altas del hemisferio norte y las condiciones húmedas en los trópicos (Bousquet et al., 2011). La fermentación entérica (debida a rumiantes) es la principal fuente antropogénica de CH_4 y ha crecido sostenidamente durante todo el periodo de estudio (del artículo de la sección 4.2) excepto durante parte de los noventa. Otros sectores importantes de emisión antropogénica de CH_4 como: gas, combustibles sólidos (principalmente carbón), y suelos agrícolas (principalmente los dedicados al arroz), tienen en común un crecimiento sustancial durante la última década, aunque en el resto del periodo de estudio considerado tienen un comportamiento heterogéneo, incluso de decrecimiento parte del tiempo. La figura 3.2.1.1 muestra bajo la denominación “Sum all other antropogenic” (suma del resto de emisiones antropogénicas) las emisiones del resto de sectores: industrial, residencial, residuos, algunos combustibles… que resultan tener en total el mismo orden de magnitud que la fermentación entérica. El crecimiento de este conjunto de sectores es bastante estable y moderado, pero con algunas interrupciones: hubo decrecimientos temporales tras la crisis del petróleo de 1973 y la crisis energética de 1979. Además, el crecimiento durante los noventa fue pequeño.

3.2.2. “Forward model”

Como se mencionó en la sección 1.4, el “forward model” puede ser euleriano o lagrangiano. Vamos a mencionar en esta subsección el modelo euleriano empleado en el artículo de la sección 4.2 que forma parte del compendio de artículos de esta memoria de tesis doctoral. En la sección 3.2.5 se considera un caso que combina un modelo euleriano y otro lagrangiano.

El “forward model” utilizado en la sección 4.2 es el modelo Oslo CTM3 (Søvde et al., 2012), que no solo es un modelo de transporte 3-D, sino que además incluye química atmosférica. La versión utilizada engloba la troposfera y la estratosfera y tiene en cuenta su acoplamiento. El modelo considera 109 especies químicas activas que afectan al CH_4 y a la capacidad de oxidación de la atmósfera.

Para ejecutar el modelo, se utilizan los campos tri-horarios de pronóstico meteorológico del modelo IFS (Integrated Forecast System; Sistema de Predicción Integrado) del ECMWF (European Centre for Medium-Range Weather Forecasts; Centro Europeo de Predicción a Plazo Medio), que se producen diariamente con un spin-up de 12 horas a partir del análisis del mediodía del día previo, y que son ensamblados para dar unos campos meteorológicos uniformes del año completo. Es necesario usar los pronósticos porque hay campos meteorológicos, como los flujos de masa convectivos, que no están disponibles en los reanálisis, y porque para mucha de la física es necesario disponer de campos integrados en el tiempo en lugar de valores instantáneos a ciertas horas (por ejemplo, campos de precipitación, flujos convectivos, nubes 3-D…). El modelo Oslo CTM3 tiene 60 niveles en la vertical, como el IFS, y un rejilla gaussiana horizontal de resolución T42 (2.8^{o}x2.8^{o} aproximadamente). El paso típico de tiempo en la integración es de 60 minutos. Los esquemas numéricos de advección a gran escala, transporte convectivo, mezcla en la capa límite planetaria, deposición seca y húmeda, foto-disociación y emisión de NO_x por rayos, vienen detallados en Søvde et al. (2012).

Como ya se mencionó en las secciones 1.1 y 3.1.5, el principal sumidero de CH_4 es su oxidación con el radical hidroxilo, fundamentalmente en la troposfera. Aproximadamente, el 90% del CH_4 atmosférico que se destruye lo hace mediante esta reacción química (Ghosh et al., 2015). El 10% restante, aproximadamente, es destruido por bacterias metanotróficas en suelos (ya mencionado en la sección 3.2.1), la reacción con radicales de cloro, y la reacción con átomos de oxígeno electrónicamente excitados, $O(^1D)$, en la estratosfera (Ghosh et al., 2015); contribuyendo a la destrucción del CH_4 (en los ochenta) en un 5.7%, 2.9% y 1.5%, respectivamente. Las tasas de reacción con los radicales hidroxilo y con los radicales de cloro dependen de la temperatura, creciendo con ésta (la temperatura está en el denominador del exponente negativo de una función exponencial).

3.2.3. Modelo conceptual para comprender la evolución del metano en la atmósfera

Además de tener fuentes y sumideros superficiales, el CH_4, a diferencia del CO_2, es destruido en el seno de la atmósfera, por lo que su comportamiento en ésta es más complejo que el del CO_2. En esta subsección, presentamos algunos razonamientos matemáticos y físicos para la atmósfera en global, con el fin de construir un modelo conceptual que permita comprender como evoluciona el CH_4 en la atmósfera, antes de tratar el caso real en el que el CH_4 es inhomogéneo en las 3 dimensiones espaciales y es transportado espacialmente.

Considerando la atmósfera en su conjunto, la masa total de CH_4 en la atmósfera, B, se relaciona con la emisión total de CH_4 a la atmósfera, E, y la pérdida total de CH_4 en la atmósfera, L, mediante la ecuación de conservación de la masa:

$$\frac{dB}{dt} = E - L \qquad (1).$$

B se puede relacionar, de forma aproximada, con la fracción molar seca media de CH_4 en las proximidades de la superficie, [CH_4], mediante un factor multiplicativo, *H*,

$$B = H \cdot [CH_4] \qquad (2),$$

siendo H igual a 2.77 TgCH4·ppb^{-1} (Fung et al., 1991; Ghosh et al., 2015). Como se ha indicado en la subsección 3.2.2, aproximadamente el 94% de la destrucción de CH_4 atmosférico tiene lugar mediante reacción química en el seno de la atmósfera, siendo la tasa de destrucción proporcional a la propia fracción molar de CH_4. Hacemos la siguiente aproximación en el resto de esta subsección:

$$L = K \cdot B \qquad (3),$$

siendo *K* el inverso de la vida media del CH_4 en la atmósfera. Usamos para la vida media el valor 9.1 años, obtenido (aproximadamente) de la Figura 3 de Ghosh et al. (2015) considerando el promedio del periodo 1970-2010, que da un valor para *K* de 0.11 año^{-1}.

En caso de que se alcance un equilibro entre las fuentes y sumideros de CH_4, la masa total de éste en la atmósfera no varía en el tiempo, de acuerdo a la Ec. (1), cumpliéndose para su valor de equilibrio, B_{eq},

$$B_{eq} = \frac{E}{K} \qquad (4).$$

En la actualidad, estamos próximos al equilibrio, y de hecho durante el periodo 2000-2006 hubo cuasi-equilibrio (véase la Figura 3.1.5.2). Vamos a ver que esta afirmación de proximidad al equilibrio está de acuerdo con los siguientes hechos indicados en WMO (2017): actualmente el 40% de las emisiones de CH_4 son naturales y el 60% antropogénicas (aproximadamente), y la concentración preindustrial (que estaba en equilibrio) era de 722 ppb (básicamente solo había emisiones naturales, parecidas en valor a las actuales) y la actual es de 1853 ppb (en 2016). Teniendo en cuenta las Ecs. (2) y (4) se tendría que cumplir, en caso de equilibrio, que

$$\frac{[CH_4]_{pre}}{[CH_4]_{act}} \cong \frac{E_n}{E_n + E_a} \qquad (5),$$

donde el subíndice: *pre* indica preindustrial, *act* indica actual, *n* indica natural y *a* indica antropogénico; y efectivamente es así, ya que el primer cociente resulta ser 0.39, mientras que el segundo vale 0.4.

Para comprender el comportamiento del CH_4 en la atmósfera cuando está fuera del equilibrio, vamos a descomponer *B* de la siguiente forma:

$$B = B_{eq} + \Delta B \qquad (6).$$

Sustituyendo la Ec. (6) en la Ec. (1) y usando las Ecs. (3) y (4) se obtiene

$$\frac{d\Delta B}{dt} = -K \cdot \Delta B - \frac{1}{K}\frac{dE}{dt} \qquad (7),$$

que muestra que *ΔB* tiende a cero por relajación exponencial con tiempo característico K^{-1}, pero tiene como “fuente” las variaciones en el tiempo de las emisiones. Si las variaciones de las emisiones tienen un tiempo característico mucho mayor que K^{-1}, estaremos muy cerca del valor de equilibrio (*ΔB* =0), mientras que si tienen un tiempo característico mucho menor que K^{-1}, estaremos en general muy alejados del equilibrio. Ese término se puede interpretar como la “velocidad” a la que se aleja el nuevo estado de equilibrio cuyo valor está cambiando, mientras que el primer término se interpreta como la "velocidad" a la que se acerca la atmósfera al estado de equilibro debido a que la destrucción de CH_4 es menor (mayor) que la emisión de éste hacia la atmósfera, al encontrarse ésta por debajo (encima) del valor de equilibrio.

Consideramos por último el caso en el que las emisiones crecen linealmente en el tiempo de forma estacionaria:

$$E = E_0 + \alpha \cdot t \qquad (8),$$

siendo E_0 la emisión en el instante de tiempo t=0. Sustituyendo la Ec. (8) en la Ec. (1) y teniendo en cuenta la Ec. (3), y aplicando técnicas estándar de resolución de Ecuaciones Diferenciales Ordinarias, se llega a que la solución es:

$$B(t) = \left(B_0 - \frac{E_0}{K}\right) e^{-K \cdot t} + \frac{E_0 + \alpha \cdot t}{K} + \frac{\alpha}{K^2}\left(e^{-K \cdot t} - 1\right) \qquad (9).$$

El primer término del lado derecho de la Ec. (9) es nulo si se parte de un B_0 de equilibrio, y en cualquier caso, para tiempos mucho mayores que K^{-1}, ese término tiende a cero. El segundo término del lado derecho de la Ec. (9) es precisamente $B_{eq}(t)$, por lo que la Ec. (9) se puede reescribir como:

$$\Delta B(t) = \Delta B_0 \cdot e^{-K \cdot t} + \frac{\alpha}{K^2}\left(e^{-K \cdot t} - 1\right) \qquad (10).$$

Vemos que, para tiempos suficientemente grandes, ΔB tiene la solución asintótica:

$$\Delta B(t \gg K^{-1}) \cong -\frac{\alpha}{K^2} \qquad (11),$$

lo que significa que $B(t)$ se queda desfasada un valor constante respecto a $B_{eq}(t)$, tanto más cuanto mayor sea la tasa de crecimiento de las emisiones.

Consideremos los números concretos de un caso ideal, para hacernos una idea de los valores numéricos que cabe esperar encontrar. Supongamos que en 1970 la emisión total de CH_4 era de 460 Tg·año^{-1}, que en 2010 era de 565 Tg·año^{-1} (valores aproximados obtenidos de la Figura 4 de Ghosh et al., 2015; curva de emisiones optimizadas) y que las emisiones crecieron linealmente entre ambos años (no fue realmente así). Nótese que el valor de equilibrio asociado a la emisión de 1970 sería 4182 Tg, y el asociado al valor de 2010 sería 5136 Tg. En ese supuesto, α=2.63 Tg·año^{-2}, con lo que utilizando la Ec. (11), ΔB=216.9 Tg, que teniendo en cuenta la Ec. (2), implicaría un desfase asintótico de 78.3 ppb en la fracción molar seca de CH_4 atmosférico respecto al valor de equilibrio. Si en 1970 ya estuviéramos en el valor asintótico, este se hubiera seguido manteniendo en el tiempo. Supongamos, por el contrario, que en 1970 se partiera de un estado de equilibrio, en ese caso, usando la Ec. (10), ΔB en 2010 sería 214.2 Tg, que implica un desfase en CH_4 respecto al valor de equilibrio de 77.3 ppb, que es bastante parecido al del otro caso considerado.

Hemos visto en esta subsección como el comportamiento del CH_4 en la atmósfera es complejo debido a la presencia de sumideros en el seno de ésta, y hemos considerado unos pocos casos idealizados que permiten comprender dicho comportamiento, antes de enfrentarnos a la realidad 3 dimensional.

3.2.4. Inversión de flujos superficiales. Uso de una combinación de modelos euleriano y lagrangiano.

El CIAI ha contribuido, a través del autor de esta memoria de tesis doctoral, con sus medidas de gases de efecto invernadero a numerosas inversiones globales de flujos superficiales de gases de efecto invernadero: Patra et al. (2009), Chevallier et al. (2010), Chevallier et al. (2011), Belikov et al. (2016), Tsuruta et al. (2017), Shirai et al. (2017)… Como ya ha sido indicado previamente, la inversión de flujos superficiales consiste en modificar los flujos superficiales a priori (dentro de su rango de incertidumbre) de forma que los campos atmosféricos simulados sean más compatibles con las observaciones atmosféricas de dichos gases. Lo que se suele hacer es minimizar una función de coste, que es la suma de dos formas cuadráticas definidas positivas. La primera tiene en cuenta las desviaciones de los flujos superficiales respecto a los valores a priori (y está normalizada teniendo en cuenta la matriz de incertidumbre de dichos flujos superficiales). La segunda tiene en cuenta las desviaciones de las fracciones molares simuladas (con el "forward model") respecto a las fracciones molares medidas (y está normalizada teniendo en cuenta la incertidumbre de las medidas, la incertidumbre del modelo y la incertidumbre de representación debida a la discretización del modelo).

Existen diferentes métodos para realizar la inversión, que simplemente mencionaremos sin comentar ningún detalle sobre su fundamento: "Ensemble Kalman Filter" (véase, por ejemplo, Tsuruta et al., 2017), "fixed-lag Kalman Smoother" (véase, por ejemplo, Shirai et al., 2017) y el método del adjunto para el cálculo del gradiente de la función de coste (Belikov et al., 2016; Chevallier et al., 2010).

Como ya se comentó en la sección 1.4, el modelo de transporte puede ser euleriano o lagrangiano, teniendo cada uno sus ventajas e inconvenientes, y siendo habitualmente el euleriano más usado en inversiones globales, mientras que el lagrangiano se suele usar más en inversiones regionales. Pero existe la interesante y potente opción de utilizar una combinación de ambos tipos de modelos y de esa forma aprovechar las ventajas de ambos. Se considera, en cada punto y tiempo de observación, el adjunto del modelo lagrangiano: el penacho "emitido" hacia atrás en el tiempo desde dicho punto (la advección sufre inversión temporal pero no la difusión), y donde va intersectando la capa límite planetaria sufre una contribución de las emisiones superficiales que haya en ese lugar. El penacho se sigue propagando hacia atrás en el tiempo hasta llegar a cierta distancia temporal respecto al punto de partida, y en ese momento es cuando se acopla con la salida del modelo euleriano, que proporciona al modelo lagrangiano los valores iniciales para la región ocupada por el penacho "inverso" en el instante de tiempo del acople. Este método ha sido usado por Belikov et al. (2016), considerando 7 días para el tiempo de acoplamiento entre el modelo lagrangiano y el euleriano, y por Shirai et al. (2017), que usó 2 días para el tiempo de acoplamiento.

3.3. Transporte de polvo sahariano

En esta sección, solo vamos a presentar la metodología utilizada en el tercer artículo del compendio que conforma esta memoria de tesis doctoral (sección 4.3). Se ha considerado también importante presentar una introducción en cierto detalle sobre las ondas de Rossby, que son las responsables últimas de las variaciones intra-estacionales de los procesos de transporte de polvo mineral objeto de estudio en el artículo de la sección 4.3.

3.3.1. Emisión de polvo sahariano

Las fuentes de polvo sahariano se encuentran básicamente en las numerosas cuencas hidrográficas interiores que existen en este vasto desierto (Ginoux et al., 2012; Prospero et al., 2002; Schepanski et al., 2007). Las fuentes de polvo saharianas son activadas principalmente por LLJs (Low Level Jets; Chorros de Niveles Bajos) asociados al viento Harmattan y al campo de viento del Monzón del Oeste Africano (Allen and Washington, 2013).

Para estimar la emisión instantánea de polvo (E) a las 00, 06, 12 y 18 horas UTC, utilizamos un método relativamente simple (Gillette and Passi, 1988; Morcrette et al., 2009; Tegen and Fung, 1994):

$$E = S \cdot V_{10}^{2}(V_{10} - V_{T}) \qquad (12),$$

donde S es el potencial de emisión de polvo (Morcrette et al., 2009), con unidades kg s^2 m^{-5}, V_{10} es la velocidad del viento a 10 metros de altura, y V_T es la velocidad de viento umbral para que se produzca levantamiento de polvo (utilizamos el valor 6.5 m/s; Helgren and Prospero, 1987; Takemura et al., 2000), obtenidos del reanálisis MACC (véase la subsección 3.3.2).

3.3.2. Medidas de AOD desde satélite y reanálisis MACC

El instrumento MODIS (MODerate resolution Imaging Spectrometer; Espectrómetro de Imagen de Resolución Moderada) proporciona datos de aerosoles sobre tierra y sobre los océanos a escala global a diario (Kaufman et al., 1997; Tanré et al., 1997). Para este estudio utilizamos medias mensuales de AOD (Aerosol Optical Depth; Espesor Óptico de Aerosoles) a 550 nm de la Colección MODIS 6 para el periodo 2003-2012 y los meses junio, julio, agosto y septiembre (JJAS). La Colección MODIS 6 proporciona un nuevo producto, obtenido uniendo los productos Deep Blue (DB) y Dark Target (DT). Con este nuevo producto también hay disponibilidad de datos tanto sobre zonas con alto albedo como sobre superficies con vegetación (Sayer et al., 2013), lo que es especialmente importante para nuestro estudio, ya que grandes áreas del dominio considerado tienen un alto albedo (Norte de África), y la tarea de obtener el AOD es más compleja. La colección MODIS 6 está disponible en ftp://ladsweb.nascom.nasa.gov/allData/6/.

Utilizamos el reanálisis MACC (Monitoring Atmospheric Composition & Climate; Monitorización de la Composición Atmosférica y del Clima) para el periodo 2003-2012 (Inness et al., 2013), que se puede descargar de la página web del ECMWF: http://apps.ecmwf.int/datasets/data/macc-reanalysis/levtype=sfc/ . Utilizamos AOD a 550 nm y la emisión de polvo instantánea, ésta última utilizando el procedimiento descrito en la subsección 3.3.1 (ya que MACC no la proporciona), para JJAS del periodo 2003-2012. Benedetti et al. (2009) y Morcrette et al. (2009, 2011) describen el módulo de reanálisis de aerosoles de MACC. Este reanálisis ha sido usado y validado extensivamente en varios estudios sobre aerosoles, de los que mencionamos aquí solo dos: Inness et al. (2013) y Cuevas et al. (2015a).

3.3.3. Reanálisis de campos meteorológicos

NCEP (National Centre for Environmental Prediction; Centro Nacional de Predicción Medioambiental) y NCAR (National Centre for Atmospheric Research; Centro Nacional de Investigación Atmosférica) cooperan produciendo reanálisis de campos atmosféricos para que sean usados por la comunidad científica en investigación atmosférica y monitorización climática (Kalnay et al., 1996). Utilizamos datos NCEP/NCAR con resolución temporal de 6 horas, así como promedios diarios y mensuales, todos ellos con resolución espacial 2.5° x 2.5°, para los meses JJAS del periodo 1980-2013.

En detalle, usamos los campos mensuales medios de: altura geopotencial a 700 hPa (m), vector viento y su módulo a 925 y 700 hPa (m s^{-1}), y temperatura a 925 hPa (K), en la región 10°N-50°N, 50°W-40°E, para el periodo 2003-2012. Además, utilizamos los campos mensuales de Omega a 300, 400, 500 y 600 hPa (Pa s^{-1}), y de la componente zonal del viento a 300 hPa (ms^{-1}), para el mismo periodo mencionado, pero en la región 5°N-70°N, 30°W-40°E. Obtenemos también secciones verticales en latitud/longitud-altura, para longitudes/latitudes específicas, de las componentes del viento meridional y zonal (m s^{-1}). Además, usamos campos mensuales de geopotencial a 200, 500, 700, 850 y 1000 hPa para realzar correlaciones con una serie temporal, para el periodo mencionado, pero en la región 0°N-90°N, 80°W-80°E.

También utilizamos los campos diarios NCEP/NCAR de geopotencial a 700 hPa, temperatura a 925, 850 y 700 hPa, Omega a 500 hPa y viento zonal a 300 hPa, para el periodo 1980-2013. Por último, utilizamos el reanálisis NCEP/NCAR a la mayor resolución temporal disponible (6 horas, con datos a las 00, 06, 12 y 18 UTC), para el periodo 1980-2013, para calcular los términos de la ecuación de la energía de la dinámica atmosférica.

3.3.4. Mapas con campos promedios, y mapas de correlación y de regresión

Con los campos mensuales mencionados, calculamos campos promedios de las diferentes variables meteorológicas para dos rangos de valores de la serie temporal de un índice de referencia de gran importancia para el transporte de polvo sahariano fuera de África.

Además, obtenemos mapas de correlación entre la mencionada serie de referencia y la serie temporal de campos de cada variable meteorológica elegida (es decir, en cada punto del mapa se representa el coeficiente de correlación de Pearson entre la serie de referencia y la serie temporal en ese punto del mapa de la variable meteorológica elegida), y mapas de regresión entre esas mismas variables, en los que se representa en cada punto la pendiente de la recta de regresión, en la que la variable dependiente es la serie temporal de la variable meteorológica en dicho punto y la variable independiente es la serie de referencia.

Para determinar el índice de confianza estadística de cada valor de correlación obtenido, se aplica el test de significación de Pearson. Además, se calculan algunas correlaciones con desfase temporal.

3.3.5. Ecuación de la energía de la dinámica atmosférica

Utilizamos la ecuación de la energía de la dinámica atmosférica para determinar qué proceso produce los desplazamientos longitudinales de la Baja Térmica Sahariana (SHL, Saharan Heat

Low), que obviamente está a una temperatura mayor que la del entorno que la rodea. La ecuación de la energía en coordenadas de presión (por ejemplo, véase Holton, 1992) es:

$$\frac{\partial T}{\partial t} = -\vec{v} \cdot \nabla_p T - \omega T \frac{\partial \ln \theta}{\partial p} + \frac{J}{c_p} \qquad (13),$$

donde el vector ***v*** es la velocidad horizontal, *T* es la temperatura, *p* es la presión, θ es la temperatura potencial, ω es la velocidad vertical en coordenadas de presión, *J* es el calentamiento diabático por unidad de masa, y c_p es el calor específico a presión constante. Esta ecuación indica que la variación en el tiempo de la temperatura en un punto fijo euleriano de rejilla, se debe a la advección horizontal de temperatura, la tendencia de la temperatura debida a omega y el calentamiento diabático. Nótese que la tendencia de la temperatura debida a omega contiene dos procesos físicos: la advección de temperatura en la vertical y el calentamiento adiabático asociado a los cambios de presión.

3.3.6. Ondas de Rossby

Las ondas de Rossby juegan un papel importante en nuestro estudio de transporte pulsado de polvo sahariano hacia el océano Atlántico subtropical y el mar Mediterráneo. Las ondas de Rossby se pueden describir mediante las ecuaciones cuasi-geostróficas de la dinámica atmosférica, válidas en la atmósfera a escala sinóptica (aquella en la que la longitud característica de variación de las variables meteorológicas es del orden de 1000 km) en latitudes medias (Holton, 1992). A esta escala se cumple la aproximación hidrostática (las ondas internas de gravedad desaparecen), y a orden dominante hay un equilibrio entre las fuerzas horizontales del gradiente de presión y de Coriolis (las ondas de sonido desaparecen). De este equilibrio, se obtiene la siguiente ecuación de diagnóstico (no sirve para hacer pronóstico):

$$\vec{V_g} = \vec{k} \times \frac{1}{\rho f} \nabla p \qquad (14),$$

donde $\vec{V_g}$ es el viento geostrófico, ***k*** es el vector unitario en dirección vertical (hacia arriba), ρ es la densidad del aire, y *f* es el parámetro de Coriolis, que viene dado por:

$$f = 2\Omega \sin \phi \qquad (15),$$

donde Ω es la velocidad angular de rotación de la Tierra, y ϕ es la latitud.

En la aproximación cuasi-geostrófica se considera que el viento es suma de dos componentes: la componente geostrófica, que es dominante, y la componente ageostrófica, que es mucho menor que la anterior en módulo (Holton, 1992). Además, se hace la aproximación del plano beta (latitudes medias), que consiste en desarrollar la Ec. (15) en serie de Taylor y quedarse solo con la parte lineal:

$$f = f_0 + \beta \cdot y \qquad (16),$$

donde *y* es la coordenada horizontal que crece hacia el polo norte, y f_0 y β son constantes. Después de combinar apropiadamente las distintas ecuaciones de la dinámica atmosférica en su forma cuasi-geostrófica, se llega a la ecuación de conservación de la vorticidad potencial cuasi-geostrófica (véase Holton, 1992):

$$\frac{D_g}{Dt}\left[\frac{1}{f_0}\nabla^2\Phi + \mathrm{f} + \frac{\partial}{\partial \mathrm{p}}\left(\frac{f_0}{\sigma}\frac{\partial\Phi}{\partial p}\right)\right] = 0 \qquad (17),$$

donde D_g/Dt es la derivada lagrangiana pero solo con la velocidad geostrófica (sin incluir la componente ageostrófica), Φ es el geopotencial,

$$\sigma = -\frac{R \cdot T}{p}\frac{\partial \ln\theta}{\partial p} \qquad (18),$$

que depende solo de *p* a orden dominante, y *R* es la constante específica del aire seco. El primer término dentro del corchete de la Ec. (17) es la vorticidad geostrófica (relativa), el segundo es la vorticidad planetaria, y el tercero es un término baroclino ("stretching vorticity"). Nótese qué en coordenadas de presión, el viento geostrófico viene dado por:

$$\vec{V}_g = \frac{1}{f_0}\vec{k} \times \nabla\Phi \qquad (19),$$

por lo que en la Ec. (17) el único campo dependiente a determinar es el geopotencial. La EDP (Ecuación en Derivadas Parciales) (17) es de orden 3 en las derivadas parciales, pero la derivada temporal euleriana solo aparece a orden 1. Esto significa que con la aproximación cuasi-geostrófica, se ha aislado un único modo ondulatorio, el de Rossby, y como hemos mencionado antes, las ondas de sonido y las internas de gravedad han sido "filtradas".

Aplicando teoría de perturbaciones lineales (por ejemplo, Holton, 1992), y considerando un flujo no perturbado zonal y uniforme en una atmósfera isoterma, U_0, la ecuación de la vorticidad potencial cuasi-geosgrófica perturbada queda:

$$\left(\frac{\partial}{\partial t} + U_0\frac{\partial}{\partial x}\right)\left[\frac{1}{f_0}\nabla^2\Phi_1 + \frac{\partial}{\partial \mathrm{p}}\left(\frac{f_0}{\sigma}\frac{\partial\Phi_1}{\partial p}\right)\right] + \frac{\beta}{f_0}\frac{\partial\Phi_1}{\partial x} = 0 \qquad (20),$$

donde Φ_1 es el geopotencial perturbado. Consideramos soluciones de Fourier de la Ec. (20) de la forma:

$$\Phi_1(x, y, p, t) = \psi\left(\frac{p}{p_r}\right)^{\alpha} \exp[i(kx + ly - \nu t)] \qquad (21),$$

donde ψ, p_r, y α son constantes, *k* es el número de onda (angular) en dirección longitudinal, *l* es el número de onda en dirección latitudinal y ν es la frecuencia angular. Al insertar la solución tipo de la Ec. (21) en la Ec. (20), resulta que solo para algunos valores de α desaparece la dependencia en la presión y la Ec. (20) se convierte en una relación de dispersión. Para los valores de α igual a 0 y -1, el término baroclino se anula, y obtenemos la relación de dispersión de las ondas de Rossby para un fluido barotrópico:

$$(\nu - kU_o)\left[-\frac{1}{f_0}(k^2 + l^2)\right] - k\frac{\beta}{f_0} = 0 \qquad (22),$$

que despejando la frecuencia angular queda como:

$$\nu = kU_0 - k\frac{\beta}{k^2 + l^2} \qquad (23),$$

y por tanto la velocidad de fase en dirección longitudinal:

$$c_x = \frac{k^2}{k^2 + l^2}\left(U_0 - \frac{\beta}{k^2 + l^2}\right) \qquad (24).$$

La onda de Rossby es dispersiva, y la velocidad de fase longitudinal es menor cuanto mayor es la longitud de onda, llegando para longitudes de onda en torno a medio perímetro de paralelo terrestre a ser estacionarias y para longitudes de onda mayores a ser retrógradas (es decir, la fase se propaga de este a oeste). La velocidad de grupo suele ser mayor que la de fase en dirección longitudinal.

Pero no solo se ha de cumplir la Ec. (20), sino también la condición de contorno inferior, que en superficie plana es w=0 (velocidad vertical) en z=0, y que en coordenadas de presión se expresa, una vez se ha tenido en cuenta la relación de viento geostrófico, de esta forma:

$$\omega_1 = \frac{p}{RT}\frac{\partial \Phi_1}{\partial t} \qquad (25).$$

Resulta que la solución con α igual a 0, no cumple la condición de contorno inferior salvo para el caso de onda estacionaria (ν=0). Por otro lado, en la solución con α igual a -1, que sí cumple la condición de contorno inferior, la energía de la onda tiende a infinito cuando *p* tiende a 0.

Las Ecs. (20) y (25) admiten soluciones no barotrópicas, en las que el término baroclino es proporcional al geopotencial perturbado. Dichas soluciones fueron obtenidas por Lindzen (1968), y no las vamos a mostrar explícitamente en esta memoria de tesis doctoral. Por ejemplo, para el caso en el que el flujo zonal no perturbado es nulo, α es igual a -2/7. La relación de dispersión queda ligeramente distinta.

En la atmósfera real de latitudes medias, el viento zonal aumenta con la altura, debido al gradiente de temperatura latitudinal (viento térmico). Para este caso, más próximo a la realidad, no existe solución analítica y el problema de autovalores ha de ser resuelto numéricamente. Así lo hicieron Geisler & Dickinson (1975).

La Ecuación Omega Cuasi-Geostrófica relaciona la "laplaciana" (no es exactamente una laplaciana, ya que la derivada segunda de *p* tiene un coeficiente) de omega con las fuentes de omega (Holton, 1992), que son: 1) variación en la vertical de la advección de vorticidad relativa y planetaria; y 2) laplaciana horizontal de la advección de temperatura. La presencia de viento zonal con cizalladura, excita las fuentes de omega. Esperamos que las ondas de Rossby libres transporten longitudinalmente su energía a lo largo de la troposfera superior, donde el viento térmico es mayor y más zonal, y que la onda de Rossby se haga notar más o menos en la baja troposfera dependiendo de la cizalladura vertical del viento zonal. Utilizamos omega como un proxy empírico de la intensidad de la onda de Rossby en la mitad inferior de la troposfera.

Por último, cabe destacar, que las proximidades de los chorros de latitudes medias actúan como guías de onda para las ondas de Rossby (Ambrizzi et al., 1995; Hoskins and Ambrizzi, 1993; and Hsu and Lin, 1992).

4. Resultados

4.1. Cuantificación rigurosa de la incertidumbre en las medidas de monóxido de carbono en la estación global VAG de Izaña: 2008-2011

4.1.1. Indicadores de calidad de la publicación

Indicadores de calidad de la publicación a fecha 4 de agosto de 2018, obtenidos de “Web Of Science” en el formato CVN de la FECYT.

Gomez-Pelaez, A. J.; Ramos, R.; Gomez-Trueba, V.; Novelli, P. C.; Campo-Hernandez, R.A statistical approach to quantify uncertainty in carbon monoxide measurements at the Izana global GAW station: 2008-2011. ATMOSPHERIC MEASUREMENT TECHNIQUES. 6 - 3, pp. 787 - 799. COPERNICUS GESELLSCHAFT MBH, 01/01/2013. ISSN 1867-1381.

Tipo de producción: Artículo

Tipo de soporte: Revista

Fuente de impacto: WOS (JCR)

Categoría: Science Edition - METEOROLOGY & ATMOSPHERIC SCIENCES

Índice de impacto: 3.206

Revista dentro del 25%: Si

Posición de publicación: 18

Num. revistas en cat.: 76

Fuente de citas: WOS

Citas: 7

4.1.2. Introducción

La comparación de las medidas de CO realizadas por diferentes laboratorios ha mostrado diferencias mayores que el objetivo de calidad de la OMM en su programa VAG (WMO, 2010). Las principales características de este gas traza vienen detalladas en la subsección 1.2. En la subsección 1.5 se detalla el emplazamiento geográfico del Observatorio Atmosférico de Izaña y las implicaciones que tiene en las condiciones atmosféricas de medida: condiciones de troposfera libre durante la noche. Durante el día, el viento ascendente de ladera (viento anabático) causado por el calentamiento radiativo del suelo, transporta a Izaña una pequeña cantidad de aire contaminado procedente de debajo de la inversión subtropical de temperatura (Fischer et al., 1998; Rodríguez et al., 2009), produciendo un incremento diurno del CO.

En este artículo del compendio de esta memoria de tesis doctoral, presentamos la configuración del sistema de medida, la función respuesta, el esquema de calibración, el procesado de datos, la serie temporal de medidas nocturnas de CO en Izaña del periodo 2008-2011, y el ciclo diario medio para cada mes (secciones del artículo 2, 3 y 6).

Determinar y dar a conocer la incertidumbre asociada a las medidas es una recomendación importante del programa OMM de medida de gases de efecto invernadero (WMO, 2010, 2016). Sin embargo, realizar un análisis de incertidumbre riguroso, teniendo en cuenta la propagación de la incertidumbre y las covarianzas entre las componentes de la incertidumbre (JCGM, 2008), es una tarea compleja. En este artículo, se presenta un análisis riguroso de la incertidumbre para las medidas de CO realizadas en Izaña (en su sección 4). Los conceptos presentados aquí pueden ser aplicados a otras estaciones VAG.

La comparación de medidas continuas (o casi-continuas) obtenidas con instrumentos in situ y medidas discretas, realizadas con muestras de aire semanales tomadas en el mismo emplazamiento, por otro laboratorio, es una forma independiente de evaluar la calidad de las medidas continuas in situ (WMO, 2016). Como parte del procedimiento de evaluación de la calidad, comparamos las medidas continuas (cada 20 minutos) realizadas in situ en Izaña con las realizadas por NOAA con matraces muestreados en Izaña (sección 5 del artículo). Las diferencias entre estas medidas son evaluadas en términos de la incertidumbre de comparación. Las diferencias promediadas en el tiempo (por ejemplo, medias anuales), también tienen en cuenta la incertidumbre de comparación.

4.1.3. Resumen en español del artículo

El artículo desarrolla un procedimiento riguroso para determinar la incertidumbre en las medidas continuas (cada 20 minutos) de CO realizadas en la estación VAG global de Izaña. El instrumento usado para medir CO, también es mencionado en la sección 3.1.2 de esta memoria. Este método es aplicable a otras estaciones de la red global VAG de la OMM. El error en las medidas es proporcionado como incertidumbre combinada estándar. Ésta tiene cuatro componentes (que se combinan cuadráticamente, véase la Ec. [3] del artículo): 1) la incertidumbre de los gases patrón OMM interpolada sobre el rango de medida; 2) la incertidumbre que tiene en cuenta el acuerdo entre los gases patrón y la función respuesta usada (es una función potencial, véase la Ec. [1]); 3) la incertidumbre debida a la repetibilidad de las inyecciones de aire ambiente y su medida; y 4) la incertidumbre propagada asociada a la consistencia temporal de los parámetros de la función respuesta (que también tiene en cuenta la covarianza entre los parámetros, véase la Ec. [6] del artículo). El valor medio de la incertidumbre estándar combinada decreció significativamente a partir de marzo de 2009, de 2.37 $\mathrm{nmol \cdot mol^{-1}}$ a 1.66 $\mathrm{nmol \cdot mol^{-1}}$. La razón de esta mejora es una muy significativa reducción en la desviación estándar de los parámetros de la función respuesta (que es la fuente dominante de incertidumbre antes de marzo de 2009). A partir de marzo de 2009 hubo una mejora en la determinación y consistencia de los parámetros de la función respuesta debido a los siguientes hechos: 1) uso de un conjunto de gases patrón OMM con un número mayor de gases de referencia y preparados más recientemente; 2) aumento de la frecuencia de inyecciones de gas de trabajo en la secuencia de calibración; y 3) uso de una puerta cerrada adyacente en la válvula de selección multi-posición para detener el flujo de gas por la espiral de muestreo y permitir el equilibrado de presión con el valor ambiente. La componente dominante de incertidumbre después de marzo de 2009, es la incertidumbre que tiene en cuenta el acuerdo entre los gases estándar y la función respuesta (1.27 $\mathrm{nmol \cdot mol^{-1}}$).

Consideramos un quinto tipo de incertidumbre, que llamamos incertidumbre de representación (véase la Ec. [12] del artículo), cuando algunos de los datos necesarios para calcular la media temporal están ausentes.

Al calcular cualquier media, ésta también tiene una incertidumbre propagada procedente de la incertidumbre de los datos que se usan para calcular la media. La ecuación de propagación depende del tipo de componente de incertidumbre, aleatoria o sistemática. Esto es debido a que hay cancelación parcial de los errores aleatorios al promediar (véase la Ec. [15] del artículo), mientras que no hay cancelación de los errores sistemáticos (véase la Ec. [16] del artículo).

Las incertidumbres de representación en las medidas in situ son mucho menores que cuando se usan muestras semanales en matraces. Por ejemplo, la incertidumbre de representación de las medias mensuales es igual a 4.98 nmol·mol^{-1} para las medidas de matraces NOAA, y 0.03 nmol·mol^{-1} para las medidas continuas (cada 20 minutos). La mayor incertidumbre en las medidas de aire de matraces es debida a la baja frecuencia del muestreo (una vez a la semana).

La serie temporal de medias diarias nocturnas en Izaña para el periodo 2008-2011 es analizada utilizando la descomposición de la subsección 3.1.5 de esta memoria, pero sin usar componentes de Fourier para la tendencia interanual. La componente interanual aumenta hasta el principio de 2010, y entonces decrece (véase la Fig. 4 y la Ec. [26] del artículo). La amplitud del ciclo estacional, determinada en el análisis mencionado de las medidas, es 40.7 nmol·mol^{-1}. El máximo al final del invierno y el mínimo a mitad del verano, observados en Izaña, son semejantes al ciclo estacional observado en muchos otros emplazamientos en latitudes medias del hemisferio norte. La autocorrelación de los residuos indica que el periodo típico de persistencia de las masas de aire para CO es de 7 días (véase la Fig. 7 del artículo).

El ciclo diurno medio por meses alcanza a mediodía un máximo de unos 5 a 6 nmol·mol^{-1} (excepto en diciembre, que apenas llega a los 4 nmol·mol^{-1}) sobre el valor de fondo nocturno de la troposfera libre (véase la Fig. 8 del artículo). Este incremento es producido por el viento anabático que transporta aire contaminado a la estación procedente de la zona de la troposfera situada bajo la inversión térmica (capa de mezcla potencialmente contaminada por emisiones antropogénicas). Las muestras de aire tomadas durante el día están sesgadas (hacia arriba) con respecto a las condiciones de fondo de la troposfera media. La magnitud de dicho sesgo depende de la hora de muestreo.

También examinamos las diferencias entre las medias horarias obtenidas mediante medidas in situ continuas y las medias de las medidas de matraces muestreados dentro de la hora considerada (solo un par de matraces simultáneos cada semana, por lo que solo hay disponible una hora cada semana para la comparación). Las incertidumbres asociadas a cada media (horaria continua y del par de matraces) permiten determinar la incertidumbre de comparación (véase la Ec. [21] del artículo), y así utilizar ésta como referencia para determinar si la diferencia es estadísticamente significativa o no. En 2008, el 47.4% de las diferencias fueron significativas, estando el 68% de ellas entre −1.26 y 6.58 nmol·mol^{-1}. En 2009-2011, solo el 24.5% de las diferencias fueron significativas, y el 68% estuvieron entre −2.39 and 2.5 nmol·mol^{-1} (este rango es en gran medida debido a la incertidumbre de comparación). Calculamos las medias totales y anuales de las diferencias entre las medidas in situ y las de matraces usando expresiones convencionales (véase la Ec. [22] del artículo), pero también medias pesadas basadas en el método de mínima varianza (véase la Ec. [23] del artículo). En el periodo 2009-2011, estas diferencias están mucho más próximas a cero que durante 2008 (véase la Fig. 6 del artículo), lo que es probablemente debido al mejor comportamiento del sistema de medida in situ de Izaña durante 2009-2011. Las diferencias medias anuales entre las medidas de matraces NOAA y las in situ (de AEMET) para 2009-2011 no son significativas (véase la Tabla 5 del artículo) y están dentro de los 2 nmol·mol^{-1} de objetivo de compatibilidad entre laboratorios de VAG.

4.1.4. Artículo original en inglés

Enlace al artículo original: https://doi.org/10.5194/amt-6-787-2013

Atmos. Meas. Tech., 6, 787–799, 2013
www.atmos-meas-tech.net/6/787/2013/
doi:10.5194/amt-6-787-2013

Atmospheric Measurement Techniques
Open Access

A statistical approach to quantify uncertainty in carbon monoxide measurements at the Izaña global GAW station: 2008–2011

A. J. Gomez-Pelaez[1], **R. Ramos**[1], **V. Gomez-Trueba**[1,2], **P. C. Novelli**[3], **and R. Campo-Hernandez**[1]

[1]Izaña Atmospheric Research Center (IARC), Meteorological State Agency of Spain (AEMET), Izaña, 38311, Spain
[2]Air Liquide España, Delegación Canarias, Candelaria, 38509, Spain
[3]National Oceanic and Atmospheric Administration, Earth System Research Laboratory, Global Monitoring Division (NOAA-ESRL-GMD), Boulder, CO 80305, USA

Correspondence to: A. J. Gomez-Pelaez (agomezp@aemet.es)

Received: 17 August 2012 – Published in Atmos. Meas. Tech. Discuss.: 21 September 2012
Revised: 20 February 2013 – Accepted: 21 February 2013 – Published: 20 March 2013

Abstract. Atmospheric CO in situ measurements are carried out at the Izaña (Tenerife) global GAW (Global Atmosphere Watch Programme of the World Meteorological Organization – WMO) mountain station using a Reduction Gas Analyser (RGA). In situ measurements at Izaña are representative of the subtropical Northeast Atlantic free troposphere, especially during nighttime. We present the measurement system configuration, the response function, the calibration scheme, the data processing, the Izaña 2008–2011 CO nocturnal time series, and the mean diurnal cycle by months.

We have developed a rigorous uncertainty analysis for carbon monoxide measurements carried out at the Izaña station, which could be applied to other GAW stations. We determine the combined standard measurement uncertainty taking into consideration four contributing components: uncertainty of the WMO standard gases interpolated over the range of measurement, the uncertainty that takes into account the agreement between the standard gases and the response function used, the uncertainty due to the repeatability of the injections, and the propagated uncertainty related to the temporal consistency of the response function parameters (which also takes into account the covariance between the parameters). The mean value of the combined standard uncertainty decreased significantly after March 2009, from 2.37 nmol mol^{-1} to 1.66 nmol mol^{-1}, due to improvements in the measurement system. A fifth type of uncertainty we call representation uncertainty is considered when some of the data necessary to compute the temporal mean are absent. Any computed mean has also a propagated uncertainty arising from the uncertainties of the data used to compute the mean. The law of propagation depends on the type of uncertainty component (random or systematic).

In situ hourly means are compared with simultaneous and collocated NOAA flask samples. The uncertainty of the differences is computed and used to determine whether the differences are significant. For 2009–2011, only 24.5 % of the differences are significant, and 68 % of the differences are between −2.39 and 2.5 nmol mol^{-1}. Total and annual mean differences are computed using conventional expressions but also expressions with weights based on the minimum variance method. The annual mean differences for 2009–2011 are well within the ±2 nmol mol^{-1} compatibility goal of GAW.

1 Introduction

Carbon monoxide affects the oxidizing capacity of the troposphere, and, in particular, plays an important role in the cycles of hydroxyl radical (OH), hydroperoxyl radical (HO_2), and ozone (O_3); e.g. see Logan et al. (1981). Carbon monoxide atmospheric lifetime ranges from 10 days in summer over continental regions to more than a year over polar regions in winter (Novelli et al., 1992). Its relatively short lifetime (as compared with long-life greenhouse gases) and uneven distribution of its sources leads to large temporal and spatial CO variations. The major sources of carbon monoxide are the combustion of fossil fuels, biomass burning, the oxidation of methane, and the oxidation of non-methane hydrocarbons.

Published by Copernicus Publications on behalf of the European Geosciences Union.

The major sink of CO is the reaction with OH, whereas surface deposition is a small sink (Ehhalt et al., 2001).

Comparisons of CO measurements among laboratories have shown differences larger than the data quality objectives stated by the World Meteorological Organization (WMO) in its Global Atmosphere Watch Programme (GAW), WMO (2010). The Izaña station (28.309° N, 16.499° W, 2373 m a.s.l.) is located on the top of a mountain on the island of Tenerife (Canary Islands, Spain), well above a strong subtropical temperature inversion layer. Mean solar time is UTC–1. In situ measurements at Izaña are representative of the subtropical Northeast Atlantic free troposphere, especially during the night period 20:00–08:00 UTC (e.g. Schmitt et al., 1988; Navascues and Rus, 1991; Armerding et al., 1997; Fischer et al., 1998; Rodríguez et al., 2009); air from below the inversion layer cannot pass above it, and there is a regime of downslope wind caused by radiative cooling of the ground. The station is located on the top of a crest, where horizontal divergence of the downslope wind and subsidence of the air from above the station occurs. During daytime an upslope wind caused by radiative heating of the ground transports to Izaña a small amount of contaminated air coming from below the subtropical temperature inversion layer (Fischer et al., 1998; Rodríguez et al., 2009), producing a diurnal increase in carbon monoxide (Sect. 6). In this paper, we present the measurement system configuration, the response function, the calibration scheme, the data processing, the Izaña 2008–2011 carbon monoxide nocturnal time series, and the mean diurnal cycle by months (Sects. 2, 3, and 6).

Reporting uncertainties associated with measurement results is strongly recommended by the WMO greenhouse gases measurement community (WMO, 2010, 2011). However, carrying out a rigorous uncertainty analysis taking into account uncertainty propagation and covariances between uncertainty components (JCGM, 2008) is a challenging task. In this paper, we present a rigorous uncertainty analysis for the carbon monoxide measurements carried out at the Izaña station (Sect. 4). The concepts presented here may be applied to other GAW stations.

The comparison between continuous (or quasi-continuous) measurements obtained by in situ instruments and discrete measurements from collocated weekly flask samples analysed by another laboratory is an independent way of assessing the quality of the continuous in situ measurements (WMO, 2011). As part of our quality assurance procedure, we compare the Izaña in situ quasi-continuous measurements with NOAA collocated flasks (Sect. 5). The differences between the measurements are evaluated in terms of their comparison uncertainty. Temporally averaged differences (e.g. annual means) also take into account the comparison uncertainty.

2 Measurement system configuration

The ambient air inlet line of the station is an 8-cm ID (inner diameter) stainless steel pipe that crosses the station building from the roof till the ground floor, with the entrance located 30 m above ground level. A pump located on the ground floor produces a high flow rate (cubic meters per minute) of ambient air. On the third floor, there is a dedicated 4-mm ID PFA line that takes air from the general inlet to the analytical system using a KNF diaphragm pump. Water vapour is removed by flowing the air through a 300-mL glass flask immersed in a −67 °C alcohol bath. The residual level of water vapour downstream this trap is 5.3 ppm. A multi-position selection valve (MPV) delivers ambient air or standard gas to the instrument.

The measurement system is based on a modified Trace Analytical gas chromatograph with mercuric oxide reduction detection (RGA). The RGA uses two chromatographic columns maintained at 105 °C: Unibeads 1S 60/80 mesh as pre-column, and Molecular Sieve 5A 60/80 mesh as main column. For both columns, the outer diameter is 3.2 mm and the length is 76.8 cm. The pre-column separates CO and H_2 from other trace gases in an air sample. The main column separates H_2 and CO before entering a bed (265 °C) containing solid mercuric oxide. Reduced gases entering the bed are oxidized and HgO reduced to Hg, which is then measured by UV radiation absorption. High-purity synthetic air is used as carrier gas. We used a stainless steel sample loop volume of 1 mL. Figure 1 shows a typical chromatogram, where the H_2 peak appears first, followed by the CO peak. Working standard gas (also called reference gas) and ambient air are injected alternatively every ten minutes.

3 Standard gases, calibrations, response function, and processing

Instrument calibrations are performed every two weeks using 3–5 WMO CO standard gases. These CO-in-air mixtures were purchased from the WMO CO CCL (Central Calibration Laboratory), which is hosted by NOAA-ESRL-GMD. They range from 62.6 to 221.2 nmol mol^{-1} and are referenced to the WMO-2004 scale. These five high-pressure cylinders serve as our laboratory standards. Table 1 shows their mole fractions with the 1-sigma uncertainty assigned in 2006 by the CCL. Before March 2009 we used 3 standard gases to define instrument characteristics, then five standards were used. Stability of the Izaña laboratory standards was evaluated in two ways, indicating there was no statistically significant drift in the mole fraction of these gases. First, in 2009, the WMO World Calibration Centre (WCC) for CO, which is hosted by EMPA, carried out an audit at the Izaña station (Zellweger et al., 2009) which included a blind analysis of five WCC travelling CO-in-air mixtures with mole fraction ranging from 88 to 201 nmol mol^{-1}. In

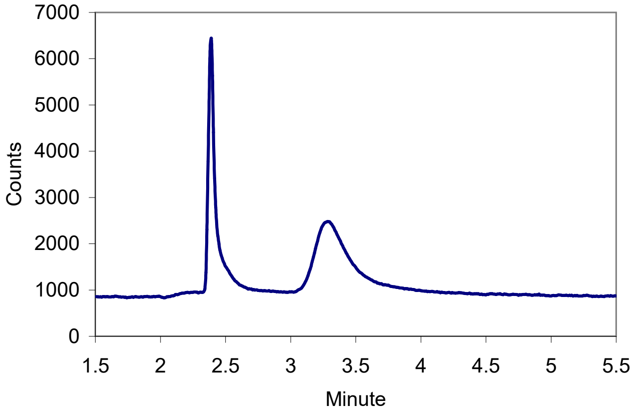

Fig. 1. Typical RGA chromatogram. The sample was injected at the 2 minute mark. The first eluted peak corresponds to H_2, whereas the second one corresponds to CO.

each analysis, repeated injections of travelling cylinder gas alternate with working gas injections. The WCC assignments initially used were on an earlier version of the WMO scale, WMO-2000 (Zellweger et al., 2009). When the WCC travelling standards were revised to the WMO-2004 scale used at Izaña, the differences in the mole fractions assigned by Izaña and the WCC ranged from -1.69 to $2.63\,\mathrm{nmol\,mol^{-1}}$ (C. Zellweger, personal communication, 2010). If we consider only the three travelling cylinders within the ambient range at Izaña ($\sim 60-150\,\mathrm{nmol\,mol^{-1}}$), the differences range from -1.69 to $0.45\,\mathrm{nmol\,mol^{-1}}$. The later values are compatible with the uncertainty in the Izaña RGA measurements (Sect. 4). Second, the stability of the laboratory standards was also evaluated by comparing Izaña in situ measurement results with results from air samples collected weekly in flasks at Izaña and analysed by NOAA-ESRL-GMD. The annual mean differences between CO results by the two laboratories are not significant for the years 2009, 2010, and 2011, and show no significant trend over this period (Sect. 5), indicating there was no significant change in the Izaña laboratory standards relative to their NOAA assignments.

The laboratory and working standards are contained in aluminium high-pressure cylinders fitted with Ceodeux brass valves (connection GCA-590). The 29-L cylinders containing the laboratory standards were obtained from Scott-Marrin, Inc, whereas the 20-L cylinders containing the working standards were obtained from Air Liquide Spain. They may differ in the type of aluminium alloy used and their internal conditioning. Two-stage high-purity regulators from Scott Specialty Gases (model 14C) are used, following the procedure for conditioning described by Lang (1998). Working gas tanks were filled to 125 bar with natural air at the Izaña station using a filling system similar to that described by Kitzis (2009). The lifetime of a working gas high-pressure tank is between 3 and 5 months (tanks are used till they reach 25 bar).

Table 1. WMO CO standard gases of the Izaña station: CO mole fraction and standard uncertainty referenced to the WMO-2004 CO scale. The mole fractions were assigned by the WMO CO CCL in 2006.

Cylinder	CO ($\mathrm{nmol\,mol^{-1}}$)	1-sigma ($\mathrm{nmol\,mol^{-1}}$)
CA06768	62.6	1.2
CA06946	91.2	0.7
CA06988	119.6	0.8
CA06968	164.5	1.1
CA06978	221.2	1.5

We determine the response function of the instrument based on the standard/reference peak height ratios (in order to minimize potential artefacts due to changes in instrument response with time):

$$r = r_{\mathrm{wg}} \left(\frac{h}{h_{\mathrm{wg}}} \right)^{\beta}, \tag{1}$$

where, r is CO mole fraction of the sample, h is peak height, and h_{wg} is the mean peak height of the bracketing working standard. In each calibration, the coefficients of the response function, r_{wg} and β, are obtained by fitting (through least-squares) the mole fractions of the standards and the mean relative heights to the logarithm of the response function. From these definitions, it follows that r_{wg} is the working gas CO mole fraction. In this paper, carbon monoxide is expressed as mole fraction ($\mathrm{nmol\,mol^{-1}}$) on the WMO-2004 scale (WMO, 2011). To quantify the goodness of the fit, we use the RMS (root mean square) residual,

$$u_{\mathrm{fit}} = \sqrt{\frac{\sum_{i=1}^{n} \left[r_i - R\left(h_i / h_{\mathrm{wg}} \right) \right]^2}{n-2}}, \tag{2}$$

where n is the number of standards, $n-2$ represents the number of degrees of freedom (JCGM, 2008) of the residuals (since the n standards have been used to compute two regression parameters) and $R(h_i/h_{\mathrm{wg}})$ is the fitted response function. Figure 2 shows the least-squares fitting of a typical calibration and the residuals with respect to this fit. Figure 3 shows the working gas mole fractions and the response function exponents obtained from calibrations conducted during 2008 to 2011.

The time-dependent response function for the working gas in use is computed using the response functions determined in its calibrations: β is computed as the mean of the calibration values, whereas a linear drift in time is allowed for r_{wg}. The CO mole fractions contained in high-pressure cylinders are known to drift with time (e.g. Novelli et al., 2003). We evaluate potential drift in working standards using a Snedecor F statistical test (e.g. Martin, 1971, chapter 8) with the null hypothesis being "mole fraction is constant",

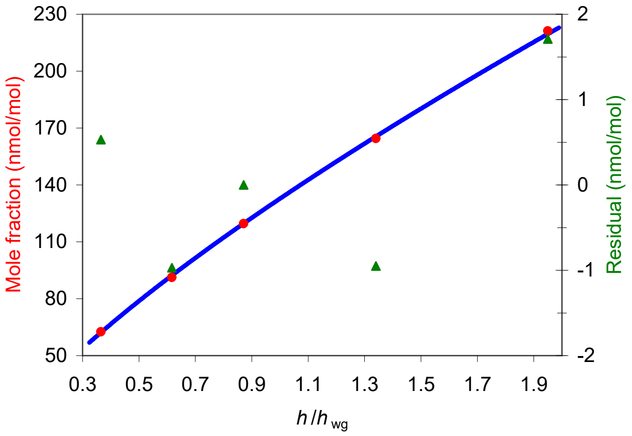

Fig. 2. Least-squares fitting of a typical calibration. The fitting curve is plotted in blue (left y-axis), the measured means are plotted in red (left y-axis), whereas the residuals with respect to the fitting curve are plotted in green (right y-axis).

and with its alternative being "linear drift in time". We require a 95 % confidence level to reject the null hypothesis. Constant mole fraction and the linear drift rate are computed using a least-squares fit with weights. The test takes into account the relative reduction of the chi-square computed with the residuals when using the linear drift instead of the constant mole fraction. To carry out the weighted least-squares fitting, a 1-sigma uncertainty for each value of r_{wg} has to be provided. The main advantage of using a Snedecor F test instead of a Chi-square test is that the 1-sigma uncertainties can be multiplied by a common factor without affecting the result of the test. Therefore, the test is not sensitive to the exact values of the uncertainties, only to their relative values. We have used u_{fit} as the 1-sigma uncertainties necessary for carrying out the weighted least-squares fitting. Six of the sixteen working gases used (see the upper graph of Fig. 3) show significant drift: five with rates ranging from -0.58 to -1.63 nmol mol^{-1} month^{-1}, and one with a positive drift of 2.75 nmol mol^{-1} month^{-1}. These rapid changes likely result from the interaction of CO with the internal surface of the cylinders and the rapid decrease in their internal pressure (from 125 to 25 bar) during the few months they are in use. According to the experience of other laboratories, CO-in-air mixtures stored in aluminium tanks are usually prone to positive drift rates, whereas drift in our working gases is primarily negative. This may be due to the type of tanks used to store the working gases or to issues related to the Izaña station filling system. We consider the drifts are accurately determined and accounted for in the data processing.

After correcting for drift, the response curves were constructed and mole fractions are determined from the air measurements. Identification and discarding of outliers uses an iterative process of three filtering steps. We begin by considering the time series of working gas injections, in detail, the $h_{\mathrm{wg}}/r_{\mathrm{wg}}$ time series. The first step uses a running mean of 7 days and the RMS departure (σ_{run}) of the residuals is computed. Data with a departure from the running mean larger than $5\sigma_{\mathrm{run}}$ are discarded. Note that the running mean is carried out only for evaluating data departures (i.e. it is not used for smoothing actual data). This procedure is run again with a 2 day running mean and a $4\sigma_{\mathrm{run}}$ threshold for discarding. Lastly, a 0.19 day running mean and a $3.5\sigma_{\mathrm{run}}$ threshold for discarding are used. Summarizing, 0.40 %, 0.64 %, and 0.61 % of the working gas injections were discarded in the first, second, and third step, respectively. The quality of measured air mole fractions is also considered. First, mole fractions are calculated only if both the previous and the posterior working gas injections are present (3.11 % of the ambient air injections were discarded by this reason). As for the working gas injections time series, an iterative process of three filtering steps is applied to the ambient air mole fraction time series using running means of 30, 3, and 0.26 days, and thresholds $4.5\sigma_{\mathrm{run}}$, $4\sigma_{\mathrm{run}}$, and $3.5\sigma_{\mathrm{run}}$ for the first, second, and third step, respectively. Summarizing, 0.11 %, 0.30 %, and 1.08 % of the ambient air samples were discarded in the first, second, and third step, respectively. Figure 4 shows daily nighttime means (20:00–08:00 UTC) for the carbon monoxide mole fraction measured at Izaña Observatory. As indicated in Sect. 1, the air sampled at the station at night is representative of the free troposphere. Processed data are submitted to the WMO World Data Centre for Greenhouse Gases.

4 Uncertainty analysis

We compute the combined standard uncertainty for hourly means as a quadratic combination of four uncertainty components: the uncertainty of the WMO standard gases interpolated over the range of measurement (u_{st}), the uncertainty that takes into account the agreement between the standard gases and the response function used (u_{fit}), the uncertainty due to the repeatability of the injections (u_{rep}), and the propagated uncertainty related to the temporal consistency of the response function parameters (u_{par}), which also takes into account the covariance between the parameters. The combined standard uncertainty (u_{tot}) is therefore given by

$$u_{\mathrm{tot}} = \sqrt{u_{\mathrm{st}}^2 + u_{\mathrm{fit}}^2 + u_{\mathrm{rep}}^2 + u_{\mathrm{par}}^2}\,, \tag{3}$$

where

$$u_{\mathrm{st}} = 7.40 \times 10^{-5} r^2 - 1.80 \times 10^{-2} r + 1.92, \tag{4}$$

u_{fit} is defined by Eq. (2),

$$u_{\mathrm{rep}} = \frac{\beta r h_{\mathrm{wg}} \sigma_{h/h_{\mathrm{wg}}}}{\sqrt{3} h}, \text{ and} \tag{5}$$

$$u_{\mathrm{par}}^2 = u_{\mathrm{pr}}^2 + u_{\mathrm{p}\beta}^2 + c. \tag{6}$$

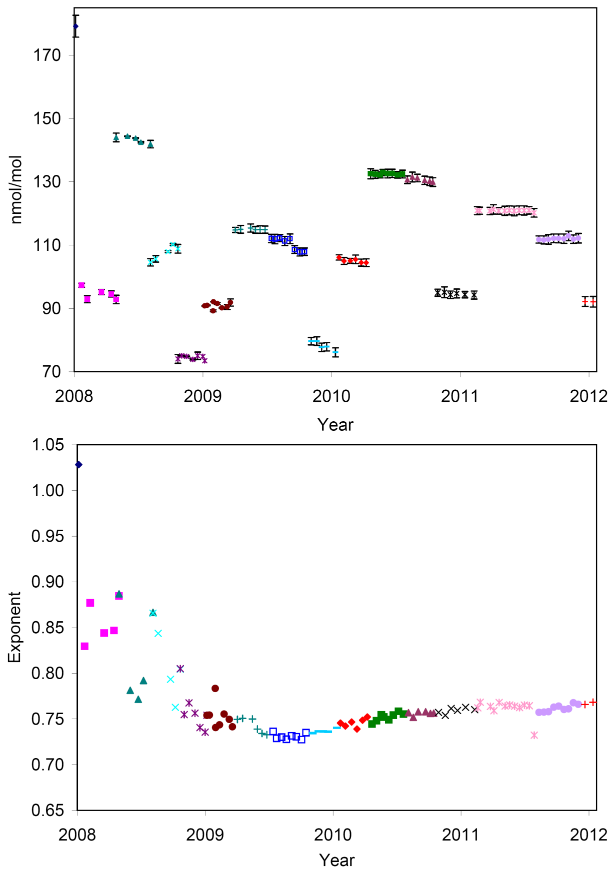

Fig. 3. Upper graph: working gas mole fractions obtained from calibrations conducted during 2008 to 2011. Error bars represent the RMS residual of each calibration, i.e. $\pm u_{\mathrm{fit}}$. Lower graph: response function exponents obtained in the calibrations. Different colours and symbols are used for the different working gases.

$$u_{\mathrm{pr}} = \frac{r}{r_{\mathrm{wg}}} \sigma_{r_{\mathrm{wg}}}, \tag{7}$$

$$u_{\mathrm{p}\beta} = r \sigma_{\beta} \left| \log \frac{h}{h_{\mathrm{wg}}} \right|, \text{ and} \tag{8}$$

$$c = 2 \frac{r^2}{r_{\mathrm{wg}}} \operatorname{covar}\left(r_{\mathrm{wg}}, \beta\right) \log \frac{h}{h_{\mathrm{wg}}}. \tag{9}$$

The units of r and u_{st} in Eq. (4) are $\mathrm{nmol\,mol^{-1}}$; $\sigma_{h/h_{\mathrm{wg}}}$ is the repeatability (standard deviation) of the relative height, which has been divided by $\sqrt{3}$ in Eq. (5) to take into account the improvement in repeatability due to using hourly means; $\sigma_{r_{\mathrm{wg}}}$ quantifies the consistence of the working gas mole fraction along its lifetime (RMS departure from linear drift or from constancy); σ_{β} is the standard deviation of the exponent; and $\operatorname{covar}\left(r_{\mathrm{wg}}, \beta\right)$ is the covariance between r_{wg} and β.

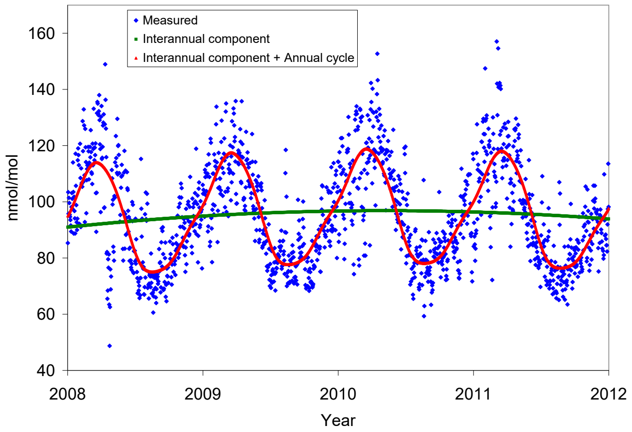

Fig. 4. Daily nighttime (20:00–08:00 UTC) mean CO mole fractions measured at Izaña Observatory (blue squares). The interannual component and the annual cycle from Eq. (26) are shown as the green and red lines, respectively.

The term u_{st} (Eq. 4) was obtained through a least-squares fit of the standard uncertainties for the WMO standard gases of the Izaña station (Table 1). Therefore, u_{st} represents the mole fraction dependent uncertainty due to the WMO standard gases, assuming they have been stable over time. As stated in Sect. 3, within the uncertainty of the measurements we do not observe significant drift in our laboratory standards. In a more general case of Eq. (4), u_{st} would account for (1) laboratory standard gas uncertainties increasing linearly in time due to undetermined potential drifts in the laboratory standards, and (2) the uncertainty in laboratory standard drift rates in case significant drifts had been determined. The term u_{fit} takes into account the disagreement between the response function and the WMO standard gases. Note that the residuals of the standards in the calibrations can have an important systematic component that remains constant for the same standard gas between successive calibrations. Therefore, a hypothetical decrease of u_{fit} when combining the information of successive calibrations cannot be expected. A mean value of u_{fit} is computed for each working gas used. As indicated in Sect. 3, the five laboratory standards detailed in Table 1 were used to determine the response function after March 2009. Before this date, a different set of three WMO standard gases was used, with CO mole fractions, $83.9\,\mathrm{nmol\,mol^{-1}}$, $151.6\,\mathrm{nmol\,mol^{-1}}$, and $165.7\,\mathrm{nmol\,mol^{-1}}$. In this period, u_{fit} is unrealistically small due to the fact that the mole fractions of two of the three standards are near. To provide a better estimate of u_{fit} for curves determined before March 2009, this uncertainty component was forced to be at least equal to the mean value of u_{fit} after March 2009.

The terms $u_{\mathrm{rep}}^2 + u_{\mathrm{par}}^2$ in Eq. (3) come from the propagation of the response function uncertainty (JCGM, 2008). Taking differentials in Eq. (1), we obtain the equation

$$\mathrm{d}r = \frac{r}{r_{\mathrm{wg}}} \mathrm{d}r_{\mathrm{wg}} + \beta r \frac{h_{\mathrm{wg}}}{h} \mathrm{d}\left(\frac{h}{h_{\mathrm{wg}}}\right) + r \log \frac{h}{h_{\mathrm{wg}}} \mathrm{d}\beta, \tag{10}$$

which relates errors (differentials). Obtaining the square of Eq. (10) and averaging over an appropriate ensemble, the terms $u_{\mathrm{rep}}^2 + u_{\mathrm{par}}^2$ are obtained. The only non-null covariance is that between the two parameters of the response function. The variables $\sigma_{r_{\mathrm{wg}}}$, σ_β, and $\mathrm{covar}(r_{\mathrm{wg}}, \beta)$ are computed using the residuals of these parameters with respect to the considered linear drift in time or constancy in time. A single value for each variable per working gas is obtained. The typical value of $\sigma_{r_{\mathrm{wg}}}$ is 1.09 nmol mol^{-1} before March 2009, and 0.40 nmol mol^{-1} after March 2009. The typical value of σ_β is 0.030 before March 2009, and 0.0044 after March 2009. The correlation coefficient between r_{wg} and β reaches significant values as high as 0.73, and as low as -0.91, with its sign dependant on the mole fraction of the working gas. Therefore, the associated covariance has to be considered in the uncertainty computation. Note that the term u_{par} has been obtained, propagating only the parameter repeatabilities. u_{par} does not include other components of the parameter uncertainties. For example, it does not include the parameter uncertainties that could be estimated for each calibration following Sect. 8.1.2 of Martin (1971). Also, it does not include the whole uncertainty of r_{wg} (the mole fraction of the working gas). Therefore, what u_{par} takes into account is the temporal consistency of the response function. The term $\sqrt{u_{\mathrm{st}}^2 + u_{\mathrm{fit}}^2}$ provides the uncertainty in the response function for each calibration event (every two weeks). However, for the rest of time instants, the response function is used without performing any calibration, and therefore the term $\sqrt{u_{\mathrm{st}}^2 + u_{\mathrm{fit}}^2 + u_{\mathrm{par}}^2}$ provides the uncertainty in the response function.

The repeatability (standard deviation) of the relative height, $\sigma_{h/h_{\mathrm{wg}}}$, is determined from the repeated injections for each standard made during instrument calibrations. It is also necessary to know the dependence of $\sigma_{h/h_{\mathrm{wg}}}$ on relative height, h/h_{wg},

$$\sigma_{h/h_{\mathrm{wg}}} = k\sqrt{1+\left(\frac{h}{h_{\mathrm{wg}}}\right)^2}, \tag{11}$$

where k is a parameter equal to $(\sigma_h)/h_{\mathrm{wg}}$, which depends on the mole fraction of the working gas and possibly on time. For the computation of the uncertainty component given by Eq. (5), Eq. (11) is used to provide $\sigma_{h/h_{\mathrm{wg}}}$ using a single (mean) value of k for each working gas used. Equation (11) has been obtained taking into account that the statistical properties of the height error do not depend on mole fraction (the error in the placement of the peak base does not depend on peak height, but on baseline noise).

Figure 5 shows the uncertainty components for the period 2008–2011. Table 2 summarizes the mean values of each uncertainty component before and after March 2009. The mean combined standard uncertainty decreased significantly after March 2009, from 2.37 nmol mol^{-1} to 1.66 nmol mol^{-1}. After March 2009, the components u_{pr}, $u_{\mathrm{p}\beta}$, and u_{par} are significantly smaller than before, reflecting an improvement in the determination and consistency of the response function parameters. Those values are particularly high during the first half of 2008. After March 2009, the single largest uncertainty component was u_{fit}, whereas before March 2009 it was u_{par}. Note that u_{pr} was larger than u_{tot} during part of 2008. According to Eq. (3), u_{tot} is larger than any of its four components (u_{st}, u_{fit}, u_{rep}, and u_{par}). However, u_{pr} and $u_{\mathrm{p}\beta}$ can be larger than u_{par} and even u_{tot} for a negative large enough covariance term c (see Eq. 6).

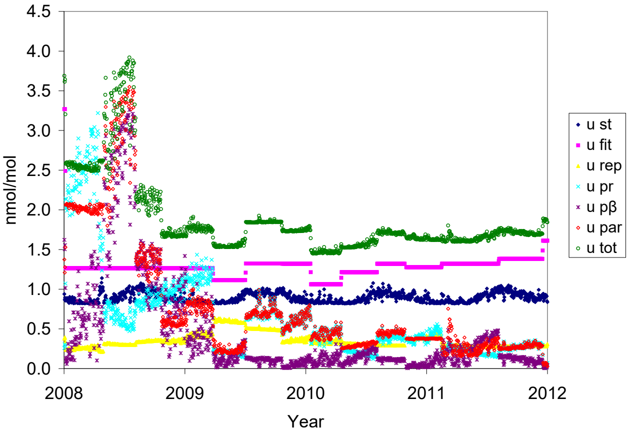

Fig. 5. Uncertainty components (daily means) of the measured CO mole fraction.

4.1 The representation uncertainty and the propagated uncertainty of the temporal mean for quasi-continuous and flask measurements

There is a fifth type of uncertainty we call representation uncertainty, u_{rs}. This is present when computing a temporal mean from a number of available data (n) that is smaller than the theoretical maximum number of independent data (N) within the time interval in which the temporal mean is defined. The temporal mean computed from the n available data may be different from the mean determined from the N data (unknown). The representation uncertainty quantifies this difference statistically. In time series analysis a hierarchy of data assemblages are possible (e.g. hourly mean, daily mean, monthly mean, annual mean), each being computed from the means of the previous level. An additional representation uncertainty is associated with each assemblage. For example, an additional representation uncertainty will appear when computing a daily mean from only 22 available hourly means ($N = 24$, and $n = 22$). The value N is known precisely for each level except for the first. For example, in the Izaña data, the lowest ensemble is the hourly mean, for which $n = 3$ and N is unknown but certainly greater than n. The additional representation uncertainty is given by the equation

$$u_{\mathrm{rs}}^2 = \frac{\sigma_{\mathrm{sam}}^2}{n}\left(\frac{N-n}{N-1}\right), \tag{12}$$

Table 2. Mean values of the uncertainty components (in nmol mol^{-1}) before and after March 2009.

Period	u_{st}	u_{fit}	u_{rep}	u_{pr}	$u_{\mathrm{p}\beta}$	u_{par}	u_{tot}
1 Jan 2008–24 Mar 2009	0.89	1.28	0.33	1.27	1.13	1.64	2.37
25 Mar 2009–31 Dec 2011	0.90	1.27	0.36	0.36	0.13	0.39	1.66

where

$$\sigma_{\mathrm{sam}} = \sqrt{\frac{1}{n-1}\sum_{i=1}^{n}(r_i - \langle r\rangle)^2} \tag{13}$$

is the standard deviation of the sample of data, $\langle r\rangle$ is the mean, and r_i is the data number i used to compute the mean. Indeed, the standard deviation of the sample of data includes the dispersion due to measurement repeatability. Before using Eq. (12), the uncertainty due to the repeatability should be subtracted quadratically from σ_{sam}, and if the result is negative convert it to zero. Note that when $N \gg n$, the term between parenthesis in Eq. (12) becomes equal to 1; in such cases the exact value of N does not matter. Equation (12) is a general statistical result that holds for the variance of the mean of a sample without replacement of size n from a finite population of size N (e.g. Martin, 1971, chapter 5). It assumes that the missing values are randomly distributed with respect to the mean. If this is not the case, the actual representation error could be larger than what the computed representation uncertainty predicts. For example, if three consecutive hours of a day are missing and they are located at an extreme of a significant diurnal cycle, the representation uncertainty will underestimate the actual representation error.

Any computed mean has also a propagated uncertainty arising from the uncertainties of the data used to compute this mean. Therefore, a temporal mean will have an additional representation uncertainty and a propagated uncertainty (both to be summed quadratically) that includes, among others, the propagated representation uncertainty arising from the previous levels of means. The uncertainty components are of two types, combined quadratically: systematic, u_{syst}; and random, u_{rand}. The law of propagation depends on the type of uncertainty. Therefore, we can write

$$u_{\langle r\rangle} = \sqrt{u_{\mathrm{rs}}^2 + u_{\langle r\rangle,\mathrm{rand}}^2 + u_{\langle r\rangle,\mathrm{syst}}^2}\,, \tag{14}$$

where $u_{\langle r\rangle}$ indicates the uncertainty of the mean, $u_{\langle r\rangle,\mathrm{rand}}$ indicates the random component of the propagated uncertainty, and $u_{\langle r\rangle,\mathrm{syst}}$ indicates the systematic component of the propagated uncertainty. For the propagation of random uncertainty, the equation

$$u_{\langle r\rangle,\mathrm{rand}}^2 = \frac{1}{n^2}\sum_{i=1}^{n} u_{\mathrm{rand}_i}^2 \tag{15}$$

holds; whereas for the propagation of systematic uncertainty, the equation

$$u_{\langle r\rangle,\mathrm{syst}}^2 = \frac{1}{n}\sum_{i=1}^{n} u_{\mathrm{syst}_i}^2 \tag{16}$$

holds, where the subindex i indicates the uncertainty of the data number i used to compute the mean. Note that in Eq. (15) there is partial cancellation of random errors, whereas in Eq. (16) there is no cancellation because the systematic error is the same (or nearly the same) for all the data used in the computation. The random uncertainty can be expressed as

$$u_{\mathrm{rand}_i} = \sqrt{u_{\mathrm{rep}_i}^2 + u_{\mathrm{rs}_i}^2}\,, \tag{17}$$

and for the systematic uncertainty

$$u_{\mathrm{syst}_i} = \sqrt{u_{\mathrm{st}_i}^2 + u_{\mathrm{fit}_i}^2 + u_{\mathrm{par}_i}^2}\,. \tag{18}$$

Note that u_{par} behaves as systematic for computing hourly, daily, and monthly means, but behaves as random for computing annual means. The component u_{fit} has systematic and random contributions, but we consider it as systematic for the uncertainty propagation (thus the propagated uncertainty may be slightly overestimated).

Table 3 shows mean values of the uncertainty components for hourly, daily nighttime, monthly, and annual means during the period 25 March 2009–31 December 2011. The hourly means correspond to the nighttime period (20:00–08:00 UTC). The mean representation uncertainty in the hourly means is 0.63 nmol mol^{-1} for the nighttime period, and 0.83 nmol mol^{-1} for the daytime period (08:00–20:00 UTC). The larger value during daytime is due to the CO diurnal cycle (Sect. 6), which makes σ_{sam} larger during daytime. Since the time coverage of the continuous in situ measurements is very high, no additional representation uncertainty components appear when computing the successive means (daily nighttime, monthly, and annual) but only the propagated representation uncertainty. Therefore, the uncertainties associated to random errors (repeatability and representation) are smaller for longer periods of averaging, while the uncertainties associated to systematic errors (u_{st} and u_{fit}) are the same for all the periods of averaging. The uncertainty u_{par} has a mixed behaviour due to the fact that its character (random or systematic) depends on the period of averaging.

As an example of the large representation uncertainty introduced when using very sparse data, we consider the ambient air samples collected weekly at Izaña Observatory

Table 3. Mean values of the uncertainty components (in nmol mol^{-1}) for different averaging periods from 25 March 2009–31 December 2011. The hourly means correspond to the nighttime period (20:00–08:00 UTC).

Type of mean	u_{st}	u_{fit}	u_{par}	u_{rep}	u_{rs}
Hourly	0.90	1.27	0.39	0.36	0.63
Daily nighttime	0.90	1.27	0.39	0.10	0.18
Monthly	0.90	1.27	0.39	0.02	0.03
Annual	0.90	1.27	0.11	0.01	0.01

since 1991 for analysis at NOAA-ESRL-GMD Carbon Cycle Greenhouse Gases Group (CCGG) as part of Cooperative Air Sampling Network (Komhyr et al., 1985; Conway et al., 1988; Thoning et al., 1995). In every sampling event, two flasks are collected nearly simultaneously. Monthly and annual means computed with such sparse flask data (typically 3 or 4 independent values per month) are subject to a large representation uncertainty. Table 4 shows mean values of the representation uncertainty in the different means determined from the NOAA measurements of flask samples. For the hourly and daily nighttime means based on a single pair of flasks, the associated σ_{sam} were computed using the quasi-continuous in situ measurements. The bias between NOAA measurements of daytime upslope air samples and the nighttime free troposphere measurements from the in situ monitoring system is considered in Sect. 6. The average standard deviation σ_{sam} of mole fractions within a month determined from NOAA measurements between 2009 and 2010 was 9.80 nmol mol^{-1}. Following the discussion above, it is not surprising that the representation uncertainties in the in situ means (Table 3) are much smaller than those from flask sampling.

5 Flasks-continuous comparison, comparison uncertainty, and means

Comparison of the results from in situ measurements and results from collocated flask air samples can be used as an independent way of assessing the quality of the continuous in situ measurements (WMO, 2011). A significant difference between a flask sample measurement result and a simultaneous in situ hourly mean is caused by two reasons: (1) the measurements have different, potentially large, errors (note that the concept of error includes the bias in the measurements of any of the laboratories); and/or (2) the air sampled by the two methods is different (i.e. both measurements have different "true values"). The second potential cause for differences between measurements will be quantified through what we call the comparison uncertainty. The statistical significance of each difference (i.e. if there are significantly different errors in both measurements) will be evaluated comparing it with its comparison uncertainty. Note that the error (unknown) is the difference between the true value and the value provided by the measurement system (JCGM, 2008). To compare in situ hourly means with simultaneous NOAA flask samples collected at Izaña (see the last paragraph of Sect. 4.1), we proceed as follows.

1. Flasks results are used only if they are defined by NOAA as representative of background conditions, their sampling and analysis pass quality control checks (a pair of flasks is rejected if the difference between the two members of the pair is greater or equal to 3 nmol mol^{-1}), and the results from both members of the pair are available. Each pair of mole fractions, r_{f1} and r_{f2}, is substituted by its mean, $\langle r_f \rangle$, and its standard deviation,

$$\sigma_f = \frac{|r_{f2} - r_{f1}|}{\sqrt{2}}. \tag{19}$$

   This standard deviation is indicative of the internal consistency of the pair.

2. The NOAA results are compared to hourly means determined in situ (the hour for which the mean is obtained must cover the time that the NOAA samples were collected). We denote the hourly mean as r_c, and the standard deviation of the sample of data within the hour as σ_c, which quantifies the departures of the instantaneous measurements from the mean. Therefore, we compute the difference

$$\mathrm{dif} = \langle r_f \rangle - r_c, \tag{20}$$

   and its comparison uncertainty

$$\sigma_{dif} = \sqrt{\sigma_f^2 + \sigma_c^2}. \tag{21}$$

   Note that we use the in situ hourly means in the comparison since the grab samples are not collected simultaneously with measurements determined at the station. Due to the different temporal character of the compared measurements, σ_c must be used in Eq. (21) instead of the standard deviation of the hourly mean. The comparison uncertainty assesses if the difference is significant. If $|\mathrm{dif}| \le 2\sigma_{dif}$, the difference is not significant, whereas if $|\mathrm{dif}| > 2\sigma_{dif}$, the difference is significant.

Figure 6 shows the time series of differences between NOAA flask samples and simultaneous in situ hourly means. Error bars indicate comparison uncertainty. Dots in red do not have associated error bar due to the absence of σ_c (corresponding to hours with only one valid in situ measurement). For 2008, 47.4 % of the differences are significant, whereas for 2009–2011, only 24.5 % of the differences are significant. Computing percentiles for the CO differences, we conclude that for 2009–2011, 68 % of the differences are between −2.39 and 2.5 nmol mol^{-1} (a large fraction of this

Table 4. Mean values of the representation uncertainty (nmol mol^{-1}) for different averaging periods from the NOAA flask air samples.

Type of mean	Additional u_{rs}	Propagated u_{rs}	Total u_{rs}	n	N
Hourly	1.09	0.00	1.09	1	$\gg 1$
Daily nighttime	3.44	1.09	3.61	1	12
Monthly	4.64	1.81	4.98	4	30
Annual	0.00	1.44	1.44	12	12

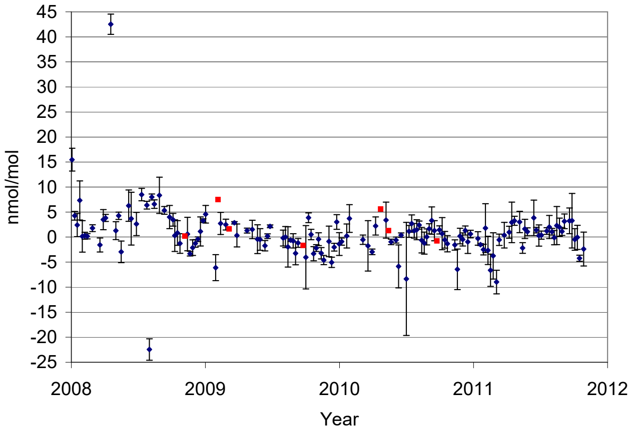

Fig. 6. Differences between NOAA flask samples and simultaneous in situ hourly means. Error bars indicate the comparison uncertainty. Differences plotted in red do not have associated uncertainty due to the presence of only one ambient air injection within the associated hour.

dispersion is caused by the comparison uncertainty, since the 68 percentile of σ_{dif} is equal to 2.28 nmol mol^{-1}), whereas for 2008, 68 % of the differences are between −1.26 and 6.58 nmol mol^{-1}.

5.1 Annual and multi-annual means

We examine differences between the in situ and flask results over annual and longer periods of time. These differences are computed using conventional expressions and two expressions weighted by the comparison uncertainty. Note that the mean difference primarily results from potential systematic errors in the measurements from both laboratories.

The conventional mean is denoted as Mean,

$$\langle \mathrm{dif} \rangle = \frac{1}{n}\sum_{i=1}^{n} \mathrm{dif}_i , \tag{22}$$

where n is the number of differences used to compute the mean. FWMean is a "full" weighted mean computed following the minimum variance method (equivalent to the maximum likelihood method for Gaussian distributions), e.g. Martin (1971, chapter 9),

$$\langle \mathrm{dif} \rangle_{\mathrm{FW}} = \frac{1}{n}\sum_{i=1}^{n} \frac{\sigma_{\mathrm{inv}}^2}{\sigma_{\mathrm{dif}i}^2} \mathrm{dif}_i , \tag{23}$$

where

$$\frac{1}{\sigma_{\mathrm{inv}}^2} = \frac{1}{n}\sum_{i=1}^{n} \frac{1}{\sigma_{\mathrm{dif}i}^2} . \tag{24}$$

This computation considers the quality of the measurements by applying weights to the differences. A difference with a larger uncertainty is considered to provide data of a lower quality and therefore the applied weight is smaller. WMean is an "intermediate" weighted mean for which Eq. (23) applies but $\sigma_{\mathrm{dif}i}^2$ is replaced by the median of σ_{dif}^2 for those $\sigma_{\mathrm{dif}i}^2$ smaller than the median of σ_{dif}^2. This avoids an excessive weight being applied to those differences with a very small $\sigma_{\mathrm{dif}i}^2$. We believe that WMean is the most appropriate estimator. Differences without an associated uncertainty and three differences in 2008 exceeding (in absolute value) 10 nmol mol^{-1} are not included in the computation of the weighted means.

Table 5 provides the mean differences between flask and in situ measurements. Smaller differences are found in 2009–2011 than in 2008. The annual mean differences for 2009–2011 are well within the ±2 nmol mol^{-1} compatibility goal of GAW (WMO, 2011). The results determined by the three approaches are not very different. The conventional annual mean differences are the closest to zero, except for 2008. This is not a general property, since, for example, for CO_2 and CH_4 we have observed many annual weighted mean differences closer to zero than the conventional mean difference.

Table 5 also shows the standard deviation of the mean, σ_{mean}. The standard deviation of the conventional mean can be determined by two approaches. First, this parameter is simply the standard deviation of the sample (SD) divided by $\sqrt{n}$ (e.g. Martin, 1971, chapter 5). Alternately, the relation

$$\sigma_{\mathrm{mean}} = \sqrt{\frac{1}{n^2}\sum_{i=1}^{n} \sigma_{\mathrm{dif}_i}^2} \tag{25}$$

holds. For the weighted means, the relation $\sigma_{\mathrm{mean}} = \sigma_{\mathrm{inv}}/\sqrt{n}$ holds (e.g. Martin, 1971, chapter 9), where σ_{inv} is given by

Table 5. Mean differences between results from the NOAA flask samples and coincident in situ hourly means (NOAA minus in situ) and standard deviations of the means (in $\text{nmol}\,\text{mol}^{-1}$). n dif denotes the number of differences available.

Period	n dif	Mean	σ_{mean}	$\text{SD}/\sqrt{n}$	WMean	σ_{mean}	FWMean	σ_{mean}
2008–2011	147	0.79	0.20	0.42	0.61	0.16	0.59	0.07
2008	39	3.23	0.35	1.36	2.48	0.31	2.16	0.15
2009	35	−0.43	0.36	0.47	−0.47	0.31	0.81	0.12
2010	38	0.02	0.48	0.44	0.25	0.31	−0.11	0.18
2011	35	0.12	0.42	0.49	0.15	0.33	−0.68	0.14

Eq. (24). Note that the σ_{mean} associated with FWMean is smaller than those associated with the other means since FWMean is obtained using the minimum variance method, and σ_{inv} is smaller for smaller values of σ_{dif}. For the conventional mean, Table 5 shows that the values of $\text{SD}/\sqrt{n}$ are larger than the values of σ_{mean}, except for 2010 due to the presence of a difference with a very large value of σ_{dif} (11.3 $\text{nmol}\,\text{mol}^{-1}$) during this year. This means that the dispersion of the differences within one year is larger than would be expected according to the values of σ_{dif_i}. Therefore, when computing weighted means, σ_{dif} does not include all the causes of variability within one year, i.e. it does not fully include the error components that behave as random within one year. Thus, when computing the weighted means, the smallest σ_{dif} are smaller than they should be, which makes FWMean not a very good estimator of the mean for this dataset.

Finally, we consider if the annual average flask versus in situ differences are significant. The mean difference, which is distributed normally according to the Central Limit theorem (e.g. see Martin, 1971, chapter 5), is significant at 95 % confidence level if $|\langle \text{dif} \rangle| > 1.96\sigma_{\text{mean}}$, where $\langle\, \text{dif}\, \rangle$ denotes annual mean difference. As Table 5 shows, the conventional mean and the "intermediate" weighted mean differences (Mean and WMean, respectively) are not significant for 2009, 2010, and 2011, whereas they are significant for 2008. Mean is not significant over the full period 2008–2011, whereas WMean is significant. The "full" weighted mean difference (FWMean) is significant for all years except 2010, but as stated previously, it is not considered a good estimator for this dataset.

6 Time series analysis

To analyse the CO time series of daily nighttime means, we carry out a least-squares fitting to a quadratic interannual component plus a constant annual cycle composed by 4 Fourier harmonics,

$$f(t) = a_0 + a_1 t + a_2 t^2 + \sum_{i=1}^{4} \left[b_i \cos(\omega_i t) + c_i \sin(\omega_i t) \right], \quad (26)$$

where t is time in days, being $t = 1$ for 1 January 2008, a_0, a_1, and a_2 are the parameters of the interannual component to be determined, b_i and c_i are the parameters of the annual cycle to be determined, and $\omega_i = 2\pi i/T$ with $T =$ 365.25 days. This fitting is the same as the one used by Novelli et al. (1998, 2003) and developed by Thoning et al. (1989).

The daily nighttime means, the fitted interannual component, and the fitted interannual component plus the fitted annual cycle are presented in Fig. 4. The RMS residual of the fit is equal to 11.5 $\text{nmol}\,\text{mol}^{-1}$. The nocturnal annual means (Table 6) were determined using the measured data when available and values from the curve fitted data when measured data were not available. As Table 6 shows, the number of days with data not available is very small. From 2008 to 2010 the CO annual mean increased by 4.0 $\text{nmol}\,\text{mol}^{-1}$ (standard uncertainty: 2.3 $\text{nmol}\,\text{mol}^{-1}$), while a decrease of 2.5 $\text{nmol}\,\text{mol}^{-1}$ (standard uncertainty: 2.2 $\text{nmol}\,\text{mol}^{-1}$) is found between 2010 and 2011.

The annual cycle, as defined by the curve (see Fig. 4), shows an amplitude from the minimum to the maximum of 40.7 $\text{nmol}\,\text{mol}^{-1}$. The annual maximum occurs in late March, while the minimum is in the middle of August. This is the seasonal cycle common to the Northern Hemisphere, which is primarily driven by reaction with OH and anthropogenic sources (e.g. Novelli et al., 1998). The annual cycle obtained here is similar to that obtained by Schmitt and Volz-Thomas (1997) using measurements carried out at Izaña from May 1993 to December 1995.

The residuals from the curve can provide information about the air parcels influencing the site. A large change in the residuals indicates a change in air mass. The persistence of the residuals can be measured computing the autocorrelation (Fig. 7). For a time-lag of 1, 2, 3, and 7 days, the autocorrelation is 0.56, 0.30, 0.21, and 0.10, respectively. We conclude the residuals are not autocorrelated after a time-lag of 7 days. Therefore, 7 days could be considered the typical period of persistence of an air mass for CO.

Figure 8 shows the carbon monoxide monthly mean diurnal cycle relative to the nocturnal background, computed using hourly data for the period 2008–2011. This reference background level was computed for each day as follows. Firstly, the averages of the pre- (00:00–07:00 UTC) and post-nights (21:00–04:00 UTC) were computed. Then, the linear drift in time passing through both averages was

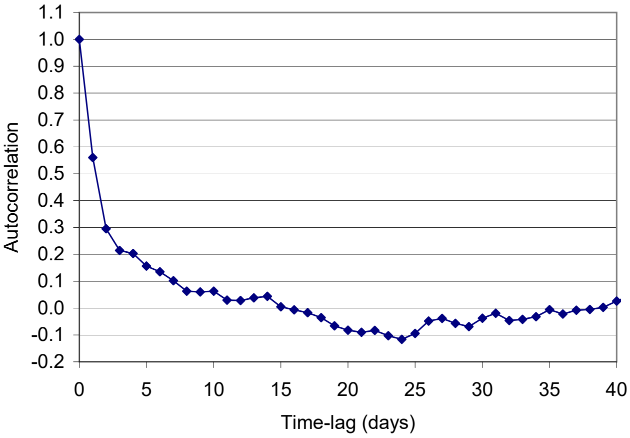

Fig. 7. Autocorrelation of the residuals from the fit determined from Eq. (26).

Table 6. Annual mean and the standard uncertainty of nighttime (20:00–08:00 UTC) CO mole fractions (in nmol mol^{-1}) measured between 2008 and 2011, and number of days with data available.

Year	CO (nmol mol^{-1})	Standard uncertainty	Available days
2008	93.63	1.63	355
2009	94.73	1.56	355
2010	97.64	1.56	351
2011	95.16	1.56	356

used as the reference background level for that day. Note, for example, that hour 1 means the hourly mean for the period 00:00–01:00 UTC. Carbon monoxide at Izaña is typically stable during the night period 20:00–08:00 UTC, starts to increase around 09:00 UTC, reaches its maximum around 13:00–15:00 UTC, before returning to the nocturnal background (Fig. 8). The amplitude of the diurnal cycle is 5–6 nmol mol^{-1}, except in December, when the amplitude is around 4 nmol mol^{-1}. The mean time of flask sampling during 2008–2011 was 10:00 UTC. That is, sampling occurred during non background conditions. There is a mean bias of approximately +1.5 nmol mol^{-1} between the air sampled with flasks and the nocturnal background conditions. During 2002–2007 the mean time of flask sampling was 15:35 UTC. Given all other effects are similar to the more recent period, CO determined from flask air samples are approximately +4.5 nmol mol^{-1} higher than nocturnal background conditions. NOAA began air sampling at Izaña in late 1991, until 2002 flasks were sampled during nighttime, but this was discontinued due to the absence of staff during nighttime.

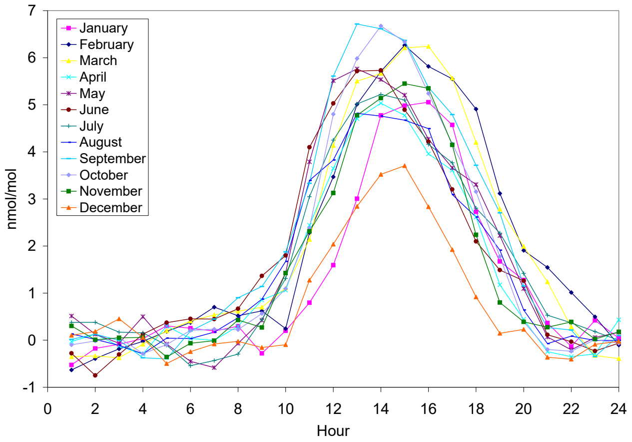

Fig. 8. Carbon monoxide mean diurnal cycle relative to the nocturnal background level.

7 Summary and conclusions

A rigorous procedure to determine the uncertainties in the semi-continuous measurements of CO made at the Izaña global GAW station has been developed. This approach is applicable to other sites in the WMO GAW global network. The error in the measurements are reported as the combined standard uncertainty. This has four components: the uncertainty of the WMO standard gases interpolated over the range of measurement, the uncertainty that takes into account the agreement between the standard gases and the response function used, the uncertainty due to the repeatability of the injections, and the propagated uncertainty related to the temporal consistency of the response function parameters (which also takes into account the covariance between the parameters). The mean value of the combined standard uncertainty decreased significantly after March 2009, from 2.37 nmol mol^{-1} to 1.66 nmol mol^{-1}. The reason for this improvement is a very significant reduction in the response function parameter standard deviations (the dominant source of uncertainty before March 2009). There was an improvement in the determination and consistency of the response function parameters due to the following facts that apply after March 2009. The improvement reflects the use of a newer and larger set of WMO standard gases, more injections of the working gas in the calibration sequence, and use of an adjacent closed port in the multiposition selection valve to stop sample loop flushing for pressure equilibration. The dominant uncertainty component after March 2009 is the uncertainty that takes into account the agreement between the standard gases and the response function (1.27 nmol mol^{-1}). A fifth type of uncertainty we call representation uncertainty is considered when some of the data necessary to compute the temporal mean are absent. Any computed mean has also a propagated uncertainty arising from the uncertainties of the data used to compute the mean. The law of propagation depends on the type of uncertainty component (random or systematic), i.e. there is partial cancellation of random errors through averaging, whereas there is no cancellation of systematic errors. The representation uncertainties in the in situ measurements are much smaller than those computed using flask samples (e.g. the representation uncertainty in the monthly means is equal to 4.98 nmol mol^{-1} for the NOAA flask measurements, and 0.03 nmol mol^{-1} for the quasi-continuous measurements). The larger uncertainty in the flask air measurements reflects the relatively sparse sampling.

The 2008–2011 Izaña carbon monoxide nocturnal time series is evaluated using a least squares fit to a quadratic interannual component plus a constant annual cycle composed by 4 Fourier harmonics. The interannual component increases till the beginning of 2010, and then decreases. The amplitude of the seasonal cycle, determined from the curve, is 40.7 nmol mol^{-1}. The late winter maximum and midsummer minimum observed at Izaña compare well with seasonal cycles reported from many other northern-hemisphere mid-latitude locations. Autocorrelation of the residuals indicates that the typical period of persistence of an air mass for CO is 7 days. The monthly mean diurnal cycle reaches a midday maximum of 4 to 6 nmol mol^{-1} above the stable nocturnal free troposphere background. This enhancement results from upslope winds which transport contaminated air coming from below the temperature inversion layer to the station. The air samples collected during the daytime are biased high with respect to mid-tropospheric background conditions. The magnitude of the bias depends on the sampling hour.

We also examine differences between hourly means determined by the in situ continuous measurements with flask air samples determined within the hour. The uncertainties in the mean results from each method allows determination of the statistical significance of the differences. During 2008, 47.4 % of the differences were significant, with 68 % of these between −1.26 and 6.58 nmol mol^{-1}. During 2009–2011, only 24.5 % of the differences were significant and 68 % were between −2.39 and 2.5 nmol mol^{-1} (this range is largely due to the comparison uncertainty). Total and annual mean differences between the grab samples and in situ measurements were computed using conventional expressions but also expressions with weights based on the minimum variance method. During the period 2009–2011 the flask in situ differences are much closer to zero than during 2008, which likely results from the better performance of the Izaña measurement system during 2009–2011. The annual mean differences between NOAA and in situ (AEMET) measurements for 2009–2011 are not significant and within the 2 nmol mol^{-1} inter-laboratory compatibility goal of GAW.

Acknowledgements. This study was developed within the Global Atmospheric Watch (GAW) Programme at the Izaña Atmospheric Research Center, financed by AEMET. We are grateful to Christoph Zellweger for advice during the configuration of the RGA, and to the Izaña observatory staff. The collaborative air sampling network operated by the NOAA-ESRL-GMD carbon cycle group is acknowledged for its many years of measurements at the observatory. We thank the editor and two anonymous referees for their comments, which helped to improve the manuscript. AJGP thanks Celia Milford for English language comments.

Edited by: O. Tarasova

References

Armerding, W., Comes, F. J., Crawack, H. J., Forberich, O., Gold, G., Ruger, C., Spiekermann, M., Walter, J., Cuevas, E., Redondas, A., Schmitt, R., and Matuska, P.: Testing the daytime oxidizing capacity of the troposphere: 1994 OH field campaign at the Izaña observatory, Tenerife, J. Geophys. Res., 102, 10603–10611, doi:10.1029/96JD03714, 1997.

Conway, T. J., Tans, P., Waterman, L. S., Thoning, K. W., Masarie, K. A., and Gammon, R. H.: Atmospheric carbon dioxide measurements in the remote global troposphere, 1981–1984, Tellus B, 40, 81–115, doi:10.1111/j.1600-0889.1988.tb00214.x, 1988.

Ehhalt, D., Prather, M., Dentener, F., Derwent, R., Dlugokencky, E., Holland, E., Isaksen, I., Katima, J., Kirchhoff, V., Matson, P., Midgley, P., and Wang, M.: Atmospheric chemistry and greenhouse gases, Chapter 4, in: Climate Change 2001: The Scientific Basis, edited by: Houghton, J. T., Ding, Y., Griggs, D. J., Noguer, M., van der Linden, P. J., Dai, X., Maskell, K., and Johnson, C. A., Cambridge University Press, Cambridge, UK, 239–287, 2001.

Fischer, H., Nikitas, C., Parchatka, U., Zenker, T., Harris, G. W., Matuska, P., Schmitt, R., Mihelcic, D., Muesgen, P., Paetz, H.-W., Schultz, M., and Volz-Thomas, A.: Trace gas measurements during the oxidizing Capacity of the Tropospheric Atmosphere campaign 1993 at Izaña, J. Geophys. Res., 103, 13505–13518, doi:10.1029/97JD01497, 1998.

JCGM: JCGM 100:2008, GUM 1995 with Minor Corrections, Evaluation of Measurement Data – guide to the Expression of Uncertainty in Measurement, Joint Committee for Guides in Metrology, Member organizations: BIPM, IEC, IFCC, ILAC, ISO, IUPAC, IUPAP, and OIML, 2008.

Kitzis, D.: Preparation and stability of standard reference air mixtures, Tech. rep., NOAA Earth System Research Laboratory, Boulder, USA, available at: http://www.esrl.noaa.gov/gmd/ccl/airstandard.html (last access: 14 September 2012), 2009.

Komhyr, W. D., Gammon, R. H., Harris, T. B., Waterman, L. S., Conway, T. J., Taylor, W. R., and Thoning, K. W.: Global atmospheric CO_2 distribution and variations from 1968–1982 NOAA/GMCC CO_2 flask sample data, J. Geophys. Res., 90, 5567–5596, doi:10.1029/JD090iD03p05567, 1985.

Lang, P. M.: Guidelines for standard gas cylinder and pressure regulator use, Tech. rep., NOAA Earth System Research Laboratory, Boulder, USA, available at: http://www.esrl.noaa.gov/gmd/ccl/reg.guide.html (last access: 14 September 2012), 1998.

Logan, J. A., Prather, M. J., Wofsy, S. C., and McElroy, M. B.: Tropospheric chemistry – a global perspective, J. Geophys. Res., 86, 7210–7254, doi:10.1029/JC086iC08p07210, 1981.

Martin, B. R.: Statistics for Physicists, Academic Press, London, UK, 1971.

Navascues, B. and Rus, C.: Carbon dioxide observations at Izana baseline station, Tenerife (Canary Islands) – 1984–1988, Tellus B, 43, 118–125, doi:10.1034/j.1600-0889.1991.t01-1-00006.x, 1991.

Novelli, P. C., Steele, P., and Tans, P. P.: Mixing ratios of carbon monoxide in the troposphere, J. Geophys. Res., 97, 20731–20750, doi:10.1029/92JD02010, 1992.

Novelli, P. C., Masarie, K. A., and Lang, P. M.: Distributions and recent changes of carbon monoxide in the lower troposphere, J. Geophys. Res., 103, 19015–19033, doi:10.1029/98JD01366, 1998.

Novelli, P. C., Masarie, K. A., Lang, P. M., Hall, B. D., Myers, R. C., and Elkins, J. W.: Reanalysis of tropospheric CO trends: effects of the 1997–1998 wildfires, J. Geophys. Res.-Atmos., 108, 4464, doi:10.1029/2002JD003031, 2003.

Rodríguez, S., González, Y., Cuevas, E., Ramos, R., Romero, P. M., Abreu-Afonso, J., and Redondas, A.: Atmospheric nanoparticle observations in the low free troposphere during upward orographic flows at Izaña Mountain Observatory, Atmos. Chem. Phys., 9, 6319–6335, doi:10.5194/acp-9-6319-2009, 2009.

Schmitt, R. and Volz-Thomas, A.: Climatology of ozone, PAN, CO, and NMHC in the free troposphere over the Southern North Atlantic, J. Atmos. Chem., 28, 245–262, 1997.

Schmitt, R., Schreiber, B., and Levin, I.: Effects of long-range transport on atmospheric trace constituents at the baseline station Tenerife (Canary Islands), J. Atmos. Chem., 7, 335–351, 1988.

Thoning, K. W., Tans, P. P., and Komhyr, W. D.: Atmospheric carbon dioxide at Mauna Loa Observatory, II – Analysis of the NOAA GMCC data, 1974–1985, J. Geophys. Res., 94, 8549–8565, doi:10.1029/JD094iD06p08549, 1989.

Thoning, K. W., Conway, T. J., Zhang, N., and Kitzis, D.: Analysis system for measurement of CO_2 mixing ratios in flask air samples, J. Atmos. Ocean. Tech., 12, 1349–1356, doi:10.1175/1520-0426(1995)012<1349:ASFMOC>2.0.CO;2, 1995.

WMO: Guidelines for the Measurement of Atmospheric Carbon Monoxide, GAW Report No. 192, World Meteorological Organization, Geneva, Switzerland, 2010.

WMO: 15th WMO/IAEA Meeting of Experts on Carbon Dioxide, Other Greenhouse Gases and Related Tracers Measurement Techniques, Jena, Germany, 7–10 September 2009, GAW Report No. 194, chap. Expert group recommendations, World Meteorological Organization, Geneva, Switzerland, 1–25, 2011.

Zellweger, C., Klausen, J., Buchmann, B., and Scheel, H. E.: System and Performance Audit of Surface Ozone, Carbon Monoxide, Methane and Nitrous Oxide at the Global GAW Station Izana, Spain, March 2009, WCC-Empa Report 09/1, 2009.

4.2. Modelización de la evolución del metano en la atmósfera en los últimos cuarenta años

4.2.1. Indicadores de calidad de la publicación

Indicadores de calidad de la publicación a fecha 4 de agosto de 2018, obtenidos de "Web Of Science" en el formato CVN de la FECYT.

Dalsoren, Stig B.; Myhre, Cathrine L.; Myhre, Gunnar; Gomez-Pelaez, Angel J.; Sovde, Ole A.; Isaksen, Ivar S. A.; Weiss, Ray F.; Harth, Christina M.Atmospheric methane evolution the last 40 years. ATMOSPHERIC CHEMISTRY AND PHYSICS. 16 - 5, pp. 3099 - 3126. COPERNICUS GESELLSCHAFT MBH, 01/01/2016. ISSN 1680-7316, ISSN 1680-7324.

Tipo de producción: Artículo

Tipo de soporte: Revista

Fuente de impacto: WOS (JCR)

Categoría: Science Edition - METEOROLOGY & ATMOSPHERIC SCIENCES

Índice de impacto: 5.318

Revista dentro del 25%: Si

Posición de publicación: 4

Num. revistas en cat.: 85

Fuente de citas: WOS

Citas: 19

4.2.2. Introducción

La fracción molar de CH_4 se ha más que doblado durante la era industrial. Aún hay incertidumbres elevadas sobre: 1) en qué medida contribuyen a las fuentes de CH_4 cada sector de actividad y cada región del mundo (Bruhwiler et al., 2014; Ciais et al., 2013; Houweling et al., 2014; Neef et al., 2010; Pison et al., 2009); 2) los factores subyacentes que contribuyen a las tendencias interanuales observadas (Bergamaschi et al., 2013; Bousquet et al., 2006, 2011; Dlugokencky et al., 2003, 2009; Ghosh et al., 2015; Levin et al., 2012); y 3) las retroalimentaciones desde la biosfera y el permafrost (Bridgham et al., 2013; Isaksen et al., 2011). Las incertidumbres en la comprensión de las fuentes, las tendencias recientes y las retroalimentaciones, limitan la exactitud de las proyecciones futuras de evolución del CH_4. Incrementar el CH_4 atmosférico aceleraría el calentamiento a corto plazo debido a su fuerte impacto en el clima en la ventana temporal de 20 años (Myhre et al., 2013a). Los niveles aumentados de CH_4 también incrementarían los niveles de O3 en superficie (Fiore et al., 2008; Isaksen et al., 2014; West and Fiore, 2005), y por tanto empeorarían el impacto de la contaminación en la vegetación, los cultivos y la salud humana.

Este estudio constituye una contribución a la comprensión del CH_4 en la atmósfera, proporcionando un detallado análisis de su evolución a escala global y regional durante los últimos 40 años. Investigamos los forzadores esenciales naturales y antropogénicos que controlan la cantidad de CH_4 en la atmósfera a lo largo del periodo, especialmente en los últimos 15 años. Se analizan tanto las fuentes como los sumideros. Los sumideros dependen de la capacidad de oxidación de la atmósfera, que viene determinada por complejas interacciones químicas y meteorológicas. Este artículo trata de identificar los componentes químicos clave y los factores meteorológicos que afectan a los cambios recientes en la capacidad de oxidación. Comparamos simulaciones obtenidas usando modelos de transporte químico con observaciones, para entender las causas de las tendencias a largo plazo y las variaciones de corto plazo (interanuales). También se busca explicación para las diferencias entre las tendencias de CH_4 observadas y modeladas.

Los métodos usados son descritos en la sección 2 del artículo, y ya han sido presentados en la sección 3.2 de esta memoria de tesis. La sección 3 del artículo presenta los resultados de nuestro análisis principal y los discute en un contexto más amplio en relación a resultados de otros estudios publicados. En el material suplementario del artículo se presentan estudios de sensibilidad adicionales. En la sección 4 del artículo se resumen los resultados obtenidos.

4.2.3. Resumen en español del artículo

Como se mencionó en la sección 3.2.2, en este estudio se utiliza el modelo Oslo CTM3, que no solo es un modelo de transporte, sino que además incluye química atmosférica, para estudiar el periodo 1970-2012. Adicionalmente a lo mencionado en la sección 3.2.2, se utilizan 18 trazadores ficticios pasivos, uno por cada sector de emisión de CH_4 considerado (la tabla S1 del material suplementario del artículo indica cuales son esos 18 sectores). Estos trazadores ficticios son emitidos continuamente y destruidos mediante decaimiento exponencial con un tiempo característico de 1 mes. Sufren transporte, pero no interaccionan químicamente. Un mes es, aproximadamente, el tiempo que tardan las emisiones recientes en dispersarse en la atmósfera lo suficiente para considerar que forman parte del fondo (background) atmosférico. Estos trazadores pasivos son usados como un proxy para la contribución de los diferentes sectores a las concentraciones de CH_4 medias mensuales en superficie, con el propósito de revelar sectores clave y qué regiones son responsables de los cambios recientes en la distribución espacial y temporal del CH_4.

La meteorología usada en este estudio cubre el periodo 1997-2012. Para los años previos hasta 1970, periodo para el que no están disponibles los campos de pronóstico utilizados (véase la sección 3.2.2), se utiliza la meteorología del año 2001, porque es un año en el que el índice ENSO es débil para todos los meses. Estudios previos han mostrado una fuerte influencia de ENSO en el CH_4 (Johnson et al., 2002; Warwick et al., 2002). La inicialización del modelo ("spin up") se hizo con una ejecución larga en la que se usaron de forma repetitiva las emisiones del año 1970 hasta que se obtuvo una cantidad de CH4 en la atmósfera estable de un año a otro de la simulación. Esto requirió ejecutar la simulación durante 27 años, debido al largo tiempo de ajuste del CH_4. Tras la inicialización, se ejecutó la simulación para el periodo 1970-2012.

La simulación denominada "principal" incluye las emisiones estándar de CH4 descritas en la sección 2.1.1 del artículo (y en la sección 3.2.1 de esta memoria de tesis). En la simulación denominada "financiera", el periodo 2009-2012 fue recalculado con unas emisiones ligeramente diferentes con el fin de evaluar si la reciente crisis financiera hubiera podido causar algún impacto significativo en los niveles de CH_4. Con un propósito similar, la simulación denominada “bio” se realizó teniendo en cuenta variaciones interanuales en las emisiones de CO y compuestos orgánicos volátiles no metánicos por parte de la vegetación. Los resultados de estas dos simulaciones especiales para estudiar la sensibilidad a estos factores son discutidos en el material suplementario del artículo. Además, la simulación con “metano fijo”, en la que no se prescriben las emisiones, sino que se deja fijo el CH_4 en superficie a los niveles mensuales de 1970 (es decir, se prescriben las condiciones de contorno de tipo Dirichlet en lugar de las de tipo Neumann), para aislar los efectos de otros componentes y de los factores meteorológicos en el CH_4 vía cambios en la capacidad de oxidación. Por último, la simulación con “meteorología fija” utiliza también en el periodo 1997-2012 la meteorología del año 2001, como en los años previos. Al comparar esta simulación con la “principal”, el impacto de la variabilidad meteorológica puede ser identificado/determinado. Todas estas simulaciones están enumeradas en la Tabla 1 del artículo.

En este estudio se hace una comparación exhaustiva de los campos de CH_4 atmosférico simulados con las medidas de estaciones de superficie para todas las regiones del planeta. La variación estacional es reproducida para la mayoría de las estaciones. El modelo también reproduce gran parte de la evolución observada del CH_4 en las escalas interanual y decadal. Las variaciones en las emisiones de los humedales son los mayores forzadores de las variaciones interanuales del CH_4.

En relación a las variaciones de las tendencias, las causas son objeto de debate (véase la sección 3 del artículo). No se alcanza consenso en la contribución relativa de los sectores de emisión individuales, ni a la atribución entre fuentes naturales y antropogénicas. El hecho de que nuestras simulaciones capturen gran parte de los cambios regionales observados, indica que el modelo de transporte y los esquemas químicos funcionan bien, y que los inventarios de emisiones usados son razonables en su distribución temporal, espacial, sectorial, y natural versus antropogénico. Sin embargo, hay algunas discrepancias importantes en el comportamiento del modelo que cuestionan la exactitud de los datos de emisión de CH_4 en ciertas regiones y periodos. Los errores potenciales en los datos de emisión son localizados para los años recientes cuando las simulaciones del modelo son más completas con respecto a los datos de entrada (emisiones, meteorología variable que se corresponde con la realidad…) y hay más medidas disponibles para comparar.

Tras un periodo con nivel de CH_4 estable entre los años 2000 y 2006, las observaciones muestran aumento del CH_4 en ambos hemisferios. Desde 2006, el modelo sobreestima el crecimiento en todas las regiones, y en particular en Asia. El gran aumento de las emisiones de CH_4 en Asia influencia las tendencias de este componente en la mayoría de las regiones del mundo. Nuestros resultados están de acuerdo con otros estudios, sugiriendo que el reciente crecimiento de las emisiones antropogénicas en Asia está sobreestimado en el inventario EDGAR v4.2. Basándonos en los resultados obtenidos con nuestro modelo y la comparación entre las emisiones ECLIPSE y EDGAR v4.2 en el material suplementario del artículo (Sec. S2), nos cuestionamos también las tendencias en las emisiones asiáticas en los años noventa y el comienzo de la década con inicio en el año 2000, en el inventario EDGAR v4.2, aunque el limitado número de estaciones de medida en Asia hace difícil validar esta conclusión.

La evolución modelada del CH_4 también depende de los cambios en el sumidero atmosférico de CH_4. La vida media del CH_4 es un indicador del sumidero de CH_4. En nuestras simulaciones, la vida media del CH_4 decrece más de un 8% entre 1970 y 2012 (véase la Fig. 15 del artículo), debido al incremento de la capacidad de oxidación de la atmósfera. Este cambio, en teoría, es producido por complejas interacciones entre un gran número de componentes químicos y factores meteorológicos. Sin embargo, nuestro análisis revela que los factores clave son los cambios en: 1) la humedad específica; 2) la proporción de emisión entre NO_x y CO; 3) las emisiones de NO_x debidas a rayos; y 4) la columna total de O_3. Es estadísticamente válido predecir la vida media del CH_4 a partir de una combinación de estos parámetros mediante una ecuación sencilla (véase la última ecuación de la sección 3.6 del artículo). Los cambios que obtenemos en la vida media del CH_4 están dentro del rango proporcionado por la mayoría de estudios de modelización "abajo-arriba" (bottom-up; este término significa que la base de la modelización son las emisiones). Sin embargo, los resultados de esos estudios no están completamente de acuerdo los estudios "arriba-abajo" (top-down; este término significa que la base de la modelización son las concentraciones atmosféricas, y mediante inversión se obtienen las emisiones a posteriori, más precisas y exactas que las a priori usadas) que usan observaciones de CH_3CCl_3 o ^{14}CO. Sin el incremento calculado en la capacidad de oxidación, el crecimiento de CH_4 en las últimas décadas hubiera sido mucho mayor.

El incremento del sumidero de CH_4 probablemente también contribuyó al estancamiento del crecimiento del CH_4 en el periodo 2001-2006. Es interesante ver que durante los últimos (pocos) años, el sumidero se desvía del comportamiento de crecimiento estacionario de las décadas previas. Gran parte de esta desviación parece ser causada por variaciones en la meteorología. Nuestras simulaciones muestran que tener en cuenta las variaciones en la meteorología tiene un fuerte efecto en el sumidero de CH_4 atmosférico. Esto, de hecho, afecta a los cambios de CH_4 interanuales y de largo plazo. La estabilización del sumidero de CH_4, fundamentalmente debida a la variabilidad meteorológica, probablemente contribuyó al incremento continuado de CH_4 en los años 2009-2012, tras las altas emisiones de los años 2007 y 2008. El largo tiempo de respuesta del CH_4 podría también contribuir al crecimiento futuro de los niveles de CH_4. Sin embargo, hay una incertidumbre extra en los resultados del modelo después de 2009 debido a la falta de inventarios de emisiones completos. Un nuevo inventario o actualización de los existentes con separación por subsectores de emisión para los últimos años (2009-2015) sería muy útil para estudios de modelización que traten de resolver las incógnitas que aún permanecen sobre el ciclo del CH_4. Esto, además, proporcionará fundamentos importantes para predecir de forma más exacta los niveles futuros de CH_4 y varias estrategias de mitigación.

4.2.4. Artículo original en inglés

Enlace al artículo original: https://doi.org/10.5194/acp-16-3099-2016

Atmos. Chem. Phys., 16, 3099–3126, 2016
www.atmos-chem-phys.net/16/3099/2016/
doi:10.5194/acp-16-3099-2016

Atmospheric Chemistry and Physics
Open Access

Atmospheric methane evolution the last 40 years

Stig B. Dalsøren[1], **Cathrine L. Myhre**[2], **Gunnar Myhre**[1], **Angel J. Gomez-Pelaez**[3], **Ole A. Søvde**[1], **Ivar S. A. Isaksen**[1,4], **Ray F. Weiss**[5], **and Christina M. Harth**[5]

[1]CICERO – Center for International Climate and Environmental Research Oslo, Oslo, Norway
[2]NILU – Norwegian Institute for Air Research, Kjeller, Norway
[3]Izaña Atmospheric Research Center (IARC), Meteorological State Agency of Spain (AEMET), Izaña, Spain
[4]University of Oslo, Department of Geosciences, Oslo, Norway
[5]Scripps Institution of Oceanography University of California, San Diego La Jolla, California, USA

Correspondence to: Stig B. Dalsøren (stigbd@cicero.oslo.no)

Received: 11 July 2015 – Published in Atmos. Chem. Phys. Discuss.: 5 November 2015
Revised: 24 February 2016 – Accepted: 26 February 2016 – Published: 9 March 2016

Abstract. Observations at surface sites show an increase in global mean surface methane (CH_4) of about 180 parts per billion (ppb) (above 10 %) over the period 1984–2012. Over this period there are large fluctuations in the annual growth rate. In this work, we investigate the atmospheric CH_4 evolution over the period 1970–2012 with the Oslo CTM3 global chemical transport model (CTM) in a bottom-up approach. We thoroughly assess data from surface measurement sites in international networks and select a subset suited for comparisons with the output from the CTM. We compare model results and observations to understand causes for both long-term trends and short-term variations. Employing Oslo CTM3 we are able to reproduce the seasonal and year-to-year variations and shifts between years with consecutive growth and stagnation, both at global and regional scales. The overall CH_4 trend over the period is reproduced, but for some periods the model fails to reproduce the strength of the growth. The model overestimates the observed growth after 2006 in all regions. This seems to be explained by an overly strong increase in anthropogenic emissions in Asia, having global impact. Our findings confirm other studies questioning the timing or strength of the emission changes in Asia in the EDGAR v4.2 emission inventory over recent decades. The evolution of CH_4 is not only controlled by changes in sources, but also by changes in the chemical loss in the atmosphere and soil uptake. The atmospheric CH_4 lifetime is an indicator of the CH_4 loss. In our simulations, the atmospheric CH_4 lifetime decreases by more than 8 % from 1970 to 2012, a significant reduction of the residence time of this important greenhouse gas. Changes in CO and NO_x emissions, specific humidity, and ozone column drive most of this, and we provide simple prognostic equations for the relations between those and the CH_4 lifetime. The reduced lifetime results in substantial growth in the chemical CH_4 loss (relative to its burden) and dampens the CH_4 growth.

1 Introduction

The atmospheric CH_4 abundance has more than doubled over the industrial era. The resulting radiative forcing is second after CO_2 in terms of anthropogenic forcing from greenhouse gases (Myhre et al., 2013). High uncertainty remains regarding the contributions from specific source sectors and regions to the CH_4 emissions (Neef et al., 2010; Kirschke et al., 2013; Houweling et al., 2014; Melton et al., 2013; Bruhwiler et al., 2014; Schwietzke et al., 2014; Bridgham et al., 2013; Pison et al., 2009; Ciais et al., 2013), the underlying factors contributing to observed trends (Dlugokencky et al., 2009, 2003; Wang et al., 2004; Kai et al., 2011; Aydin et al., 2011; Simpson et al., 2012; Bousquet et al., 2006, 2011; Pison et al., 2013; Bergamaschi et al., 2013; Monteil et al., 2011; Ghosh et al., 2015; Nisbet et al., 2014; Fiore et al., 2006; Levin et al., 2012), and in feedbacks from the biosphere and permafrost (Bridgham et al., 2013; Melton et al., 2013; Isaksen et al., 2011; O'Connor et al., 2010). The uncertainties in our understanding of current budgets, recent trends, and feedbacks limit confidence in accurately projecting the future evolution of CH_4. Increasing atmospheric CH_4 would accelerate near-term warming, due to its strong climate impact on a 20-year time frame (Myhre et al., 2013). Enhanced CH_4 levels would also increase the ozone levels in surface air (Fiore et al., 2008, 2012; West and Fiore, 2005; Isaksen et al., 2014), and thereby worsen air pollution impacts on vegetation, crops, and human health.

This study seeks to increase our understanding of CH_4 by providing a detailed analysis on global and regional CH_4 evolution over the last 40 years. We investigate essential natural and anthropogenic drivers controlling the atmospheric CH_4 budget over the period, with a particular focus on the last 15 years. We perform a balanced analysis of both sources and sinks. The sinks depend on the atmospheric oxidation capacity, which is determined by complex chemical and meteorological interactions. This study tries to reveal the key chemical components and meteorological factors affecting recent changes in the oxidation capacity. We compare model studies and observations to understand causes for both long-term trends and short-term variations (year-to-year). We also address reasons for differences between observed and modelled CH_4 trends. The methods used are described in Sect. 2. Section 3 presents the results from our main analysis and discuss them in a broader context related to findings from other studies. Additional sensitivity studies are presented in the Supplement. In Sect. 4 we summarize our findings.

2 Methods and approach

2.1 Emissions and sinks

2.1.1 Methane

We used CH_4 emissions for anthropogenic sources from EDGAR v4.2 (EC-JRC/PBL, 2011) and biomass-burning and natural sources from Bousquet et al. (2011). In addition we used soil uptake from Bousquet et al. (2011). Combination of two emission inventories (EDGAR v4.2 and Bousquet et al., 2011) makes it possible to study the impacts of many emission sectors (18 in total, see Table S1 in the Supplement for the sectors and specifications of the categories). The EDGAR inventory covers the period 1970–2008 while the Bousquet et al. (2011) data covers the period 1984–2009. Since we study the period 1970–2012 extrapolations were made for the years not covered by the data sets. For all years from 1970 to 1984 we used natural and biomass-burning emissions and soil uptake for 1984. For 2010–2012 we used 2009 data for these sources. For the anthropogenic emissions we extrapolated the change from the period 2007–2008 to the period 2009–2012. The rather simple extrapolations result in additional uncertainties in the model outcome for these years. Figure S1 in the Supplement shows how the emissions are included in the model for the different time periods. The total emissions and emissions from major sectors are shown in Fig. 1. There is a large growth in total emissions from 1970 to 2012. However, shorter periods with declining emissions occur due to large inter-annual variability in natural emissions, especially from wetlands which is the largest emission sector. The inter-annual variation in wetland emissions tends to be anti-correlated with the ENSO index (Bousquet et al., 2006; Hodson et al., 2011). Low natural emissions also occur due to lower global temperatures in the years after the Pinatubo eruption. In the 1990s the growth in anthropogenic emissions are small, mainly caused by the economic collapse of the former USSR. From 2000 to 2006 the total emissions are quite stable, and this is caused by decreasing wetland emissions due to dry conditions in the tropics in combination with increasing anthropogenic emissions. From 2006 there is a strong growth in total emissions due to large wetland emissions and a continuing growth of anthropogenic emissions. The abrupt increase in 2007 is mainly explained by high wetland emissions caused by high temperatures at high latitudes in the Northern Hemisphere, and wet conditions in the tropics (Bousquet et al., 2011). Enteric fermentation (due to ruminants) is the main anthropogenic emission sector and it grows steadily except for a period in the 1990s. Some other major anthropogenic sectors like gas, solid fuel (mostly coal) and agricultural soils (mostly rice) even decrease over shorter periods but have in common a substantial growth over the last decade. The sum of several smaller anthropogenic emission sectors (industry, residential, waste, some fossil, etc.) are also shown in Fig. 1. This sum termed "other anthropogenic sectors" is of the same magnitude as enteric fermentation. The growth is rather stable and moderate with some interruptions: temporary declines occur after the oil crisis in 1973 and the energy crisis in 1979. The growth is also small during the 1990s.

We also explore a possible impact of the recent financial crisis using an alternative extrapolation of anthropogenic emissions for the period 2009–2012. Here, the emissions from petroleum and solid fuel production and distribution were scaled with BP Statistical Review of World Energy (http://www.bp.com/en/global/corporate/energy-economics/statistical-review-of-world-energy.html) numbers for gas production, oil and coal consumption resulting in a drop in total emissions in 2009 (Fig. 1). However, the evolution from 2010 with this alternative extrapolation is rather similar to that for the standard extrapolation. The EDGAR v4.2 inventory was recently extended to include also the years 2009–2012. In Fig. S2 (Supplement) we compare our extrapolations with the new data and also include a comparison to ECLIPSE v5a emissions that are available for part of our study period (1990–2015, 5-year intervals).

2.1.2 Other components

Anthropogenic emissions of CO, NO_x, sulfur and NMVOCs were taken from the EDGAR v4.2 inventory (EC-JRC/PBL, 2011). Similar extrapolation was done as for the CH_4 emissions to cover the period 2009–2012. For biomass-burning

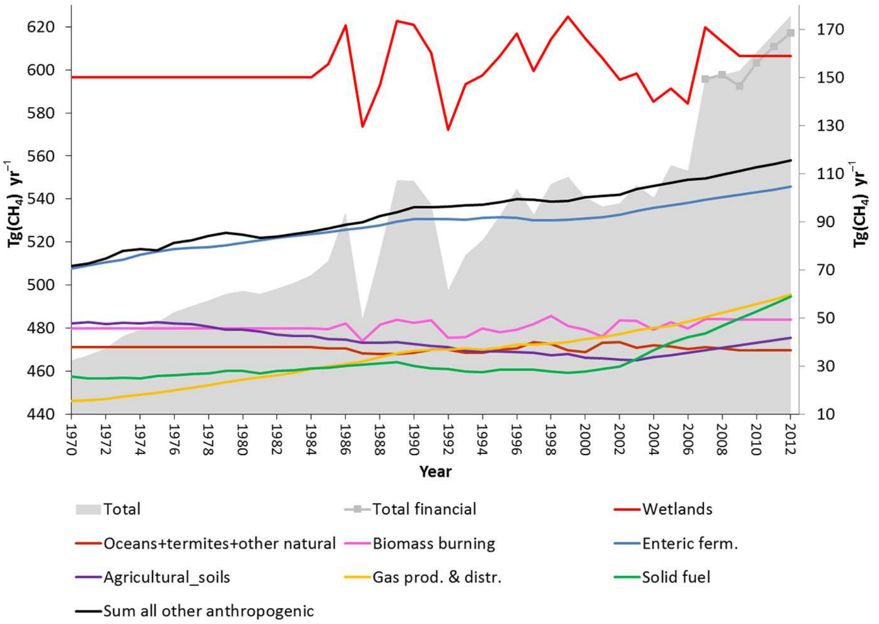

Figure 1. Emissions used in the model simulations. The grey shaded area is the total CH_4 emissions (left y axis). The total emissions in the alternative extrapolation accounting for the financial crisis are shown from 2006 and onwards as the grey line with markers. The other coloured lines are the CH_4 emissions from the main emission sectors (right y axis).

emissions we used GFEDv3 (van der Werf et al., 2010) for the period 1997–2012. In the period 1970–1996 we used year-2001 emissions from GFEDv3. 2001 was taken as a proxy for an average year since it has a weak ENSO index for all months (see next section for more discussion on this).

The parametrization and inter-annual variation of lightning NO_x emissions are described in Søvde et al. (2012). For other natural emissions we used emission data for 2000 for all years. The oceanic emissions of CO and NMVOCs and soil NO_x emissions are from RETRO (Schultz et al., 2008). Sources for natural sulfur emissions are described in Berglen et al. (2004). The emissions from vegetation of CO and NMVOCs are from MEGANv2 (Guenther et al., 2006). Recently a new data set (Sindelarova et al., 2014) with MEGAN emissions covering the period 1980–2010 became available. This data set was used in a sensitivity study to investigate whether inter-annual variations in CO and NMVOCs emissions from vegetation are important for the CH_4 evolution.

2.2 Chemical transport model

The emission data over the period 1970–2012 was used as input in the Oslo CTM3 model. A coupled tropospheric and stratospheric version was used. The model was run with 109 chemical active species affecting CH_4 and atmospheric oxidation capacity. In addition we added 18 passive fictitious tracers for each of the CH_4 emission sectors listed in Table S1. The traces were continuously emitted and then given an e-folding lifetime of 1 month, undergoing transport but not interacting chemically. The passive tracers were used as a proxy for the different sector's contribution to monthly mean surface CH_4 concentrations. The aim was to reveal key sectors and regions behind recent changes in spatial distribution or temporal evolution of CH_4.

Oslo CTM3 was described and evaluated by Søvde et al. (2012) and used for studying CH_4 lifetime changes in Holmes et al. (2013). Oslo CTM3 is an update of Oslo CTM2 which has been used in a number of previous studies of stratospheric and tropospheric chemistry, including studies on CH_4 (Dalsøren et al., 2010, 2011; Dalsøren and Isaksen, 2006; Isaksen et al., 2011).

The Oslo CTM3 simulations were driven with 3-hourly meteorological forecast data from the European Centre for Medium-Range Weather Forecasts (ECMWF) Integrated Forecast System (IFS) model (see Søvde et al., 2012, for details). These data are 36-h forecasts produced with 12 h of spin-up starting from an ERA-Interim analysis at noon on the previous day. The meteorological data used in this study cover the period 1997–October 2012. For the years ahead of 1997, year-2001 meteorology was used. 2001 was chosen since this is a year with weak ENSO index for all months. Previous studies have shown a strong influence of ENSO events on CH_4 (Holmes et al., 2013; Warwick et al., 2002; Johnson et al., 2002). Initially the model was spun up in a long run with repetitive 1970 emissions until we obtained a stable atmospheric CH_4 burden from one year to the next. Due to the long adjustment time of CH_4 it took 27 years to get CH_4 in equilibrium. After the spin up a set of simulations (Table 1) were made for the period 1970 to 2012. The "main"

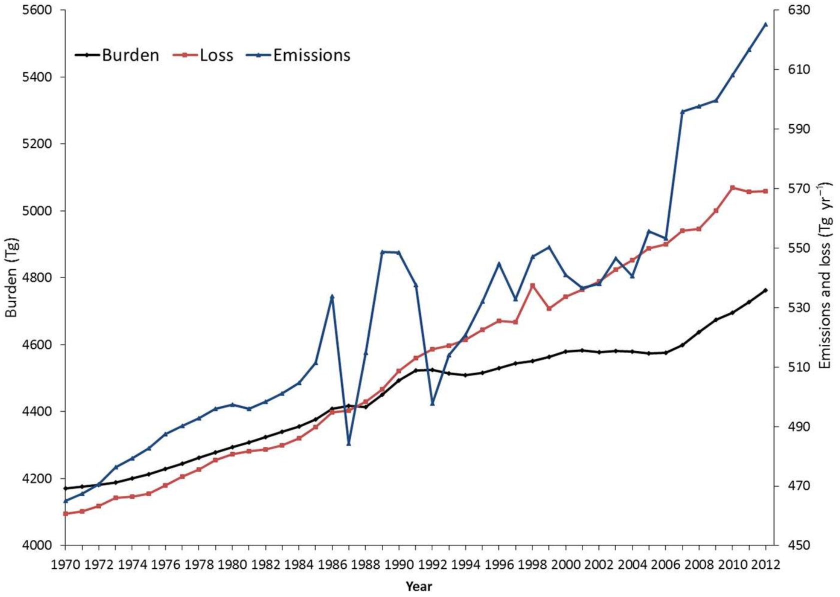

Figure 2. Global CH_4 budget in the main Oslo CTM3 simulation over the period 1970–2012: atmospheric burden (left y axis); loss: atmospheric chemical destruction + soil uptake (right y axis); and total emissions (right y axis).

Table 1. Overview of simulations performed with the Oslo CTM3 model.

Simulation name	Period	Characteristics	Difference from main simulation
Main	1970–Oct 2012	Standard emissions described in Sect. 2.1.1. Meteorology described in this section.	
Fixed methane	1970–Oct 2012		*No prescription of methane emissions*. Surface methane levels kept fixed. Monthly mean 1970 levels used repeatedly for all years
Fixed meteorology	1997–Oct 2012		*Year-2001 meteorology*
Financial*	2009–Oct 2012		*Alternative extrapolation* of anthropogenic emissions to account for the *financial crisis*
Bio*	1980–2012		*Inter-annual variation* in *biogenic* emissions of NMVOCs and CO

* Results (and setup) from these simulations are mainly discussed in the Supplement.

simulation includes the standard CH_4 emissions described in Sect. 2.1.1. In the "financial" simulation, the period 2009–2012 was rerun with slightly different emissions evaluating whether the recent financial crisis had any significant impact on CH_4 levels. With a similar purpose a "bio" simulation was performed accounting for inter-annual variation in emissions of CO and NMVOCs from vegetation. The results from the two sensitivity studies on emissions are discussed in the Supplement. In the "fixed methane" simulation, the prescription of methane emissions was turned off and surface CH_4 was kept fixed at monthly mean 1970 levels (i.e., boundary condition of Dirichlet type instead of Neumann type) to isolate the effect of other components and meteorological factors on CH_4 via changes in oxidation capacity. In the "fixed met" simulation, the period 1997–2012 was repeated using year-2001 meteorology for all years. By comparing this run with the "main" simulation the impact of meteorological variability could be discerned.

2.3 Observations

To get insights into the drivers of the changes on regional level, and reveal strengths and discrepancies in model performance we compared the model results to surface CH_4 observations. We thoroughly assessed the surface sites providing CH_4 measurements to the World Data Center for Greenhouse Gases (WDCGG) (http://ds.data.jma.go.jp/gmd/wdcgg/), and picked out a subset of sites for comparison.

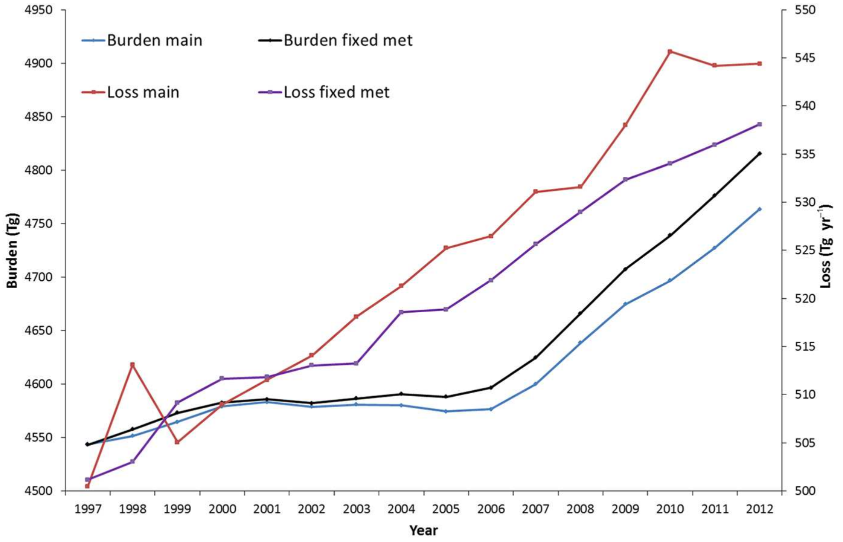

Figure 3. Atmospheric CH_4 burden and atmospheric chemical loss for the simulation with "fixed meteorology" and the "main" simulation.

Criteria for selection were the length of measurement record (coverage over most of the time periods of interest), access to continuous time series with few gaps, time resolution (at least 2–3 measurement per month), coverage of different regions of the Earth, and site characteristics (e.g. elevation, topography, and influence of pollution episodes). The last point was evaluated in relation to the resolution of the CTM. From this analysis, 71 observational data sets from 64 stations in the WDCGG database were selected as suited for comparisons with the CTM results. Comparisons for some of these stations are shown in Sects. 3.3 and 3.4.

3 The methane evolution and decisive factors over the period 1970–2012

3.1 Global methane budget

Figure 2 shows the evolution of the CH_4 budget over the period 1970–2012 for the main simulation. It presents total burden and loss calculated by the forward CTM run and the emissions applied in this simulation. The total burden shown in black is balanced by the emissions (blue) and the loss (red). There is a steady growth in atmospheric CH_4 burden from 1970 to the beginning of the 1990s, then a short period of decline after the Mount Pinatubo volcanic eruption in 1991. After 1994 there is a slight increase in CH_4 burden towards the millennium. Then the CH_4 burden is stable for 5–6 years. After 2006 there is a rapid growth in CH_4 burden.

The evolution of emissions and the modelled CH_4 burden share many common features (Fig. 2). However, the growth in emissions is about 35 % from 1970 to 2012, while the growth in atmospheric burden is about 15 % (additional burden increase after 2012 due to the long response time of CH_4, is not accounted for in this number). The CH_4 burden increased less than expected solely from the increase in CH_4 emissions since a growth in the atmospheric CH_4 loss occurred over the period. The growth in instantaneous atmospheric CH_4 loss is almost 25 %. In the period 2001–2006 when emissions were quite stable increasing CH_4 loss likely contributed to the stagnation of the CH_4 growth. Interestingly, for 2010–2012, the loss deviates from its steady increase over the previous decades. A stabilization of the CH_4 loss probably contributed to the continuing increase (2009–2012) in CH_4 burden after the high emission years 2007 and 2008. Due to the long response time of CH_4 this change in the loss pattern might also contribute to future growth in CH_4. However, there are additional uncertainties in the model burden and loss after 2009 due to the extrapolation of emissions after this year.

Especially after 1997 and the introduction of variation in meteorology, we see that the loss follows a different path than the burden. Comparing the main model simulation with the one with fixed meteorology (Fig. 3) for the period 1997–2012 it becomes evident that inclusion of varying meteorological factors is important to take into account to understand the development of the CH_4 budget. This was also shown in other studies (Johnson et al., 2002; Fiore et al., 2006; Warwick et al., 2002; Holmes et al., 2013). If there had been no variation in meteorology and only changes in emissions, the CH_4 loss would have been significantly different and there would have been a stronger increase in CH_4 burden after 2006. Meteorological variability explains to a large degree much of the stabilization of CH_4 loss after 2010, and might thereby explain part of the large CH_4 burden increase in 2011 and 2012. Around the millennium we see a stabilization of the loss in the simulation with fixed meteorology, but increased loss in the main run. This implies that meteorological variations contribute to a prolonged period (2003–2006) of sta-

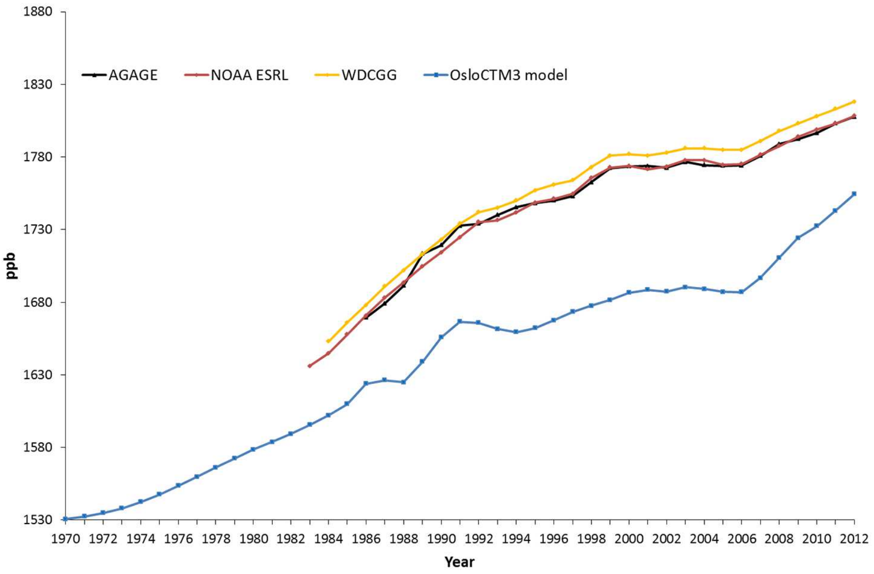

Figure 4. Global mean surface CH_4 mixing ratio in the main model simulation compared to global mean surface CH_4 mixing ratio calculated from the global networks AGAGE (http://agage.eas.gatech.edu/data_archive/global_mean/global_mean_md.txt), NOAA ESRL (http://www.esrl.noaa.gov/gmd/ccgg/mbl/data.php), and WDCGG (http://ds.data.jma.go.jp/gmd/wdcgg/pub/global/globalmean.html).

bilization in CH_4 burden (Fig. 3). From the comparison in Fig. 3 it can also be seen that it is meteorological factors and not emissions that cause the large enhancements of CH_4 loss in 1998 (El Niño event) and 2010 (warm year on global scale). Such episodes do not show up as immediate perturbations of the CH_4 burden (Figs. 2 and 3) due to the long response time of atmospheric CH_4. Meteorology and other drivers for the modelled evolution of methane loss are discussed in detail in Sects. 3.5–3.6.

3.2 Evolution of global mean surface methane

Figure 4 compares the global mean surface CH_4 in the main model simulation, to global mean surface CH_4 calculated from networks of surface stations. The main picture is discussed in this section while more detailed evaluations of CH_4 development on continental scale, trends, and interannual variations are made in the following sections. The time evolution of global mean surface CH_4 is very similar for the three observational networks shown in Fig. 4 but there are some differences for the absolute methane level. The AGAGE (mountain and coastal sites) and NOAA ESRL (sites in the marine boundary layer) stations are distant from large pollution sources. WDCGG uses curve fitting and data extension methods very similar to those developed by NOAA and many of the same stations (Tsutsumi et al., 2009), but in addition to marine boundary layer sites, WDCGG includes many continental locations strongly influenced by local sources and sinks (http://www.esrl.noaa.gov/gmd/ccgg/mbl/mbl.html). The methane emission estimates from Bousquet et al. (2011) are optimized against atmospheric observations. Since we only use their natural and biomass-burning emission inventories, we use different anthropogenic emissions (from EDGAR), and the OH field in their inverse model is substantially different from our modelled OH, there is no guarantee that our model will match observations.

Our model generally reproduces the different periods of growth and stagnation and the overall observed increase in concentration from 1984 to 2012 of almost 180 ppb is replicated. This gives us confidence when evaluating the decisive drivers explaining the variable evolution over time. However, the model fails to reproduce the strength of the growth rate during some eras, for instance the growth since 2006 is overestimated. Over the whole period the model also underestimate the observed CH_4 level. Even though there are also large uncertainties in total CH_4 emission levels (Kirschke et al., 2013; Ciais et al., 2013), we find it more likely that our model overestimates the atmospheric CH_4 sink. In a recent model inter-comparison, the multi-model global mean CH_4 lifetime was underestimated by 5–13 % (Naik et al., 2013) compared to observational estimates. Our study shows a similar underestimation of CH_4 lifetime. Though the multi-model lifetime is within the uncertainty range of observations, it is likely that models tend to overestimate OH abundances in the Northern Hemisphere (Naik et al., 2013; Strode et al., 2015; Patra et al., 2014).

3.3 Methane evolution and emission drivers in different regions

In the Supplement, we explain how the CH_4 mole fraction can be split into two components: a quite uniform background component and an inhomogeneous recently emitted component. The latter is advected and mixed, and when

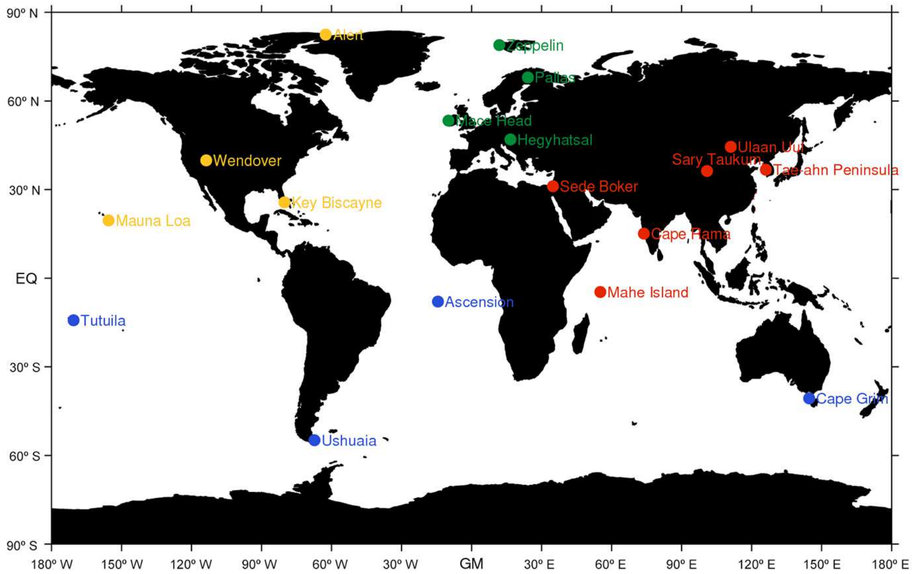

Figure 5. Location of the 18 surface stations used in comparison between measurements and model in this section. Blue: stations in the Southern Hemisphere; orange: stations in or near North America; green: stations in or near Europe; red: stations in or near Asia.

achieving a good mixing (after 1–2 months) it is converted into the background component. We show how the use of a 1-month e-folding fictitious tracer (total tracer) is valid as a proxy for the inhomogeneous component. The CH_4 surface emissions act as the sources for the tracer. In the Supplement we use the continuity equation for the CH_4 mole fraction (CH_4 model) as starting point and further arguments to derive the following approximation:

$$\begin{aligned} &< \mathrm{CH_4\ model} > -[< \mathrm{CH_4\ model} >] \\ &= B \times (< \mathrm{total\ tracer} > -[< \mathrm{total\ tracer} >]) \\ &+ \mathrm{residual}, \end{aligned} \tag{1}$$

where [ ] denotes longitudinal mean along a whole terrestrial parallel and <> denotes annual running mean. We are interested in the inter-annual variation of CH_4, so we have carried out annual running means to remove the strong seasonal cycle. The subtraction of longitudinal means on each side of Eq. (1) removes the influence of differences in lifetimes (the mean lifetime of CH_4 is around 9 years, whereas the mean lifetime of the total tracer is 1 month). B and "residual" are constants (or almost constant) if the prerequisites discussed in the Supplement (Sect. S3, last paragraph) are met. We expect B to be near or equal to 1 and residual to be small. If B and residual were exactly constant, the Pearson linear correlation coefficient between $< \mathrm{CH_4\ model} > -[< \mathrm{CH_4\ model} >]$ and $< \mathrm{total\ tracer} > -[< \mathrm{total\ tracer} >]$ would be exactly equal to 1. The tracer approach then gives valuable information concerning the contribution to CH_4 variation from recent regional–local emission or transport changes. We therefore use the correlation coefficient (indeed, its square, R^2: the coefficient of determination obtained when performing a linear least-square fit between both magnitudes in Eq. 1 to determine B and residual) as one criterion when selecting interesting stations for methane trend studies. Only stations where R^2 is higher than 0.5 is used. This criterion excludes only a small number of the available stations. In addition, we use the general station selection criteria discussed earlier in the manuscript (sufficient coverage in the different world regions, long time series etc., see Sect. 2.3). Figure 5 shows the locations of stations used in Figs. 6–10 for detailed trend analysis and evaluation of model performance.

Table 2 shows R^2, the constants B and residual, and RMSE from a linear fit of the variables in Eq. (1). All stations except one (reason for exception at the Wendover station is discussed in the Supplement) have R^2 above 0.8. Such high coefficients support that the approximation in Eq. (1) is useful for these stations. As expected, B is usually larger than 1. The fictitious tracer will underestimate somewhat the inhomogeneous recently emitted CH_4, in particular at remote stations, because part of it is removed by the e-folding sink before being smoothed to the characteristic variation length of the background. Mauna Loa is probably the most remote station and located at high altitude. It has the largest B and residual. Alert, Tutuila, Mahe Island, and Key Biscayne are also remote stations that have a high B. As explained below the tracers play a small role in explaining CH_4 at Cape Grim and Ushuaia, where B is below 1.

In the upper panels of Figs. 6–10, the model results are scaled to the observed mean CH_4 level over the periods of measurements to better discern differences in trends between observations and model. The scaling procedure is explained in the Supplement. In general, the model reproduces the seasonal and year-to-year variations very well with high coeffi-

Table 2. Coefficient of determination (R^2) between $<$ CH4model $>$ $-[<$ CH_4 model $>]$ and $<$ total tracer $>$ $-[<$ total tracer $>]$ for stations shown in Figs. 5–10. Parameters for Eq. (1) and RMSE for a linear fit between $<$ CH_4 model $>$ $-[<$ CH_4 model $>]$ and $<$ total tracer $>$ $-[<$ total tracer $>]$.

Station	Figure	R^2 between $<$ CH_4 model $>$ $-[<$ CH_4 model $>]$ and $<$ total tracer $>$ $-[<$ total tracer $>]$	residual	B	RMSE
Ascension Island	6a	0.80	−3.01	1.21	0.74
Tutuila	6b	0.87	5.08	1.49	0.82
Cape Grim	6c	0.98	−0.15	0.97	0.05
Ushuaia	6d	0.83	−0.27	0.94	0.09
Alert	7a	0.69	−2.16	1.66	0.85
Wendover	7b	0.54	−5.74	0.78	1.07
Key Biscayne	7c	0.95	6.10	1.38	1.40
Mauna Loa	7d	0.87	18.41	1.80	1.27
Zeppelinfjellet	8a	0.91	−1.67	1.13	0.59
Pallas–Sammaltun	8b	0.95	−3.38	1.18	0.75
Mace Head	8c	0.97	−3.28	1.16	0.56
Hegyhatsal	8d	1.00	−2.46	1.15	0.96
Sede Boker	9a	0.83	5.41	1.23	0.97
Ulaan Uul	9b	0.95	1.15	1.10	0.65
Sary Taukum	9c	0.97	−8.27	1.11	0.96
Tae-ahn Peninsula	9d	0.97	0.77	1.07	1.15
Cape Rama	10a	0.92	−9.60	1.24	1.02
Mahe Island	10b	0.85	6.68	1.42	1.22

cients of determination, R^2, for most stations (the median is 0.76, and R^2 is above 0.65 for 15 of 18 stations). The model performance is lower at highly polluted sites due to large gradients in concentrations and non-linearity of oxidant chemistry not fully captured by a global model with coarse resolution (approximately $2.8° \times 2.8°$). The model also captures the long-term evolution of CH_4 seen in the observations but overestimates the increase after 2005 at most stations.

The stations in the Southern Hemisphere (Fig. 6) are located far from the dominating emissions sources, and the CH_4 concentration is to a large degree determined by transport and chemical loss. The high coefficients of determination ranging from 0.92 to 0.95 and reproduction of the seasonality and trends indicate that our model is performing excellent with respect to transport and seasonal variation in the chemical loss.

As seen in the mid panels, Ascension Island (Fig. 6a) and Tutuila (Fig. 6b) have negative $<$ total tracer $>$ $-[<$ total tracer $>]$. Since these are rather remote stations, their tracer levels are below the longitudinal mean. The modelled CH_4 evolution from 1990 to 2005 is well correlated with the development of the natural tracers. However, changes in natural emissions do not seem to explain the periods with large growth before 1990 and for the period 2005–2012. While the model underestimates the growth before 1990 it overestimates the growth in the recent years. The small steady increases in contributions from all anthropogenic sectors only has a minor contribution to the modelled CH_4 increase for these periods. However, since these source tracers have an e-folding lifetime of 1 month their evolution is only representative for changes in contribution from regional sources. Inter-hemispheric transport occurs on longer timescales; hence, changes in large anthropogenic sources in the Northern Hemisphere most likely also had a significant contribution as discussed below. At Ascension Island, extra strong influences of regional sources ($<$ CH_4 model $>$ $-[<$ CH_4 model $>]$ change different from zero) are mainly associated with El Niño episodes (1987, 1997–1998, and 2004–2005). In the 1997–1998 period, there are peaks both for the natural tracer and $<$ total tracer $>$ $-[<$ total tracer $>]$ indicating a rise in nearby natural emissions and/or transport from such a source. For 1987 a regional drop in natural emissions has a smaller impact at Ascension compared to the whole latitude band. At Tutuila $<$ total tracer $>$ $-[<$ total tracer $>]$ decreases over time due to a relatively larger increase in the latitudinal mean anthropogenic tracers (not shown), especially enteric fermentation. This explains why the CH_4 growth at the site ($<$ CH_4 model $>$) is slightly less than the mean latitudinal ($[<$ CH_4 model $>]$) growth.

Ushuaia (Fig. 6c) and Cape Grim (Fig. 6d) are the southernmost stations. In the mid panels it can be seen that both terms on the right side in Eq. (1) are small ($B \times (<$ total tracer $>$ $-[<$ total tracer $>]$ and residuals) resulting in small ($<$ CH_4 model $>$ $-[<$ CH_4 model $>]$). This indicates that the contribution to CH_4 from regional emissions are small and that long-range transport from other latitudes is de-

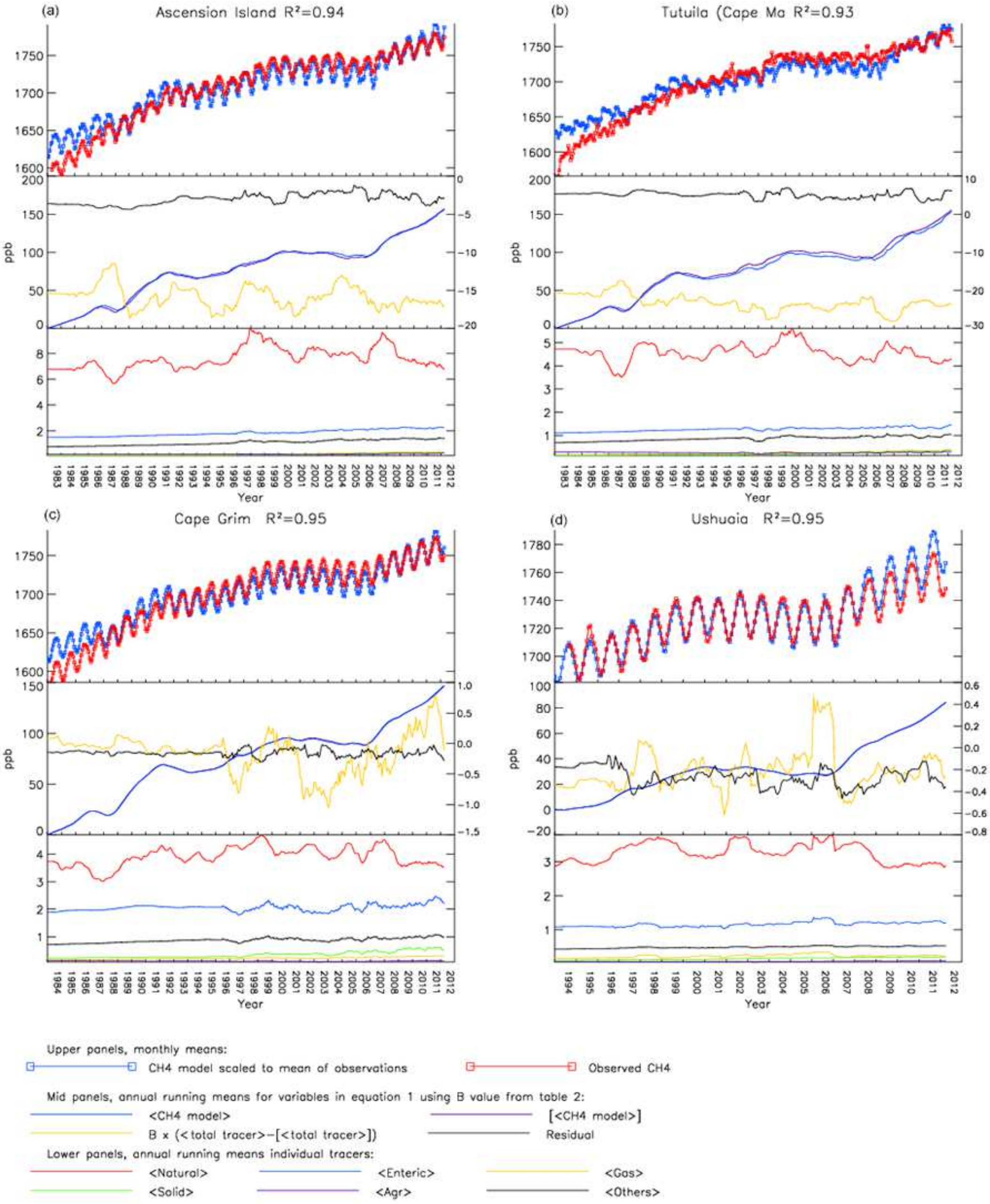

Figure 6. Evolution of CH_4 and tracers at stations (**a**: Ascension Island, **b**: Tutuila, **c**: Cape Grim, **d**: Ushuaia) in the Southern Hemisphere. Upper panel in each figure: comparison of monthly mean surface CH_4 in model and observations. The model results are scaled to the observed mean CH_4 level over the periods of measurements. Mid panels: variables from Eq. (1). $<>$ denotes annual running mean, [ ] denotes longitudinal mean. Left y axis: $< CH_4 \text{ model} >$ and $[< CH_4 \text{ model} >]$ are scaled down to be initialized to zero in the first year. Right y axis: $B \times (< \text{total tracer} > - [< \text{total tracer} >])$ and residual. Lower panels: Evolution of various emission tracers, see Table S1 in the Supplement for detailed information.

cisive. Distant latitudinal transport is not seen by the tracer term if it takes more than around 2 months. Such transport would also result in very similar $< CH_4 \text{ model} >$ and $[< CH_4 \text{ model} >]$ since atmospheric species with lifetime of that timescale or longer are quite homogenously distributed over latitudinal bands. Since both the emissions and their trends are small at high southern latitudes, the distant transport likely originates from low latitudes in the Southern Hemisphere or the Northern Hemisphere.

At stations in or near North America (Fig. 7) the model reproduces the observed trends with increases in the 1980s, less change in the period 1990–2005 and increase from 2006.

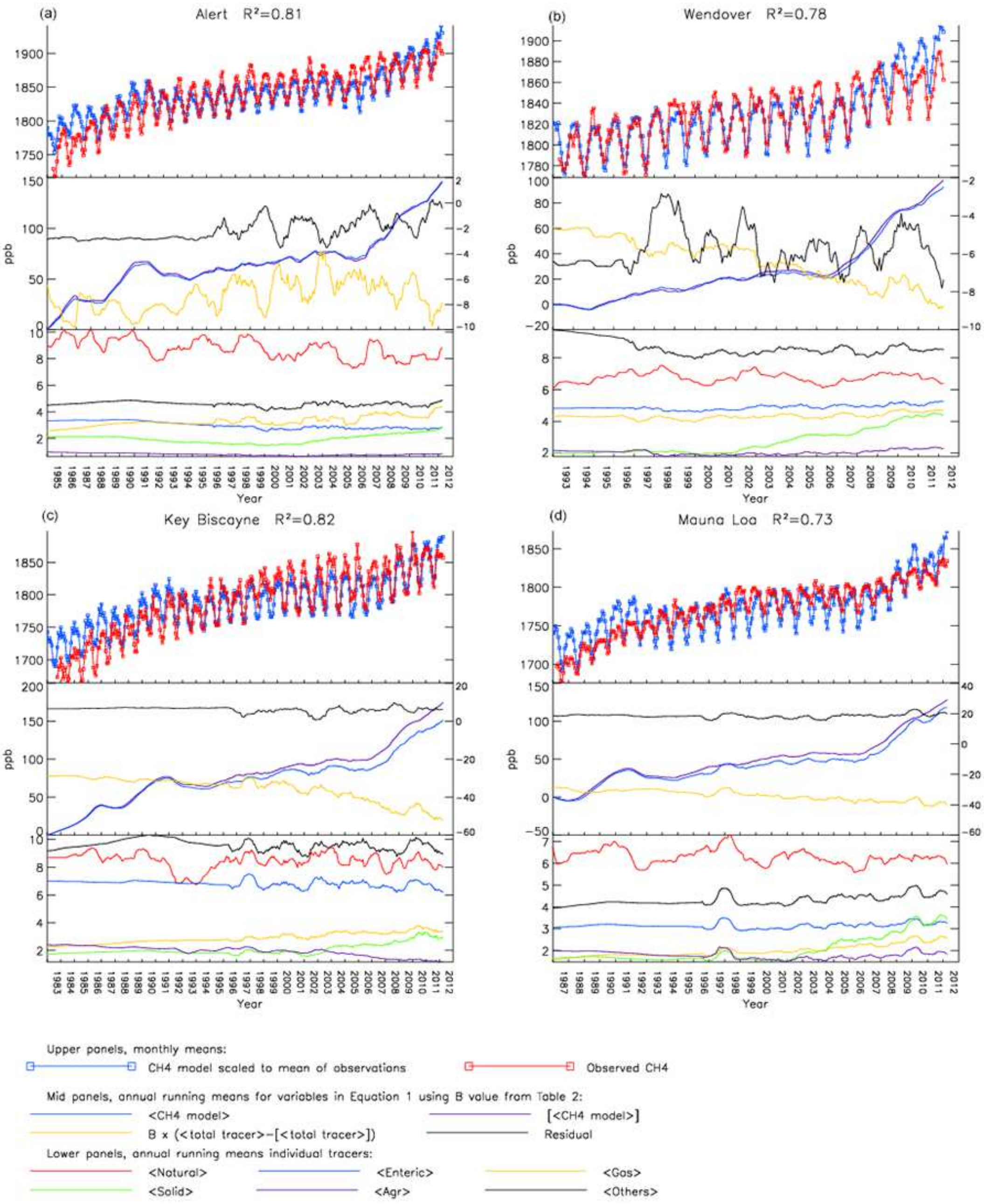

Figure 7. Evolution of CH_4 and tracers at stations (**a**: Alert, **b**: Wendover, **c**: Key Biscayne, **d**: Mauna Loa) in or near North America. See Fig. 6 caption for further description.

For the latest period, the increase in the model is larger than that observed. The seasonal and year-to-year variations are well represented by the model at all stations (coefficients of determination from 0.73 to 0.82). Key Biscayne (Fig. 7c) and Mauna Loa (Fig. 7d) have relatively large negative $<$ total tracer $> -[<$ total tracer $>]$ which shows that these are background stations and that important emission sources exist at their latitude. The tracer difference is quite small and negative at Alert (Fig. 7b) and since the residual is quite close to zero, this may indicate small sources at the station latitude. The contribution from natural emissions is decisive for year-to-year variations at all four stations in Fig. 7, and the influence of emission from the gas sector increases gradually. Key Biscayne situated in the boundary layer (Fig. 7c) is mostly influenced by emissions from the American continent, and the rest of the anthropogenic sectors have moderately declining impact after 1990. However, this decline occurs only initially for the solid fuel (mainly

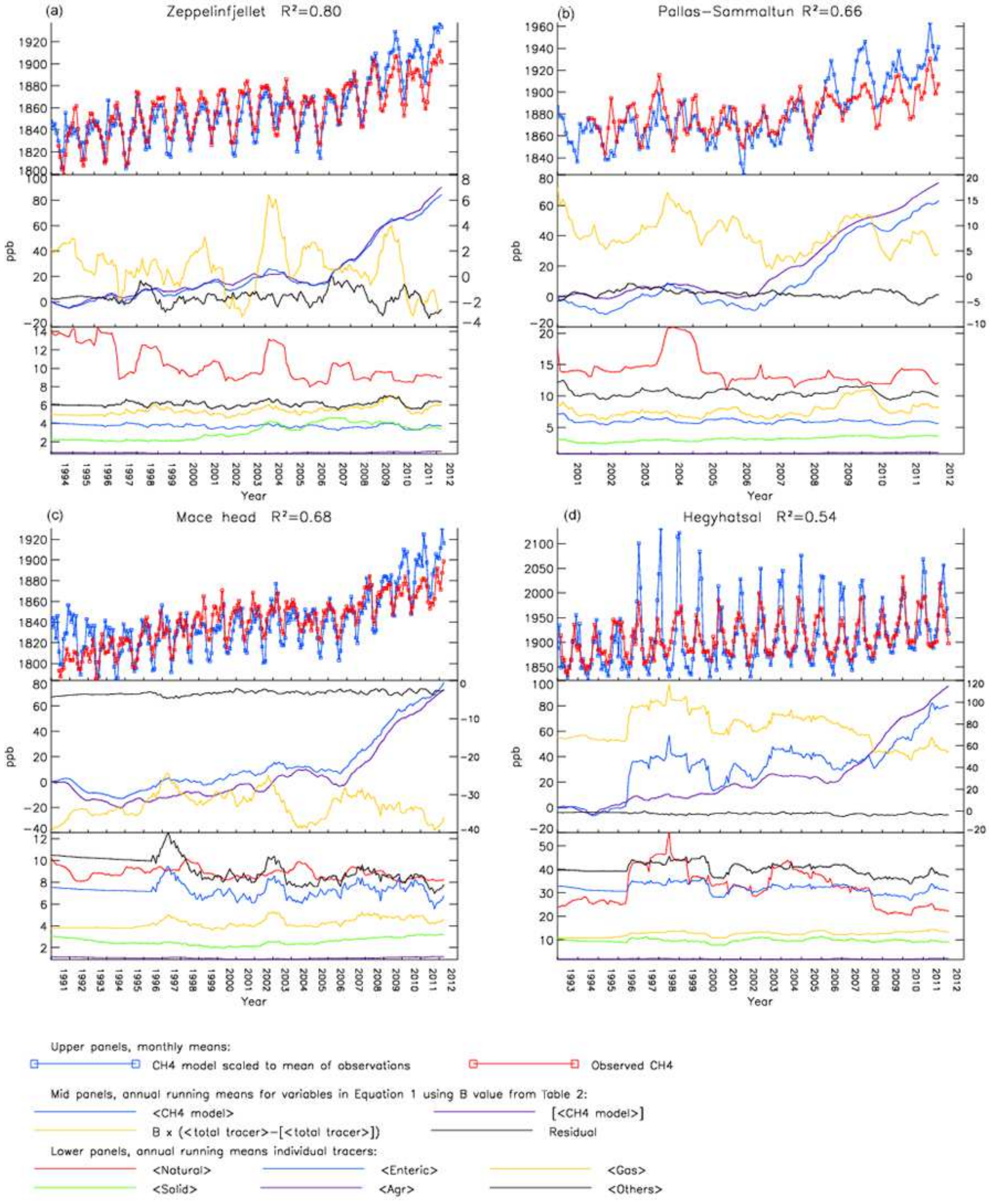

Figure 8. Evolution of CH_4 and tracers at stations (**a**: Zeppelinfjellet, **b**: Pallas–Sammaltun, **c**: Mace Head, **d**: Hegyhatsal) in or near Europe. See Fig. 6 caption for further description.

coal) sector as its contribution increases from 2003 and onwards. The same occurs for this sector at Alert (Fig. 7a). It corresponds with the start of an increase in US fugitive solid fuel emissions in the applied EDGAR v4.2 inventory. The increase in US coal emissions from 2003 to 2008 is almost 12 % in EDGAR v4.2. An increase of 28 % is found from 2005 to 2010 in the EPA inventory (EPA, 2012). At the high altitude sites Mauna Loa and Wendover (Fig. 7b and d) there are small or large increases in the contribution from all anthropogenic sectors from the year 2000 and onwards. These stations are subject to efficient transport from Asia at high altitudes. There are large emission increases after 2000 in eastern Asia in the EDGAR v4.2 inventory (Bergamaschi et al., 2013). Especially coal related emissions in China show a strong increase with a doubling from 2000 to 2008.

At Wendover, Mauna Loa and Key Biscayne $<\text{total tracer}> - [<\text{total tracer}>]$ decrease over the 3 decades studied (Fig. 7, mid panels). Several emission sectors contribute. The implication is a lower growth rate for $<CH_4\text{ model}>$ than for $[<CH_4\text{ model}>]$ (Fig. 7, mid

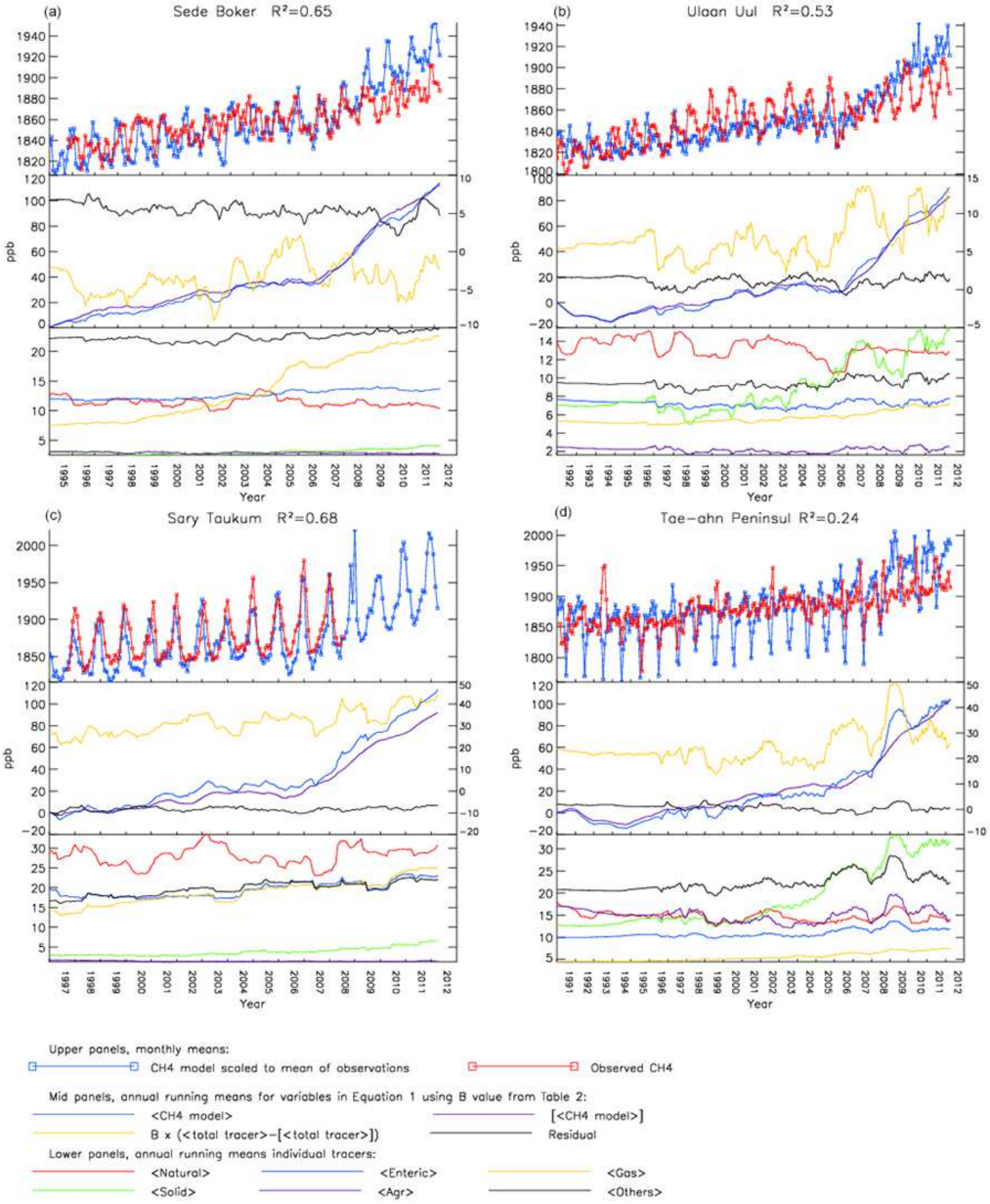

Figure 9. Evolution of CH_4 and tracers at stations (**a**: Sede Boker, **b**: Ulaan Uul, **c**: Sary Taukum, **d**: Tae-ahn Peninsula) near Asian emission sources. See Fig. 6 caption for further description.

panels); i.e. other locations (for Asian stations, see discussion below) at the same latitudes have a larger trend in CH_4. There are large fluctuations of tracer transport to Mauna Loa in 1997–1998 and 2010–2011 that strongly impacts $< CH_4$ model $>$. The observations also show changes in growth and seasonal pattern during these years.

At the Arctic site Zeppelin (Fig. 8a), located on the coast of western Svalbard, there is a small CH_4 increase both in model and observations up to 2004. A large part of the CH_4 variability in the period 1997–1999 (Morimoto et al., 2006) was due to fluctuations in wetland and biomass-burning emissions. Our modelled variation in the natural source tracer conforms to the fluctuations deduced from the isotopic measurements of Morimoto et al. (2006). Seasonal tracer analysis (not shown) is in agreement with the conclusion of Fisher et al. (2011), who found that wetlands and gas are the main contributors in summer and winter, respectively. A CH_4 concentration drop from 2004 to 2006 seems to mainly be explained

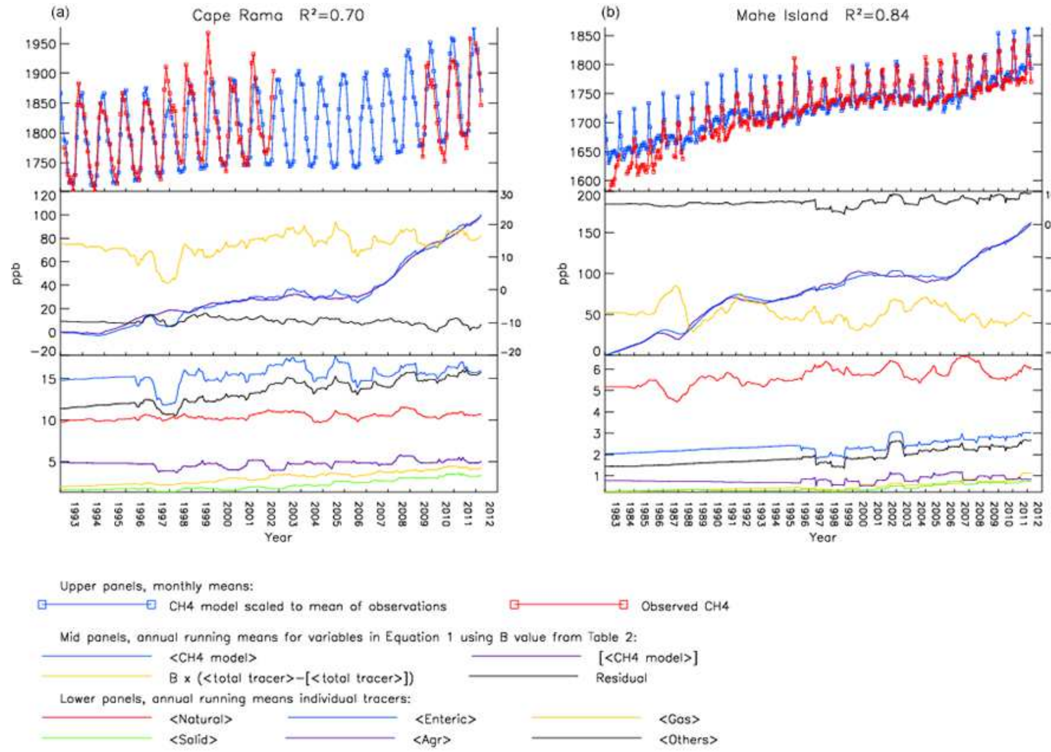

Figure 10. Evolution of CH_4 and tracers at stations (**a**: Cape Rama, **b**: Mahe Island) in background/outflowing air in or near Asia. See Fig. 6 caption for further description.

by natural source contribution in the model falling from a period maximum in 2004 to low values in 2005–2006. This is also the case for the sub-Arctic site Pallas (Fig. 8b) located in a region characterized by forest and wetlands. Gas, enteric fermentation and various other small regional anthropogenic sources seems to contribute to the CH_4 increase at Zeppelin after 2006. The contribution from natural emissions and recent regional coal mining peaked in 2007. A quite strong CH_4 enhancement occurs for 2009–2010 in both the model and observations. The longitudinal mean tracers for individual sectors are almost stable to declining (not shown) while contribution from the $<$ gas $>$ and some other tracers show a small maximum (lower panel Fig. 8a and b). Pallas has a similar pattern. The runs with fixed meteorology suggest enhanced transport from Russia passing major gas fields and Pallas.

Mace Head (Fig. 8c) is a rural background coastal site in Europe. The result of $<$ total tracer $> -[<$ total tracer $>]$ is quite large and negative, suggesting important emission sources along the station's latitude. In the beginning of the 1990s, there is a mismatch between declining model concentrations and the increase found from the observations. Some of the decrease in the model is due to decreasing contributions from solid fuel (mainly coal), enteric fermentation and other regional anthropogenic sources. The station experiences unusual meteorological conditions in the ENSO year 1997, as there are abrupt shifts in concentrations of CH_4 and several of the anthropogenic tracers having small year-to-year variations in emissions. Similarly, there seems to be transport of less polluted air masses to the station in 2004 compared to earlier years resulting in lower CH_4 concentration in measurements and model in 2004 and 2005. Several regional sources seem to have small contributions to the modelled and observed CH_4 increases from 2006 to 2009. After 2009 we extrapolate emission trends due to lack of emission inventories and this may be the reason why the model doesn't reproduce the observed levelling off in growth in 2010 and 2011.

The model has larger discrepancies at Hegyhatsal, a semi-polluted site in central Europe (Fig. 8d). Despite seasonal issues the model performance is reasonable for the long-term CH_4 changes. In years with high contributions from natural sources, the seasonal maxima tend to be too high in the model. It could be that the coarse model resolution results in too much transport from nearby wetlands or that the emission inventory has overly large natural emissions in surrounding regions. $<$ total tracer $> -[<$ total tracer $>]$ is very large and positive meaning that the station is very sensitive to emissions close upwind. The evolution of $<$ CH_4 model $>$ therefore deviates strongly from the longitudinal mean $[<$ CH_4 model $>]$. The deviation starts in 1996 when a sharp increase in natural emission occurs. From 2003 to 2008 there is a period with stable to declining modelled CH_4 concentrations. This is caused by decreasing central European emissions particularly from enteric fermentation and the category “other anthropogenic sectors” together with decreasing or fluctuating natural sources.

In general, the model reproduces the features in the observations over and near Asia quite well (Figs. 9 and 10) with coefficient of determination in the range of 0.24–0.84. For the trends, the overestimation after 2006 is higher here than modelled in other world regions (Figs. 6–8). Gas is the major cause of increases in CH_4 in Israel (Sede Boker, Fig. 9a). The increase of the $<$ gas $>$ tracer is much larger than for the longitudinal mean [$<$ gas $>$], suggesting important emission increases from nearby gas fields. Small changes in regional natural emissions and in the category “other anthropogenic sources” (lower panel) are correlated with the modelled year-to-year variations (upper panel). The station in Kazakhstan (Fig. 9c) is downwind of large sources ($<$ total tracer $>$ $-$[$<$ total tracer $>$] large and positive), and the modelled CH_4 increase after 2005 is much larger than for the longitudinal mean. Also at this station, the CH_4 trend is heavily influenced by gas, although not to the same extent as in Israel. Other regional anthropogenic emission changes also contribute somewhat to the modelled CH_4 increase over recent years. High natural emissions in 2008–2009 also had an impact. Since we use repetitive year-2009 natural emissions for the latter years, it could be that the contribution from this source is too large after 2009. Unfortunately, the modelled CH_4 increase cannot be confirmed by measurements since data at the station is missing after 2008.

Regional solid fuel emissions (mainly coal) is the main cause of last-decade-modelled CH_4 increase in eastern continental Asia (Ulaan Uul and Tae-ahn Peninsula, Fig. 9b and d), but gas and other reginal anthropogenic sectors also contribute. There is large growth in $<$ CH_4 model $>$ for Ulaan Uul in 2006–2007 and 2010 mainly due to peaks in the contribution from solid fuel sources, but also other anthropogenic sectors have a role in this. Similar pattern appears for Tae-ahn Peninsula in 2009. The first peak at Ulaan Uul is also partly seen in the observations, but the existence of the latest episode and the event at Tae-ahn Peninsula is less clear from the measurements. Our tracer analysis for Minamitorishima (not shown), a background station affected by outflow from the Asian continent indicates less continental outflow in 2007. For these polluted continental sites the correlation coefficients are lower than for the other stations. The coarse resolution of the model has problems resolving large gradients in concentrations and non-linearity of oxidant chemistry. At Tae-ahn Peninsula $<$ CH_4 model $>$ starts increasing in 2005, while the increase at Ulaan Uul first starts in 2006. At Ulaan Uul decreasing regional natural emissions over the period 2000–2005 seems to compensate for the large increase of solid fuel emissions from around 2000.

For Cape Rama in India (Fig. 10a, the observations show signatures of both Northern Hemispheric and Southern Hemispheric (NH and SH) air masses (Bhattacharya et al., 2009). Mixed with regional fluxes and varying chemical loss, this results in large seasonal variation. During the summer monsoon, the station is located south of the inter-tropical convergence zone. Air arriving during this period (June to September) represent tropical or SH oceanic air masses and the station is upwind of Mahe Island (Fig. 10b). During the winter monsoon the situation is opposite. There is outflow from the continent affecting both Cape Rama and Mahe Island. The ENSO event in 1997 seems to have opposite effects on modelled and observed CH_4 variability at Cape Rama. Despite that, the model does a reasonable job in reproducing the measurements. Most regional tracers show stable to upward levels over the period of comparison and likely contribute to a small fraction of the modelled CH_4 trend. At Mahe Island in the SH (Fig. 10b), the CH_4 concentration peaks sharply during NH winter when the station is influenced by outflow from continental Asia. The station is therefore an indicator of inflow to the SH. This feature is well captured by the model. Over the last decade, there is a small and continuous rise in the levels of all anthropogenic tracers at the station. This coincides with large emission increases in Asia, suggesting that the recent development in Asia has some influence on the SH.

3.4 Methane evolution and emission drivers over distinct time periods

Figure 11 compares the latitudinal distribution of surface CH_4 in the model and observations. Generally, the model and the observational approach reveal the same pattern and characteristics both in time and space, although some clear differences are evident. From 1985 to the early 1990s, there is a homogeneous growth in the observations (Fig. 11b). The model (Fig. 11a) also has growth over the same period but a distinct period (1987–1988) with no growth, corresponding to smaller emissions from wetlands and biomass burning (Fig. 1). 1987–1988 were El Niño years, and there is a tendency of low wetland emissions for those years, e.g. an anti-correlation between wetland emissions and ENSO index (Hodson et al., 2011). One possibility is that our applied emission inventory for natural CH_4 sources (Bousquet et al., 2011) has overly large variability in wetland emissions in the 1980s and overly strong reductions in wetland emissions in 1987–1988. Bousquet et al. (2006) state that bias in OH inferred from methyl chloroform (CH_3CCl_3) observations (Bousquet et al., 2005) could account for some of the variability that they attributed to wetland emissions. Later findings (Montzka et al., 2011) support this. If OH changes are set to zero instead of the large variability in the 1980s, suggested by early CH_3CCl_3 studies (Bousquet et al., 2005), the fluctuations in wetland emissions are dampened by 50 %. On the other hand, the model simulation has no year-to-year variation in meteorology before 1997, and the meteorology used corresponds to the year 2001, which has a weak ENSO

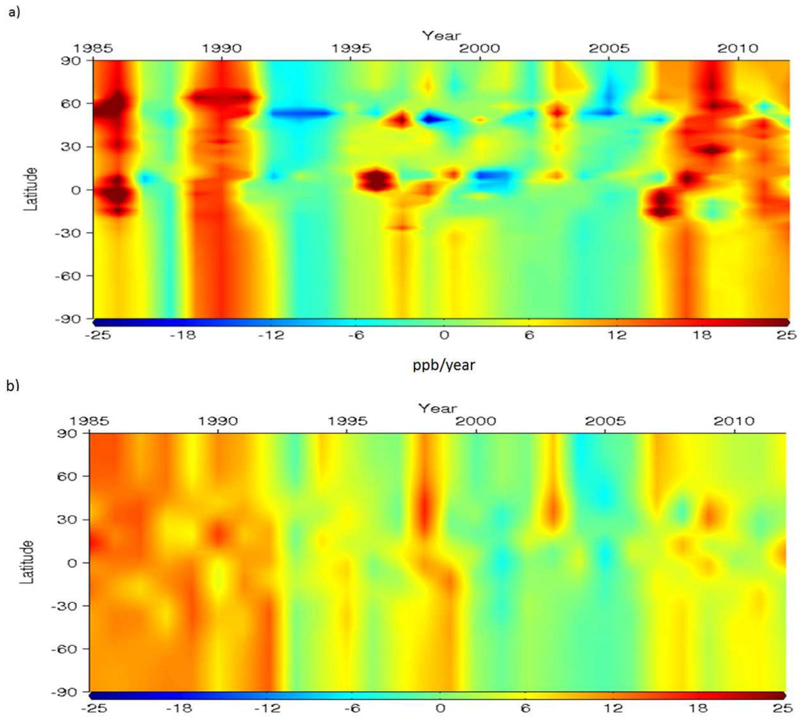

Figure 11. CH_4 year-to-year variation (ppb) in surface CH_4 in model **(a)** compared to the levels of surface CH_4 estimated from observations **(b)** in various latitudinal bands based on the NOAA ESRL network of surface stations (Ciais et al., 2013, and data set provided by Edward J. Dlugokencky, personal communication, 2015).

index. Therefore, during the 1987–1988 El Niño, the meteorology used is less representative than for other years with weaker ENSO. In the two periods of CH_4 growth before and after 1987–1988, the CH_4 increase is strong in the model (Fig. 11a) in the Northern Hemisphere and might be overestimated. However, it might be that the model is able to better capture latitudinal gradients, as only a few measurement sites are available to make latitudinal averages for the 1980s. In 1992 and 1993 there is a pause in the CH_4 growth in the measurements (Fig. 11b) at all latitudes. This pause has been explained as a consequence of the Mount Pinatubo volcanic eruption in 1991 (Dlugokencky et al., 1996; Bekki and Law, 1997; Bânda et al., 2013). The eruption results in an initial increase in the CH_4 growth rate (less OH) lasting for half a year. This is due to backscattering by volcanic stratospheric aerosols, which reduces the UV radiation to the troposphere. After that, the growth rate due to Pinatubo becomes negative (more OH plus less natural methane emissions are the dominating effects) reaching a minimum after 2 years (1993), before levelling off towards zero after 5 years. The main cause of the OH increase is reduction in stratospheric ozone allowing more UV radiation to the troposphere. In contrast to the measurements the model shows a stronger decrease in CH_4 after the eruption, and the pause in CH_4 growth is longer. This might be due the fact that the model does not fully include all factors affecting CH_4 related to the Mount Pinatubo eruption. Reduced emissions are implicitly included in the natural CH_4 emission inventories, but changes in meteorology (temperature, water vapour, etc.) and volcanic SO_2 and sulphate aerosols in the stratosphere, are not accounted for in the simulations. In the period 1994–1997 the model struggles to reproduce the latitudinal distribution of growth (Fig. 11). The model seems to have overly large growth in the Tropics probably due to a small but significant growth in wetland and biomass-burning emissions in the period (Fig. 1).

In the next paragraphs, we study whether the model is able to reproduce CH_4 measurements when we split the time frame into shorter epochs that measured distinct different growth rates. The splits are made within the period 1998–2009 when our simulations have both inter-annual variation in meteorology and complete emission data (no extrapolations made). We have only included observation sites that have measurements available for all months within the given time period, see Sect. 2.3 for details about data selection.

Figure 12 shows the modelled CH_4 growth in the CTM in the period 1998–2000, compared to the observed changes at various sites. The model seems to slightly underestimate increases at several stations. The largest underestimation occur in eastern Asia. In parts of eastern Asia and some other regions in the Northern Hemisphere there are declines in modelled CH_4 concentrations caused by decreased contribution from several anthropogenic sectors. Increased emissions

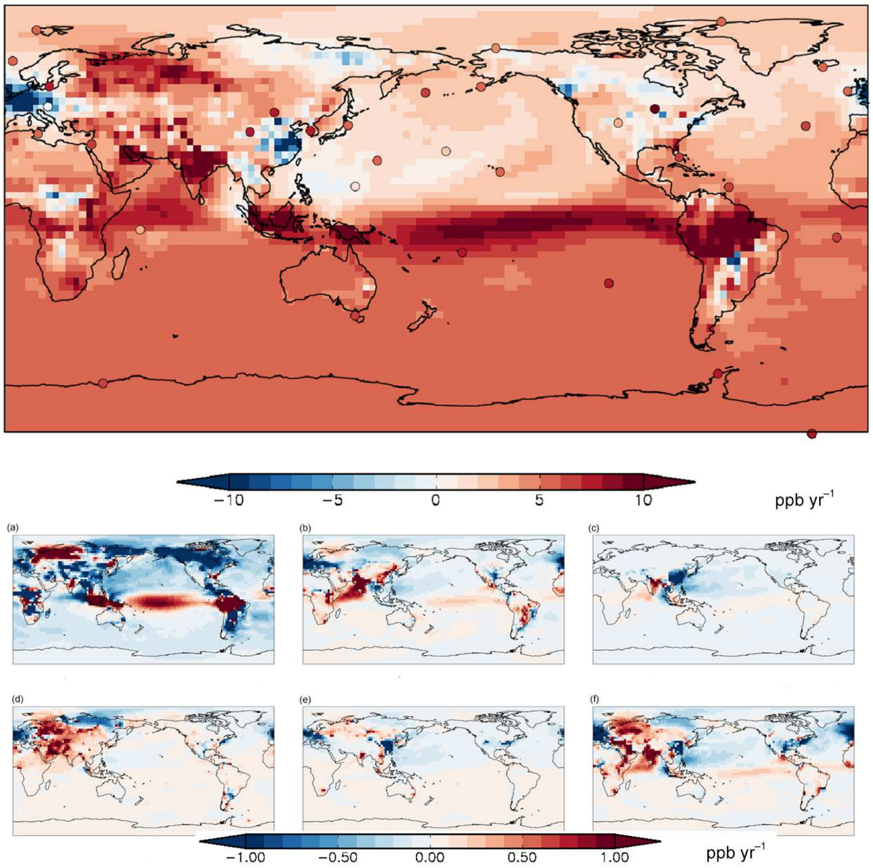

Figure 12. (Upper panel) Mean year-to-year growth (ppb yr^{-1}) in surface CH_4 in Oslo CTM3 over the period 1998–2000. The 32 circles show the observed growth rates over the same period. The stations picked for comparison are based on the criteria described in Sect. 2.3, and only observation sites that have measurements available for all months within the given time is included. **(a–f)** Mean year-to-year growth ppb yr^{-1}) of emission tracers in the same period. **(a)** Natural (wetlands + other natural + biomass burning), **(b)** enteric, **(c)** agricultural soils, **(d)** gas, **(e)** solid fuel, **(f)** the sum of all other anthropogenic tracers.

from gas fields in Russia, the Middle East, and in several anthropogenic tracers over India explain why these are the regions in the Northern Hemisphere with largest modelled CH_4 increase.

Earlier studies find that a low CH_4 growth rate in the 1990s is mostly caused by lower fugitive fossil fuel emissions from oil and gas industries, mainly due to the collapse of the Soviet Union (Bousquet et al., 2006; Simpson et al., 2012; Dlugokencky et al., 2003; Aydin et al., 2011). Another important factor is decreased emissions from rice paddies. Lower emissions from agricultural soils last until around the year 2000 in the EDGAR v4.2 inventory (Fig. 1) and are also evident in Fig. 12c. Kai et al. (2011) exclude fossil fuel emissions as the primary cause of the slowdown of CH_4 growth. According to their isotopic studies, it is more likely long-term reductions in agricultural emissions from rice crops in Asia, or alternatively another microbial source in the Northern Hemisphere that is the major factor. Another isotope study (Levin et al., 2012) disagrees and finds that both fossil and microbial emissions were quite stable.

Wetland and biomass burning sources seem to play the key role for the variations in the model from 1997 to 2000 (Fig. 12a). They were particularly large in 1998 due to the 1997–1998 El Niño (Chen and Prinn, 2006; Simpson et al., 2002; Dlugokencky et al., 2001; Bousquet et al., 2006; Pison et al., 2013; Spahni et al., 2011; Hodson et al., 2011). Simpson et al. (2002) also conclude that the increase in observed surface CH_4 between 1996 and 2000 was driven primarily by a large growth in 1998. Both model and measurements have the strongest growth (Fig. 12) in the Southern Hemisphere, which had large wetland emissions in 1998 (Bousquet et al., 2006; Dlugokencky et al., 2001). In the model, slowly rising anthropogenic emissions in the Southern Hemisphere also seems to contribute (Fig. 12b–f). Natural emissions (Fig. 12a) are also important for the irregular pattern seen at mid-to-high northern latitudes. This is expected due to the 1997–1998 ENSO-event, showing a dip in high northern wetland emissions in 1997 followed by unusual large emissions in 1998 (Bousquet et al., 2006; Dlugokencky et al., 2001). During the ENSO event, the zonal pattern in the

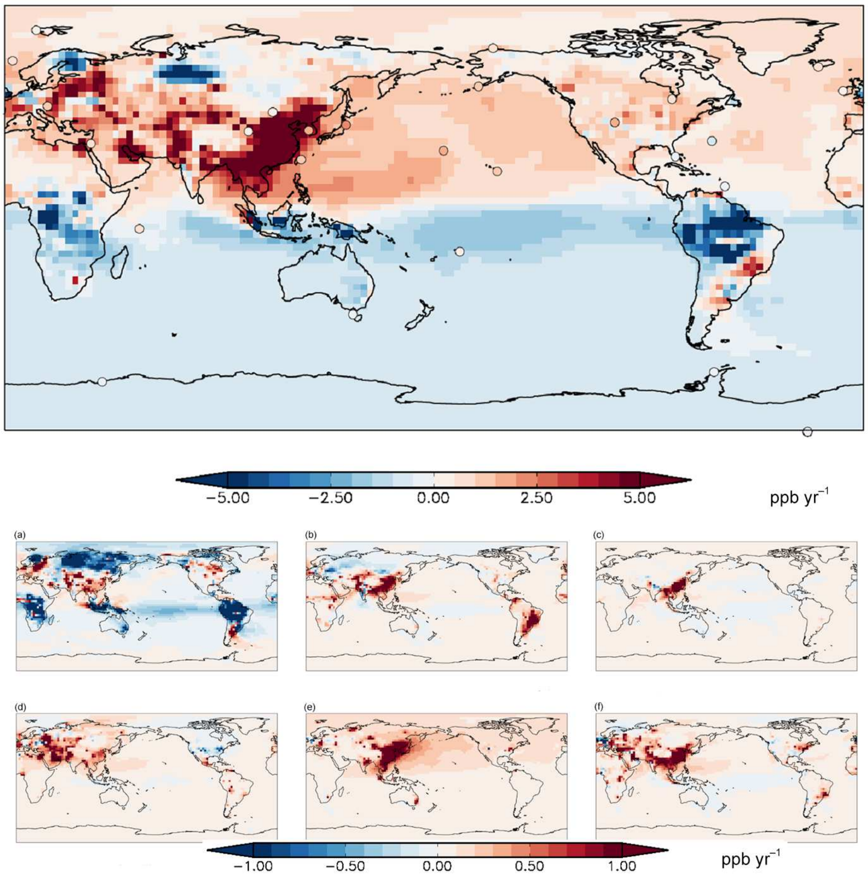

Figure 13. (Upper panel) Mean year-to-year growth (ppb yr^{-1}) in surface CH_4 in Oslo CTM3 over the period 2001–2006. The 25 circles show the observed growth rates over the same period. The stations picked for comparison is based on the criteria described in Sect. 2.3, and only observation sites that have measurements available for all months within the given time is included. **(a–f)** Mean year-to-year growth (ppb yr^{-1}) of emission tracers in the same period. **(a)** Natural (wetlands + other natural + biomass burning), **(b)** enteric, **(c)** agricultural soils, **(d)** gas, **(e)** solid fuel, **(f)** the sum of all other anthropogenic tracers.

model and measurements (Fig. 11) is very similar for the Southern Hemisphere but there are larger differences for the Northern Hemisphere.

During 2000–2006 the CH_4 growth levelled off and there was a period with stagnation in global mean growth rate (Fig. 13). The agreement between the zonal averages from the model and the measurement approach is excellent, both with regards to timing and strength of the growth (Figs. 11 and 13). The 2002–2003 anomaly in the Northern Hemisphere is captured by the model (Fig. 11) and explained by enhanced emissions from biomass burning in Indonesia and boreal Asia (Bergamaschi et al., 2013; Simpson et al., 2006; van der Werf et al., 2010).

The EDGAR v4.2 inventory applied here and in other studies (e.g. Bergamaschi et al., 2013) show that global anthropogenic emissions rise substantially, especially in Asia after the year 2000. This increase in the anthropogenic emissions is compensated by a drop in northern tropical wetland emissions associated with years of dry conditions (Bousquet et al., 2006, 2011). Monteil et al. (2011) find that moderate increases in anthropogenic emissions and decreased wetland emissions together with moderate increasing OH can explain the stagnation in CH_4 growth from 2000. Bergamaschi et al. (2013), assuming constant OH, also finds a decrease in wetland emissions but that a large increase in anthropogenic emissions first occurs from 2006 and beyond. Uncertainty in wetland emissions in the period is well illustrated by Pison et al. (2013). Using different methods to estimate global wetland emissions from 2000 to 2006, Pison et al. (2013) finds either a decrease or an increase. On the other hand, increase in both wetland and anthropogenic emission would not conform to the observed stable global mean CH_4 levels in this period. Spahni et al. (2011) found a small decrease in wetland emissions from 1999–2004 followed by an increase from 2004 to 2008. Our model results from simulations with declining natural emissions and increasing anthropogenic emissions (Fig. 1) reproduce the measurements in most regions (Fig. 13). Eastern Asian stations are exceptions. Gas and solid fuels (coal) (Fig. 13d, e) are causing much of the modelled increases over southern and eastern Asia.

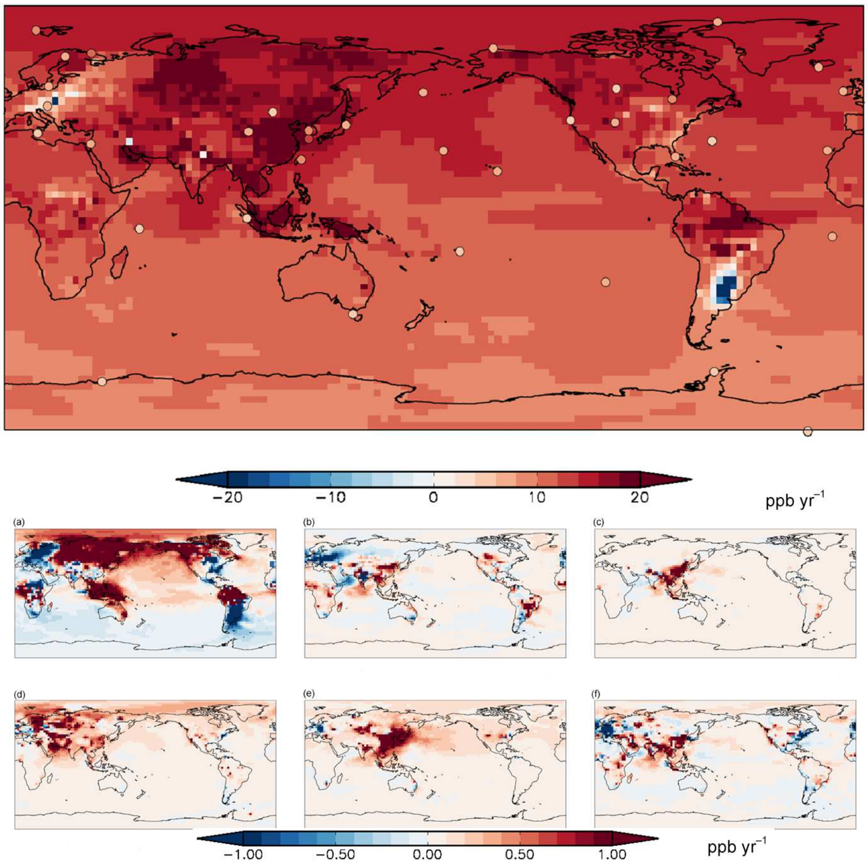

Figure 14. (Upper panel) Mean year-to-year growth (ppb yr^{-1}) in surface CH_4 in Oslo CTM3 over the period 2007–2009. The 36 circles show the observed growth rates over the same period. The stations picked for comparison are based on the criteria described in Sect. 2.3, and only observation sites that have measurements available for all months within the given time is included. **(a–f)** Mean year-to-year growth (ppb yr^{-1}) in mole fraction of emission tracers in the same period. **(a)** Natural (wetlands + other natural + biomass burning), **(b)** enteric, **(c)** agricultural soils, **(d)** gas, **(e)** solid fuel, **(f)** the sum of all other anthropogenic tracers.

Since the observation at the eastern Asian stations close to large anthropogenic sources show smaller changes it is plausible that the emission growth is overly strong in the applied EDGAR v4.2 inventory, for this region. However, it is difficult to be conclusive since the few observation sites available are situated in zones with sharp gradients in modelled concentration changes. The EDGAR v4.2 emissions from the region increase gradually between 2000 and 2008, with a larger growth rate after 2002. Findings from Bergamaschi et al. (2013) question this as they suggest a large increase mostly since 2006.

The period 2007 to 2009 is characterized by strong growth in observed global mean growth rate and even stronger growth in the model (Figs. 11 and 14). The model overestimation seems to occur almost everywhere. Due to the long lifetime of CH_4, strong increase in regional emissions has a global impact. Increases in anthropogenic sources in Asia (e.g. Figs. 9, 14b–f), in particular, natural gas in the Middle East and solid fuel (coal) in eastern Asia have large contributions. The influence from emission increases in these regions can be seen at downwind stations over and near northern America and in the Southern Hemisphere (Seychelles) (see Figs. 6 and 7). For the Southern Hemisphere a small steady increase in several regional anthropogenic emissions also contributes. For the Arctic stations the responsible sectors for the recent increase and their geographical origin varies but high wetland emissions in 2007–2008, gas in Russia, and coal and other anthropogenic emissions in Asia seem to play a central roles (Figs. 7, 8 and 14). For North America anthropogenic emissions increase in the central and eastern US and decrease in the eastern parts (Fig. 14). A similar west–east gradient is seen over the continent for natural sources but this is likely temporary due to special conditions in 2007–2008. These factors, together with the distant contributions from rising emissions in eastern Asia explain the modelled CH_4 trends. In central Europe there is a decline in modelled CH_4 due to a combination of declining emissions from enteric fermentation, solid fuels (coal), and several other anthropogenic sectors (Fig. 14b, d, f), and fluctuations in natural emissions (Fig. 14a). A decrease over a small region of

South America is mainly explained by variations in natural emissions (Fig. 14a).

Other studies (Kirschke et al., 2013; Rigby et al., 2008; Bergamaschi et al., 2013; Bousquet et al., 2011; Dlugokencky et al., 2009; Crevoisier et al., 2013; Bruhwiler et al., 2014) attribute the resumed strong growth of observed (Dlugokencky et al., 2009; Rigby et al., 2008; Frankenberg et al., 2011; Sussmann et al., 2012; Crevoisier et al., 2013) global CH_4 levels after 2006 to increases in both natural and anthropogenic emissions. However, the share of natural vs. anthropogenic contribution varies in the different studies. The studies agree that abnormally high temperatures at high northern latitudes in 2007 and increased tropical rainfall in 2007 and 2008 resulted in large wetland emissions these years. There is also a likely contribution from forest fires in the autumn of 2006 due to drought in Indonesia (Bergamaschi et al., 2013; Worden et al., 2013). Top-down (Bergamaschi et al., 2013; Bousquet et al., 2006, 2011; Kirschke et al., 2013; Bruhwiler et al., 2014) and bottom-up studies (EC-JRC/PBL, 2011; Schwietzke et al., 2014; Höglund-Isaksson, 2012; EPA, 2012) suggest steady moderate to substantial increases in anthropogenic emissions in the period 2007–2009. Much of this is due to intensification of oil and shale gas extraction in the United States and coal exploitation in China.

Using the EDGAR v4.0 inventory as input to a CTM and observations of CH_4 and its isotopic composition Monteil et al. (2011) led to the conclusion that a reduction of biomass burning and/or of the growth rate of fossil fuel emissions is needed to explain the observed growth after 2005. The differences between the EDGAR v4.0 and EDGAR v4.2 used in this study are moderate. Other bottom-up inventories (EPA, 2012; Höglund-Isaksson, 2012; Schwietzke et al., 2014) report lower increases in anthropogenic emissions, see also comparison with ECLIPSE emission in the Supplement. Using the mean of the EPA and EDGAR v4.2 inventory for anthropogenic emissions, Kirschke et al. (2013) find that either is the increase in fossil fuel emissions overestimated by inventories, or the sensitivity of wetland emissions to temperature and precipitation is too large in wetland emission models. Schwietzke et al. (2014) and the top-down studies by Bergamaschi et al. (2013) and Bruhwiler et al. (2014) conclude that the EDGAR v4.2 emission inventory overestimates the recent emission growth in Asia. This is especially the case for coal mining in China. From our results above, it is plausible that overly high growth of fossil fuel emissions, in particular in Asia, is the reason why the recent CH_4 growth is higher in our model than for the observations. However, in 2007 and 2008 much of the increase in the model in the Northern Hemisphere is driven by high natural wetland emissions. Our natural emissions are from Bousquet et al. (2011) who attributes much of the 2007–2008 increase in total emissions to wetlands. According to Bergamaschi et al. (2013) a substantial fraction of the total increase is attributed to anthropogenic emissions. There is therefore a possibility that we could combine two emission inventories (anthropogenic from EDGAR v4.2 and natural from Bousquet et al., 2011) that both have overly large growth in the period 2006–2008.

Extrapolating anthropogenic emissions that likely have overly strong growth probably explain why the model also overestimates the CH_4 growth from 2009 to 2012. Mismatch between the spatial distributions of the model and measurements (Fig. 11) on regional scales from 2009 to 2012 are expected due to the extrapolation of anthropogenic emissions and use of constant 2009 natural and biomass-burning emissions. Of these, especially wetland emissions have large spatial and temporal variation from year to year.

3.5 Changes in methane lifetime

The modelled evolution of CH_4 is not only decided by changes in sources but also changes in the atmospheric CH_4 loss and soil uptake. The CH_4 lifetime is an indicator of the CH_4 loss. The lifetime is dependent on the efficiency of soil uptake (Curry, 2009) as well as on concentrations of atmospheric chemical components reacting with CH_4, including the kinetic rates of the corresponding reactions. It also depends on how efficiently the emitted CH_4 is transported between regions with differences in loss rate. Our prescribed fields for soil uptake (Bousquet et al., 2011) are responsible for about 5 % of the loss and the difference between the year with smallest and largest soil uptake is only 2 %. The main reactant removing CH_4 chemically in the atmosphere is OH, but there is also a small loss due to reactions with excited atomic oxygen (O^1D) and chlorine (Lelieveld et al., 1998; Crutzen, 1991). Due to the limited influence of soil uptake, chlorine, and O^1D we will hereafter focus on the role of changes in OH and the kinetic loss rate for this reaction. A number of components (CO, NO_x, NMVOCs, CH_4, SO_2, aerosols, meteorological factors, solar radiation) control the atmospheric OH level and the kinetic loss rate (Dalsøren and Isaksen, 2006; Lelieveld et al., 2004; Holmes et al., 2013; Levy, 1971). Due to the extremely high reactivity of OH, measurements on large scale are impossible (Heard and Pilling, 2003). Forward models have been employed to calculate the OH evolution over time on global scale. Another alternative is inverse models in combination with observations of ^{14}CO , CH_3CCl_3 or other long-lived species reacting with OH. This section discusses the modelled evolution of CH_4 lifetime in this study and compares it to findings from other relevant studies on CH_4 lifetime and OH change. In the section thereafter we try to identify the key drivers behind the modelled changes in CH_4 lifetime.

The overall picture from the main simulation (blue lines Fig. 15) is that there is a clear decrease in the CH_4 lifetime over the last 4 decades, more than 8 % from 1970 to 2012 and a similar increase in OH concentration. Of particular importance are large increases in OH over Southeast Asia, mainly due to strong growth in NO_x emissions. From 2000–2010 the modelled tropospheric OH column increase by 10–20 % over China and India (not shown). In Fig. 15, the reaction rate

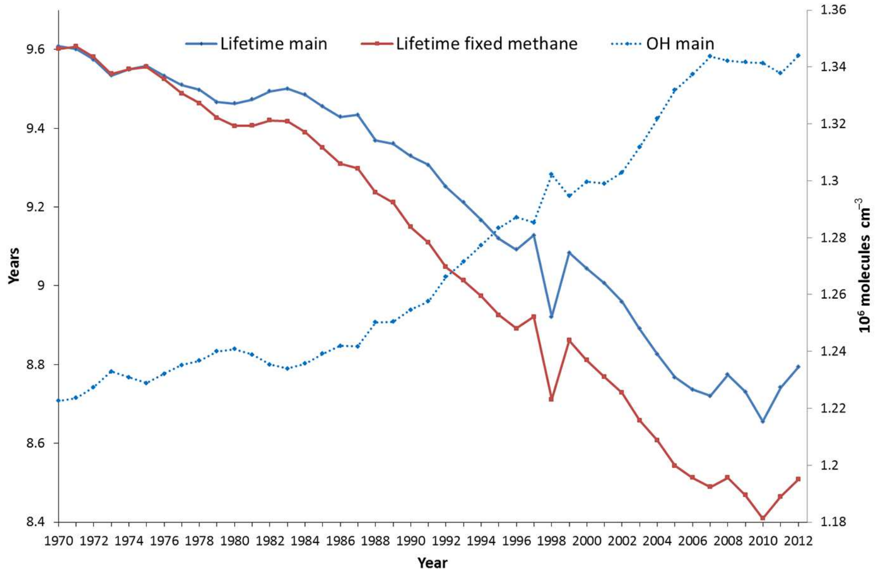

Figure 15. Evolution of yearly global average atmospheric instantaneous CH_4 lifetime in the main and fixed methane simulations (left y axis). Evolution of yearly global average atmospheric OH concentration in the main simulation (right y axis) using the reaction rate with CH_4 as averaging kernel.

with methane is used as an averaging kernel to examine the OH change relevant for changes in methane lifetime. There is a very strong anti-correlation between the evolution of OH and methane lifetime suggesting causality. This is especially the case for the period 1970–1997 run without inter-annual variation in meteorology resulting in a static $CH_4 + OH$ reaction rate (k) for these years. The lifetimes in the fixed CH_4 run (red line) and the main CH_4 run (blue line) are highly correlated. This is another way of illustrating that OH ($k \times OH$), and not the CH_4 burden itself, is driving the long-term evolution and year-to-year variations of CH_4 lifetime. However, some influence from CH_4 fluctuations is evident in a few of the years studied (mainly in the 1980s), with large variations in CH_4 emissions (Fig. 1). CH_4 itself is important for its own lifetime length (blue line well above red line), due to the decrease in the OH concentration produced by the reaction with the CH_4.

Other forward models also suggest a similar decrease in CH_4 lifetime due to an increase in global OH concentrations the recent decades (Karlsdóttir and Isaksen, 2000; Dentener et al., 2003; Wang et al., 2004; Dalsøren and Isaksen, 2006; Fiore et al., 2006; John et al., 2012; Holmes et al., 2013; Naik et al., 2013). However, some of these studies focus on the effect of certain factors (emissions or meteorology) and do not cover changes in all central physical and chemical parameters affecting CH_4 lifetime. Using observations of CH_4 and its isotopic composition, Monteil et al. (2011) find that moderate ($< 5\,\%$ per decade) increases in global OH over the period 1980–2006 are needed to explain the observed slowdown in the growth rate of atmospheric CH_4 at the end of that period. In contrast, large increases in OH in the 1980s and a large negative trend for the 1990s were inferred from CH_3CCl_3 observations (Prinn et al., 2005, 2001; Krol and Lelieveld, 2003; Bousquet et al., 2005; Montzka et al., 2000). These studies also found large inter-annual variability of OH. However, the studies were debated (Krol and Lelieveld, 2003; Lelieveld et al., 2006; Bousquet et al., 2005; Wang et al., 2008) and it was shown that largely reduced variations and trends are possible within the uncertainties bonds of the CH_3CCl_3 emission inventory. In a more recent analysis of CH_3CCl_3, measurements for the period 1998–2007 Montzka et al. (2011) find small inter-annual OH variability and trends and attribute previously estimated large year-to-year OH variations before 1998 to uncertainties in CH_3CCl_3 emissions and representation issues due to the sparse observation network. Kai et al. (2011) find that relatively stable dD-CH_4 suggested small changes in the OH sink between 1998 and 2005. Rigby et al. (2008) finds declining OH from 2004 to 2007. Bousquet et al. (2011) also finds a decline in 2007 and 2008, compared to 2006. However the decline is much less than that found by Rigby et al. (2008). Holmes et al. (2013) concludes that better understanding of systematic differences between different CH_3CCl_3 observation networks is required before using them as constraints on inter-annual variability of CH_4 lifetime and OH. Using ^{14}CO Manning et al. (2005) finds no significant long-term trend in OH in the Southern Hemisphere but short-term large variations persisting for a few months. Like CH_3CCl_3 there are uncertainties related to inferring OH from ^{14}CO (Krol et al., 2008). Ghosh et al. (2015) does not consider trends in OH but anyway they find a decrease in CH_4 lifetime over the last century and attribute it to temperature increase (larger reaction rate)

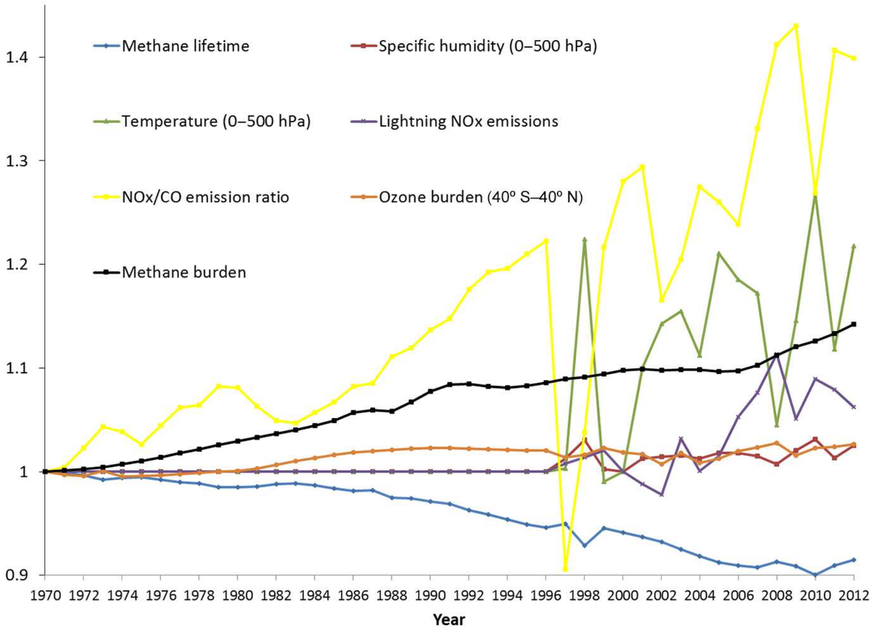

Figure 16. Development in atmospheric CH_4 lifetime and key parameters known to influence CH_4 lifetime. All variables values are relative to 1970. (To make it apparent in the figure, temperature variations are relative to the Celsius scale).

and the increase of stratospheric chlorine (larger loss through reaction with Cl).

It is evident from the above discussion that there are uncertainties related to all methods (models, CH_3CCl_3, and ^{14}CO) and missing consensus on OH trends. To increase understanding and facilitate discussion, it is important not to stop by a derived number for change in OH or methane lifetime, but investigate the major drivers for the changes. The next section address drivers in this model study.

3.6 Major drivers for changes in the methane lifetime

Figure 16 shows the evolution of main factors known to determine atmospheric CH_4 lifetime. The factors chosen are based on the study by Dalsøren and Isaksen (2006) and Holmes et al. (2013).

Using the NO_x / CO emission ratio and linear regression analysis (Dalsøren and Isaksen, 2006) found a simple equation describing the evolution of OH resulting from emission changes in the period 1990–2001. In general, CO emission increases lead to an overall reduction in current global averaged OH levels. An increase in NO_x emissions increases global OH as long as it takes place outside highly polluted regions. In this study the general picture is that the NO_x / CO emission ratio increases over the 1970–2012 period (Fig. 16). Despite the general increase, periods of declining ratio can be seen both after the oil crisis in 1973 and the energy crisis in 1979. This occurs since NO_x emissions are more affected than CO emissions. After 1997 when we include year-to-year variation in emissions from vegetation fires the NO_x / CO emission ratio is more variable. Large drops in ratio can be seen in years with high incidences of fires resulting in large CO emissions. This is typical for ENSO episodes (1997–1998) and warm years (2010). Agreement with observed CO trends (see comparison in Supplement Sect. S5) indicates that the modelled changes of CO and OH, and applied CO emissions are internally consistent.

Holmes et al. (2013) found formulas for predicting CH_4 lifetime due to changes in meteorology using some of the factors shown in Fig. 16. It is only from 1997 that our simulations include inter-annual variation in meteorology. We find that variations in global averaged specific humidity and temperature are highly correlated with each other and a 6-month delayed ENSO index. This is reasonable as this is a typical response time for physical and chemical signals to propagate from one hemisphere to the other. High temperature and specific humidity, meaning high water vapour content, is for instance found in the ENSO year 1998 and warm year 2010 (Fig. 16). Variations in these parameters are important for the CH_4 lifetime since the reaction rate (k) between OH and CH_4 is highly temperature dependent and water vapour is a precursor of OH (Levy, 1971). The production of OH is also dependent on UV radiation and thereby the atmospheric ozone column absorbing such radiation (Rohrer and Berresheim, 2006). The highest UV radiation is found at low latitudes and the ozone burden between 40° S and 40° N is regarded as a useful indicator (Holmes et al., 2013). The emissions of NO_x from lightning are dependent on a number of meteorological factors and thereby quite variable from year to year (Fig. 16).

In this section we investigate whether simplified expressions for the evolution of CH_4 lifetime can be found based on

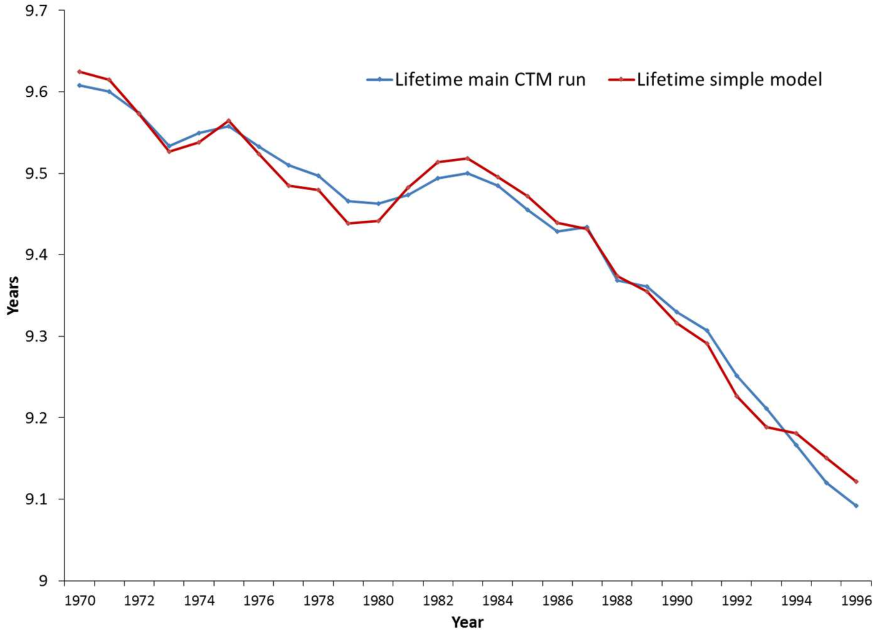

Figure 17. CH_4 lifetime evolution 1970–1996. Comparison of the main model simulation (blue line) with CH_4 lifetime from the simple model (red line) obtained from multiple linear regression.

the parameters in Fig. 16. Such equations could be very useful for fast prediction of future development of CH_4 lifetime and CH_4 burden. Since we study different time periods than Dalsøren and Isaksen (2006) and Holmes et al. (2013), and both emissions and meteorology are perturbed in our simulations, it is not obvious that simplified equations would be statistically valid.

Figure 17 shows the results of multiple linear regression analysis performed to describe the CH_4 lifetime over the period 1970 to 1996. For this period, fixed year-to-year meteorology was used in the main model simulation. This means that parameters like lightning NO_x, temperature, and specific humidity (Fig. 16) can be kept out of the regression analysis. The equation best reproducing ($R^2 = 0.99$) the lifetime evolution from the main run (Fig. 17) and having statistical significant linear relations between its parameters and CH_4 lifetime is the following:

$$CH_4 \text{ lifetime (yr)} = 11.9 - 21.4 \times (NO_x/CO)_{\text{emissions}}.$$

This confirms the analysis from previous sections suggesting that CH_4 itself has small influence on the variation in CH_4 lifetime during this period. The same seems to be the case for variations in ozone column. A similar simple equation was found by Dalsøren and Isaksen (2006). This suggests that near-future variation of CH_4 lifetime due to changes in emissions can be predicted solely by looking at the ratio of NO_x to CO emissions. However, it should be noted that the region of emission change is important (Berntsen et al., 2006). This is especially the case for NO_x emissions due to the short atmospheric NO_x lifetime. For instance, changes in NO_x emissions at low latitudes with moderate pollution levels (OH response is non-linear) would have profound impacts on CH_4 lifetime due to the temperature dependency of the reaction between CH_4 and OH.

The blue line in Fig. 18 shows the lifetime over the period 1997–2012 as predicted by the main model run. The red line shows the best fit from a simple parametric model. Because the main CTM run for this period include year-to-year variation in meteorology, the simple regression model need more parameters to reproduce the evolution. Still, a simplified equation ($R^2 = 0.99$) is statistically valid, predicting the CH_4 lifetime by a linear combination of the parameters specific humidity (q), NO_x / CO emission ratio $(NO_x\,/\,CO)_e$, lightning NO_x emissions $(LNO_x)_e$, and O_3 column:

$$CH_4 \text{ lifetime (yr)} = 0.07 \times O_{3\text{column}} - 4.80 \times (NO_x/CO)_e - 0.04 \times q - 1.21 \times (LNO_x)_e.$$

It should be noted that specific humidity and temperature have almost identical year-to-year variation, and it is therefore not given which of these parameters should be used.

4 Summary and conclusions

Uncertainties in physical and chemical processes in models, input data on emissions and meteorology, and limited spatial and temporal coverage of measurement data, have made it hard for both bottom-up and top-down studies to settle the global CH_4 budget, untangle the causes for recent trends, and predict future evolution (Ciais et al., 2013; Kirschke et al.,

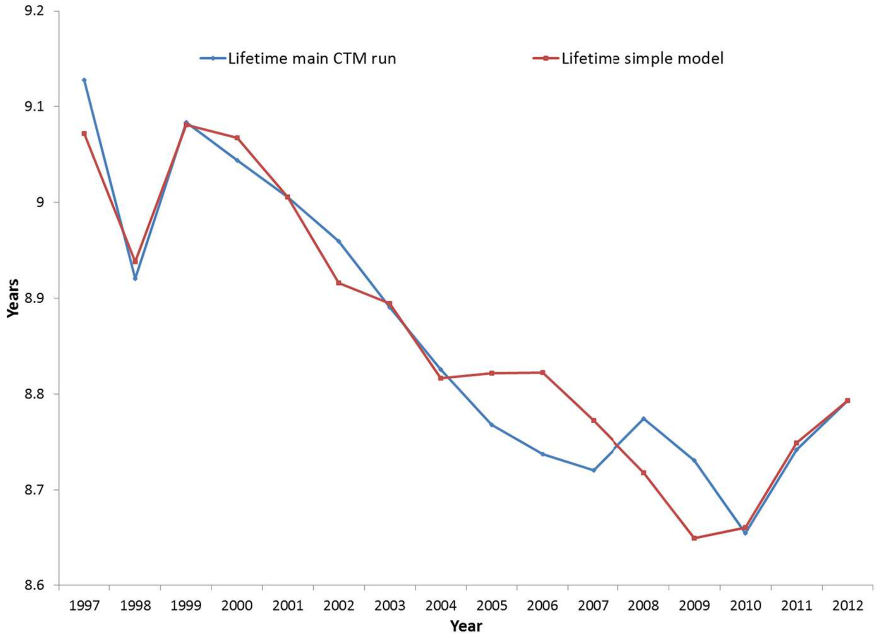

Figure 18. CH_4 lifetime evolution 1997–2012. Comparison of main model simulation (blue line) with CH_4 lifetime from simple model (red line) obtained from multiple linear regression.

2013; Nisbet et al., 2014). As the quality and detail level of models, input data, and measurements progress, the chances of understanding more pieces in the big puzzle increase. This study is an effort in such a perspective.

In our bottom-up approach, a global chemical transport model (CTM) was used to study the evolution of atmospheric CH_4 over the period 1970–2012. The study includes a thorough comparison with CH_4 measurements from surface stations covering all regions of the globe. The seasonal variations are reproduced at most stations. The model also reproduces much the observed evolution of CH_4 on both inter-annual and decadal time scales. Variations in wetland emissions are the major drivers for year-to-year variation of CH_4. Regarding trends, the causes are much debated, as discussed in the previous sections. Consensus is neither reached on the relative contribution from individual emission sectors, nor on the share of natural vs. anthropogenic sources. The fact that our simulations capture much of the observed regional changes indicates that our transport and chemistry schemes perform well and that applied emission inventories are reasonable with regard to temporal, spatial, sectoral, and natural vs. anthropogenic distribution of emissions. However, there are some larger discrepancies in model performance questioning the accuracy of the CH_4 emission data in certain regions and periods. Potential flaws in emission data are pinpointed for recent years when our model simulations are more complete with regard to input data (e.g. emissions, variable meteorology, etc.) and there are more measurements available for comparison. After a period of stable CH_4 levels from 2000 to 2006, observations show increasing levels from 2006 in both hemispheres. From 2006, the model overestimates the growth in all regions, in particular in Asia. Large emission growth in Asia influences the CH_4 trends in most world regions. Our findings support other studies, suggesting that the recent growth in Asian anthropogenic emissions is too high in the EDGAR v4.2 inventory. Based on our model results and the comparison between ECLIPSE and EDGAR v4.2 emissions in the Supplement (Sect. S2) we also question the Asian emission trends in the 1990s and beginning of the 2000s in the EDGAR v4.2 inventory, although the limited number of measurement sites in Asia makes it difficult to validate this.

The modelled evolution of CH_4 is also dependent on changes in the atmospheric CH_4 loss. The CH_4 lifetime is an indicator of the CH_4 loss. In our simulations, the CH_4 lifetime decreases by more than 8 % from 1970 to 2012. The reason for the large change is increased atmospheric oxidation capacity. Such changes are in theory driven by complex interactions between a number of chemical components and meteorological factors. However, our analysis reveals that key factors for the development are changes in specific humidity, NO_x / CO emission ratio, lightning NO_x emissions, and total ozone column. It is statistically valid to predict the CH_4 lifetime by a combination of these parameters in a simple equation. The calculated change in CH_4 lifetime is within the range reported by most other bottom-up model studies. However, findings from these studies do not fully agree with top-down approaches using observations of CH_3CCl_3 or ^{14}CO.

Without the calculated increase in oxidation capacity, the CH_4 growth over the last decades would have been much higher. Increasing CH_4 loss also likely contributed to the stagnation of CH_4 growth in the period 2001–2006. Interestingly, over the last few years, the loss deviates from its steady increase over the previous decades. Much of this deviation seems to be caused by variation in meteorology. Our simulations reveal that accounting for variation in meteorology has a strong effect on the atmospheric CH_4 loss. This in turn affects both inter-annual and long-term changes in CH_4 burden. A stabilization of the CH_4 loss, mainly due to meteorological variability, likely contributed to a continuing increase (2009–2012) in CH_4 burden after high emission years in 2007 and 2008. Due to the long response time of CH_4 this could also contribute to future CH_4 growth. However, there are extra uncertainties in the model results after 2009 due to lack of comprehensive emission inventories. A new inventory or update of existing ones with sector–vice separation of emission for recent years (2009–2015) would be a very valuable piece for model studies trying to close the gaps in the CH_4 puzzle. It will also provide important fundament for more accurate predictions of future CH_4 levels and various mitigation strategies.

The Supplement related to this article is available online at doi:10.5194/acp-16-3099-2016-supplement.

Acknowledgements. This work was funded by the Norwegian Research Council project GAME (Causes and effects of Global and Arctic changes in the Methane budget), grant no. 207587, under the program NORKLIMA, and the EU project ACCESS (Arctic Climate Change Economy and Society). ACCESS received funding from the European Union under grant agreement no. 265863 within the Ocean of Tomorrow call of the European Commission Seventh Framework Programme. We are grateful to Phillipe Bousquet for providing and sharing data sets on methane emissions. The work and conclusions of the paper could not been achieved without globally distributed observational data and we acknowledge all data providers, and the great efforts of AGAGE, NOAA ESRL, and The World Data Centre for Greenhouse Gases (WDCGG) under the GAW programme for making data public and available. Specific thanks go to Nina Paramonova, Hsiang J. Wang, Simon O'Doherty, Yasunori Tohjima, Edward J. Dlugokencky, who are the PIs of the observation data shown in Figs. 6–10 and 12–14. We also thank Edward J. Dlugokencky for sharing the observational based data set for Fig. 11, and WDCGG and Paul Novelli for sharing CO data sets used in Fig. S5 of the supplement.

Edited by: P. Jöckel

References

Aydin, M., Verhulst, K. R., Saltzman, E. S., Battle, M. O., Montzka, S. A., Blake, D. R., Tang, Q., and Prather, M. J.: Recent decreases in fossil-fuel emissions of ethane and methane derived from firn air, Nature, 476, 198–201, 2011.

Bânda, N., Krol, M., van Weele, M., van Noije, T., and Röckmann, T.: Analysis of global methane changes after the 1991 Pinatubo volcanic eruption, Atmos. Chem. Phys., 13, 2267–2281, doi:10.5194/acp-13-2267-2013, 2013.

Bekki, S. and Law, K. S.: Sensitivity of the atmospheric CH_4 growth rate to global temperature changes observed from 1980 to 1992, Tellus B, 49, 409–416, doi:10.1034/j.1600-0889.49.issue4.6.x, 1997.

Bergamaschi, P., Houweling, S., Segers, A., Krol, M., Frankenberg, C., Scheepmaker, R. A., Dlugokencky, E., Wofsy, S. C., Kort, E. A., Sweeney, C., Schuck, T., Brenninkmeijer, C., Chen, H., Beck, V., and Gerbig, C.: Atmospheric CH_4 in the first decade of the 21st century: Inverse modeling analysis using SCIAMACHY satellite retrievals and NOAA surface measurements, J. Geophys. Res.-Atmos., 118, 7350–7369, doi:10.1002/jgrd.50480, 2013.

Berglen, T., Berntsen, T., Isaksen, I., and Sundet, J.: A global model of the coupled sulfur/oxidant chemistry in the troposphere: The sulfur cycle, J. Geophys. Res.-Atmos., 109, D19310, doi:10.1029/2003JD003948, 2004.

Berntsen, T., Fuglestvedt, J., Myhre, G., Stordal, F., and Berglen, T.: Abatement of Greenhouse Gases: Does Location Matter?, Climatic Change, 74, 377–411, doi:10.1007/s10584-006-0433-4, 2006.

Bhattacharya, S. K., Borole, D. V., Francey, R. J., Allison, C. E., Steele, L. P., Krummel, P., Langenfelds, R., Masarie, K. A., Tiwari, Y. K., and Patra, P. K.: Trace gases and CO_2 isotope records from Cabo de Rama, India, Curr. Sci., 97, 1336–1344, 2009.

Bousquet, P., Hauglustaine, D. A., Peylin, P., Carouge, C., and Ciais, P.: Two decades of OH variability as inferred by an inversion of atmospheric transport and chemistry of methyl chloroform, Atmos. Chem. Phys., 5, 2635–2656, doi:10.5194/acp-5-2635-2005, 2005.

Bousquet, P., Ciais, P., Miller, J. B., Dlugokencky, E. J., Hauglustaine, D. A., Prigent, C., Van der Werf, G. R., Peylin, P., Brunke, E. G., Carouge, C., Langenfelds, R. L., Lathiere, J., Papa, F., Ramonet, M., Schmidt, M., Steele, L. P., Tyler, S. C., and White, J.: Contribution of anthropogenic and natural sources to atmospheric methane variability, Nature, 443, 439–443, 2006.

Bousquet, P., Ringeval, B., Pison, I., Dlugokencky, E. J., Brunke, E.-G., Carouge, C., Chevallier, F., Fortems-Cheiney, A., Frankenberg, C., Hauglustaine, D. A., Krummel, P. B., Langenfelds, R. L., Ramonet, M., Schmidt, M., Steele, L. P., Szopa, S., Yver, C., Viovy, N., and Ciais, P.: Source attribution of the changes in atmospheric methane for 2006–2008, Atmos. Chem. Phys., 11, 3689–3700, doi:10.5194/acp-11-3689-2011, 2011.

Bridgham, S. D., Cadillo-Quiroz, H., Keller, J. K., and Zhuang, Q.: Methane emissions from wetlands: biogeochemical, microbial, and modeling perspectives from local to global scales, Glob. Change Biol., 19, 1325–1346, doi:10.1111/gcb.12131, 2013.

Bruhwiler, L., Dlugokencky, E., Masarie, K., Ishizawa, M., Andrews, A., Miller, J., Sweeney, C., Tans, P., and Worthy, D.: CarbonTracker-CH_4: an assimilation system for estimating emissions of atmospheric methane, Atmos. Chem. Phys., 14, 8269–8293, doi:10.5194/acp-14-8269-2014, 2014.

Chen, Y.-H. and Prinn, R. G.: Estimation of atmospheric methane emissions between 1996 and 2001 using a three-dimensional global chemical transport model, J. Geophys. Res.-Atmos., 111, D10307, doi:10.1029/2005JD006058, 2006.

Ciais, P., Sabine, C., Bala, G., Bopp, L., Brovkin, V., Canadell, J., Chhabra, A., DeFries, R., Galloway, J., Heimann, M., Jones, C., Le Quéré, C., Myneni, R. B., Piao, S., and Thornton, P.: Carbon and Other Biogeochemical Cycles, in: Climate Change 2013: The Physical Science Basis. Contribution of Working Group I to the Fifth Assessment Report of the Intergovernmental Panel on Climate Change, edited by: Stocker, T. F., Qin, D., Plattner, G.-K., Tignor, M., Allen, S. K., Boschung, J., Nauels, A., Xia, Y., Bex, V., and Midgley, P. M., Cambridge University Press, Cambridge, United Kingdom and New York, NY, USA, 465–570, 2013.

Crevoisier, C., Nobileau, D., Armante, R., Crépeau, L., Machida, T., Sawa, Y., Matsueda, H., Schuck, T., Thonat, T., Pernin, J., Scott, N. A., and Chédin, A.: The 2007–2011 evolution of tropical methane in the mid-troposphere as seen from space by MetOp-A/IASI, Atmos. Chem. Phys., 13, 4279–4289, doi:10.5194/acp-13-4279-2013, 2013.

Crutzen, P. J.: Methane's sinks and sources, Nature, 350, 380–381, 1991.

Curry, C. L.: The consumption of atmospheric methane by soil in a simulated future climate, Biogeosciences, 6, 2355–2367, doi:10.5194/bg-6-2355-2009, 2009.

Dalsøren, S. B. and Isaksen, I. S. A.: CTM study of changes in tropospheric hydroxyl distribution 1990–2001 and its impact on methane, Geophys. Res. Lett., 33, L23811, doi:10.1029/2006GL027295, 2006.

Dalsøren, S., Eide, M., Myhre, G., Endresen, O., Isaksen, I., and Fuglestvedt, J.: Impacts of the Large Increase in International Ship Traffic 2000–2007 on Tropospheric Ozone and Methane, Environ. Sci. Technol., 2482–2489, doi:10.1021/es902628e, 2010.

Dalsøren, S. B., Isaksen, I. S. A., Li, L., and Richter, A.: Effect of emission changes in Southeast Asia on global hydroxyl and methane lifetime, Tellus B, 61, 588–601, doi:10.3402/tellusb.v61i4.16857, 2011.

Dentener, F., van Weele, M., Krol, M., Houweling, S., and van Velthoven, P.: Trends and inter-annual variability of methane emissions derived from 1979–1993 global CTM simulations, Atmos. Chem. Phys., 3, 73–88, doi:10.5194/acp-3-73-2003, 2003.

Dlugokencky, E. J., Dutton, E. G., Novelli, P. C., Tans, P. P., Masarie, K. A., Lantz, K. O., and Madronich, S.: Changes in CH_4 and CO growth rates after the eruption of Mt. Pinatubo and their link with changes in tropical tropospheric UV flux, Geophys. Res. Lett., 23, 2761–2764, doi:10.1029/96GL02638, 1996.

Dlugokencky, E. J., Walter, B. P., Masarie, K. A., Lang, P. M., and Kasischke, E. S.: Measurements of an anomalous global methane increase during 1998, Geophys. Res. Lett., 28, 499–502, doi:10.1029/2000GL012119, 2001.

Dlugokencky, E. J., Houweling, S., Bruhwiler, L., Masarie, K. A., Lang, P. M., Miller, J. B., and Tans, P. P.: Atmospheric methane levels off: Temporary pause or a new steady-state?, Geophys. Res. Lett., 30, 1992, doi:10.1029/2003GL018126, 2003.

Dlugokencky, E. J., Bruhwiler, L., White, J. W. C., Emmons, L. K., Novelli, P. C., Montzka, S. A., Masarie, K. A., Lang, P. M., Crotwell, A. M., Miller, J. B., and Gatti, L. V.: Observational constraints on recent increases in the atmospheric CH4 burden, Geophys. Res. Lett., 36, L18803, doi:10.1029/2009GL039780, 2009.

EC-JRC/PBL: Emission Database for Global Atmospheric Research (EDGAR), release version 4.2., available at: http://edgar.jrc.ec.europa.eu (last access: February 2016), 2011.

EPA: Global Anthropogenic Non-CO_2 Greenhouse Gas Emissions: 1990–2030, US Environmental Protection Agency Washington, DC, 2012.

Fiore, A. M., Horowitz, L. W., Dlugokencky, E. J., and West, J. J.: Impact of meteorology and emissions on methane trends, 1990–2004, Geophys. Res. Lett., 33, L12809, doi:10.1029/2006GL026199, 2006.

Fiore, A. M., West, J. J., Horowitz, L. W., Naik, V., and Schwarzkopf, M. D.: Characterizing the tropospheric ozone response to methane emission controls and the benefits to climate and air quality, J. Geophys. Res.-Atmos., 113, D08307, doi:10.1029/2007JD009162, 2008.

Fiore, A. M., Naik, V., Spracklen, D. V., Steiner, A., Unger, N., Prather, M., Bergmann, D., Cameron-Smith, P. J., Cionni, I., Collins, W. J., Dalsøren, S., Eyring, V., Folberth, G. A., Ginoux, P., Horowitz, L. W., Josse, B., Lamarque, J.-F., MacKenzie, I. A., Nagashima, T., O'Connor, F. M., Righi, M., Rumbold, S. T., Shindell, D. T., Skeie, R. B., Sudo, K., Szopa, S., Takemura, T., and Zeng, G.: Global air quality and climate, Chem. Soc. Rev., 41, 6663–6683, doi:10.1039/C2CS35095E, 2012.

Fisher, R. E., Sriskantharajah, S., Lowry, D., Lanoisellé, M., Fowler, C. M. R., James, R. H., Hermansen, O., Lund Myhre, C., Stohl, A., Greinert, J., Nisbet-Jones, P. B. R., Mienert, J., and Nisbet, E. G.: Arctic methane sources: Isotopic evidence for atmospheric inputs, Geophys. Res. Lett., 38, L21803, doi:10.1029/2011GL049319, 2011.

Frankenberg, C., Aben, I., Bergamaschi, P., Dlugokencky, E. J., van Hees, R., Houweling, S., van der Meer, P., Snel, R., and Tol, P.: Global column-averaged methane mixing ratios from 2003 to 2009 as derived from SCIAMACHY: Trends and variability, J. Geophys. Res.-Atmos., 116, D04302, doi:10.1029/2010JD014849, 2011.

Ghosh, A., Patra, P. K., Ishijima, K., Umezawa, T., Ito, A., Etheridge, D. M., Sugawara, S., Kawamura, K., Miller, J. B., Dlugokencky, E. J., Krummel, P. B., Fraser, P. J., Steele, L. P., Langenfelds, R. L., Trudinger, C. M., White, J. W. C., Vaughn, B., Saeki, T., Aoki, S., and Nakazawa, T.: Variations in global methane sources and sinks during 1910–2010, Atmos. Chem. Phys., 15, 2595–2612, doi:10.5194/acp-15-2595-2015, 2015.

Guenther, A., Karl, T., Harley, P., Wiedinmyer, C., Palmer, P. I., and Geron, C.: Estimates of global terrestrial isoprene emissions using MEGAN (Model of Emissions of Gases and Aerosols from Nature), Atmos. Chem. Phys., 6, 3181–3210, doi:10.5194/acp-6-3181-2006, 2006.

Heard, D. E. and Pilling, M. J.: Measurement of OH and HO_2 in the Troposphere, Chem. Rev., 103, 5163–5198, doi:10.1021/cr020522s, 2003.

Hodson, E. L., Poulter, B., Zimmermann, N. E., Prigent, C., and Kaplan, J. O.: The El Niño–Southern Oscillation and wetland methane interannual variability, Geophys. Res. Lett., 38, L08810, doi:10.1029/2011GL046861, 2011.

Holmes, C. D., Prather, M. J., Søvde, O. A., and Myhre, G.: Future methane, hydroxyl, and their uncertainties: key climate and emission parameters for future predictions, Atmos. Chem. Phys., 13, 285–302, doi:10.5194/acp-13-285-2013, 2013.

Houweling, S., Krol, M., Bergamaschi, P., Frankenberg, C., Dlugokencky, E. J., Morino, I., Notholt, J., Sherlock, V., Wunch, D., Beck, V., Gerbig, C., Chen, H., Kort, E. A., Röckmann, T., and Aben, I.: A multi-year methane inversion using SCIAMACHY, accounting for systematic errors using TCCON measurements, Atmos. Chem. Phys., 14, 3991-4012, doi:10.5194/acp-14-3991-2014, 2014.

Höglund-Isaksson, L.: Global anthropogenic methane emissions 2005–2030: technical mitigation potentials and costs, Atmos. Chem. Phys., 12, 9079–9096, doi:10.5194/acp-12-9079-2012, 2012.

Isaksen, I., Berntsen, T., Dalsøren, S., Eleftheratos, K., Orsolini, Y., Rognerud, B., Stordal, F., Søvde, O., Zerefos, C., and Holmes, C.: Atmospheric Ozone and Methane in a Changing Climate, Atmosphere, 5, 518–535, 2014.

Isaksen, I. S. A., Gauss, M., Myhre, G., Walter Anthony, K. M., and Ruppel, C.: Strong atmospheric chemistry feedback to climate warming from Arctic methane emissions, Global Biogeochem. Cy., 25, GB2002, doi:10.1029/2010GB003845, 2011.

John, J. G., Fiore, A. M., Naik, V., Horowitz, L. W., and Dunne, J. P.: Climate versus emission drivers of methane lifetime against loss by tropospheric OH from 1860–2100, Atmos. Chem. Phys., 12, 12021–12036, doi:10.5194/acp-12-12021-2012, 2012.

Johnson, C. E., Stevenson, D. S., Collins, W. J., and Derwent, R. G.: Interannual variability in methane growth rate simulated with a coupled Ocean-Atmosphere-Chemistry model, Geophys. Res. Lett., 29, 9-1–9-4, doi:10.1029/2002GL015269, 2002.

Kai, F. M., Tyler, S. C., Randerson, J. T., and Blake, D. R.: Reduced methane growth rate explained by decreased Northern Hemisphere microbial sources, Nature, 476, 194–197, 2011.

Karlsdóttir, S. and Isaksen, I. S. A.: Changing methane lifetime: Possible cause for reduced growth, Geophys. Res. Lett., 27, 93–96, doi:10.1029/1999GL010860, 2000.

Kirschke, S., Bousquet, P., Ciais, P., Saunois, M., Canadell, J. G., Dlugokencky, E. J., Bergamaschi, P., Bergmann, D., Blake, D. R., Bruhwiler, L., Cameron-Smith, P., Castaldi, S., Chevallier, F., Feng, L., Fraser, A., Heimann, M., Hodson, E. L., Houweling, S., Josse, B., Fraser, P. J., Krummel, P. B., Lamarque, J.-F., Langenfelds, R. L., Le Quere, C., Naik, V., O'Doherty, S., Palmer, P. I., Pison, I., Plummer, D., Poulter, B., Prinn, R. G., Rigby, M., Ringeval, B., Santini, M., Schmidt, M., Shindell, D. T., Simpson, I. J., Spahni, R., Steele, L. P., Strode, S. A., Sudo, K., Szopa, S., van der Werf, G. R., Voulgarakis, A., van Weele, M., Weiss, R. F., Williams, J. E., and Zeng, G.: Three decades of global methane sources and sinks, Nat. Geosci., 6, 813–823, doi:10.1038/ngeo1955, 2013.

Krol, M. and Lelieveld, J.: Can the variability in tropospheric OH be deduced from measurements of 1,1,1-trichloroethane (methyl chloroform)?, J. Geophys. Res.-Atmos., 108, 4125, doi:10.1029/2002JD002423, 2003.

Krol, M. C., Meirink, J. F., Bergamaschi, P., Mak, J. E., Lowe, D., Jöckel, P., Houweling, S., and Röckmann, T.: What can ^{14}CO measurements tell us about OH?, Atmos. Chem. Phys., 8, 5033–5044, doi:10.5194/acp-8-5033-2008, 2008.

Lelieveld, J. O. S., Crutzen, P. J., and Dentener, F. J.: Changing concentration, lifetime and climate forcing of atmospheric methane, Tellus B, 50, 128–150, doi:10.1034/j.1600-0889.1998.t01-1-00002.x, 1998.

Lelieveld, J., Dentener, F. J., Peters, W., and Krol, M. C.: On the role of hydroxyl radicals in the self-cleansing capacity of the troposphere, Atmos. Chem. Phys., 4, 2337–2344, doi:10.5194/acp-4-2337-2004, 2004.

Lelieveld, J., Brenninkmeijer, C. A. M., Joeckel, P., Isaksen, I. S. A., Krol, M. C., Mak, J. E., Dlugokencky, E., Montzka, S. A., Novelli, P. C., Peters, W., and Tans, P. P.: New Directions: Watching over tropospheric hydroxyl (OH), Atmos. Environ., 40, 5741–5743, doi:10.1016/j.atmosenv.2006.04.008, 2006.

Levin, I., Veidt, C., Vaughn, B. H., Brailsford, G., Bromley, T., Heinz, R., Lowe, D., Miller, J. B., Posz, C., and White, J. W. C.: No inter-hemispheric $\delta^{13}CH_4$ trend observed, Nature, 486, E3–E4, 2012.

Levy, H.: Normal Atmosphere: Large Radical and Formaldehyde Concentrations Predicted, Science, 173, 141–143, doi:10.1126/science.173.3992.141, 1971.

Manning, M. R., Lowe, D. C., Moss, R. C., Bodeker, G. E., and Allan, W.: Short-term variations in the oxidizing power of the atmosphere, Nature, 436, 1001–1004, 2005.

Melton, J. R., Wania, R., Hodson, E. L., Poulter, B., Ringeval, B., Spahni, R., Bohn, T., Avis, C. A., Beerling, D. J., Chen, G., Eliseev, A. V., Denisov, S. N., Hopcroft, P. O., Lettenmaier, D. P., Riley, W. J., Singarayer, J. S., Subin, Z. M., Tian, H., Zürcher, S., Brovkin, V., van Bodegom, P. M., Kleinen, T., Yu, Z. C., and Kaplan, J. O.: Present state of global wetland extent and wetland methane modelling: conclusions from a model intercomparison project (WETCHIMP), Biogeosciences, 10, 753–788, doi:10.5194/bg-10-753-2013, 2013.

Monteil, G., Houweling, S., Dlugockenky, E. J., Maenhout, G., Vaughn, B. H., White, J. W. C., and Rockmann, T.: Interpreting methane variations in the past two decades using measurements of CH_4 mixing ratio and isotopic composition, Atmos. Chem. Phys., 11, 9141–9153, doi:10.5194/acp-11-9141-2011, 2011.

Montzka, S. A., Spivakovsky, C. M., Butler, J. H., Elkins, J. W., Lock, L. T., and Mondeel, D. J.: New Observational Constraints for Atmospheric Hydroxyl on Global and Hemispheric Scales, Science, 288, 500–503, doi:10.1126/science.288.5465.500, 2000.

Montzka, S. A., Krol, M., Dlugokencky, E., Hall, B., Jöckel, P., and Lelieveld, J.: Small Interannual Variability of Global Atmospheric Hydroxyl, Science, 331, 67–69, doi:10.1126/science.1197640, 2011.

Morimoto, S., Aoki, S., Nakazawa, T., and Yamanouchi, T.: Temporal variations of the carbon isotopic ratio of atmospheric methane observed at Ny Ålesund, Svalbard from 1996 to 2004, Geophys. Res. Lett., 33, L01807, doi:10.1029/2005GL024648, 2006.

Myhre, G., Shindell, D., Bréon, F.-M., Collins, W., Fuglestvedt, J., Huang, J., Koch, D., Lamarque, J.-F., Lee, D., Mendoza, B., Nakajima, T., Robock, A., Stephens, G., Takemura, T., and Zhang, H.: Anthropogenic and natural radiative forcing, in: Climate Change 2013: The Physical Science Basis. Contribution of Working Group I to the Fifth Assessment Report of the Intergovernmental Panel on Climate Change, edited by: Stocker, T. F., Qin, D., Plattner, G.-K., Tignor, M., Allen, S. K., Doschung, J., Nauels, A., Xia, Y., Bex, V., and Midgley, P. M., Cambridge University Press, 659–740, 2013.

Naik, V., Voulgarakis, A., Fiore, A. M., Horowitz, L. W., Lamarque, J.-F., Lin, M., Prather, M. J., Young, P. J., Bergmann, D., Cameron-Smith, P. J., Cionni, I., Collins, W. J., Dalsøren, S. B., Doherty, R., Eyring, V., Faluvegi, G., Folberth, G. A., Josse, B., Lee, Y. H., MacKenzie, I. A., Nagashima, T., van Noije, T. P. C., Plummer, D. A., Righi, M., Rumbold, S. T., Skeie, R., Shindell, D. T., Stevenson, D. S., Strode, S., Sudo, K., Szopa, S., and Zeng, G.: Preindustrial to present-day changes in tropospheric hydroxyl radical and methane lifetime from the Atmospheric Chemistry and Climate Model Intercomparison Project (ACCMIP), Atmos. Chem. Phys., 13, 5277–5298, doi:10.5194/acp-13-5277-2013, 2013.

Neef, L., van Weele, M., and van Velthoven, P.: Optimal estimation of the present-day global methane budget, Global Biogeochem. Cy., 24, GB4024, doi:10.1029/2009GB003661, 2010.

Nisbet, E. G., Dlugokencky, E. J., and Bousquet, P.: Methane on the Rise – Again, Science, 343, 493–495, doi:10.1126/science.1247828, 2014.

O'Connor, F. M., Boucher, O., Gedney, N., Jones, C. D., Folberth, G. A., Coppell, R., Friedlingstein, P., Collins, W. J., Chappellaz, J., Ridley, J., and Johnson, C. E.: Possible role of wetlands, permafrost, and methane hydrates in the methane cycle under future climate change: A review, Rev. Geophys., 48, RG4005, doi:10.1029/2010RG000326, 2010.

Patra, P. K., Krol, M. C., Montzka, S. A., Arnold, T., Atlas, E. L., Lintner, B. R., Stephens, B. B., Xiang, B., Elkins, J. W., Fraser, P. J., Ghosh, A., Hintsa, E. J., Hurst, D. F., Ishijima, K., Krummel, P. B., Miller, B. R., Miyazaki, K., Moore, F. L., Muhle, J., O'Doherty, S., Prinn, R. G., Steele, L. P., Takigawa, M., Wang, H. J., Weiss, R. F., Wofsy, S. C., and Young, D.: Observational evidence for interhemispheric hydroxyl-radical parity, Nature, 513, 219–223, doi:10.1038/nature13721, 2014.

Pison, I., Bousquet, P., Chevallier, F., Szopa, S., and Hauglustaine, D.: Multi-species inversion of CH_4, CO and H_2 emissions from surface measurements, Atmos. Chem. Phys., 9, 5281–5297, doi:10.5194/acp-9-5281-2009, 2009.

Pison, I., Ringeval, B., Bousquet, P., Prigent, C., and Papa, F.: Stable atmospheric methane in the 2000s: key-role of emissions from natural wetlands, Atmos. Chem. Phys., 13, 11609–11623, doi:10.5194/acp-13-11609-2013, 2013.

Prinn, R. G., Huang, J., Weiss, R. F., Cunnold, D. M., Fraser, P. J., Simmonds, P. G., McCulloch, A., Harth, C., Salameh, P., O'Doherty, S., Wang, R. H. J., Porter, L., and Miller, B. R.: Evidence for Substantial Variations of Atmospheric Hydroxyl Radicals in the Past Two Decades, Science, 292, 1882–1888, doi:10.1126/science.1058673, 2001.

Prinn, R. G., Huang, J., Weiss, R. F., Cunnold, D. M., Fraser, P. J., Simmonds, P. G., McCulloch, A., Harth, C., Reimann, S., Salameh, P., O'Doherty, S., Wang, R. H. J., Porter, L. W., Miller, B. R., and Krummel, P. B.: Evidence for variability of atmospheric hydroxyl radicals over the past quarter century, Geophys. Res. Lett., 32, L07809, doi:10.1029/2004GL022228, 2005.

Rigby, M., Prinn, R. G., Fraser, P. J., Simmonds, P. G., Langenfelds, R. L., Huang, J., Cunnold, D. M., Steele, L. P., Krummel, P. B., Weiss, R. F., O'Doherty, S., Salameh, P. K., Wang, H. J., Harth, C. M., Mühle, J., and Porter, L. W.: Renewed growth of atmospheric methane, Geophys. Res. Lett., 35, L22805, doi:10.1029/2008GL036037, 2008.

Rohrer, F. and Berresheim, H.: Strong correlation between levels of tropospheric hydroxyl radicals and solar ultraviolet radiation, Nature, 442, 184–187, 2006.

Schultz, M., van het Bolscher, M., Pulles, T., Brand, R., Pereira, J., Spessa, A., Dalsøren, S., van Nojie, T., Szopa, S., and Schultz, M.: Emission data sets and methodologies for estimating emissions, REanalysis of the TROpospheric chemical composition over the past 40 years, A long-term global modeling study of tropospheric chemistry funded under the 5th EU framework programme, EU-Contract No. EVK2-CT-2002-00170, 2008.

Schwietzke, S., Griffin, W. M., Matthews, H. S., and Bruhwiler, L. M. P.: Global Bottom-Up Fossil Fuel Fugitive Methane and Ethane Emissions Inventory for Atmospheric Modeling, ACS Sustainable Chemistry & Engineering, 2, 1992–2001, doi:10.1021/sc500163h, 2014.

Simpson, I. J., Chen, T.-Y., Blake, D. R., and Rowland, F. S.: Implications of the recent fluctuations in the growth rate of tropospheric methane, Geophys. Res. Lett., 29, 117-111–117-114, doi:10.1029/2001GL014521, 2002.

Simpson, I. J., Rowland, F. S., Meinardi, S., and Blake, D. R.: Influence of biomass burning during recent fluctuations in the slow growth of global tropospheric methane, Geophys. Res. Lett., 33, L22808, doi:10.1029/2006GL027330, 2006.

Simpson, I. J., Sulbaek Andersen, M. P., Meinardi, S., Bruhwiler, L., Blake, N. J., Helmig, D., Rowland, F. S., and Blake, D. R.: Long-term decline of global atmospheric ethane concentrations and implications for methane, Nature, 488, 490–494, 2012.

Sindelarova, K., Granier, C., Bouarar, I., Guenther, A., Tilmes, S., Stavrakou, T., Müller, J.-F., Kuhn, U., Stefani, P., and Knorr, W.: Global data set of biogenic VOC emissions calculated by the MEGAN model over the last 30 years, Atmos. Chem. Phys., 14, 9317–9341, doi:10.5194/acp-14-9317-2014, 2014.

Spahni, R., Wania, R., Neef, L., van Weele, M., Pison, I., Bousquet, P., Frankenberg, C., Foster, P. N., Joos, F., Prentice, I. C., and van Velthoven, P.: Constraining global methane emissions and uptake by ecosystems, Biogeosciences, 8, 1643–1665, doi:10.5194/bg-8-1643-2011, 2011.

Strode, S. A., Duncan, B. N., Yegorova, E. A., Kouatchou, J., Ziemke, J. R., and Douglass, A. R.: Implications of carbon monoxide bias for methane lifetime and atmospheric composition in chemistry climate models, Atmos. Chem. Phys., 15, 11789–11805, doi:10.5194/acp-15-11789-2015, 2015.

Sussmann, R., Forster, F., Rettinger, M., and Bousquet, P.: Renewed methane increase for five years (2007–2011) observed by solar FTIR spectrometry, Atmos. Chem. Phys., 12, 4885–4891, doi:10.5194/acp-12-4885-2012, 2012.

Søvde, O. A., Prather, M. J., Isaksen, I. S. A., Berntsen, T. K., Stordal, F., Zhu, X., Holmes, C. D., and Hsu, J.: The chemical transport model Oslo CTM3, Geosci. Model Dev., 5, 1441–1469, doi:10.5194/gmd-5-1441-2012, 2012.

Tsutsumi, Y., Kazumasa, M., Takatoshi, H., Masaaki, I., and Conway, T. J.: Technical Report of Global Analysis Method for Major Greenhouse Gases by the World Data Center for Greenhouse Gases, WMO, 2009.

van der Werf, G. R., Randerson, J. T., Giglio, L., Collatz, G. J., Mu, M., Kasibhatla, P. S., Morton, D. C., DeFries, R. S., Jin, Y., and van Leeuwen, T. T.: Global fire emissions and the contribution of deforestation, savanna, forest, agricultural, and peat fires (1997–

2009), Atmos. Chem. Phys., 10, 11707–11735, doi:10.5194/acp-10-11707-2010, 2010.

Wang, J. S., Logan, J. A., McElroy, M. B., Duncan, B. N., Megretskaia, I. A., and Yantosca, R. M.: A 3-D model analysis of the slowdown and interannual variability in the methane growth rate from 1988 to 1997, Global Biogeochem. Cy., 18, GB3011, doi:10.1029/2003GB002180, 2004.

Wang, J. S., McElroy, M. B., Logan, J. A., Palmer, P. I., Chameides, W. L., Wang, Y., and Megretskaia, I. A.: A quantitative assessment of uncertainties affecting estimates of global mean OH derived from methyl chloroform observations, J. Geophys. Res.-Atmos., 113, D12302, doi:10.1029/2007JD008496, 2008.

Warwick, N. J., Bekki, S., Law, K. S., Nisbet, E. G., and Pyle, J. A.: The impact of meteorology on the interannual growth rate of atmospheric methane, Geophys. Res. Lett., 29, 1947, doi:10.1029/2002GL015282, 2002.

West, J. J. and Fiore, A. M.: Management of Tropospheric Ozone by Reducing Methane Emissions, Environ. Sci. Technol., 39, 4685–4691, doi:10.1021/es048629f, 2005.

Worden, J., Jiang, Z., Jones, D. B. A., Alvarado, M., Bowman, K., Frankenberg, C., Kort, E. A., Kulawik, S. S., Lee, M., Liu, J., Payne, V., Wecht, K., and Worden, H.: El Niño, the 2006 Indonesian peat fires, and the distribution of atmospheric methane, Geophys. Res. Lett., 40, 4938–4943, doi:10.1002/grl.50937, 2013.

Supplement of Atmos. Chem. Phys., 16, 3099–3126, 2016
http://www.atmos-chem-phys.net/16/3099/2016/
doi:10.5194/acp-16-3099-2016-supplement

Supplement of

Atmospheric methane evolution the last 40 years

Stig B. Dalsøren et al.

Correspondence to: Stig B. Dalsøren (stigbd@cicero.oslo.no)

S1 Setup of emission inventories in model simulations

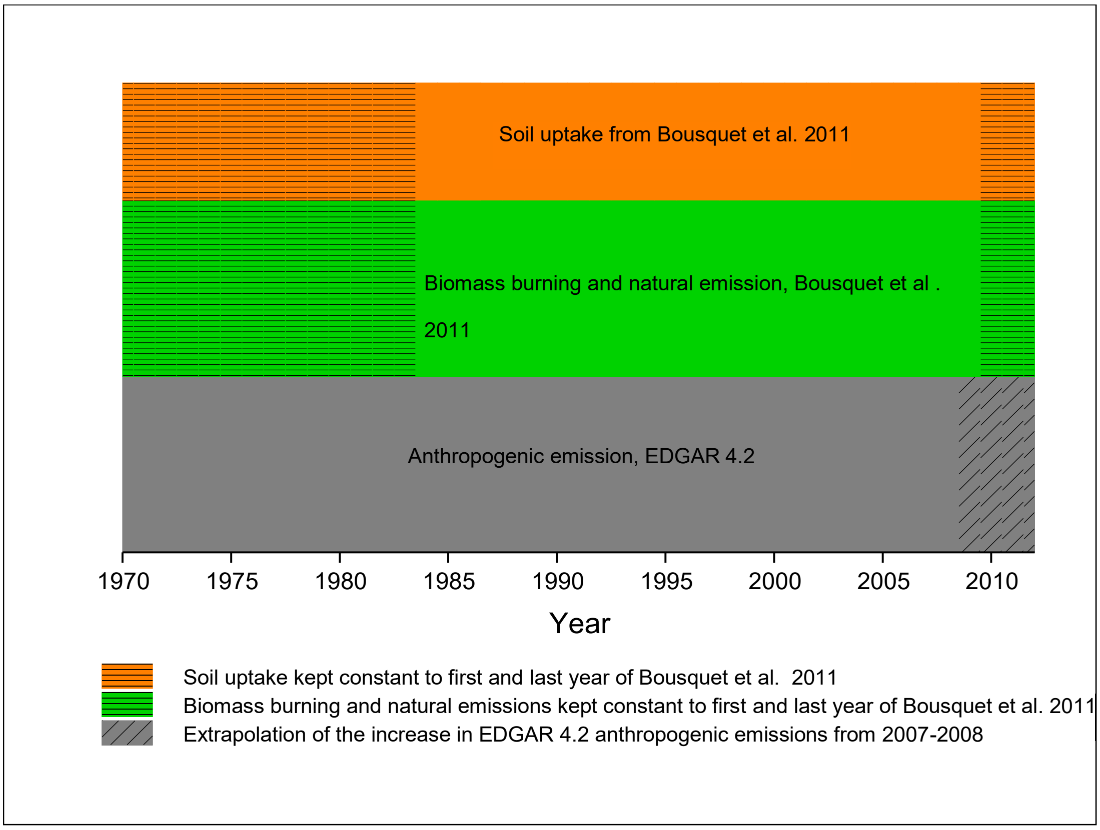

Figure S1. Overview of how emission inventories are included in the model for different time periods.

S2 Emission sectors and tracers

Table S1. List of CH_4 emission sectors and emission tracers used in the model simulations. The text colours in column 1 and 2 shows the legend colours in Fig. 1 and Fig. 6-10.

Wetlands	Emissions shown in Fig. 1	Tracer from these sectors shown in Fig. 6-10, 12-14, named “Natural”
Biomass burning	Emissions shown in Fig. 1	
Oceans+Termites+other natural	Emissions shown in Fig. 1	
Enteric fermentation	Emissions shown in Fig. 1	Tracer from this sector shown in Fig. 6-10, 12-14
Agricultural soils	Emissions shown in Fig. 1	Tracer from this sector shown in Fig. 6-10, 12-14
Solid fuels: Fugitive from solids	Emissions shown in Fig. 1	Tracer from this sector shown in Fig. 6-10, 12-14
Gas production and distribution	Emissions shown in Fig. 1	Tracer from this sector shown in Fig. 6-10, 12-14
Sum all other anthropogenic (those listed below)	Emissions shown in Fig. 1	Tracer from this sector shown in Fig. 6-10, 12-14
Solid waste		
Waste water		
Residential		
Manure management		
Energy manufacturing transformation		

Agricultural waste burning		
Road transportation		
Fossil fuel fires		
Non-road transportation		
Oil production and refineries		
Industrial process and product use		

The EDGAR v4.2 inventory was recently extended with the years 2009-2012. In this update abbreviated FT 2012 a somewhat simplified (Fast Track) approach was used and other emission components (NOx, CO, NMVOCs) have not been updated yet. In Fig. S2 we compare our extrapolations after 2008 with the new data. We also compare the EDGAR inventory to the ECLIPSE v5a emission inventory that are available for part of our study period (1990-2015), on 5-year intervals: http://www.iiasa.ac.at/web/home/research/researchPrograms/ECLIPSEv5.html).

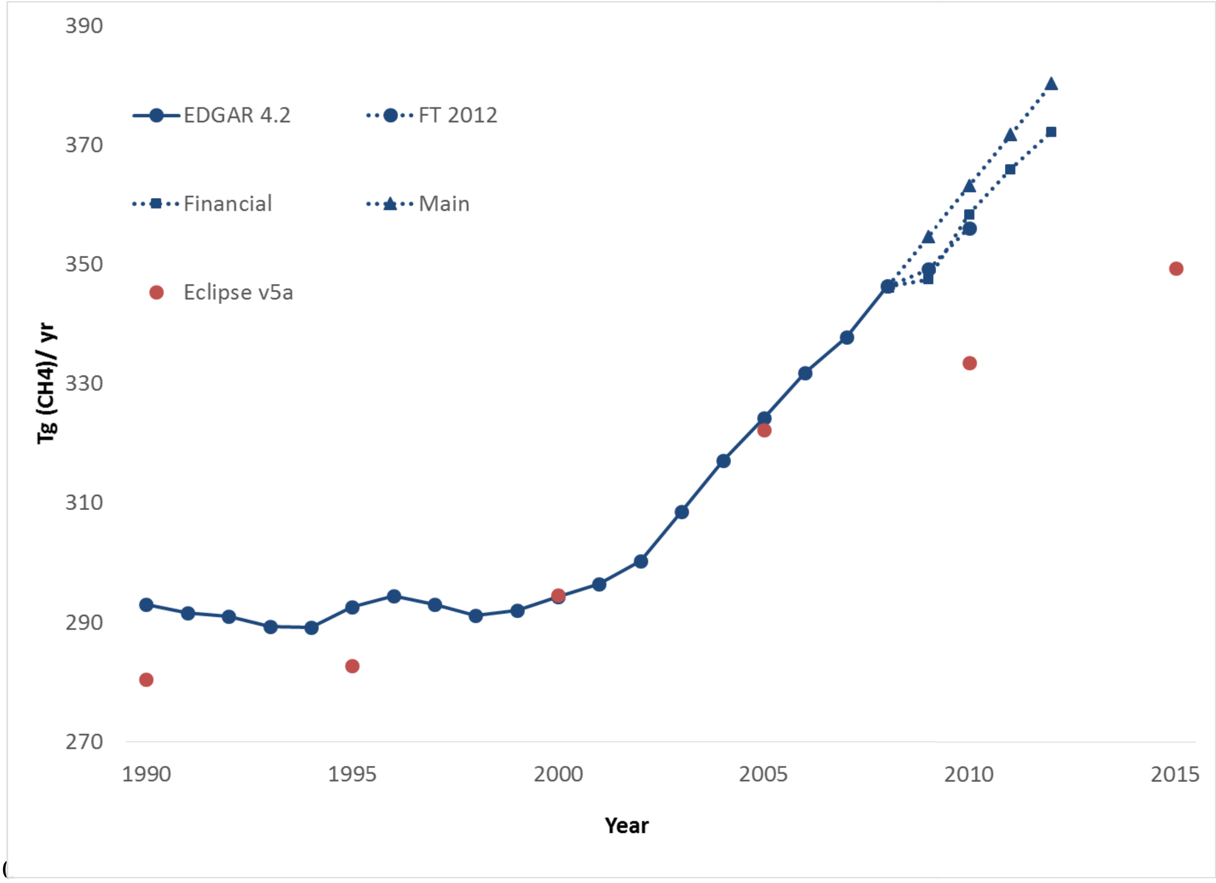

Figure S2. Comparison of emission inventories. The EDGAR v4.2 extended with the EDGAR FT2012 update compared to the extrapolations (main, financial) we made due to missing data at the start-up of this study. A comparison to the ECLIPSE v5a inventory is also shown.

The EDGAR FT 2012 curve in Fig. S2 ends in 2010 since it is not possible to exclude biomass burning for the numbers available for 2011 and 2012. From the figure it is evident that our simple baseline extrapolation (main) likely overestimates the emissions after 2008 and that the approach trying to take into account the financial crisis is closer to reality. In that approach BP statistics for gas production, oil and coal consumption were used to scale relevant methane emission from oil, gas and coal production. If this approach were to be used to set up a consistent baseline emission inventory, these BP factors should also be used to scale emissions of other compounds (e.g. CO and NOx). This would be more complicated and introduce uncertainties as it is less clear how to use the BP factors to scale emissions for road traffic, power plants etc., which constitute a substantial share of the emissions for these compounds. Therefore, a simpler extrapolation based on changes for previous years was preferred as baseline since it can be used in a consistent way for all emitted compounds.

The total emissions in the EDGAR and ECLIPSE inventories are rather similar but there are large differences in temporal evolution. ECLIPSE has larger emission growth from 1995 to 2000 and much smaller growth from 2005-2010. In the main text we explain why we think the time evolution in the ECLIPSE inventory is more realistic. The step from 2010 to 2015 in ECLIPSE is scenario based but should give some direction on where current emission levels are.

S3 Theoretical foundation of the use of the fictitious tracers

As indicated in Sect. 2.2 of the main paper, the simulations used 18 passive fictitious tracers for each of the CH_4 emission sectors listed in Table S1. The tracers were continuously emitted and then given an e-folding lifetime of 1 month undergoing transport but not interacting chemically. These tracers were used as a proxy for the different sector's recent contribution to monthly mean surface CH_4 concentrations, with the aim of revealing key sectors and regions behind recent changes in spatial distribution or temporal evolution of CH_4. In this section, we provide the theoretical foundation that justifies the use of these fictitious tracers.

Firstly, we summarize the results obtained in this section. We split the CH_4 mole fraction into two components: a quite uniform background component (r_B) and an inhomogeneous recently emitted component (r_R); the fictitious tracer being a proxy for the second component. The CH_4 surface emissions act as the sources for r_R (not for r_B), then this component is advected and mixed, and when achieving a good mixing (after 1-2 months) it is converted into r_B. Since the life time of r_R is of around 1 month (much smaller than the mean CH_4 lifetime), the chemical destruction acting on r_R is almost negligible (only acts on r_B). The same reason makes $|r_B| >> |r_R|$, except very near strong CH_4 emission sources.

We start with the continuity equation for the CH_4 mole fraction (r) in dry air:

$$\frac{Dr}{Dt} = -\frac{1}{n}\nabla \cdot \vec{F}_D(r) - \sum_i k_i \cdot c_i \cdot r \qquad (1),$$

where D/Dt is the Lagrangian time derivate, n is the number density (mol/m^3) of the dry air, the vector F_D is the diffusive flux due to turbulence (i.e., unresolved flow by the spatial scale of the model), k_i is the reaction rate with the trace gas i and c_i is the number density of the trace gas i. Note that the diffusive flux is linear in r (e.g., proportional to the gradient of r), even in the case in which the flux is non local (e.g., see Holtslag & Boville, 1993), as well as the rest of the terms of Eq. (1). The surface sources and sinks enter as the boundary conditions of Equation (1).

Now, we split Eq. (1) into two equations (this is our definition for the components r_B and r_R; we do not base our definition in spatial averages):

$$\frac{Dr_B}{Dt} = -\frac{1}{n}\nabla \cdot \vec{F}_D(r_B) - \sum_i k_i \cdot c_i \cdot r_B + P(r_R) \qquad (2),$$

$$\frac{Dr_R}{Dt} = -\frac{1}{n}\nabla \cdot \vec{F}_D(r_R) - \sum_i k_i \cdot c_i \cdot r_R - P(r_R) \qquad (3),$$

where the chemical losses in Eq. (3) will be almost negligible except very near strong CH_4 sources (as explained in the second paragraph of this section), and P is a linear projector onto a complete set of vectors (spectral components) for wavelengths larger than around 6,000 km. This projector continuously removes the smoothed part of r_R, which is continuously created as the emitted CH_4 becomes well mixed, and converts it into r_B. The CH_4 surface emissions are only included as boundary conditions for Eq. (3) (not for Eq. (2)). The CH_4 surface sink is only included as boundary condition for Eq. (2). Note that summing Eqs. (2) and (3), Eq. (1) is obtained. The reason for chosen 6,000 km as threshold wavelength is: 1) The mid-latitude synoptic scale motions have a characteristic variation length, L, of around 1,000 km (e.g., see Holton, 1992), and their associated wavelength is therefore of around 6,000 km. 2) Synoptic scale latitudinal motions are able to build up mole fraction inhomogeneities by advection of the CH_4 climatological latitudinal pattern. 3) What makes more sense is to convert r_R into r_B around the smaller scale in which the background by itself can build up inhomogeneities. Anyway, in the main article we plot and analyse monthly averages, therefore the mole fraction mark due to synoptic motions will be smoothed.

In the main paper, instead of using the non-local projector operator for coupling r_R and r_B, we use a simpler local proxy for this purpose: a volumetric sink for r_R with an e-folding lifetime of 1 month (A x r_R instead of $P(r_R)$, with $A=1$ month^{-1}). This process can approximately mimic the projector behaviour: it transforms r_R into r_B at a rate similar to that in which the projector acts (i.e., the rate at which mixing is able to smooth the emitted CH_4 till the 1,000 km characteristic variation length at which the projector starts to act). Indeed, r_R will be underestimated a bit because part of it will be removed by the 1-month lifetime e-folding sink before being smoothed to the 1,000 km characteristic variation length. The time needed to mix a species throughout a hemisphere is about 1 to 2 months, whereas 1 to 2 years are needed to mix a species through the entire Earth troposphere (Seinfeld and Pandis, 1998).

Now, we introduce the following notation: (Eulerian) annual means are denoted as < > (in the main paper we use annual running means since we are interested in the inter-annual variation of CH_4), whereas longitudinal means along a whole terrestrial parallel are denoted as [ ]. Each variable can be decomposed in two components: the mean and the deviation from the average, for instance:

$$r = \langle r \rangle + r' \qquad (4)$$

$$r = [r] + r^* \qquad (5)$$

$$\langle r \rangle = [\langle r \rangle] + \langle r \rangle^* \qquad (6)$$

where ‘ denotes time fluctuations and * denotes longitudinal fluctuations.

We have found (see the main paper) that there is a high correlation between $\langle r\rangle^*$ and $\langle r_R\rangle^*$ for most of the stations, with r_R defined using the local 1-month e-folding sink. Writing Eqs. (1) and (3) in conservative form, and expanding each variable simultaneously into its longitudinal and time components, in a similar fashion than Sect. 4.1.1 of Peixoto and Oort (1992), we have obtained quite complex PDEs (Partial differential Equations) linear in $\langle r\rangle^*$ and $\langle r_R\rangle^*$, respectively. Both equations are very similar (it is out of the scope of this paper to present such equations), and the main differences are:

a) a term containing the flux [<r>] <**v**>* appears in the first equation, whereas [<r_R>] <**v**>* appears in the second equation (they are no homogeneous terms of the corresponding PDEs).

b) a chemical term containing <k_i c_i>* [<r_B>] appears in the first equation, whereas the term –A n <r_R>* appears in the second equation.

We expect these terms are usually small (because we expect <**v**>* and <k_i c_i>* are usually small; these are the prerequisites mentioned in the main paper), except the term –A n <r_R>* that we think it is compensated in the other PDE by a larger mixing (due to differential advection and turbulent diffusion), which tends to convert <r>* into [<r>]. If both PDEs were identical, there would be a linear relation between their solutions, and the time linear correlation coefficient between the solutions would be exactly 1.

However, the few small differences between both PDEs make the time correlation coefficient between the solutions smaller than one. Note that <r>* changes along the corresponding parallel. For locations with |<r>*| small (i.e., <r> closes to [<r>]) compared to the maximum and minimum within the parallel, the relative contribution of the terms different (between the PDEs) may be larger and therefore the correlation coefficient smaller for these locations (this might explain the case of the Wendover station). As mentioned in the previous paragraph, r_R will be underestimated a bit when using the 1-month e-folding sink term, and this fact can contribute to the offset between <r>* and <r_R>*, and might explain why for most of the stations |<r>*|> |<r_R>*|.

S4 Scaling procedure

As noted in the main text the model in general underestimates the observed surface methane levels and likely reasons are discussed there. In Fig. 6-10 in the main article, the model results are scaled to the observed mean over the periods of measurements to better discern differences in trends between observations and model. To do this the absolute difference between the model output and the measurements is calculated for each year in the period 1970-2012. The mean of these differences is then added to the modelled values for all years. The model values are sampled from the gridbox with the closest location to the geographical position of the stations. Likewise, the model layer best corresponding to the station altitude is used.

S5 Discussion of sensitivity studies

S5.1 Influence of inter-annual variation in emissions from vegetation

In the “main” simulation discussed in the main article, natural emission data for 2000 were used for all years and all components except CH_4. The emissions from vegetation of CO and NMVOCs are from MEGAN (Guenther et al., 2006). Recently a new dataset (Sindelarova et al., 2014) with MEGAN emissions covering the period 1980-2010 became available. This dataset was used in the “bio” simulation to investigate whether inter-annual variations in CO and NMVOCs emissions from vegetation are important for the CH_4 evolution. Variations in these emissions affect OH levels which in turn influence the atmospheric CH_4 loss. Fig. S3 shows that surface CH_4 levels are higher in the “bio” simulation. Due to the long response time of CH_4 the difference between the two simulations grows over the first two decades. The higher CH_4 level is expected since the emissions (illustrated by the isoprene emission curves in Fig. S3) in the new inventory are higher for most years compared to the constant year 2000 emissions in the old inventory. Larger emissions of components like isoprene and CO results in lower OH values and reduced CH_4 loss. However, accounting for inter-annual variation of vegetation emissions of CO and NMVOCs does not shift the periods of growth and stagnation. Neither does it lead to larger year to year fluctuations in CH_4 levels. Compared to surface measurements (discussed in section 3.2 of the main article) the underestimation of CH_4 levels is less in the “bio” simulation, except from that there is no improvement in model performance.

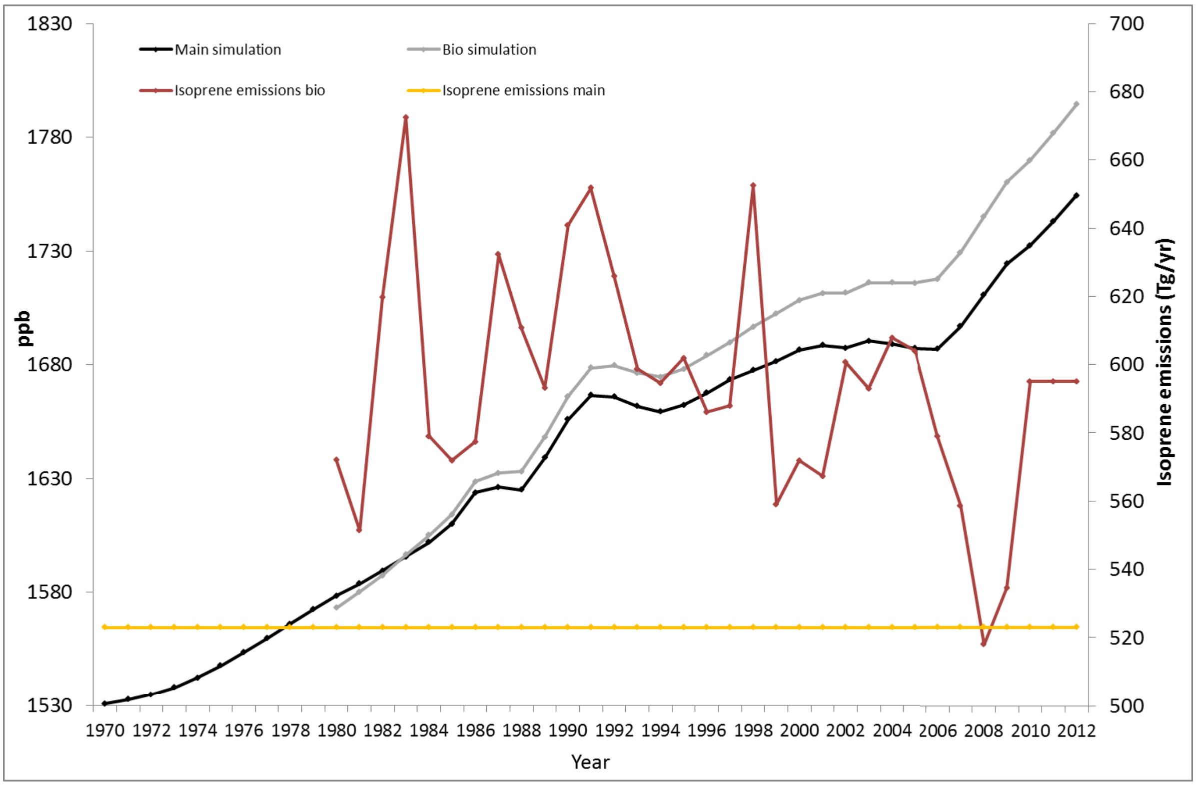

Figure S3. Surface CH_4 levels and isoprene emissions in main simulation and bio simulation.

S5.2 Influence of financial crisis.

The period 2009-2012 was rerun with slightly different emissions evaluating whether the recent financial crisis had any significant impact on CH_4 levels. Here, the emissions from petroleum and solid fuel production and distribution were scaled with BP Statistical Review of World Energy (bp.com/statisticalreview) numbers for gas production, oil and coal consumption resulting in a drop in total emissions in 2009 (Fig. 1, main article and Fig. S4). However, the evolution in emissions from 2010 with this alternative extrapolation is rather similar to that for the standard extrapolation. Due to the drop in emissions in 2009 in the "financial" run methane loss after 2009 is lower than for the "main" simulation (Fig. S4). The emission growth in 2011 and 2012 is also slightly lower in the financial simulation. This results in declining methane loss for these years in the "financial" simulation. In contrast the methane loss in 2011 and 2012 is rather stable in the "main" simulation. Despite differences for the methane loss the methane burden is very similar in the two simulations. Therefore, it seems likely that the financial crisis had small impact on the methane burden, but due to the long methane lifetime some of the difference in methane loss could manifest as burden changes after 2012, which is the end-year of our simulations.

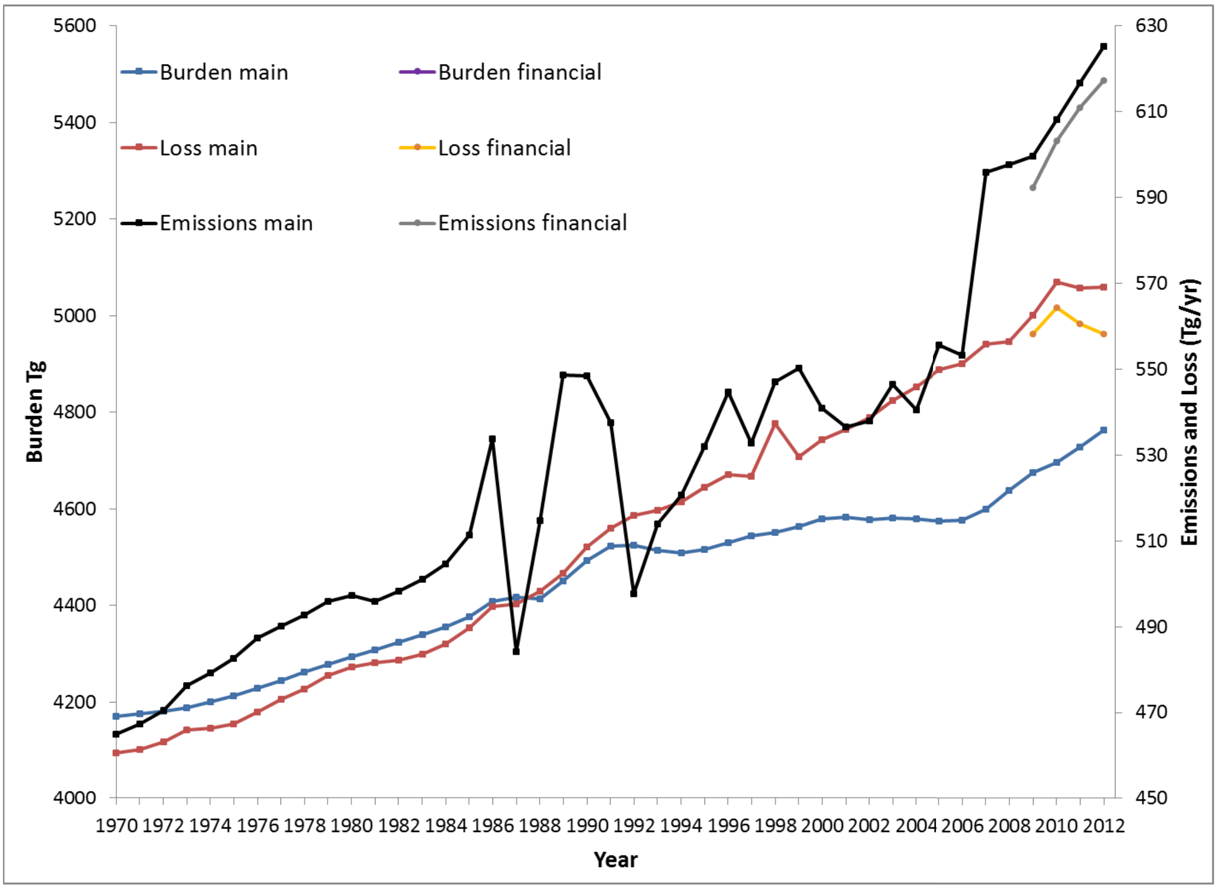

Figure S4. Methane budget in main and financial simulations.

S6 Comparison with CO observations

Since reaction with OH is the major loss of CO from the atmosphere a comparison with CO measurements indicates whether modelled trends in CO and OH, and the applied CO emission inventory are internally consistent.. In this section, a first elementary evaluation is made based on comparison between our model results and observation-based estimates of global mean surface CO levels (Fig. S5). There is very good agreement for the long term evolution (years-decades). The same is the case for short term (year to year) variations, especially after 1996 when our simulations include inter-annual variability in meteorology and biomass burning emissions (CO, NOx and NMVOCs). Our simulations do not fully account for the effect of the Pinatubo eruption and this also explains parts of the model discrepancy for the early nineties. Fig. S6 shows that the modeled gradual decline in CO levels over the period 1991-2012 is caused by stable to moderately declining CO emissions over the period combined with increasing OH for most of the period. Much of the large year to year fluctuations in CO levels (black line) are due to variation in emissions (purple line) caused by irregular occurrence and extent of vegetation fires. To summarize, the good agreement between our model and the observation based estimates supports that the modelled CO, applied CO emission inventory, and calculated OH changes are internally consistenti.

The WDCGG global mean estimate is higher than the NOAA ESRL (Fig. S5) since NOAA ESRL is based on relatively unpolluted marine boundary layer stations while WDCGG include inland stations in their calculations. CO is more unevenly mixed than CH_4 due to its shorter lifetime. How polluted versus un-polluted air masses go in the global mean calculations therefore matters. The modeled global mean is based on all grid-boxes in the lowest model layer and one reason for its higher value might be the above mentioned sensitivity. However, comparing seasonal distributions (not shown) the model seems to overestimate CO levels throughout the Northern Hemisphere summer season and that is likely the main reason for its higher global mean.

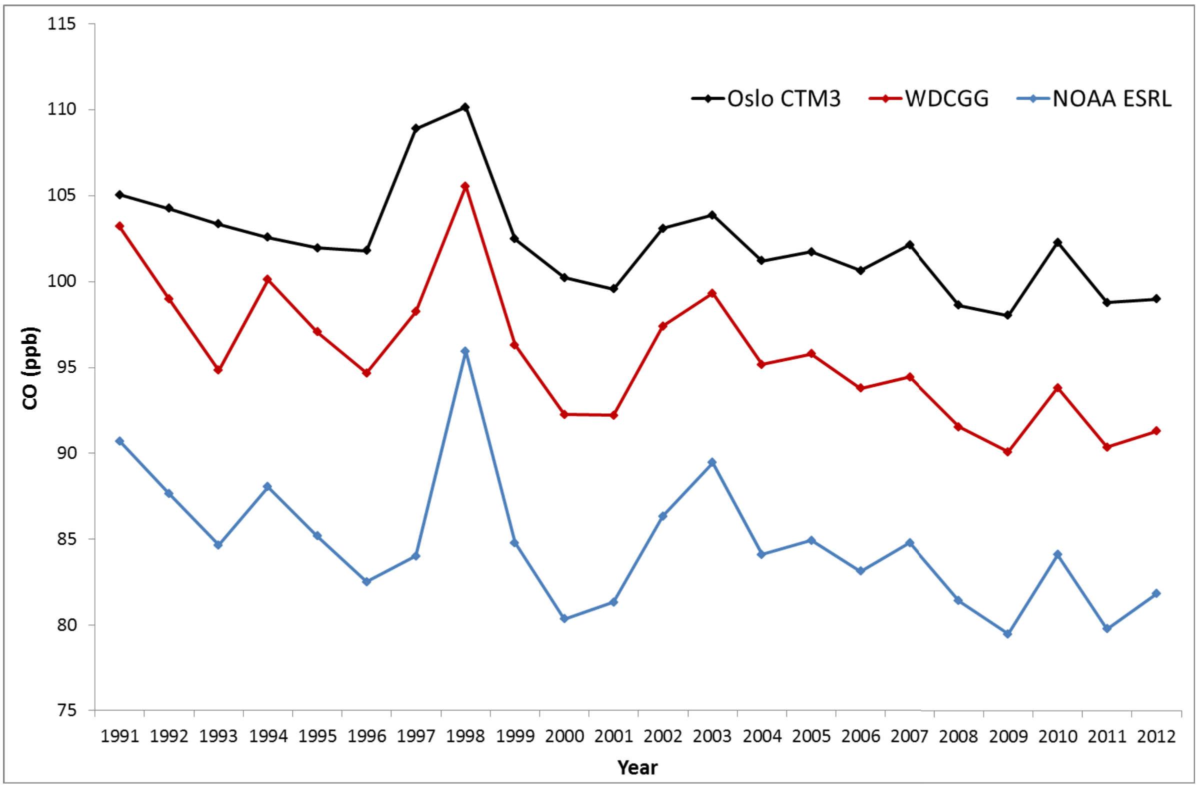

Figure S5. Comparison of model and observation based yearly global mean surface CO for the period 1991-2012. NOAA ESRL data set provided by Paul Novelli, personal communication. WDCGG data set (WMO/WDCGG/GAW (2015) provided by WDCGG, personal communication.

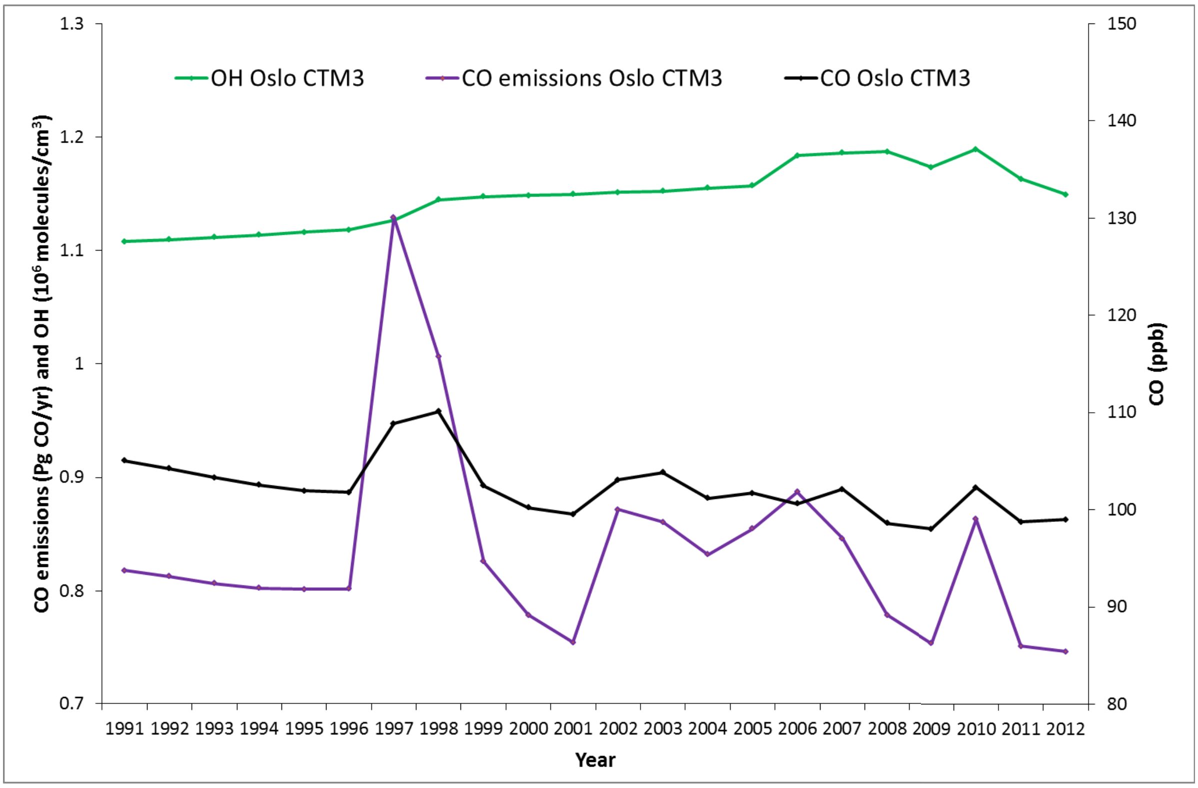

Figure S6. Yearly global average atmospheric OH concentration in the main simulation using the reaction rate with CO as averaging kernel and yearly total global CO emissions (left y-axis). Modeled global mean surface CO (right y-axis).

Acknowledgements

We thank WDCGG and Paul Novelli for providing and sharing CO datasets used in figure Figure S5.

References

Bousquet, P., Ringeval, B., Pison, I., Dlugokencky, E. J., Brunke, E. G., Carouge, C., Chevallier, F., Fortems-Cheiney, A., Frankenberg, C., Hauglustaine, D. A., Krummel, P. B., Langenfelds, R. L., Ramonet, M., Schmidt, M., Steele, L. P., Szopa, S., Yver, C., Viovy, N., and Ciais, P.: Source attribution of the changes in atmospheric methane for 2006–2008, Atmos. Chem. Phys., 11, 3689-3700, 10.5194/acp-11-3689-2011, 2011.

Guenther, A., Karl, T., Harley, P., Wiedinmyer, C., Palmer, P. I., and Geron, C.: Estimates of global terrestrial isoprene emissions using MEGAN (Model of Emissions of Gases and Aerosols from Nature), Atmos. Chem. Phys., 6, 3181-3210, 10.5194/acp-6-3181-2006, 2006.

Holton, J. R.: An introduction to dynamic meteorology, 3er edition, Academic Press, San Diego, USA, 1992

Holtslag, A. A. M., and Boville, B. A.: LOCAL VERSUS NONLOCAL BOUNDARY-LAYER DIFFUSION IN A GLOBAL CLIMATE MODEL, Journal of Climate, 6, 1825-1842, 10.1175/1520-0442(1993)006<1825:lvnbld>2.0.co;2, 1993.

Peixoto, J. P., and Oort, A. H.: Physics of climate, Springer-Verlag, New York, USA, 1992.

Seinfeld, J. H., and Pandis, S. N.: Atmospheric chemistry and physics: from air pollution to climate change, John Wiley & Sons, New York, USA, 1998

Sindelarova, K., Granier, C., Bouarar, I., Guenther, A., Tilmes, S., Stavrakou, T., Müller, J. F., Kuhn, U., Stefani, P., and Knorr, W.: Global dataset of biogenic VOC emissions calculated by the MEGAN model over the last 30 years, Atmos. Chem. Phys. Discuss., 14, 10725-10788, 10.5194/acpd-14-10725-2014, 2014.

WMO/WDCGG/GAW: Data Summary report, No.39, 2015. Available at http://ds.data.jma.go.jp/gmd/wdcgg/pub/products/summary/sum39/sum39.pdf

4.3. La naturaleza pulsante del transporte a gran escala del polvo sahariano como resultado de la interacción entre las ondas de Rossby y la Intensidad del Dipolo Norteafricano

4.3.1. Indicadores de calidad de la publicación

Indicadores de calidad de la publicación a fecha 4 de agosto de 2018, obtenidos de "Web Of Science" en el formato CVN de la FECYT.

Cuevas, E.; Gomez-Pelaez, J.; Rodriguez, S.; Terradellas, E.; Basart, S.; Garcia, R. D.; Garcia, O. E.; Alonso-Perez, S.The pulsating nature of large-scale Saharan dust transport as a result of interplays between mid-latitude Rossby waves and the North African Dipole Intensity. ATMOSPHERIC ENVIRONMENT. 167, pp. 586 - 602. PERGAMON-ELSEVIER SCIENCE LTD, 01/10/2017. ISSN 1352-2310, ISSN 1873-2844.

Tipo de producción: Artículo

Tipo de soporte: Revista

Fuente de impacto: WOS (JCR)

Categoría: Science Edition - METEOROLOGY & ATMOSPHERIC SCIENCES

Índice de impacto: 3.708

Revista dentro del 25%: Si

Posición de publicación: 16

Num. revistas en cat.: 86

Fuente de citas: WOS

Citas: 1

4.3.2. Introducción

En la sección 1.3 de esta memoria de tesis doctoral ya se introdujo la importancia del polvo atmosférico, y en particular, el papel dominante del polvo sahariano. El polvo mineral atmosférico procedente de los desiertos es el aerosol más abundante en la atmósfera tras la sal marina (Huneeus et al., 2013). Un buen conocimiento de la variabilidad a diferentes escalas espaciotemporales de los flujos de polvo salientes del Sahara, es absolutamente esencial para evaluar la variabilidad inducida por el polvo sahariano en los cambios observados en el clima, la calidad del aire, y los ecosistemas, así como para mejorar la capacidad de predicción operativa de las tormentas de polvo (Benedetti et al., 2014; Huneeus et al., 2011; Stein et al., 2015).

La emisión y transporte de polvo africano muestra una alta variabilidad temporal, desde diurna (Cuesta et al., 2009) hasta multi-decadal (Evan et al., 2016; Wang et al., 2015). La variabilidad estacional ha sido estudiada razonablemente bien en las regiones afectadas (Barnaba and Gobbi, 2004; Prospero et al., 2014, y referencias que mencionan). Tegen (2003) investigó el papel jugado por la circulación atmosférica en la variabilidad interanual de la frecuencia de activación de fuentes de polvo mineral. Las variaciones interanuales de los flujos de polvo salientes son relativamente bien conocidas para el periodo de invierno (Nakamae and Shiotani, 2013), que están fundamentalmente asociadas a la NAO (North Atlantic Oscillation; Oscilación del Atlántico Norte; Chiapello et al., 2005; Ginoux et al., 2004).

Sin embargo, solo recientemente se han realizado estudios sobre las variaciones interanuales de los flujos de polvo sahariano salientes durante el periodo de verano (Engelstaedter et al., 2009; Rodríguez et al., 2015). En esta estación es cuando la movilización de polvo sahariano muestra su máximo (Engelstaedter and Washington, 2007).

Rodríguez et al. (2015) introdujo el índice NAFDI (North African Dipole Intensity; Intensidad del Dipolo Norte Africano), que es la diferencia de las anomalías de altura geopotencial a 700 hPa (Z700) entre dos regiones norteafricanas próximas a la costa atlántica (5-8ºW): una subtropical (30-32ºN, Marruecos) y la otra tropical (10-13ºN, Bamako). Ese artículo encontró correlación a escala interanual (solo para meses de agosto) entre el índice NAFDI y la salida de polvo sahariano hacia el Atlántico subtropical. Parece por tanto razonable pensar que existe una relación entre el NAFDI y la emisión de polvo en el Sahara. Sin embargo, aquel artículo no estudió si el NAFDI tiene variaciones intra-estacionales y si éstas correlacionan con el conocido carácter pulsado de las salidas de polvo sahariano hacia el Atlántico subtropical y el Mediterráneo (Prospero and Mayol-Bracero, 2003, y referencias que contiene). En este artículo del compendio de esta tesis doctoral, identificamos los procesos atmosféricos que producen el comportamiento pulsado de las salidas de polvo del Norte de África a escala intra-estacional.

La posición e intensidad de la SHL (Lavaysse et al., 2009) es importante para entender la movilización de polvo regional porque los cambios en la SHL están asociados a procesos de activación de emisión de polvo meso-escalares como las corrientes de densidad, jets de niveles bajos, y varios fenómenos convectivos presentes en la zona de convergencia intertropical (Allen and Washington, 2013; Lavaysse et al., 2010; Marsham et al., 2013; Roehrig et al., 2011). En este artículo, nos planteamos si hay alguna relación estadística entre NAFDI y la fase de la SHL a escala intra-estacional, y en caso afirmativo, quien conduce a quien y a través de que mecanismo físico. La “fase de la SHL” hace referencia a su desplazamiento longitudinal respecto a su posición media, siendo fase Oeste (Este) aquella en la que la SHL se encuentra desplazada hacia el Oeste (Este). Chauvin et al. (2010) encontró una relación estadística entre la posición longitudinal de la SHL y las ondas de Rossby de latitudes medias (MLRWs; midlatitude Rossby waves) sobre África del Norte.

Objetivos de este estudio: 1) investigar los cambios intra-estacionales durante el verano (Junio-Septiembre; JJAS) en el transporte de polvo sobre el Sahara y las regiones de salida de África producidos por los cambios en el NAFDI; 2) identificar y analizar los procesos atmosféricos que pudieran estar conectando las variaciones del NAFDI con los cambios en la posición de la SHL; e 3) identificar y cuantificar el mecanismo físico atmosférico por el que las MLRWs pudieran estar modulando en la escala intra-estacional la fase de la SHL, y presumiblemente también las variaciones del NAFDI.

Las observaciones de satélite y los campos de reanálisis usados se detallan en la sección 2 del artículo (y en las secciones 3.3.2 y 3.3.3 de esta memoria de tesis). La sección 3 del artículo presenta los resultados principales y los analiza: relaciones entre la fase del NAFDI, patrones de transporte de polvo y campos meteorológicos, así como las interacciones físicas entre el NAFDI, la SHL y las MLRWs. La sección 4 del artículo resume las conclusiones.

4.3.3. Resumen en español del artículo

La sección 3.3 de esta memoria de tesis presenta la metodología utilizada en este estudio de transporte de polvo sahariano, que complementa los resultados obtenidos por Rodríguez et al. (2015). Ellos mostraron una variación interanual (solo los meses de agosto fueron estudiados) en los flujos de salida de polvo hacia el Atlántico Norte Subtropical (SNA) asociada a las variaciones del NAFDI.

En este estudio mostramos que NAFDI también presenta una notable variación intra-estacional. Además, para cada fase del NAFDI, hay patrones específicos a gran escala de anomalías de AOD sobre el SNA, la cuenca del Mediterráneo, y el interior del Norte de África, durante el periodo de verano, dependiendo solo débilmente del mes específico de verano. Esto apunta a que NAFDI modula los flujos de salida de polvo hacia el SNA y el Mediterráneo, alternando entre uno y otro. Para NAFDI positivo, las anomalías positivas de AOD se observan en el Sahara occidental y el SNA, mientras que para NAFDI negativo, éstas aparecen en el Sahara central-oriental y en el Mediterráneo central-occidental.

Por primera vez, se demuestra que existe una estrecha relación entre la fase Oeste (Este) de la SHL y la fase positiva (negativa) del NAFDI. El coeficiente de correlación de Pearson entre los nuevos índices diarios SHLLSI (SHL Longitudinal Shift Index, Índice de Desplazamiento Longitudinal SHL; véase la Ec. [2] del artículo) y NAFDIDI (semejante al NAFDI, pero diario en lugar de mensual; véase la Ec. [1] del artículo), para el periodo desde finales de Junio a mediados de Septiembre en el periodo 1980-2013 es 0.70. Esta correlación se incrementa hasta 0.78 cuando SHLLSI es retrasado (lagged) 1 día detrás de NAFDIDI.

Usando la ecuación de la energía de la dinámica atmosférica (Ec. [3] del artículo) y el reanálisis NCEP/NCAR, mostramos que la advección horizontal diferencial de temperatura, que es debida a la anomalía diaria de velocidad horizontal asociada a NAFDI, conduce la evolución temporal del desplazamiento longitudinal de la SHL.

Estimaciones preliminares de la emisión de polvo usando el reanálisis MACC apuntan a que los cambios en NAFDI podrían estar relacionados con la intensificación/debilitamiento de las fuentes de polvo en el Sahara central-occidental. Específicamente, el NAFDI positivo parece favorecer la movilización de polvo en el Sahara Occidental, norte de Mauritania, y Argelia central.

Las variaciones intra-estacionales del NAFDI son producidas por aquellas MLRWs que se propagan sobre el Norte de África que penetran lo suficiente en la baja troposfera. Construimos un modelo de regresión multi-lineal por mínimos cuadrados para describir el NAFDI en función del WA300 (anomalía diaria de viento zonal NCEP a 300 hPa, en m/s, con el signo invertido, en el sur de Marruecos, 10ºW, 30ºN), que cuantifica la amplitud de la onda y su fase a 300 hPa, y OM500 (Omega diario NCEP a 500 hPa, en Pa/s, sobre el norte de Argelia; 32.5ºN, 2.5ºE), que cuantifica la penetración de la onda en la baja troposfera. La correlación lineal es 0.656.

Como conclusión final resumida, los resultados de este estudio muestran que las variaciones intra-estacionales del NAFDI son provocadas por aquellas MLRWs que imponen su estado perturbado a la troposfera baja del Norte de África, y que NAFDI conduce a su vez los desplazamientos Oeste-Este de la SHL, el transporte pulsado de polvo sahariano sobre el SNA y la cuenca del Mediterráneo, y los cambios intra-estacionales en la localización espacial e intensidad de la movilización de polvo sobre el Sahara. El análisis de los procesos que producen las variaciones interanuales del NAFDI está fuera del objetivo de este artículo.

4.3.4. Artículo original en inglés

Enlace al artículo original: https://doi.org/10.1016/j.atmosenv.2017.08.059

Atmospheric Environment 167 (2017) 586–602

Contents lists available at ScienceDirect

Atmospheric Environment

journal homepage: www.elsevier.com/locate/atmosenv

The pulsating nature of large-scale Saharan dust transport as a result of interplays between mid-latitude Rossby waves and the North African Dipole Intensity

E. Cuevas [a], *, A.J. Gómez-Peláez [a], S. Rodríguez [a], E. Terradellas [b], S. Basart [c], R.D. García [a], [d], O.E. García [a], S. Alonso-Pérez [e]

[a] Izaña Atmospheric Research Centre (AEMET), c/ La Marina 20, 38001 Santa Cruz de Tenerife, Spain
[b] SDS-WAS Regional Centre (AEMET), Edificio Nexus II, c/ Jordi Girona 29, 08034 Barcelona, Spain
[c] Earth Sciences Department, Barcelona Supercomputing Centre, Edificio Nexus II, c/ Jordi Girona 29, 08034 Barcelona, Spain
[d] Air Liquide S.A., Delegación de Canarias, Plaza Industrial Valle Güímar Manz, 38500 Güímar, Santa Cruz de Tenerife, Spain
[e] Universidad Europea de Canarias, Campus de la Orotava, c/ Inocencio García 1, 38300 La Orotava, Santa Cruz de Tenerife, Spain

HIGHLIGHTS

- Saharan dust transport out of Africa shows a pulsed behaviour.
- The North African Dipole Intensity (NAFDI) modulates Saharan dust export.
- NAFDI intra-seasonal variations are driven by mid-latitude Rossby waves.
- NAFDI drives the temporal evolution of the Saharan Heat Low longitudinal shift.
- NAFDI may modulate dust emission in central-western Sahara.

GRAPHICAL ABSTRACT

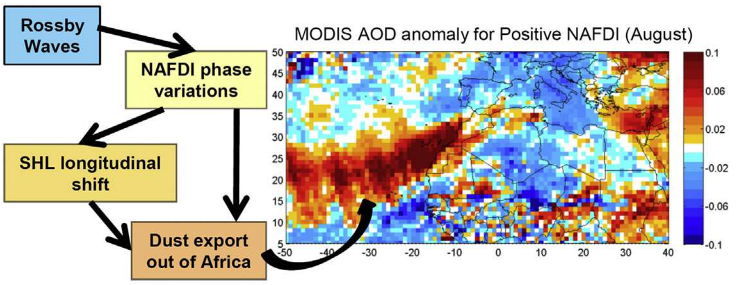

ARTICLE INFO

Article history:
Received 13 April 2017
Received in revised form
25 August 2017
Accepted 28 August 2017
Available online 30 August 2017

Keywords:
NAFDI
Rossby waves
SHL
Sahara
Dust
MODIS AOD
Atmospheric dynamics

ABSTRACT

It was previously shown that during August the export of Saharan dust to the Atlantic was strongly affected by the difference of the 700-hPa geopotential height anomaly between the subtropics and the tropics over North Africa, which was termed the North African Dipole Intensity (NAFDI). In this work a more comprehensive analysis of the NAFDI is performed, focusing on the entire summer dust season (June–September), and examining the interactions between the mid-latitude Rossby waves (MLRWs) and NAFDI. Widespread and notable aerosol optical depth (AOD) monthly anomalies are found for each NAFDI-phase over the dust corridors off the Sahara, indicating that NAFDI presents intra-seasonal variability and drives dust transport over both the Mediterranean basin and the North Atlantic. Those summer months with the same NAFDI-phase show similar AOD-anomaly patterns. Variations in NAFDI-phase also control the displacement of the Saharan Heat Low (SHL) westwards or eastwards through horizontal advection of temperature over Morocco-Western Sahara or eastern Algeria-Western Libya, respectively. The connection between the SHL and the NAFDI is quantified statistically by introducing two new daily indexes that account for their respective phases (NAFDI daily index -NAFDIDI-, and SHL longitudinal shift index -SHLLSI-) and explained physically using the energy equation of the atmospheric dynamics. The Pearson's correlation coefficient between the one–day-lag SHLLSI and the NAFDIDI for an extended summer season (1980–2013) is 0.78. A positive NAFDI is associated with the West-phase of the SHL, dust sources intensification on central Algeria, and positive AOD anomalies over this region and the Subtropical North Atlantic. A negative NAFDI is associated with the East-phase of the SHL, and positive

---

* Corresponding author.
E-mail address: ecuevasa@aemet.es (E. Cuevas).

http://dx.doi.org/10.1016/j.atmosenv.2017.08.059

AOD anomalies over central-eastern Sahara and the central-western Mediterranean Sea. The results point out that the phase changes of NAFDI at intra-seasonal time scale are conducted by those MLRWs that penetrate deeply into the low troposphere.

1. Introduction

Mineral dust from deserts is the second most important contributor to the global atmospheric aerosol burden after sea-salt aerosols (Huneeus et al., 2013 and references herein). The largest and most active dust source worldwide is the Sahara desert (i.e., Ginoux et al., 2012; Goudie and Middleton, 2001) with an emission range between 400 and 2200 Tg yr^{-1}. Dust impacts on climate (i.e. Foltz and McPhaden, 2008; Prospero and Lamb, 2003; Tegen and Torres, 2005), air quality (e.g., Prospero, 1999; Prospero et al., 2014) and health (e.g., Díaz et al., 2012; Karanasiou et al., 2012; Prospero and Lamb, 2003). The Saharan Air Layer (SAL), usually heavily laden with mineral dust, reaches regions as far away as the Caribbean and the Americas (e.g., Adams et al., 2012; Gläser et al., 2015; Perry et al., 1997; Prospero and Carlson, 1972). Dust also reaches the Mediterranean basin (Basart et al., 2009; Moulin et al., 1998) with implication even in the compliance of European air quality standards (Escudero et al., 2007; Marconi et al., 2014; Rodríguez et al., 2001). In the Sahel region, dust is associated with meningitis epidemics during the dry season (Pérez García-Pando et al., 2014; Thomson et al., 2006). Concerning ecosystems, the Saharan dust deposition fertilises the Amazon rainforest (Yu et al., 2015) and triggers marine phytoplankton growth in both the North Atlantic (Ravelo-Pérez et al., 2016) and the Mediterranean Sea (Gallisai et al., 2014), playing a key subsequent role in controlling the chemical composition of sea-water and hence in the carbon cycle (Conway and John, 2014).

Given this wide variety of impacts, a good knowledge of Saharan dust outflows variability at different spatiotemporal scales is absolutely essential to assess the variability induced by Saharan dust in changes observed in climate, air quality, and ecosystems, as well as to improve operational forecasting capabilities to predict dust storms (Benedetti et al., 2014; Huneeus et al., 2011; Stein et al., 2015).

African dust emission and transport exhibits a high variability from diurnal (Cuesta et al., 2009) to multi-decadal time scales (Wang et al., 2015; Evan et al., 2016). The seasonal variation of Saharan dust outflows has been reasonably well studied in affected regions (Barnaba and Gobbi, 2004; Israelevich et al., 2012; Prospero et al., 2014, and references therein). Tegen (2013) investigated the role of the atmospheric circulation in the inter-annual variability of dust source activation frequency. Inter-annual dust outflows variations are relatively well known in the winter period (Nakamae and Shiotani, 2013), which are mostly associated with the North Atlantic Oscillation (Chiapello et al., 2005; Ginoux et al., 2004). However, only in recent years research on inter-annual variations of Saharan dust outflows during the summer period has been carried out (i.e., Ben-Ami et al., 2009; Engelstaedter et al., 2009; Rodríguez et al., 2015). In this season Saharan dust mobilization shows its peak (Engelstaedter and Washington, 2007).

Rodríguez et al. (2015) introduced the North African Dipole Intensity (NAFDI) index, which is the difference of the 700-hPa geopotential height (Z700) anomalies averaged over the subtropical (30-32°N, Morocco) and the tropical (10-13°N, Bamako) North Africa regions close to the Atlantic coast (at 5-8°W). These authors used satellite Aerosol Index and the 28-year-long in-situ dust concentration record at the high-mountain Izaña Observatory to explain the influence of changes in the NAFDI intensity to the dust outflows from west Sahara to the tropical Atlantic in August. Note that a similar approach was applied later to account for dust transport in southwest Asia with the Caspian Sea-Hindu Kush Index (CasHKI) (Kaskaoutis et al., 2016). Since inter-annual variability in dust outflows towards the North Atlantic is observed (Rodríguez et al., 2015), it seems reasonable to expect a certain relationship between NAFDI and dust emissions over the Sahara. On the other hand, Rodríguez et al. (2015) did not determine whether the NAFDI and associated dust outflows show intra-seasonal variations whereas it is well known that dust transport occurs in the form of strong pulses along the Mediterranean-Europe-Middle-East and North-Atlantic-Caribbean-North-America routes (Guerzoni et al., 1999; Prospero, 1996; Prospero and Mayol-Bracero, 2003). In this paper we answer the following question: what atmospheric processes produce the pulsed behaviour of dust outflows observed at the intra-seasonal time scale?

It is well known that changes in the strength and location of the Saharan heat low (SHL) (Lavaysse et al., 2009) constitute a crucial issue for understanding regional dust mobilization because changes in the SHL are tightly linked to the activation of some key meso-scale processes such as density currents, low-level jets (LLJ), and severe convective phenomena present in the equatorial convergence zone (Allen and Washington, 2013; Knippertz and Todd, 2010; Lavaysse et al., 2010a; Marsham et al., 2013; Roehrig et al., 2011). Since the SHL is associated with dust mobilization processes over the Sahara and NAFDI drives Saharan dust transport out of Africa, the following questions arise: 1) Is there a statistically significant relationship between the SHL-phase changes and the intra-seasonal variations we might find in NAFDI?; 2) If so, which of them acts as a driver of the other, and through which physical mechanism? On the other hand, the SHL is also a central meteorological system associated to the West African monsoon (Sultan and Janicot, 2003), which interacts with mid-latitude circulation (Chauvin et al., 2010; Knippertz, 2008, 2010; Lavaysse et al., 2010b; Roehrig et al., 2011). However, the specific reasons that might explain the SHL shifts and changes in intensity as well as in the associated atmospheric dust loadings are still poorly understood (Engelstaedter et al., 2015). According to Chauvin et al. (2010), the longitudinal position of the SHL is linked to the propagation of mid-latitude Rossby waves (MLRWs) over North Africa. However, these authors did not explore in detail nor identify the subjacent atmospheric processes behind that statistical relation. Therefore, we wonder about the role that MLRWs might play in the intra-seasonal variability of NAFDI, and if it is possible to explain the mechanisms that control the interaction between Rossby waves and the NAFDI and SHL phases.

To properly address these questions we set the following objectives in this study: 1) investigate intra-seasonal changes in dust transport over the Sahara and outflow regions driven by changes in NAFDI during summertime (June–September; hereinafter denoted as JJAS); 2) identify and analyse the atmospheric processes which might connect NAFDI variations with changes in the SHL position; and 3) identify and quantify the atmospheric physical mechanisms by which MLRWs might modulate at intra-seasonal scale the SHL-phase, and presumably also the NAFDI variations.

The satellite-based observations and reanalysis fields used in this study are detailed in section 2. In section 3, the main results are presented and discussed: relationships between NAFDI phases and specific patterns of dust transport and meteorological fields, as well as physical interactions between the NAFDI, the SHL and MLRWs. Finally, the conclusions are summarized in Section 4.

2. Data and methodology

2.1. MACC reanalysis

The 2003–2012 MACC (Monitoring Atmospheric Composition & Climate) reanalysis has been used in the present study. This reanalysis, described in Inness et al. (2013), can be downloaded from the http://apps.ecmwf.int/datasets/data/macc-reanalysis/levtype=sfc/ site from the ECMWF (European Centre for Medium-Range Weather Forecasts). AOD at 550 nm and derived estimated instantaneous dust emission at 06, 09, 12, 15 and 18 UTC for JJAS in the period 2003–2012 have been used in our analysis. Dust emission is not provided by MACC reanalysis and has been estimated following the method described in Section 3.2.3.

A description of the reanalysis aerosol modules is provided by Benedetti et al. (2009), and Morcrette et al. (2009, 2011). The MACC reanalysis has been extensively used and validated in several studies on aerosols (Bellouin et al., 2013; Cesnulyte et al., 2014; Eskes et al., 2015; Inness et al., 2013) and mineral dust (Cuevas et al., 2015) studies.

2.2. MODIS data

The MODIS (MODerate resolution Imaging Spectrometer) provides aerosol data over both land and ocean (Kaufman et al., 1997; Tanré et al., 1997) at global scale on a daily basis.

For this study AOD (at 500 nm) monthly means from the MODIS-Collection 6 in the period 2003–2012 for JJAS have been used. MODIS-Collection 6 provides a new product, obtained by merging Deep Blue (DB) and Dark Target (DT) datasets. This new product allows to extend the coverage to bright lands as well as vegetated surfaces (Sayer et al., 2013). MODIS-Collection 6 dataset is particularly important in our analysis since large areas of the considered geographic domain (Northern Africa) show high reflectivity, where the AOD retrieval is not an easy task. MODIS-Collection 6 is available at ftp://ladsweb.nascom.nasa.gov/allData/6/.

2.3. NCEP/NCAR reanalysis

The NCEP (National Centre for Environmental Prediction) and the NCAR (National Centre for Atmospheric Research) cooperates producing reanalysed atmospheric fields for the research and climate monitoring communities (Kalnay et al., 1996).

NCEP/NCAR 6-hourly, daily, and monthly-mean data with a 2.5° lat. x 2.5° lon. resolution for JJAS, in the period 1980–2013, have been used in this study. In detail: monthly average fields of geopotential height at 700 hPa (m), wind vector and speed at 925 and 700 hPa (ms-1), and temperature at 925 hPa (K), within the 10°N-50°N, 50°W-40°E region, for the period 2003–2012 have been obtained. Monthly Omega fields at 300, 400, 500 and 600 hPa (Pas-1), and the zonal wind component at 300 hPa (ms-1) for the period 1980–2013, have been downloaded for the 5°N-70°N, 30°W-40°E domain. Monthly meridional and zonal wind components (ms-1) latitude/longitude-height cross-sections for specific longitudes/latitudes have been obtained. Monthly correlation plots between NAFDI and 200, 500, 700, 850 and 1000 hPa geopotential height fields, for the 0°N-90°N, 80°W-80°E domain, have been calculated for the period 1980–2013.

Daily NCEP/NCAR geopotential height at 700 hPa, temperature at 925, 850 and 700 hPa, Omega at 500 hPa, and zonal wind at 300 hPa, for the period 1980–2013, have been used to calculate the NAFDIDI (section 3.2.1), SHLLSI (section 3.2.1), OM500 (section 3.3) and WA300 (section 3.3) daily indexes, respectively.

NCEP NCAR reanalysis with the highest time resolution available (6-hourly, with data at 00, 06, 12 and 18 UTC), for the period 1980–2013, has been used to compute the terms of the energy-equation as explained in Supplement S7.

3. Results and discussion

3.1. Role of NAFDI in dust outflows and associated meteorological patterns

In this study we use the NAFDI concept established by Rodríguez et al. (2015). The two points chosen by those authors in the definition of the NAFDI were located over Mali and Morocco following the 7°W meridian because they wanted to analyse and characterize the transport of Saharan dust toward the North Atlantic. Since the Z700 s at these two points show a positive correlation (0.2–0.3, significant at the 80% level), the Z700 variations are not entirely independent from each other.

However, selecting the south point in the same parallel but shifted to the east (~5°E; Northern Nigeria), the flow anomaly is perpendicular to the line along which the NAFDI is computed (not shown), and therefore it can be accounted by the geostrophic wind anomaly associated to the geopotential height anomaly that defines NAFDI, and we obtain a zero correlation between the two Z700s. Therefore, in this paper, we use a new NAFDI monthly index (also called NAFDI) defined as the monthly Z700 anomaly between Morocco and Nigeria. An independent result that supports the proposed improvement is that the total in situ dust concentrations recorded at Izaña in August and the original long-term NAFDI data series in the period 1987–2014 (Rodríguez et al., 2015) present a Pearson's monthly correlation of 0.67 (significant at the 99.98% level), whereas it is equal to 0.72 (significant at the 99.997% level) with the improved NAFDI monthly index.

The new NAFDI index is used for categorizing months and subsequently average in time the associated MODIS AOD spatial fields and some dust transport-related atmospheric parameters. Specifically, we use NAFDI values for JJAS within the period 1980–2013. Taking into account the monthly-mean NAFDI value, we have classified the summer months into the following groups: negative (<-0.4), positive ($>+0.4$), and neutral (between -0.4 and $+ 0.4$) NAFDI months. Considering the distribution of absolute monthly mean values, the neutral NAFDI region is delimited approximately by the 25th percentile. The spatial correlation plots shown in the Supplement of this paper are also computed using monthly means. Therefore, the critical value for having a significant Pearson's correlation with a 95% confidence level is 0.34.

The MODIS AOD mean anomaly field for each summer month and NAFDI-phase was calculated respect to the AOD mean field corresponding to all the occurrences of that summer month in the period 2003–2012. The AOD anomaly fields for JJAS for the positive and negative NAFDI phases are shown in Fig. 1. Extensive and notable AOD anomalies, associated outflows off the Sahara are notable. For positive NAFDI a broad positive ENE-WSW axis-shaped AOD anomaly over the subtropical North Atlantic (SNA) is observed, in agreement with results from Rodríguez et al. (2015), which showed a good relationship between TOMS/OMI Aerosol Index (AI) and NAFDI for August months. This positive AOD anomaly during positive NAFDI over the SNA is rather weak and small in June, sharpening notably in July and August, while in September a

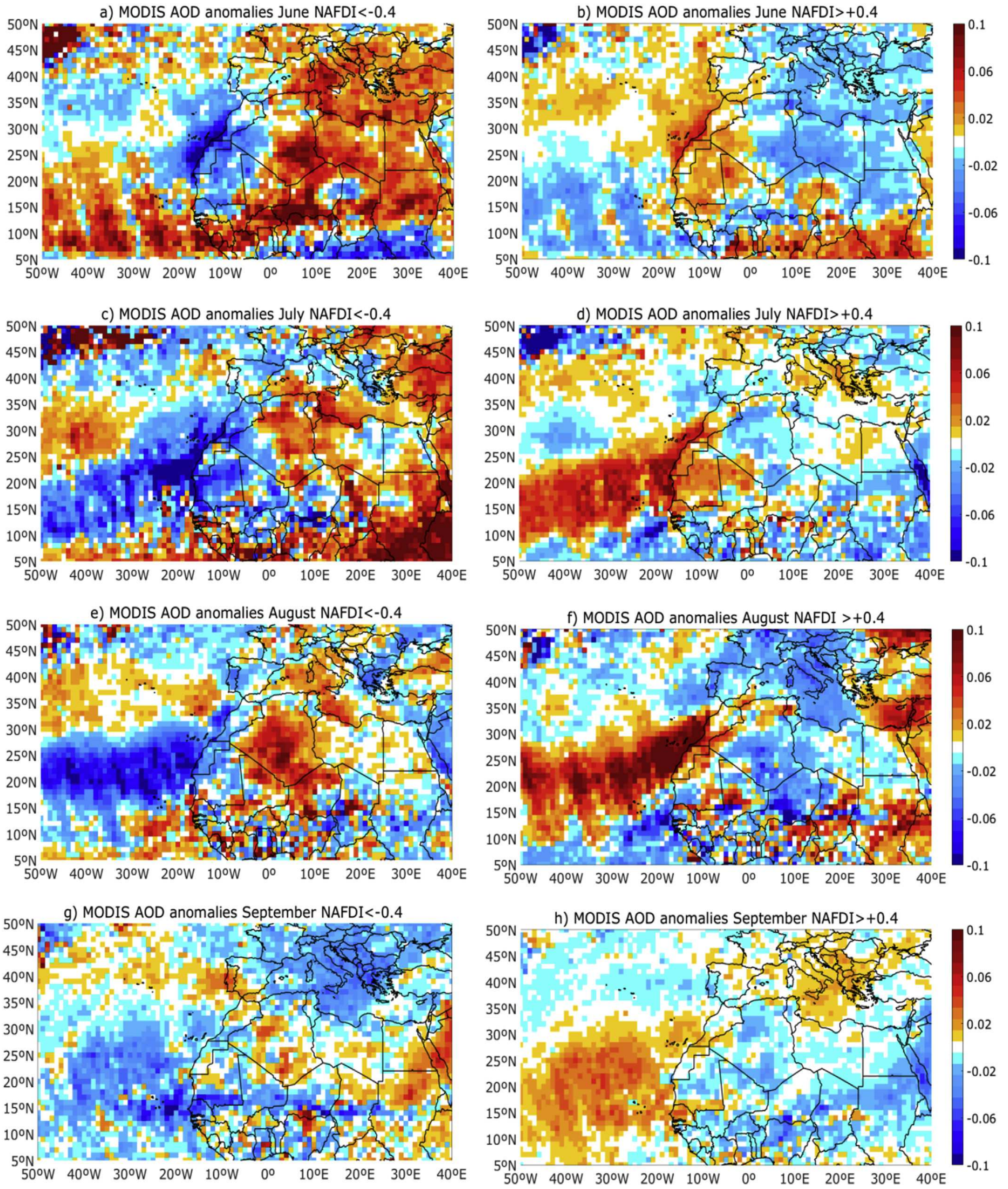

Fig. 1. AOD mean anomaly fields from MODIS (merged Deep-Blue and Dark-Target) for June, July, August, and September months with negative (a, c, e, and g) and positive (b, d, f, and h) NAFDI (2003–2012). (For interpretation of the references to colour in this figure legend, the reader is referred to the web version of this article.)

weakened contrast between positive and negative NAFDI is observed (Fig. 1).

For negative NAFDI, a second noteworthy pattern is observed in June over the tropical North Atlantic with a positive AOD anomaly, and strong negative AOD anomaly in the SNA in July and August, while September shows a neutral behaviour. A third major AOD-pattern contrast between the NAFDI phases is observed over the central-western Mediterranean (CWM) basin and southern Europe, where positive AOD anomalies are registered during negative NAFDI, and vice versa. This pattern is particularly unequivocal in June, when the highest frequencies of Saharan dust outbreaks into the CWM take place (Marconi et al., 2014).

It should be noted that within the same summer there are months showing both positive and negative NAFDI phases (intra-seasonal variation), which are also different from year to year (inter-annual variation). However, the AOD anomaly patterns are similar for all the summer months with the same NAFDI phases. This suggests that the observed dust transport patterns may be driven by NAFDI, since the latter is associated with the large-scale wind anomaly in the lower troposphere over North-Western Africa. This relationship complements and extends previous results from Rodríguez et al. (2015). Moreover, we find positive AOD anomalies over central-western Sahara (CWS) dust sources, particularly over Algeria (Fig. 1) for positive NAFDI. The opposite is found for negative NAFDI. AOD anomalies from MACC reanalysis have been also obtained for each summer month in the same way as done for MODIS. The results, not taking into account small-scale details and the exact signal intensity, are quite similar to those obtained with MODIS for each NAFDI-phase (see Supplement S2). In the Sahel, the summer period is the rainy season in which frequent short-term convective meso-scale processes that raise huge amounts of dust take place (Marticorena et al., 2010). The high frequency of convective clouds in summertime in this region also implies a significantly lower daily AOD data availability, which may be the cause of the spatially highly variable means for both NAFDI phases over this region, in spite of the fact there is no significant (spatially consistent) correlation with NAFDI. If we take into account the fact that AOD positive anomalies over the SNA normally match up low AOD over the CWM, and vice versa, we can hypothesize that the same meteorological driver favours Saharan dust transport toward one region or another. Considering that Z700 is the most effective level for dust transport over the SNA (Rodríguez et al., 2015, and references therein), we explored the Z700 patterns corresponding to each NAFDI-phase. In June, July and August, and slightly less in September, we observe marked differences in the Z700 patterns corresponding to each phase (Fig. 2), with a significant strengthening of Z700 over Morocco for positive NAFDI. During negative NAFDI a deep SW-NE axis-shaped trough extends from the western edge of Europe and North Africa to the SNA.

This trough displaces further away the Azores high, which also become slightly elongated to the NE, from the North African high (at 700 hPa), being located the latter in a more Eastern position over the continent. Conversely, during the positive NAFDI-phase both anticyclones strengthen and get closer at 700 hPa, merging into an apparent single huge Azores high extending over much North Africa. Gkikas et al. (2015) found a quite similar pattern, which accounts for, leastwise, 50% of all mineral dust intrusions in the entire Mediterranean basin (Cluster#2). The Z700 pattern found under negative NAFDI also agrees with that proposed by Varga et al. (2014) when discussing Saharan dust outbreaks into the CWM basin. The deeper trough present during negative NAFDI over the eastern North Atlantic at 700 hPa is also observed at other levels. Monthly correlation plots between the geopotential height fields, ranging from 200 to 1000 hPa, and NAFDI for summer months have been calculated (see Supplement S3). These plots show very similar correlation patterns at standard 850, 700, 500 and 200 hPa levels, and even vaguely at 1000 hPa. All these facts suggest that the NAFDI variations at intra-seasonal scale might be driven by MLRWs. The relationship between the NAFDI and MLRWs is addressed in Subsection 3.3.

The NCEP/NCAR monthly averaged wind plots at 700 hPa (Fig. 3) show relatively strong NE/ENE winds over the Western Sahara, northern Mauritania and central Algeria that extends into the SNA for positive NAFDI, mainly in July and August. This increase in north-easterly wind component over these regions for positive NAFDI is clearly seen in the wind anomalies at 700 hPa shown in Supplement S1. These results agree with the positive AOD anomaly detected by MODIS on these regions (Fig. 1).

Under negative NAFDI we observe an increase in airflow from North Africa to CWM and, simultaneously, stronger westerly winds over the Mediterranean region. The same consistency over time is observed for the period July–August 1980–2013 from monthly correlation fields between NAFDI and 700 hPa meridional (impact on the Mediterranean basin) and zonal (impact on the SNA) wind components (not shown here). Correlations between 700-hPa zonal wind and NAFDI of −0.7 are found over Western Sahara, Northern Mauritania, and central Algeria. Correlations between NAFDI and meridional wind of −0.7 are found over north-eastern Algeria, Tunisia and north-western Libya. These results indicate that the good correlations between NAFDI and the zonal wind toward the Atlantic Ocean and the meridional component toward the Mediterranean Sea constitute a permanent feature maintained over decades.

The associated 700-hPa wind field is weak over the CWS (Algeria and Western Sahara) in June and September (Fig. 3a, b, g and h) whereas in July and August it intensifies significantly with a clear easterly component during positive NAFDI (Fig. 3c, d, e and f). This is the reason for which the marked contrast between the AOD patterns for positive and negative NAFDI in July and August over the SNA is not observed in June and September.

The longitudinal variation of the zonal wind component in a vertical cross-section along 28°N, calculated from NCEP/NCAR reanalysis (Fig. 4), shows that in June the westerlies dominate (positive values) above the coast of Africa under both NAFDI phases, greatly hindering the transport of dusty air masses from the CWS convective boundary layer (CBL) (Cuesta et al., 2009) to the SNA. The same situation is found for the rest of the summer months under negative NAFDI. However, under positive NAFDI, in July and August, and to a lesser extent in September, the easterlies (negative zonal wind component) dominate from 700 to 900 hPa, favouring westwards intrusions of the SAL, and hence, transport of dusty air masses over the SNA. It should be noted that 28°N is the latitude of the Izaña Observatory where Rodríguez et al. (2015) observed in the free-troposphere maximum in-situ dust levels for positive NAFDI.

Concerning the Mediterranean basin, the latitudinal variation of the meridional wind component in a vertical cross-section along 9°E, calculated from NCEP/NCAR reanalysis (Fig. 5), shows that a predominant northerly wind component restrains the arrival of Saharan air masses into the CWM basin under positive NAFDI. Conversely, dust outbreaks into the CWM are favoured under negative NAFDI because of the existence of a dominant Southerly wind component above 900 hPa in June, which is also observed to a lesser extent in July and August, and very weakened in September. This result agrees with other studies that characterize the vertical structure of the SAL over the CWM (Marconi et al., 2014; Mona et al., 2006).

3.2. Statistical and physical connections between the NAFDI and the Saharan heat low longitudinal shift

We have found for each NAFDI phase specific spatial patterns of

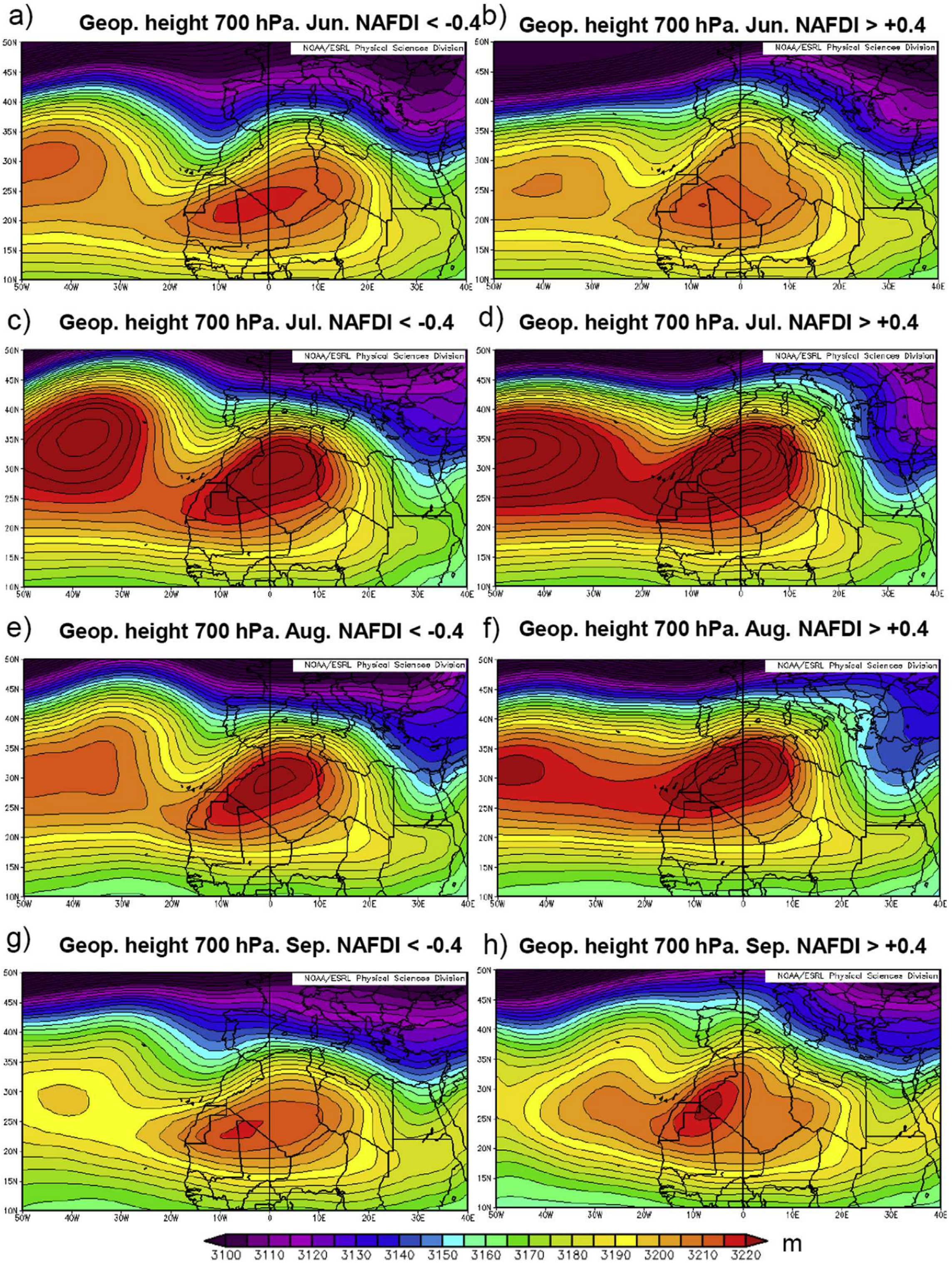

Fig. 2. Z700 (m) means for June, July, August, and September months with negative (a, c, e, and g) and positive (b, d, f, and h) NAFDI (2003–2012) from NCEP/NCAR reanalysis.

several key meteorological variables, which are quite similar to those found in Chauvin et al. (2010) for the SHL West and East phases, suggesting there could be a physical connection between the NAFDI and the location of the SHL. The most noteworthy are: 1) the location and spread of the Azores high; 2) the 925-hPa temperature anomaly over the Western Sahara and most of Morocco (Fig. 6); 3) the low-level winds over Libya, Morocco and Western Sahara.

There are some more indications about the relationship between NAFDI variations and longitudinal displacements of the SHL: when NAFDI is negative, the oceanic low-level (925 hPa) relatively-cold (compared with the surrounding area) southward flow reaching North Africa within the 10°W-20°W band (shown in Supplement S4) penetrates deeper in North Africa and comes from

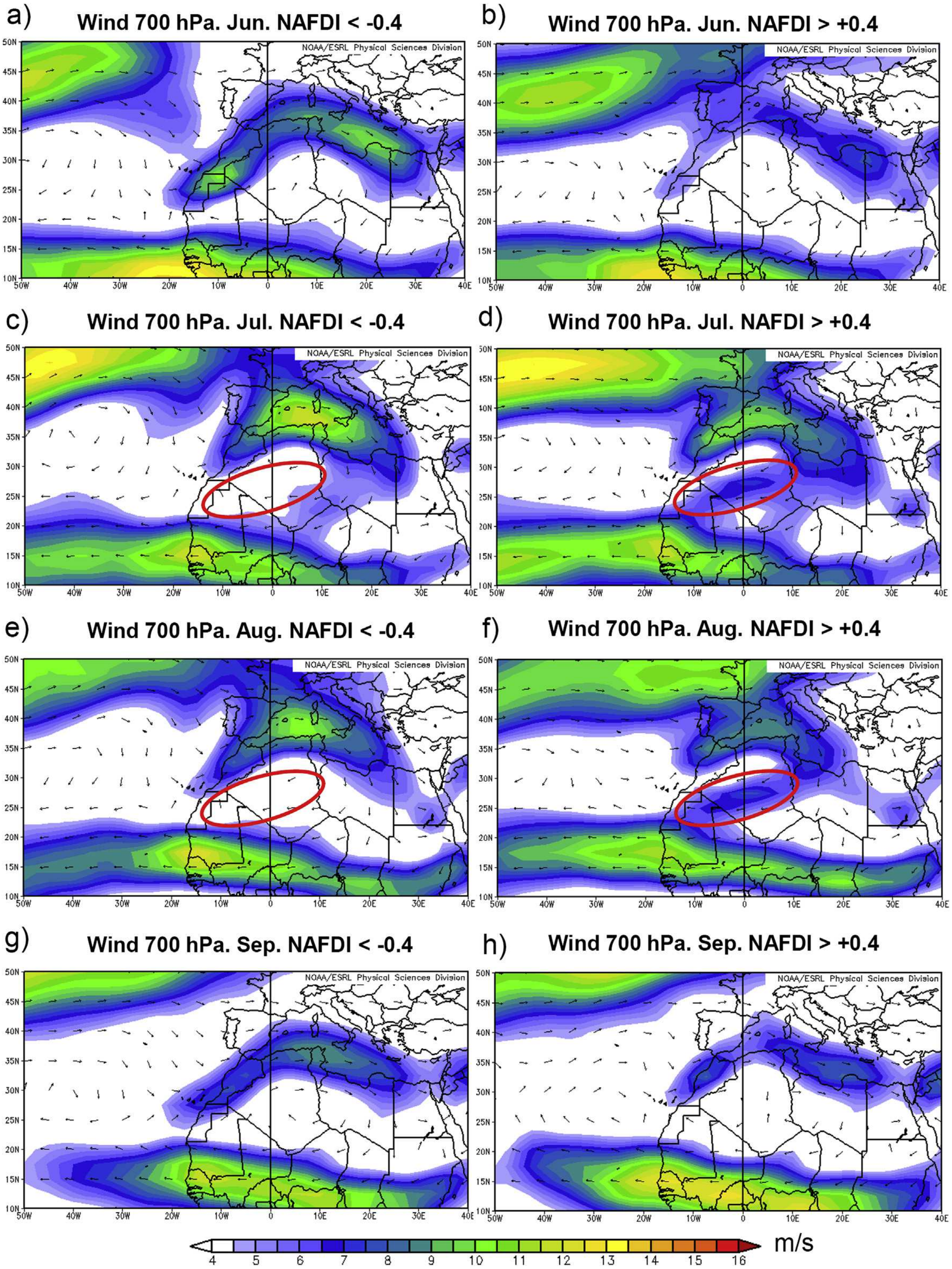

Fig. 3. 700-hPa wind (m s-1) means for June, July, August, and September months with negative (a, c, e and g) and positive (b, d, f and h) NAFDI (2003–2012) from NCEP/NCAR reanalysis. Encircled in red is the region comprising the Western Sahara, northern Mauritania and central Algeria where strengthened NE/ENE winds are observed in July and August for positive NAFDI. (For interpretation of the references to colour in this figure legend, the reader is referred to the web version of this article.)

more northern latitudes. This flow produces a negative geopotential-thickness advection that causes a deep trough (Fig. 2), and cools the land surface over Morocco and Western Sahara (Fig. 6). This scenario likely contributes to maintain the SHL in its East phase. This is in agreement with finding a negative anomaly of the CBL height over Western Sahara and Morocco, and a positive CBL-height anomaly over eastern Algeria and north-western Libya for negative NAFDI (shown in Supplement S5).

The striking connection between the SHL and NAFDI phases is quantified and explained physically in this subsection.

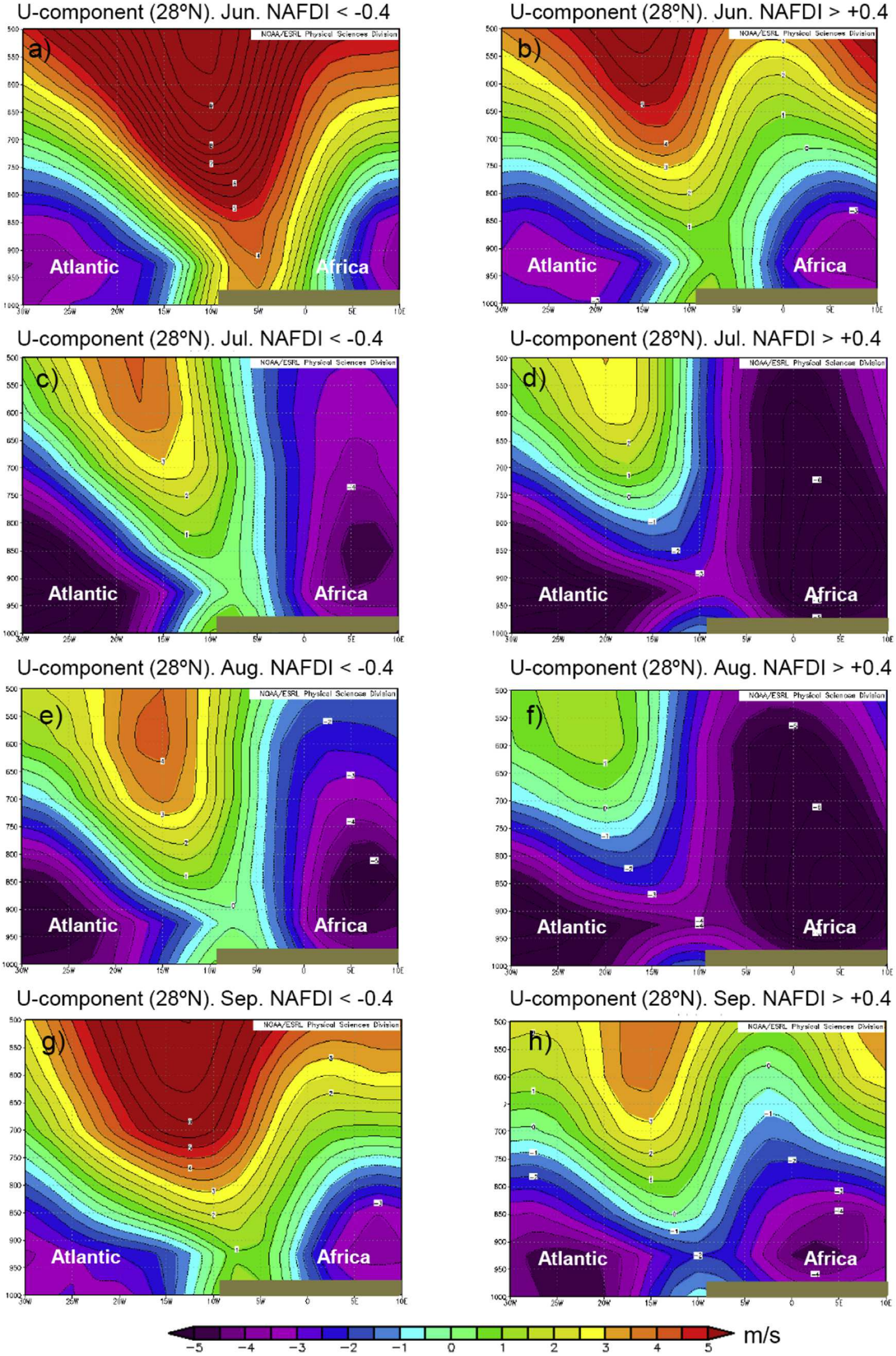

Fig. 4. Mean-zonal-wind-component (m s-1) longitude-height cross-sections along 28° N (CWS and SNA) for June, July, August, and September months with negative (a, c, e, and g) and positive (b, d, f, and h) NAFDI (2003–2012) from NCEP/NCAR reanalysis.

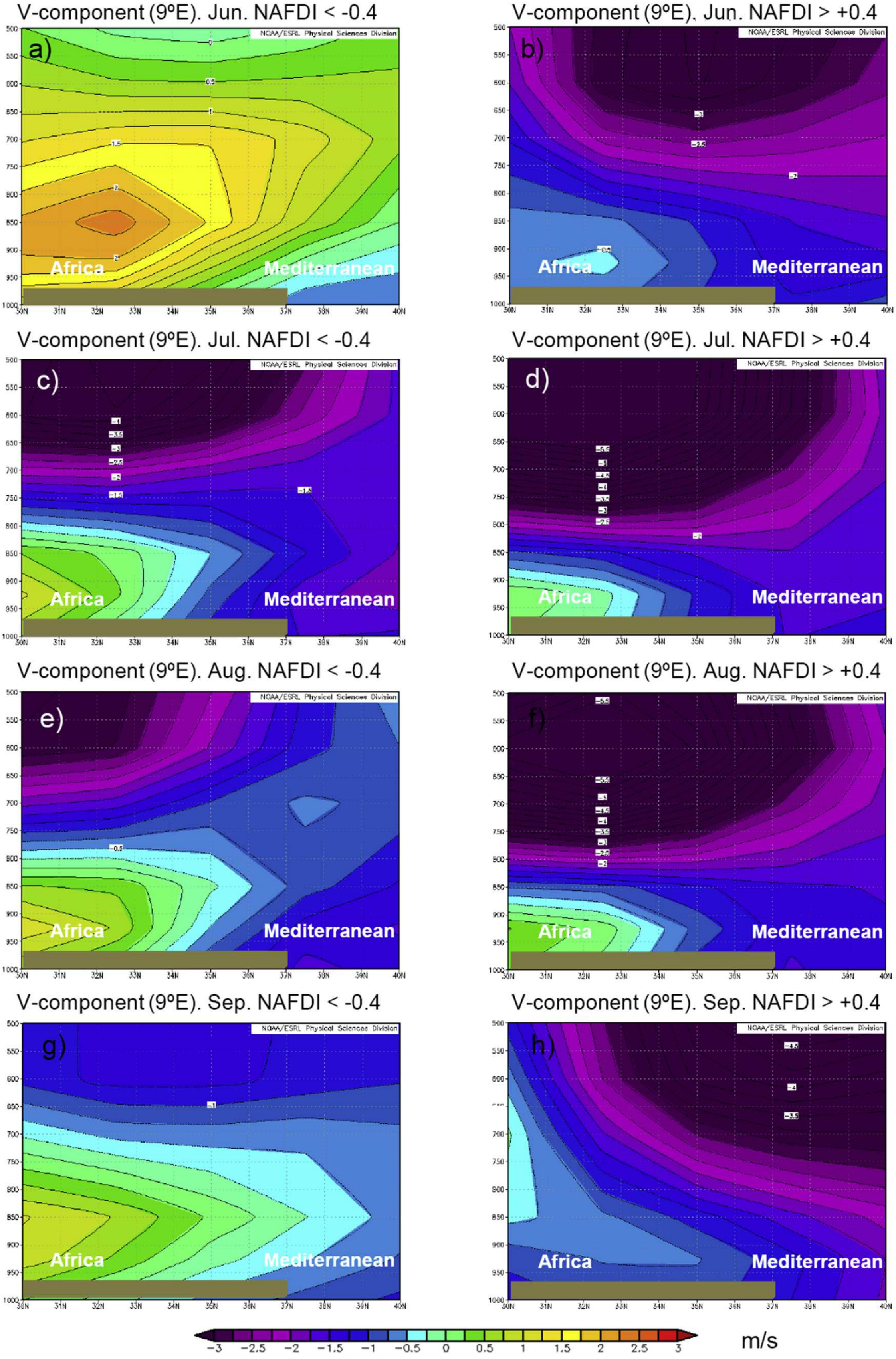

Fig. 5. Mean-meridional-wind-component (m s-1) latitude-height cross-sections along 9°E (Northern Africa and CWM) for June, July, August, and September months with negative (a, c, e, and g) and positive (b, d, f, and h) NAFDI (2003–2012) from NCEP/NCAR reanalysis.

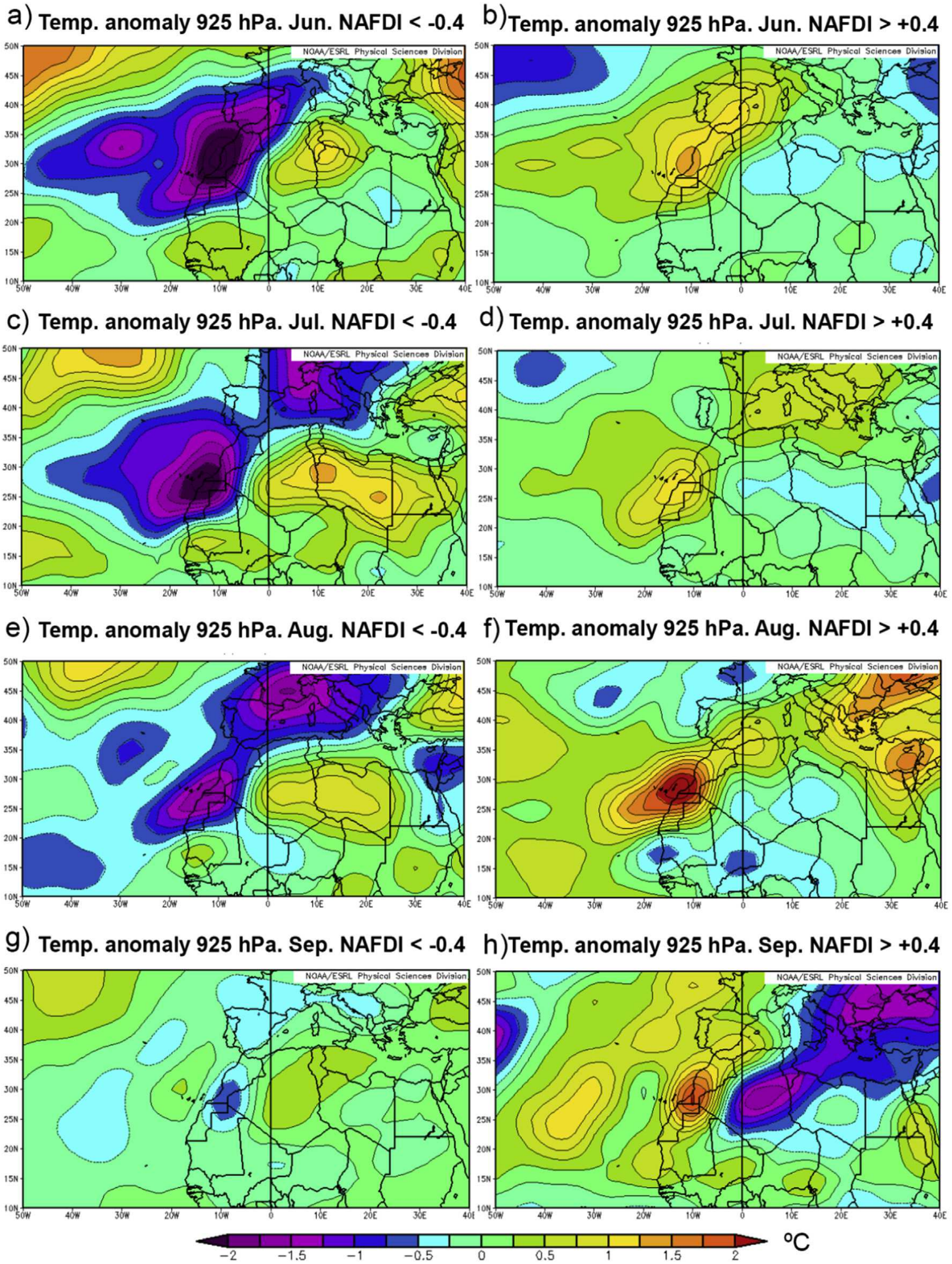

Fig. 6. Mean 925-hPa temperature anomaly (K) for June, July, August, and September months with negative (a, c, e, and g) and positive (b, d, f, and h) NAFDI (2003–2012) from NCEP/NCAR reanalysis.

3.2.1. Statistical relationship between NAFDI and SHL

Lavaysse et al. (2009) defined the WAHL (West African Heat Low) location using the Low-Level Atmospheric Thickness (LLAT), where low-level means the pressure range 925–700 hPa. The LLAT depends linearly on the air average temperature between those pressure levels. Lavaysse et al. (2013) determined the longitudinal shift of the SHL (see their Fig. 5c and d) performing an Empirical Orthogonal Function analysis (EOF) carried out exclusively in the region where the SHL uses to be during the summer, being the time frequencies associated to the displacement higher than 1/25 day^{-1}.

Below it is shown that the evolution in time of the NAFDI and the longitudinal shift of the SHL are tightly linked on a daily basis. Positive NAFDI corresponds to the SHL West-phase, and negative NAFDI to the SHL East-phase.

Firstly, we compute a NAFDI daily index we call NAFDIDI for the 20 Jun. - 17 Sept. period using the NCEP reanalysis for the years 1980–2013. This period corresponds to the SHL period when the WAHL is located above the Sahara desert, according to Lavaysse et al. (2009). The daily index NAFDIDI is calculated as follows:

$$NAFDIDI = \frac{1}{10}((\Phi_{Mo} - <\Phi>_{Mo}) - (\Phi_{Ni} - <\Phi>_{Ni})) \qquad (1)$$

where,

- Φ is the NCEP/NCAR daily average Z700 (m) for the considered day, at 5°W, 30°N (central Morocco) when the sub-index *Mo* is used, and at 5°E, 12.5°N (north Nigeria) when the sub-index *Ni* is used.
- $< >$ denotes mean of the geopotential height (m) for the corresponding day of the year throughout 1981–2010 (reference period), and then applying a 29-day running average to the mean, for smoothing out the aleatory residuals.

It has also been introduced the daily SHL Longitudinal Shift Index (SHLLSI) as:

$$SHLLSI = \sum_n \frac{w_n}{3}[(T_{Wn} - <T_{Wn}>) - (T_{En} - <T_{En}>)] \qquad (2)$$

where T_{Wn} is the air temperature (K) at the pressure level n, 12.5°W and 25°N, T_{En} is the air temperature (K) at the level n, 7.5°E and 20°N, and the operator $< >$ has defined in the previous paragraph (now applying on temperature instead of geopotential height). Those coordinates were chosen employing the locus of the minimum and maximum of the dipolar pattern corresponding to the SHL-location eigenvector shown in Fig. 5c of Lavaysse et al. (2013). The pressure levels n at which the summation is performed are 925, 850 and 700 hPa, in agreement with the pressure range 925–700 hPa used by Lavaysse et al. (2013) to identify the location of the SHL. The weights w_n are 0.5 for 925 hPa, 1.5 for 850 hPa, and 1 for 700 hPa, and were obtained integrating using the trapezoidal rule.

The close relationship between the daily SHLLSI and NAFDIDI for the 20 Jun.–17 Sept. 1980–2013 period (hereinafter denoted as 1980–2013 period) is shown in Fig. 7.

Fig. 7 also shows that the East-phase SHLLSI values (negative NAFDIDI) use to be greater in absolute value (and more infrequent) than the corresponding to the West-phase (positive NAFDIDI). The Pearson correlation coefficient (hereinafter, Pearson's r) between the daily SHLLSI and NAFDIDI is 0.70 (significant at the 99.999% level; see Supplement S6 for a description of the method used to compute confidence levels). We computed also the Pearson's r between the SHLLSI time series and the eigenvalue time series (shown in Fig. 6c of Lavaysse et al., 2013) associated to the mentioned EOF for the 2007–2011 period (for the same summer period as in the present paper), finding a r = −0.74. The negativity sign comes since Lavaysse et al. (2013) considered as positive the SHL East-phase.

We have explored the causality of the relationship between the

Table 1
Time-lagged Pearson's r between the SHLLSI and NAFDIDI for the 1980–2013 period. “Time lag” (in days) means the SHLLSI lag behind the NAFDIDI.

Time lag	Pearson's r
−1	0.515
0	0.702
1	**0.783**
2	0.718
3	0.563

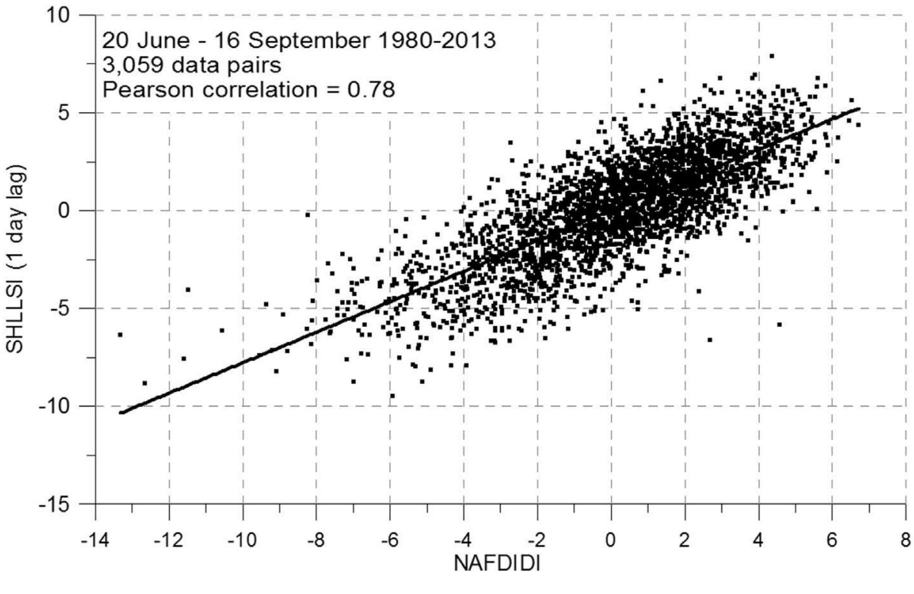

Fig. 7. NAFDIDI vs. SHLLSI one-day lagged for the summer period 1980–2013. The Pearson daily correlation value (0.78) is significant with a 99.999% confidence level.

NAFDIDI and the SHLLSI computing the Pearson's r with time-lag between them for the 1980–2013 period. Time-lag Pearson's r are shown in Table 1. The larger Pearson's r, 0.78 (significant at the 99.999% level), is obtained when the SHLLSI is 1-day lagged after the NAFDIDI. The correlation is even higher (0.864) if the one-day time-lagged correlation is performed after applying to both time series a 5-day running average. However, the Pearson's r is < 0.52 when NAFDIDI is lagged 1 day after the SHLLSI, which is actually lower than that obtained when the SHLLSI is lagged 3 days after the NAFDIDI (Table 1). There is a confidence level of 92.9% about the fact that the one-day lagged correlation is significantly larger than the no lagged correlation (the method used to compute confidence levels is described in Supplement S6). These results indicate that NAFDI changes occur before the displacement of the SHL.

The different monthly behaviour concerning dust transport in June and September compared with July and August, observed in Sect. 3.1, might be also caused by a combination of the following two facts: 1) the SHL is only present during 10 days of June and 17 days of September; and 2) the SHL is located in a more south-eastern position during June and September (e.g., Fig. 4 of Lavaysse et al., 2009).

3.2.2. Physical mechanics by which NAFDI drives the SHL longitudinal shifts

In this sub-section we show, using the energy equation of the atmospheric dynamics and the NCEP/NCAR reanalysis, that NAFDI drives SHL longitudinal displacements through horizontal advection of temperature. The energy equation in pressure coordinates (e.g., Holton, 1992) is:

$$\frac{\partial T}{\partial t} = -\boldsymbol{v}\cdot\nabla_p T - \omega T\frac{\partial \ln\theta}{\partial p} + \frac{J}{c_p}, \tag{3}$$

where $\boldsymbol{v}$ is the horizontal velocity, p is the pressure, θ is the potential temperature, ω is the vertical velocity in pressure coordinates, J is the diabatic heating per mass unit, and c_p is the specific heat at constant pressure. This equation indicates that the variation in time of the temperature at a fixed Eulerian grid point is due to the horizontal advection of temperature, the temperature tendency due to omega and the diabatic heating. Note that the temperature tendency due to omega indeed contains the vertical advection of temperature and the adiabatic heating associated to the pressure changes.

Combining Eqs. (2) and (3), the following equation for the time evolution of the SHLLSI is obtained, which involves variables and gradients at the two geographical points used to define the SHLLSI denoted with the sub-indexes W and E and the three pressure levels n (925, 850 and 700 hPa):

$$\frac{\partial SHLLSI}{\partial t} = HAdv + Ome + Diab - \sum_n \frac{w_n}{3}\frac{\partial(<T_{Wn}> - <T_{En}>)}{\partial t}, \tag{4}$$

where

$$HAdv = \sum_n \frac{w_n}{3}\left(-\boldsymbol{v_{Wn}}\cdot\nabla_p T_{Wn} + \boldsymbol{v_{En}}\cdot\nabla_p T_{En}\right), \tag{5}$$

and

$$Ome = \sum_n \frac{w_n}{3}\left(-\omega_{Wn}T_{Wn}\frac{\partial \ln\theta_{Wn}}{\partial p} + \omega_{En}T_{En}\frac{\partial \ln\theta_{En}}{\partial p}\right), \tag{6}$$

Table 2
Mean anomaly of the terms of Eq. (4) for different regions of the "phase space" with axes SHLLSI and its time derivative (see the main text of the paper).

Stage	*HAdv* (K/day)	*Ome* (K/day)	*Diab* (K/day)
Transition from East to West	1.08	0.04	0.81
Building West	2.30	−0.89	0.50
West Equilibrium	1.50	−1.26	−0.21
Decreasing West	0.50	−1.47	−0.91
Transition from West to East	−1.12	−0.40	−0.45
Building East	−3.06	1.51	−0.60
East Equilibrium	−1.47	1.47	0.02
Decreasing East	0.03	1.43	0.57
Neutral equilibrium	0.31	−0.48	0.13

$$Diab = \sum_n \frac{w_n}{3}\left(\frac{J_{Wn} - J_{En}}{c_p}\right). \tag{7}$$

Equation (4) indicates that the variation in time of the SHLLSI is due to the differential, West minus East, horizontal advection of temperature (*HAdv*), the differential temperature tendency due to omega (*Ome*), the differential diabatic heating (*Diab*), and the variation in time of the climatological reference temperatures used in the SHLLSI definition (see Eq. (2)).

We have computed each of the terms in Eq. (4) at 6-hourly timescale for the 1980–2013 period and thereafter obtained daily averages (see details in Supplement S7). The contribution of the last term of Eq. (4) is negligible. We have computed the mean anomaly of each term of the Eq. (4), for different regions of the "phase space" delimited by the tertiles of SHLLSI and the quartiles of its time derivative (Table 2). Tertiles are appropriate for SHLLSI since they split the phase space in (significant) East, neutral and West phases, however for its time derivative we use quartiles since they allow distinguish between strong change rates (extreme quartiles) and weak change rates (central quartiles), which we consider as representative of states of quasi-equilibrium. Extreme quartiles are considered as indicative of transitions between phases when the phase is neutral, and as indicative of building or decreasing of a phase when the phase is not neutral. Table 2 follows this nomenclature and avoids indicating explicitly the tertiles and quartiles for easiness of reading and interpretation.

The differential horizontal advection of temperature (*HAdv*) drives the departure of SHLLSI from its neutral position ("Building" stages in Table 2). Quasi-stationary extreme SHLLSI phases ("Equilibrium" stages in Table 2) are possible due to the building up of a negative feedback (mainly in *Ome*) that tends to restore SHLLSI to its neutral phase. Once the driver starts to diminish, the negative feedback restores SHLLSI to its neutral position ("Decreasing" stages in Table 2). This interpretation is also supported by the statistics presented below.

We define the "driving stage" as the time periods in which SHLLSI >0 and its time derivative is in the 4th quartile, or SHLLSI<0 and its time derivative is in the 1st quartile. On the other hand, we define the "restoring stage" as the time period in which SHLLSI<0 and its time derivative is in the 4th quartile, or SHLLSI>0 and its time derivative is in the 1st quartile. During the "driving stage" the daily Pearson correlation between the time derivative of SHLLSI and HAdv is 0.740 (significant at the 99.999% level), while the correlation between SHLLSI and (Diab + Ome) is −0.072 (not significant). On the contrary, during the "restoring stage", the daily Pearson correlation between the time derivative of SHLLSI and (Diab + Ome) is 0.647 (significant at the 99.97% level), while the correlation between SHLLSI and HAdv is 0.160 (not significant).

Now the question is, what drives HAdv? Below it is shown that the answer is the NAFDI. The daily Pearson correlation between NAFDIDI and: a) *HAdv* is 0.612 (0.767 under the "driving stage";

both correlations are significant at the 99.999% level), b) (*Ome + Diab)* is −0.471 (significant at the 99.999% level). This suggests that *HAdv* is driven by the daily horizontal velocity anomaly associated to NAFDI, which has been obtained by fitting the daily velocity as a linear function of NAFDIDI, for the full period considered. Note that, in essence, NAFDI is a large-scale geostrophic wind anomaly. In order to confirm this hypothesis, we have computed a *synthetic HAdv* using the daily wind anomaly associated to NAFDIDI and the mean climatological temperature gradient. The daily correlation between *HAdv* and this *synthetic HAdv* is 0.767 under the "driving stage". This indicates that NAFDI drives the time variation of the SHL longitudinal shift through horizontal advection of temperature. Moreover, the daily correlation between NAFDIDI and the time derivative of SHLLSI is 0.770 under the "driving stage" (for all the stages: 0.260, which is significant at the 99.8% level). Finally, the daily correlation between SHLLSI and its time derivative during the "restoring stage" is −0.745 (0.000 for all the stages), which is significant at the 99.999% level and supports the existence of the negative feedback that tends to restore SHLLSI to its "neutral stage".

3.2.3. Possible impact on dust sources activation over the CWS

Saharan dust sources are basically found in the many interior drainage basins that exist in this vast desert (Ginoux et al., 2012; Middleton and Goudie, 2001; Prospero et al., 2002; Schepanski et al., 2007). Dust sources in the Sahara are principally triggered by LLJs associated to the Harmattan wind and the West African Monsoon wind field (Allen and Washington, 2013; Conway and John, 2014), which are modulated somehow by intensity changes and longitudinal shift of the SHL (e.g. Couvreux et al., 2010; Lavaysse et al., 2010a,b), and the latter, in turn, by variations of NAFDI.

The MODIS AOD anomaly fields show that, a substantial increase of dust over the western-most part of the CWS is observed under positive NAFDI (SHL West-phase; see Fig. 1), while the opposite occurs with negative NAFDI. However, from only AOD data it is not possible to differentiate between dust emitted locally and dust advected from other source regions.

Considering the above, and as a preliminary approach, we have calculated dust emissions in order to ascertain whether NAFDI and SHL-phase changes exert a potential impact on intensification or abatement of dust sources in different regions of the Sahara at large scale. Following a relatively simple approach for the dust emission estimation (e.g., Gillette and Passi, 1988; Morcrette et al., 2009; Tegen and Fung, 1994), we have computed the instantaneous emission (E) at the hours 00, 06, 12 and 18 GMT, using the following equation:

$$E = SV_{10}^{2}(V_{10} - V_{T}) \tag{8}$$

where S is the dust emission potential (Morcrette et al., 2009), V_{10} is the wind velocity at 10-m height, and V_T is a dust-raise threshold wind velocity set to be 6.5 ms^{-1} (Helgren and Prospero, 1987; Takemura et al., 2000), obtained from MACC reanalysis. Then, we have computed averages for each summer month and each phase of NAFDI. The dust emission patterns agree (Fig. 8) quite well with the multi-model mean June–September dust emission distribution from 14 global models contributing to the fifth Coupled Model Intercomparison Project (Todd and Cavazos-Guerra, 2016).

The main differences in dust emissions over the CWS between the positive and negative NAFDI phases for each month are described below. In June, for negative NAFDI (Fig. 8a), there is an increase in Chotts el Jerïd and Melrhir (northeast of Algeria and Tunisia) marked as region 1 in Fig. 8), which are known relevant dust sources (Ginoux et al., 2012; Rodríguez et al., 2011). This is consistent with the abundant dust outflow towards the Mediterranean Sea for this month under negative NAFDI (Fig. 1a). There is a notable activation of the Grand-Erg Occidental dust source, identified by Ginoux et al. (2012), during positive NAFDI for all months (region 2; Fig. 8). This agrees with significant dust mobilization under positive NAFDI in the so-called Subtropical Saharan Stripe region (Rodríguez et al., 2015). Quite similar emissions in the Tiris Zemmour region (Western Sahara; region 3, Fig. 8) during both NAFDI phases are observed.

The CWS was the object of a detailed dust-source study carried out by Ashpole and Washington (2013) in two specific regions: the TP (Algeria-Mali-Niger triple-point border) and the MAB (northern Mali-Algeria border), both marked in Fig. 8. They observed that the SHL is more frequently found over central and southern Algeria (SHL East-Phase) when dust appears in the proximities of the TP, while when dust is predominantly in the MAB, the SHL is normally found over northern Mauritania, northwest Mali, and westernmost Algeria (SHL West-phase). The averaged emissions we have computed clearly agree with Ashpole and Washington (2013) in the MBA case, whilst for the TP region the agreement is not so clear. Most likely, MACC underestimates dust emissions in TP because most of the dust raised on this region in summertime is caused by mesoscale convective systems, as reported by Marticorena et al. (2010), which MACC cannot reproduce well (Cuevas et al., 2015).

These preliminary rough estimates on dust emissions suggest that changes in NAFDI might be also related with the intensification/weakening of dust sources in the CWS. However, further accurate analysis using more complex high-resolution dust emission modelling are needed to confirm these results. Similar to these results in the Sahara, Kaskaoutis et al. (2017) found with model simulations that high CasHKI modes are associated with higher dust emissions and concentrations over the South West Asia.

3.3. Connection between mid-latitude Rossby waves and NAFDI

Using NCEP2 reanalysis, Chauvin et al. (2010) carried out EOF analyses to the potential-temperature field at 850 hPa over a North African region. They observed that the arrival to southwest Europe and northwest Africa of MLRWs propagating along the North-Atlantic-North-African waveguide drives, someway, the SHL phases. Here we show that the intra-seasonal geopotential height variations at synoptic scales associated to NAFDI seem to be indeed the changing lower-level state imposed by the MLRWs propagating along the upper troposphere. We have already mentioned in Sect. 3.1 that the Z700 pattern associated to NAFDI is also present at the pressure levels 850, 500 and 200 hPa (see Supplement S3), and even vaguely at 1000 hPa. That result was based on monthly correlations. In this section, we consider daily data.

Geisler and Dickinson (1975) computed Rossby modes considering an atmospheric background state having an empirical variation of the zonal wind with altitude. In Supplement S8 we show that: 1) the vertical variation of the background wind allows the MLRB having a quite prominent amplitude in the low and mid-troposphere; and 2) there is an empirical relationship, over the region of interest, between the 500-hPa Omega amplitude and the variation in altitude of the background flow using NCEP/NCAR reanalysis data. These results seem to indicate that the impact of a MLRB in the lower levels depends on its ability to penetrate into the low-troposphere additionally to on its amplitude in the upper portion of the troposphere. The former can be quantified using Omega at 500 hPa.

Taking into account those results, we employ the daily NCEP 500-hPa Omega (Pa/s) to quantify the entry of the MLRB into the low-troposphere over North Africa, and denote it as OM500. The selected geographical location over Northern Algeria (32.5° N, 2.5°

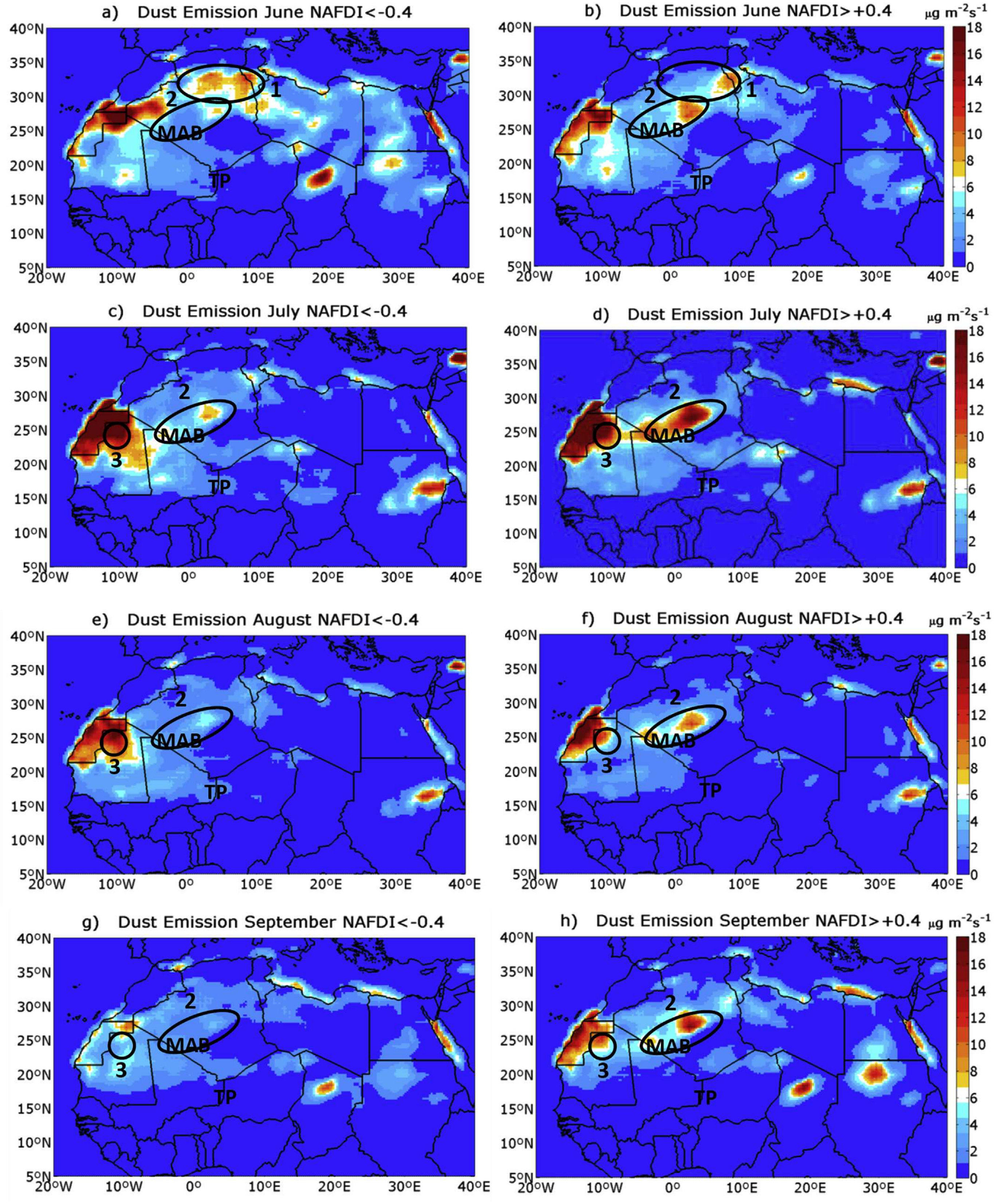

Fig. 8. Mean dust emission (μg $m^{-2}s^{-1}$) calculated from MACC reanalysis for June, July, August, and September months with negative (a, c, e, and g) and positive (b, d, f, and h) NAFDI (2003–2012).

E) was chosen because the correlation between the NAFDI and the 500-hPa omega field presents, for the 1980–2013 August months, a relative maximum (~0.6). A very similar behaviour is observed for the full June–September period (see Supplement S9). We chose the 500-hPa level due to the fact that it is an intermediate level and therefore the wind shear at this level might represent approximately the mean corresponding to the full troposphere, and it is not sensitive to the unwanted SHL-feedback. The hypothetical impact of the Saharan CBL in OM500 is ruled out because: 1) The maximum monthly mean CBL height at this point, from ECMWF reanalysis, is observed in July, being 4664 ± 297 (1 standard deviation) m under negative NAFDI and 4510 ± 198 m under positive NAFDI; and 2) the monthly NCEP regression (Pa/s/NAFDI) and correlation plots between NAFDI and upper-level (300, 400 and 500 hPa) omega fields for 1980–2013 June–September months show quite similar patterns (see Supplement S9), and it is very clear that the 300 and 400 hPa levels are not affected at all by the Saharan CBL. On the contrary, the corresponding correlation pattern at 600 hPa is shifted to the south, which might be a sign of the Saharan CBL impact at this lower level.

We employ the NCEP daily 300-hPa zonal Wind Anomaly (m/s) with its sign inverted, and denote it as WA300, to quantify approximately the phase and amplitude of the MLRW at this level over North Africa. The selected geographical location in South Morocco (10° W; 30° N) corresponds to a maximum negative correlation (<- 0.8) at the upper levels between the NAFDI for August months and the zonal wind (similar results hold for the entire summer period as shown in Supplement S9). Note that we have calculated the anomaly with respect to the daily climatology smoothed by a 29-day running mean, as for the daily SHLLSI and NAFDIDI computations, and therefore we have ruled out climatological changes in the zonal wind of the waveguide. We have also computed the vertical profile of the Rossby wave amplitude (see Supplement S8) and found that it is very similar to that corresponding to one of the external modes that Geisler and Dickinson (1975) obtained.

After smoothing the time series using 5-day running average, the correlation between the NAFDIDI and a linear combination of WA300 and OM500 is 0.656 (significant at the 99.999% level). The mentioned linear combination was obtained carrying out a least-square regression of NAFDIDI as a linear polynomial of WA300 and OM500. These results point out that WA300 and OM500 are quasi-independent (the correlation between them is 0.105, being 0.205 if a 5-day running average is previously used) that account for different features of the MLRB, as discussed previously.

The power spectra of the NAFDIDI, SHLLSI, and LCWAOM (the linear combination of WA300 and OM500 time series mentioned in the previous paragraph) time series for the period 1980–2013 have been computed using Fast Fourier Transform, being the overall structure of all those spectra considerably similar. The power spectrum for NAFDIDI for the intermediate time-scale domain (10–30 days), which is the MLRW temporal domain (e.g., Ambrizzi et al., 1995), shows that the majority of the strong peaks are present too in the SHLLSI spectrum, finding that a lot of them correspond as well to LCWAOM peaks (see Supplement S10). These results indicate that NAFDI seems to quantify the intra-seasonal changes in the lower-level intensity of those MLRWs that penetrate deep enough to impose their perturbation to the lower-troposphere background meteorological fields over Northern Africa. These intra-seasonal changes seem to explain the pulsating nature of the Saharan-dust large-scale export out of Northern Africa.

4. Conclusions

The main conclusions of this study are as follows:

1 We have complemented the findings of Rodríguez et al. (2015). They reported an inter-annual variation (only August months were studied) in dust outflows towards the Subtropical Atlantic associated to the variations of NAFDI. In this paper we have shown that NAFDI also presents a notable intra-seasonal variation. Moreover, for each phase of the NAFDI, specific large scale patterns of AOD anomalies over the SNA, the Mediterranean basin, and the interior of North Africa are found during the summer period, depending only weakly on the specific summer month. This suggests that NAFDI modulates dust outflows towards the SNA and the Mediterranean into alternate phasing. Moreover, under positive NAFDI, positive AOD anomalies are observed in the Western Sahara and SNA, while during negative NAFDI they are found in central-eastern Sahara and CWM regions.

2 For the first time, it has been shown there is a close relationship between SHL West (East) phase and positive (negative) NAFDI. The Pearson's r between the newly introduced daily SHLLSI and NAFDIDI data series for the period between late June and mid-September (1980–2013) is 0.70. This correlation increases to 0.78 when the SHLLSI is 1-day lagged behind NAFDIDI.

3 Using the energy equation of the atmospheric dynamics and the NCEP/NCAR reanalysis, we have shown that the differential horizontal advection of temperature, which is in turn due to the daily horizontal velocity anomaly associated to NAFDI, drives the temporal evolution of the longitudinal displacement of the SHL.

4 Preliminary estimates on dust emissions from MACC reanalysis suggest that changes in NAFDI may be related with the intensification/weakening of dust sources in CWS. Specifically, positive NAFDI seems to favour dust mobilization in Western Sahara, northern Mauritania, and central Algeria.

5 NAFDI intra-seasonal variations are driven by those MLRWs propagating over North Africa that penetrate sufficiently into the lower troposphere. A multi-linear least square regression model has been built to describe the NAFDI as a function of WA300, which quantifies the wave amplitude and phase at 300 hPa, and OM500, which quantifies the wave penetration into the lower troposphere. It presents a linear correlation of 0.656.

Summarizing, the results of this study indicate that the NAFDI intra-seasonal variations are driven by those MLRWs that impose their perturbation to the lower-troposphere over Northern Africa, and that NAFDI drives, in turn, the SHL West-East displacements, the pulsed transport of Saharan-dust over the SNA and the Mediterranean basin, and the spatial and intensity intra-seasonal changes in dust mobilization over the Sahara.

The analysis of the processes that drive the inter-annual variations of NAFDI is beyond the scope of the present paper, and is the subject of an on-going study.

Acknowledgements

This work is part of the research activities developed by the WMO SDS-WAS Regional Centre for Northern Africa, Middle East and Europe, held by AEMET and BSC-CNS. This study also contributes to Copernicus Atmosphere Monitoring Service (CAMS). Our acknowledgment to ECMWF for providing MACC-dust reanalysis. The authors wish to thank NCEP/NCAR Reanalysis Project. We acknowledge NASA LADS for providing MODIS data. The University of Granada (Spain) and its “Physics and Space Sciences” PhD Programme are acknowledged by A. J. Gómez-Peláez and E. Cuevas. AEROATLAN project (CGL2015-17 66229-P), co-funded by the Ministry of Economy and Competitiveness of Spain and the

European Regional Development Fund contributed to this study. Sara Basart acknowledges the CICYT project (CGL2013-46736).

Appendix A. Supplementary data

Supplementary data related to this article can be found at http://dx.doi.org/10.1016/j.atmosenv.2017.08.059.

References

Adams, A.M., Prospero, J.M., Zhang, C., 2012. CALIPSO derived three-dimensional structure of aerosol over the Atlantic Basin and adjacent continents. J. Clim. 25, 6862–6879. http://dx.doi.org/10.1175/JCLI-D-11-00672.1.

Allen, C.J.T., Washington, R., 2013. The low-level jet dust emission mechanism in the central Sahara: observations from Bordj-Badji Mokhtar during the June 2011 fennec intensive observation period. J. Geophys. Res. Atmos. 119, 2990–3015. http://dx.doi.org/10.1002/2013JD020594.

Ambrizzi, T., Hoskins, B.J., Hsu, H.H., 1995. Rossby-wave propagation and teleconnection patterns in the austral winter. J. Atmos. Sci. 52, 3661–3672.

Ashpole, I., Washington, R., 2013. Intraseasonal variability and atmospheric controls on daily dust occurrence frequency over the central and Western Sahara during the boreal summer. J. Geophys. Res.-Atmos 118, 12915–12926. http://dx.doi.org/10.1002/2013JD020267.

Barnaba, F., Gobbi, G.P., 2004. Aerosol seasonal variability over the Mediterranean region and relative impact of maritime, continental and Saharan dust particles over the basin from MODIS data in the year 2001. Atmos. Chem. Phys. 4, 2367–2391. http://dx.doi.org/10.5194/acp-4-2367-2004.

Basart, S., Pérez, C., Cuevas, E., Baldasano, J.M., Gobbi, G.P., 2009. Aerosol characterization in Northern Africa, Northeastern Atlantic, Mediterranean basin and Middle East from direct-sun AERONET observations. Atmos. Chem. Phys. 9, 8265–8282.

Bellouin, N., Quaas, J., Morcrette, J.-J., Boucher, O., 2013. Estimates of aerosol radiative forcing from the MACC re-analysis. Atmos. Chem. Phys. 13, 2045–2062. http://dx.doi.org/10.5194/acp-13-2045-2013.

Ben-Ami, Y., Koren, I., Altaratz, O., 2009. Patterns of North African dust transport over the Atlantic: winter vs. summer, based on CALIPSO first year data. Atmos. Chem. Phys. 9, 7867–7875. http://dx.doi.org/10.5194/acp-9-7867-2009.

Benedetti, A., Morcrette, J.-J., Boucher, O., Dethof, A., Engelen, R.J., Fisher, M., Flentjes, H., Huneeus, N., Jones, L., Kaiser, J.W., Kinne, S., Mangold, A., Razinger, M., Simmons, A.J., Suttie, M., the GEMS-AER team, 2009. Aerosol analysis and forecast in the ECMWF integrated forecast system. Part II: data assimilation. J. Geophys. Res. 114, D13205. http://dx.doi.org/10.1029/2008JD011115.

Benedetti, A., Baldasano, J.M., Basart, S., Benincasa, F., Boucher, O., Brooks, M., Chen, J.-P., Colarco, P.R., Gong, S., Huneeus, N., Jones, L., Lu, S., Menut, L., Morcrette, J.-J., Mulcahy, J., Nickovic, S., Pérez, C., Reid, J.S., Sekiyama, T.T., Tanaka, T.Y., Terradellas, E., Westphal, D.L., Zhang, X.-Y., Zhou, C.-H., 2014. Numerical prediction of dust. In: Knippertz, P., Stuut, J.-B. (Eds.), Mineral Dust – a Key Player in the Earth System. Springer, Dordrecht, pp. 230–240.

Cesnulyte, V., Lindfors, A.V., Pitkänen, M.R.A., Lehtinen, K.E.J., Morcrette, J.-J., Arola, A., 2014. Comparing ECMWF AOD with AERONET observations at visible and UV wavelengths. Atmos. Chem. Phys. 14, 593–608. http://dx.doi.org/10.5194/acp-14-593-2014.

Chauvin, F., Roehrig, R., Lafore, J.-P., 2010. Intraseasonal variability of the Saharan heat low and its link with midlatitudes. J. Clim. 23, 2544–2561. http://dx.doi.org/10.1175/2010JCLI3093.1.

Chiapello, I., Moulin, C., Prospero, J.M., 2005. Understanding the long-term variability of African dust transport across the Atlantic as recorded in both Barbados surface concentrations and large-scale Total Ozone Mapping Spectrometer (TOMS) optical thickness. J. Geophys. Res. 110, D18S10. http://dx.doi.org/10.1029/2004JD005132.

Conway, T.M., John, S.G., 2014. Quantification of dissolved iron sources to the North Atlantic Ocean. Nature 511, 212–215. http://dx.doi.org/10.1038/nature13482.

Couvreux, F., Guichard, F., Bock, O., Campistron, B., Lafore, J.-P., Redelsperger, J.-L., 2010. Synoptic variability of the monsoon flux over West Africa prior to the onset. Q. J. R. Meteorol. Soc. 136 (S1), 159–173. http://dx.doi.org/10.1002/qj.473.

Cuesta, J., Marsham, J.H., Parker, D.J., Flamant, C., 2009. Dynamical mechanisms controlling the vertical redistribution of dust and the thermodynamic structure of the West Saharan atmospheric boundary layer during summer. Atmos. Sci. Lett. 10, 34–42. http://dx.doi.org/10.1002/asl.207.

Cuevas, E., Camino, C., Benedetti, A., Basart, S., Terradellas, E., Baldasano, J.M., Morcrette, J.J., Marticorena, B., Goloub, P., Mortier, A., Berjón, A., Hernández, Y., Gil-Ojeda, M., Schulz, M., 2015. The MACC-II 2007–2008 reanalysis: atmospheric dust evaluation and characterization over northern Africa and the Middle East. Atmos. Chem. Phys. 15, 3991–4024. http://dx.doi.org/10.5194/acp-15-3991-2015.

Díaz, J., Tobías, A., Linares, C., 2012. Saharan dust and association between particulate matter and case-specific mortality: a casecrossover analysis in Madrid (Spain). Environ. Health 11, 1–6. http://dx.doi.org/10.1186/1476-069X-11-11.

Engelstaedter, S., Washington, R., 2007. Atmospheric controls on the annual cycle of North African dust. J. Geophys. Res. 112, D17111. http://dx.doi.org/10.1029/2006JD007195.

Engelstaedter, S., Washington, R., Mahowald, N., 2009. Impact of changes in atmospheric conditions in modulating summer dust concentration at Barbados: a back-trajectory analysis. J. Geophys. Res. 114, D17111. http://dx.doi.org/10.1029/2008JD011180.

Engelstaedter, S., Washington, R., Flamant, C., Parker, D.J., Allen, C.J.T., Todd, M.C., 2015. The Saharan heat low and moisture transport pathways in the central Sahara—multiaircraft observations and Africa-LAM evaluation. J. Geophys. Res. 120 (10), 4417–4442. http://dx.doi.org/10.1002/2015JD023123.

Escudero, M., Querol, X., Ávila, A., Cuevas, E., 2007. Origin of the exceedances of the European daily PM limit value in regional background áreas of Spain. Atmos. Environ. 41, 730–744.

Eskes, H., Huijnen, V., Arola, A., Benedictow, A., Blechschmidt, A.-M., Botek, E., Boucher, O., Bouarar, I., Chabrillat, S., Cuevas, E., Engelen, R., Flentje, H., Gaudel, A., Griesfeller, J., Jones, L., Kapsomenakis, J., Katragkou, E., Kinne, S., Langerock, B., Razinger, M., Richter, A., Schultz, M., Schulz, M., Sudarchikova, N., Thouret, V., Vrekoussis, M., Wagner, A., Zerefos, C., 2015. Validation of reactive gases and aerosols in the MACC global analysis and forecast system. Geosci. Model Dev. 8, 3523–3543. http://dx.doi.org/10.5194/gmd-8-3523-2015.

Evan, A.T., Flamant, C., Gaetani, M., Guichard, F., 2016. The past, present and future of African dust. Nature 531 (7595), 493–495.

Foltz, G.R., McPhaden, M.J., 2008. Impact of Saharan dust on tropical North Atlantic SST. J. Clim. 21, 5048–5060.

Gallisai, R., Peters, F., Volpe, G., Basart, S., Baldasano, J.M., 2014. Saharan dust deposition may affect phytoplankton growth in the Mediterranean Sea at ecological time scales. PloS one 9 (10), e110762.

Geisler, J.E., Dickinson, R.E., 1975. External Rossby modes on a beta-plane with realistic vertical wind shear. J. Atmos. Sci. 32, 2082–2093.

Gillette, D.A., Passi, R., 1988. Modeling dust emission caused by wind erosion. J. Geophys. Res.93 D11, 14233–14242. http://dx.doi.org/10.1029/JD093iD11p14233.

Ginoux, P., Prospero, J.M., Torres, O., Chin, M., 2004. Long-term simulation of global dust distribution with the GOCART model: correlation with North Atlantic Oscillation. Environ. Modell. Softw. 19, 113–128.

Ginoux, P., Prospero, J.M., Gill, T.E., Hsu, N.C., Zhao, M., 2012. Global-scale attribution of anthropogenic and natural dust sources and their emission rates based on MODIS Deep Blue aerosol products. Rev. Geophys 50, RG3005. http://dx.doi.org/10.1029/2012RG000388.

Gkikas, A., Houssos, E.E., Lolis, C.J., Bartzokas, A., Mihalopoulos, N., Hatzianastassiou, N., 2015. Atmospheric circulation evolution related to desert dust episodes over the Mediterranean. Q. J. R. Meteorol. Soc. 141 (690), 1634–1645.

Gläser, G., Wernli, H., Kerkweg, A., Teubler, F., 2015. The transatlantic dust transport from North Africa to the Americas—its characteristics and source regions. J. Geophys. Res. Atmos. 120, 11,231–11,252. http://dx.doi.org/10.1002/2015JD023792.

Goudie, A.S., Middleton, N.J., 2001. Saharan dust storms: nature and consequences. Earth Sci. Rev. 56 (1), 179–204.

Guerzoni, S., Chester, R., Dulac, F., Herut, B., Loye-Pilot, M.-D., Measures, C., Migon, C., Molinaroli, E., Moulin, C., Rossini, P., Saydam, C., Soudine, A., Ziveri, P., 1999. The role of atmospheric deposition in the biogeochemistry of the Mediterranean Sea. Prog. Oceanogr. 44, 147–190.

Helgren, D.M., Prospero, J.M., 1987. Wind velocities associated with dust deflation events in the Western Sahara. J. Clim. Appl. Meteorol. 26, 1147–1151.

Holton, J.R., 1992. An Introduction to Dynamic Meteorology, Third Edition, International Geophysics Series, vol. 48. Academic Press, San Diego, California.

Huneeus, N., Schulz, M., Balkanski, Y., Griesfeller, J., Prospero, J., Kinne, S., Bauer, S., Boucher, O., Chin, M., Dentener, F., Diehl, T., Easter, R., Fillmore, D., Ghan, S., Ginoux, P., Grini, A., Horowitz, L., Koch, D., Krol, M.C., Landing, W., Liu, X., Mahowald, N., Miller, R., Morcrette, J.-J., Myhre, G., Penner, J., Perlwitz, J., Stier, P., Takemura, T., Zender, C.S., 2011. Global dust model intercomparison in AeroCom phase I. Atmos. Chem. Phys. 11, 7781–7816. http://dx.doi.org/10.5194/acp-11-7781-2011.

Huneeus, N., Boucher, O., Chevallier, F., 2013. Atmospheric inversion of SO2 and primary aerosol emissions for the year 2010. Atmos. Chem. Phys. 13, 6555–6573. http://dx.doi.org/10.5194/acp-13-6555-2013.

Inness, A., Baier, F., Benedetti, A., Bouarar, I., Chabrillat, S., Clark, H., Clerbaux, C., Coheur, P., Engelen, R.J., Errera, Q., Flemming, J., George, M., Granier, C., Hadji-Lazaro, J., Huijnen, V., Hurtmans, D., Jones, L., Kaiser, J.W., Kapsomenakis, J., Lefever, K., Leitão, J., Razinger, M., Richter, A., Schultz, M.G., Simmons, A.J., Suttie, M., Stein, O., Thépaut, J.-N., Thouret, V., Vrekoussis, M., Zerefos, C., the MACC team, 2013. The MACC reanalysis: an 8 yr data set of atmospheric composition. Atmos.Chem. Phys. 13, 4073–4109. http://dx.doi.org/10.5194/acp-13-4073-2013.

Israelevich, P., Ganor, E., Alpert, P., Kishcha, P., Stupp, A., 2012. Predominant transport paths of Saharan dust over the mediterranean sea to Europe. J. Geophys. Res. 117, D02205. http://dx.doi.org/10.1029/2011JD016482.

Kalnay, E., Kanamitsu, M., Kistler, R., Collins, W., Deaven, D., Gandin, L., Iredell, M., Saha, S., White, G., Woollen, J., Zhu, Y., Leetmaa, A., Reynolds, R., Chelliah, M., Ebisuzaki, W., Higgins, W., Janowiak, J., Mo, K.C., Ropelewski, C., Wang, J., Jenne, R., Joseph, D., 1996. The NCEP/NCAR 40-year reanalysis project. B. Am. Meteorol. Soc. 77, 437–471.

Karanasiou, A., Moreno, N., Moreno, T., Viana, M., de Leeuw, F., Querol, X., 2012. Health effects from Sahara dust episodes in Europe: literature review and research gaps. Environ. Int. 47, 107–114.

Kaskaoutis, D.G., Houssos, E.E., Rashki, A., Francois, P., Legrand, M., Goto, D., Bartzokas, A., Kambezidis, H.D., Takemura, T., 2016. The Caspian sea-hindu Kush index (CasHKI): a regulatory factor for dust activity over southwest Asia. Glob. Planet. Change 137, 10–23.

Kaskaoutis, D.G., Alireza, R., Houssos, E.E., Legrand, M., Francois, P., Bartzokas, A., Kambezidis, H.D., Dumka, U.C., Goto, D., Takemura, T., 2017. Assessment of changes in atmospheric dynamics and dust activity over southwest Asia using the Caspian Sea–Hindu Kush Index. Int. J. Climatol. http://dx.doi.org/10.1002/joc.5053.

Kaufman, Y.J., Tanré, D., Remer, L.A., Vermote, E.F., Chu, A., Holben, B.N., 1997. Operational remote sensing of tropospheric aerosol over land from EOS moderate resolution imaging spectroradiometer. J. Geophys. Res. 102, 17–51.

Knippertz, P., 2008. Dust emissions in the West African heat trough—the role of the diurnal cycle and of extratropical disturbances. Meteorol. Z 17 (5), 553–563.

Knippertz, P., Todd, M.C., 2010. The central west Saharan dust hot spot and its relation to African easterly waves and extratropical disturbances. J. Geophys. Res. 115, D12117. http://dx.doi.org/10.1029/2009JD012819.

Lavaysse, C., Flamant, C., Janicot, S., Parker, D.J., Lafore, J.-P., Sultan, B., Pelon, J., 2009. Seasonal evolution of the West African heat low: a climatological perspective. Clim. Dyn. 33, 313–330.

Lavaysse, C., Flamant, C., Janicot, S., 2010a. Regional-scale convection patterns during strong and weak phases of the Saharan heat low. Atmos. Sci. Lett. 11, 255–264. http://dx.doi.org/10.1002/asl.284.

Lavaysse, C., Flamant, C., Janicot, S., Knippertz, P., 2010b. Links between African easterly waves, mid-latitude circulation and the intra seasonal pulsations of the West African Heat Low. Quart. J. Roy. Meteor. Soc. 136, 141–158. http://dx.doi.org/10.1002/qj.555.

Lavaysse, C., Eymard, L., Flamant, C., Karbou, F., Mimouni, M., Saci, A., 2013. Monitoring the West African heat low at seasonal and intra-seasonal timescales using AMSU-A sounder. Atmos. Sci. Lett. 14, 263–271.

Marconi, M., Sferlazzo, D.M., Becagli, S., Bommarito, C., Calzolai, G., Chiari, M., di Sarra, A., Ghedini, C., Gómez-Amo, J.L., Lucarelli, F., Meloni, D., Monteleone, F., Nava, S., Pace, G., Piacentino, S., Rugi, F., Severi, M., Traversi, R., Udisti, R., 2014. Saharan dust aerosol over the central Mediterranean Sea: PM10 chemical composition and concentration versus optical columnar measurements. Atmos. Chem. Phys. 14, 2039–2054. http://dx.doi.org/10.5194/acp-14-2039-2014.

Marsham, J.H., Hobby, M., Allen, C.J.T., Banks, J.R., Bart, M., Brooks, B.J., Cavazos-Guerra, C., Engelstaedter, S., Gascoyne, M., Lima, A.R., Martins, J.V., McQuaid, J.B., O'Leary, A., Ouchene, B., Ouladichir, A., Parker, D.J., Saci, A., Salah-Ferroudj, M., Todd, M.C., Washington, R., 2013. Meteorology and dust in the central Sahara: observations from Fennec supersite-1 during the June 2011 intensive observation period. J. Geophys. Res. 118, 4069–4089. http://dx.doi.org/10.1002/jgrd.50211.

Marticorena, B., Chatenet, B., Rajot, J.L., Traoré, S., Coulibaly, M., Diallo, A., Koné, I., Maman, A., NDiaye, T., Zakou, A., 2010. Temporal variability of mineral dust concentrations over West Africa: analyses of a pluriannual monitoring from the AMMA Sahelian Dust Transect. Atmos. Chem. Phys. 10, 8899–8915. http://dx.doi.org/10.5194/acp-10-8899-2010.

Middleton, N.J., Goudie, A.S., 2001. Saharan dust: sources and trajectories. Trans. Inst. Br. Geogr. 26, 165–181. http://dx.doi.org/10.1111/1475-5661.00013.

Mona, L., Amodeo, A., Pandolfi, M., Pappalardo, G., 2006. Saharan dust intrusions in the Mediterranean area: three years of Raman lidar measurements. J. Geophys. Res. 111, D16203. http://dx.doi.org/10.1029/2005JD006569.

Morcrette, J.-J., Boucher, O., Jones, L., Salmond, D., Bechtold, P., Beljaars, A., Benedetti, A., Bonet, A., Kaiser, J.W., Razinger, M., Schulz, M., Serrar, S., Simmons, A.J., Sofiev, M., Suttie, M., Tompkins, A.M., Untch, A., 2009. Aerosol analysis and forecast in the ECMWF integrated forecast system. Part I: forward modelling. J. Geophys. Res. 114, D06206. http://dx.doi.org/10.1029/2008JD011235.

Morcrette, J.-J., Benedetti, A., Jones, L., Kaiser, J.W., Razinger, M., Suttie, M., 2011. Prognostic Aerosols in the ECMWF IFS: MACC vs. GEMS Aerosols, vol. 659. ECMWF Tech Memo available at: http://old.ecmwf.int/publications/library/ecpublications/_pdf/tm/601–700/tm659.pdf. (Accessed 4 November 2014).

Moulin, C., Lambert, C.E., Dayan, U., Masson, V., Ramonet, M., Bousquet, P., Legrand, M., Balkanski, Y.J., Guelle, W., Marticorena, B., Bergametti, G., Dulac, F., 1998. Satellite climatology of African dust transport in the Mediterranean atmosphere. J. Geophys. Res. 103, 13137–13144.

Nakamae, K., Shiotani, M., 2013. Interannual variability in Saharan dust over the North Atlantic Ocean and its relation to meteorological fields during Northern winter. Atmos. Res. 120, 336–346.

Pérez García-Pando, C., Stanton, M.C., Diggle, P.J., Trzaska, S., Miller, R.L., Perlwitz, J.P., Baldasano, J.M., Cuevas, E., Ceccato, P., Yaka, P., Thomson, M.C., 2014. Soil dust aerosols and wind as predictors of seasonal meningitis incidence in Niger. Environ. Health Perspect. 122, 679–686. http://dx.doi.org/10.1289/ehp.1306640.

Perry, K.D., Cahill, T.A., Eldred, R.A., Dutcher, D.D., Gill, T.E., 1997. Long-range transport of North African dust to the eastern United States. J. Geophys. Res. 102 (D10), 11225–11238. http://dx.doi.org/10.1029/97JD00260.

Prospero, J.M., Carlson, T.N., 1972. Vertical and areal distribution of Saharan dust over the western equatorial North Atlantic ocean. J. Geophys. Res. 77, 5255–5265.

Prospero, J.M., 1996. Saharan dust transport over the North Atlantic Ocean and mediterranean: an overview. In: Guerzoni, S., Chester, R. (Eds.), The Impact of Desert Dust across the Mediterranean, vol. 11. Kluwer Academic Publisher. http://dx.doi.org/10.1007/978-94-017-3354-0_13. Series Environmental Science and Technology Library, pp. 133–151, ISBN 978-94-017-3354-0,.

Prospero, J.M., 1999. Long-range transport of mineral dust in the global atmosphere: impact of African dust on the environment of the southeastern United States. PNAS 96 (7), 3396–3403. http://dx.doi.org/10.1073/pnas.96.7.3396.

Prospero, J.M., Ginoux, P., Torres, O., Nicholson, S., Gill, T., 2002. Environmental characterization of global sources of atmospheric soil dust identified with the NIMBUS7 Total Ozone Mapping Spectrometer (TOMS) absorbing aerosol product. Rev. Geophys. 40 (1), 1002. http://dx.doi.org/10.1029/2000RG000095.

Prospero, J.M., Lamb, P.J., 2003. African droughts and dust transport to the Caribbean: climate change implications. Science 302, 1024–1027. http://dx.doi.org/10.1126/science.1089915.

Prospero, J.M., Mayol-Bracero, O., 2003. Understanding the transport and impact of African dust on the Caribbean basin. Bull. Am. Meteorol. Soc. 94, 1329–1337. BAMS-D-12-00142.1, 2013.

Prospero, J.M., Collard, F.-X., Molinié, J., Jeannot, A., 2014. Characterizing the annual cycle of African dust transport to the Caribbean Basin and South America and its impact on the environment and air quality. Glob. Biogeochem. Cycles 29. http://dx.doi.org/10.1002/2013GB004802.

Ravelo-Pérez, L.M., Rodríguez, S., Galindo, L., García, M.I., Alastuey, A., López-Solano, J., 2016. Soluble iron dust export in the high altitude Saharan Air Layer. Atmos. Environ. 133, 49–59.

Roehrig, R., Chauvin, F., Lafore, J.-P., 2011. 10-25-Day intraseasonal variability of convection over the Sahel: a role of the Saharan heat low and midlatitudes. J. Clim. 24 (22), 5863–5878. http://dx.doi.org/10.1175/2011JCLI3960.1.

Rodríguez, S., Querol, X., Alastuey, A., Kallos, G., Kakaliagou, O., 2001. Saharan dust contributions to PM10 and TSP levels in Southern and Eastern Spain. Atmos. Environ. 35, 2433–2447.

Rodríguez, S., Alastuey, A., Alonso-Pérez, S., Querol, X., Cuevas, E., Abreu-Afonso, J., Viana, M., Pérez, N., Pandolfi, M., de la Rosa, J., 2011. Transport of desert dust mixed with North African industrial pollutants in the subtropical Saharan Air Layer. Atmos. Chem. Phys. 11, 6663–6685. http://dx.doi.org/10.5194/acp-11-6663-2011.

Rodríguez, S., Cuevas, E., Prospero, J.M., Alastuey, A., Querol, X., López-Solano, J., García, M.I., Alonso-Pérez, S., 2015. Modulation of Saharan dust export by the North African dipole. Atmos. Chem. Phys. 15, 7471–7486. http://dx.doi.org/10.5194/acp-15-7471-2015.

Sayer, A.M., Hsu, N.C., Bettenhausen, C., Jeong, M.-J., 2013. Validation and uncertainty estimates for MODIS Collection 6 "Deep Blue" aerosol data. J. Geophys. Res. Atmos. 118, 7864–7872. http://dx.doi.org/10.1002/jgrd.50600.

Schepanski, K., Tegen, I., Laurent, B., Heinold, B., Macke, A., 2007. A new Saharan dust source activation frequency map derived from MSG-SEVIRI IR-channels. Geophys. Res. Lett. 34, L18803. http://dx.doi.org/10.1029/2007GL030168.

Stein, A.F., Draxler, R.R., Rolph, G.D., Stunder, B.J.B., Cohen, M.D., Ngan, F., 2015. NOAA's HYSPLIT atmospheric transport and dispersion modeling system. Bull. Amer. Meteor. Soc. 96, 2059–2077.

Sultan, B., Janicot, S., 2003. The West African monsoon dynamics. Part II: the "preonset" and "onset" of the summer monsoon. J. Clim. 16 (21), 3407–3427. http://dx.doi.org/10.1175/1520-0442(2003)016<3407:TWAMDP>2.0.CO;2.

Takemura, T., Okamoto, H., Maruyama, Y., Numaguti, A., Higurashi, A., Nakajima, T., 2000. Global three-dimensional simulation of aerosol optical thickness distribution of various origins. J. Geophys. Res. 105, 17853–17873. http://dx.doi.org/10.1029/2000JD900265.

Tanré, D., Kaufman, Y.J., Herman, M., Mattoo, S., 1997. Remote sensing of aerosol properties over oceans using the MODIS/EOS spectral radiances. J. Geophys. Res. 102, 16971–16988. http://dx.doi.org/10.1029/96JD03437.

Tegen, I., 2003. Modeling the mineral dust aerosol cycle in the climate system. Quat. Sci. Rev. 22, 1821–1834. http://dx.doi.org/10.1016/S0277-3791(03)00163-X.

Tegen, I., Fung, I., 1994. Modeling of mineral dust transport in the atmosphere: sources, transport, and optical thickness. J. Geophys. Res. 99, 22897–22914. http://dx.doi.org/10.1029/94JD01928.

Tegen, I., Torres, R., 2005. Global iron connections: desert dust, ocean biogeochemistry and climate. Science 308, 67–71.

Thomson, M.C., Molesworth, A.M., Djingarey, M.H., Yameogo, K.R., Belanger, F., Cuevas, L.E., 2006. Potential of environmental models to predict meningitis epidemics in Africa. Trop. Med. Int. Health 11, 781–788.

Todd, M., Cavazos-Guerra, C., 2016. Dust aerosol emission over the Sahara during summertime from cloud-aerosol lidar with orthogonal polarization (CALIOP) observations. Atmos. Environ. 128, 147–157.

Varga, G., Ùjvári, G., Kovács, J., 2014. Spatiotemporal patterns of Saharan dust outbreaks in the Mediterranean basin. Aeolian Res. 15, 151–160. http://dx.doi.org/10.1016/j.aeolia.2014.06.005.

Wang, W., Evan, A.T., Flamant, C., Lavaysse, C., 2015. On the decadal scale correlation between African dust and Sahel rainfall: the role of Saharan heat low–forced winds. Sci. Adv. 1 (9), e1500646. http://dx.doi.org/10.1126/sciadv.1500646.

Yu, H., Chin, M., Yuan, T., Bian, H., Remer, L.A., Prospero, J.M., Omar, A., Winker, D., Yang, Y., Zhang, Y., Zhang, Z., Zhao, C., 2015. The fertilizing role of African dust in the Amazon rainforest: A first multiyear assessment based on data from Cloud-Aerosol Lidar and Infrared Pathfinder Satellite Observations. Geophys. Res. Lett. 42, 1984–1991. http://dx.doi.org/10.1002/2015GL063040.

Supplement of

The pulsating nature of large-scale Saharan dust transport as a result of interplays between mid-latitude Rossby waves and the North African Dipole Intensity

E. Cuevas[1], A. J. Gómez-Peláez[1], S. Rodríguez[1], E. Terradellas[2], S. Basart[3], R. D. García[1,4], O. E. García[1], and S. Alonso-Pérez[5]

[1]Izaña Atmospheric Research Centre (AEMET), c/ La Marina, 20, 38001 Santa Cruz de Tenerife, Spain

[2]SDS-WAS Regional Centre (AEMET), Edificio Nexus II, c/ Jordi Girona, 29, 08034 Barcelona, Spain

[3]Earth Sciences Department, Barcelona Supercomputing Centre, Edificio Nexus II, c/ Jordi Girona, 29, 08034 Barcelona, Spain

[4]Air Liquide S.A., Delegación de Canarias, Plaza Industrial Valle Güímar Manz, 38500 Güímar, Santa Cruz de Tenerife, Spain

[5]Universidad Europea de Canarias, Campus de la Orotava, c/ Inocencio García 1, 38300 La Orotava, Santa Cruz de Tenerife, Spain

Corresponding author: E. Cuevas (ecuevasa@aemet.es), tel.: +34922151718

S1. Wind anomaly at 700 hPa for summer months with negative and positive NAFDI, in the period 2003-2012.

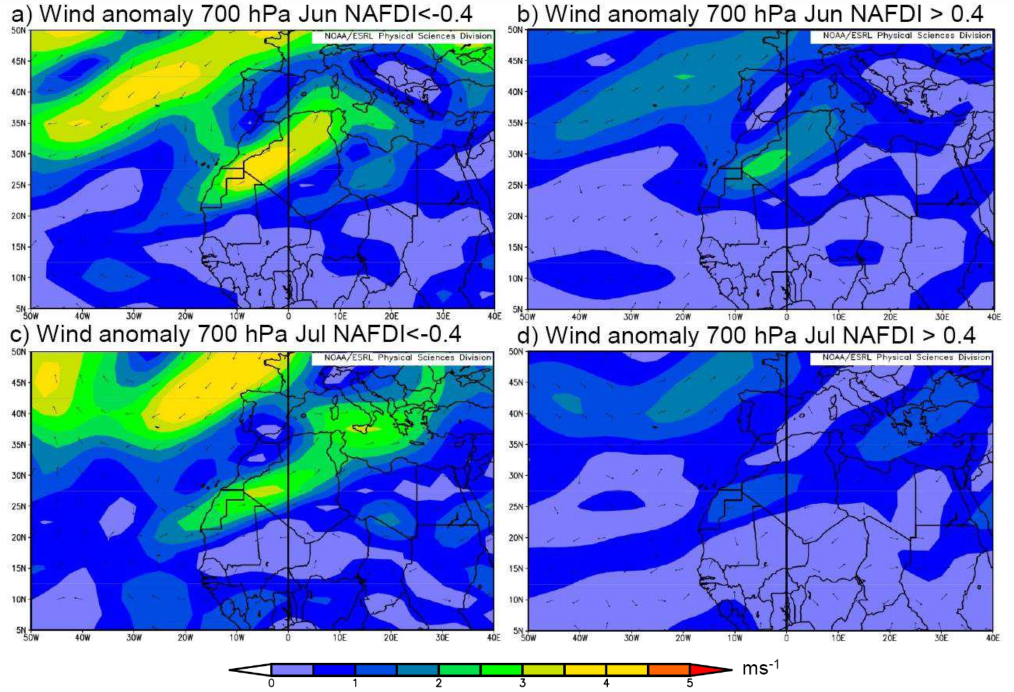

a) Wind anomaly 700 hPa Jun NAFDI<-0.4

b) Wind anomaly 700 hPa Jun NAFDI > 0.4

c) Wind anomaly 700 hPa Jul NAFDI<-0.4

d) Wind anomaly 700 hPa Jul NAFDI > 0.4

Figure S1a. Monthly anomalies of NCEP/NCAR wind vector and speed at 700 hPa for June and, July for negative (a and c) and positive (b and d,) NAFDI phases in the period 2003-2012.

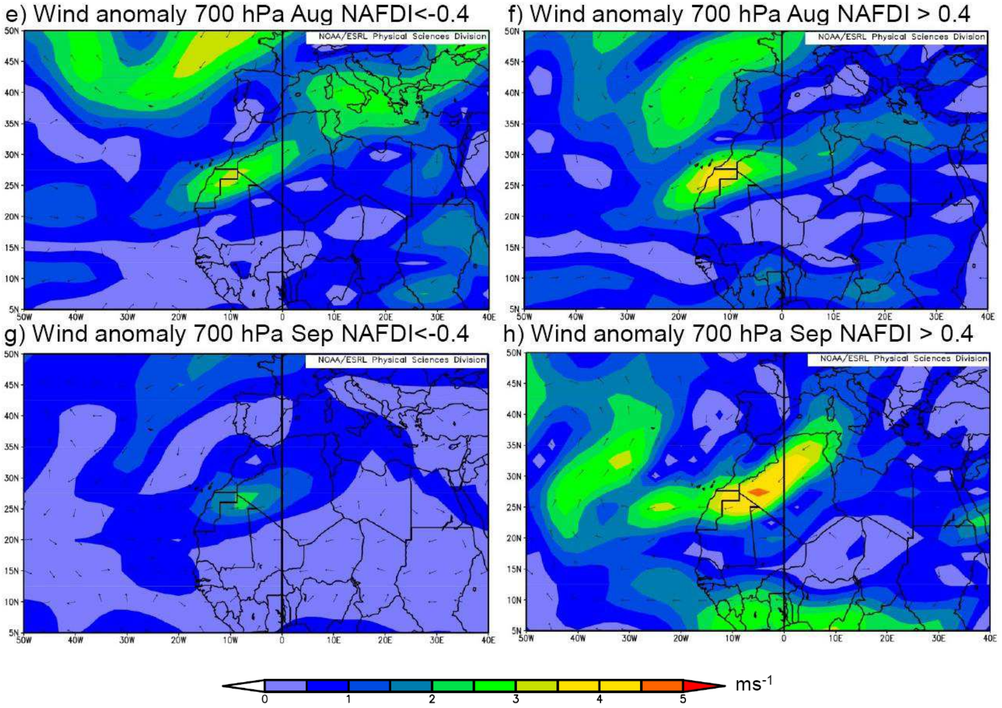
e) Wind anomaly 700 hPa Aug NAFDI<-0.4

f) Wind anomaly 700 hPa Aug NAFDI > 0.4

g) Wind anomaly 700 hPa Sep NAFDI<-0.4

h) Wind anomaly 700 hPa Sep NAFDI > 0.4

Figure S1b. Monthly anomalies of NCEP/NCAR wind vector and speed at 700 hPa for August and September, for negative (e and g) and positive (f and h) NAFDI phases in the period 2003-2012.

S2. Averaged AOD anomalies from MACC in summer for negative and positive NAFDI.

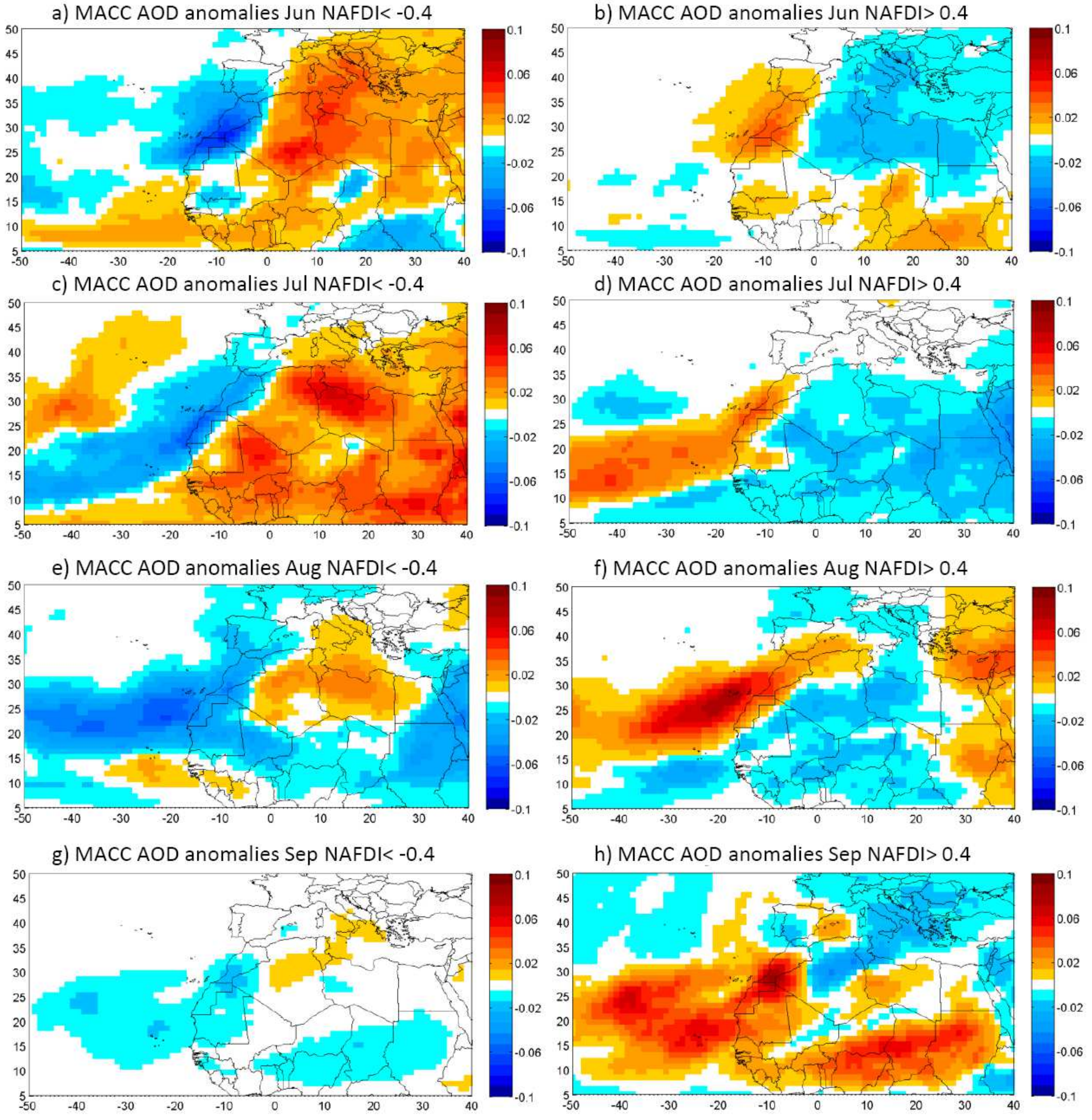

Figure S2. Averaged AOD anomalies from MACC reanalysis for summer months (June, July, August, and September) with negative (a, c, e, and g) and positive (b, d, f, and h) NAFDI phases, in the period 2003-2012. These plots were obtained by averaging the AOD anomalies for each month and each phase of the NAFDI.

S3. Monthly correlation plots between NAFDI and 200, 500, 700, 850 and 1000 hPa geopotential height in July and August, for the period 1980-2013.

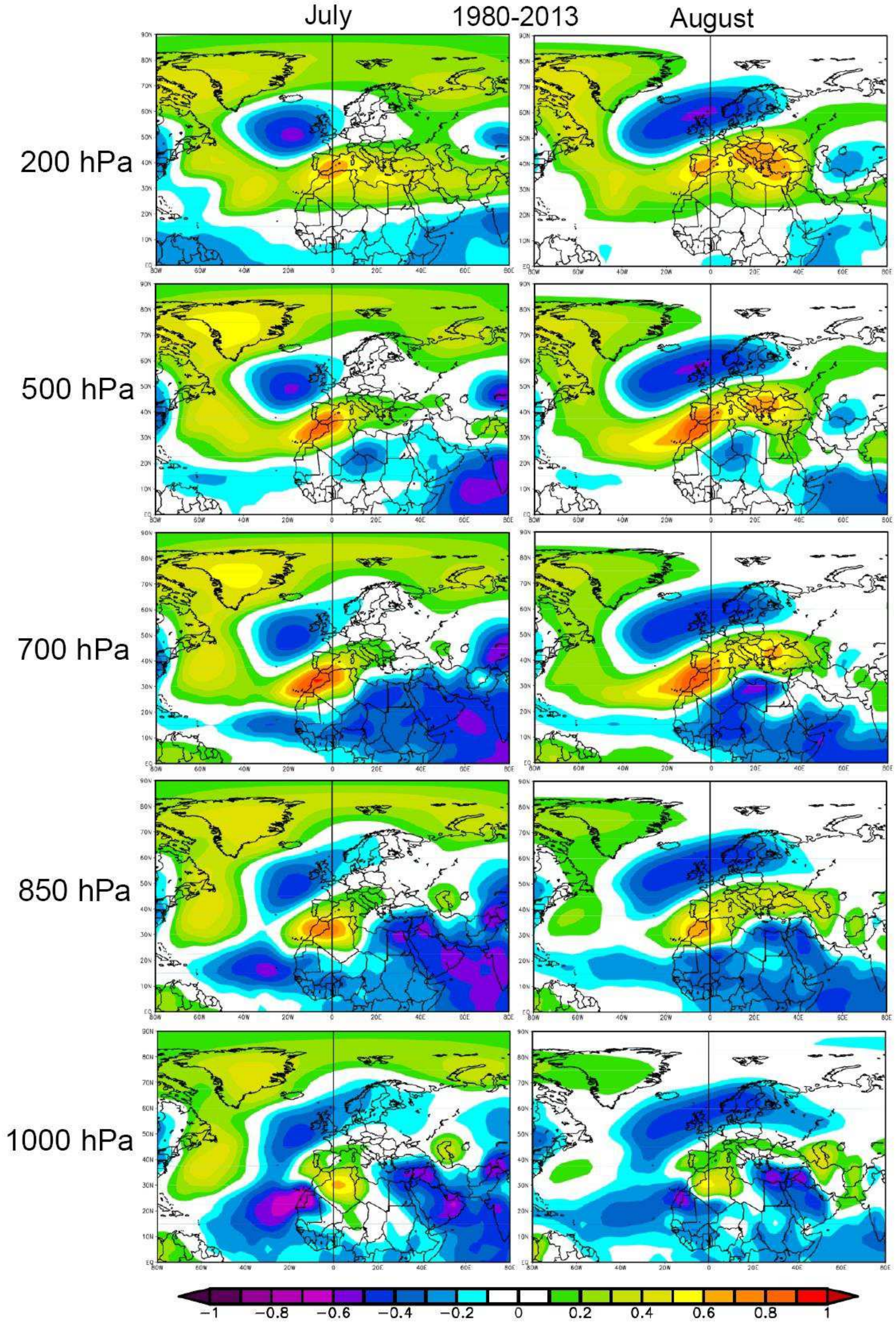

Figure S3. NCEP monthly correlation plots between NAFDI and 200, 500, 700, 850 and 1000 hPa geopotential height fields in July (left column) and August (right column), for the period 1980-2013. Correlations greater (in absolute value) than 0.34 are significant with a 95% confidence level.

S4. Wind vector and speed at 925 hPa for summer months (June, July, August, and September) with positive and negative NAFDI phases, in the period 2003-2012.

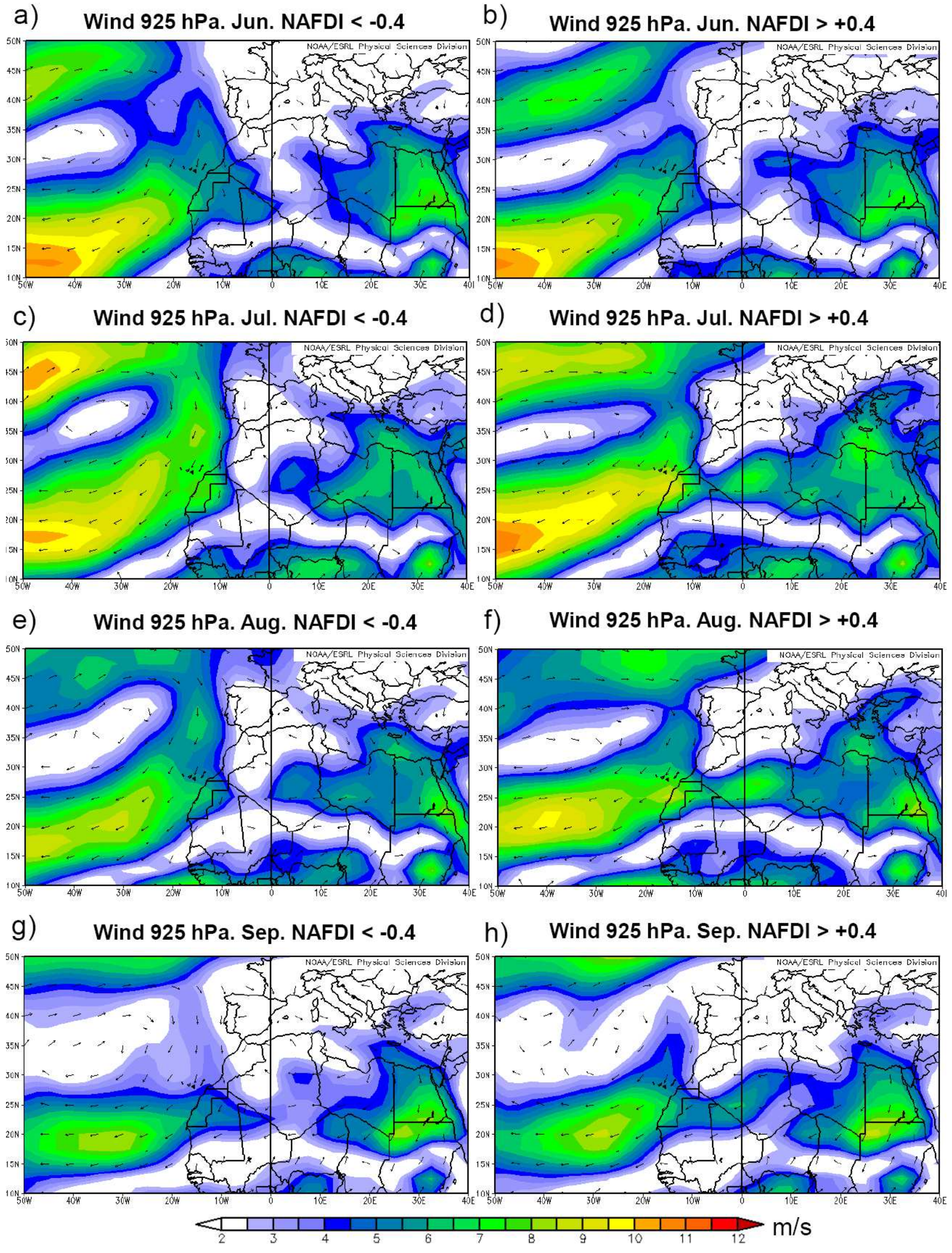

Figure S4. Monthly averages of NCEP/NCAR wind vector and speed at 925 hPa for summer months (June, July, August, and September) with negative (a, c, e, and g) and positive (b, d, f and h) NAFDI phases, in the period 2003-2012.

S5. Convective boundary layer (CBL) height (m) anomalies for summer months

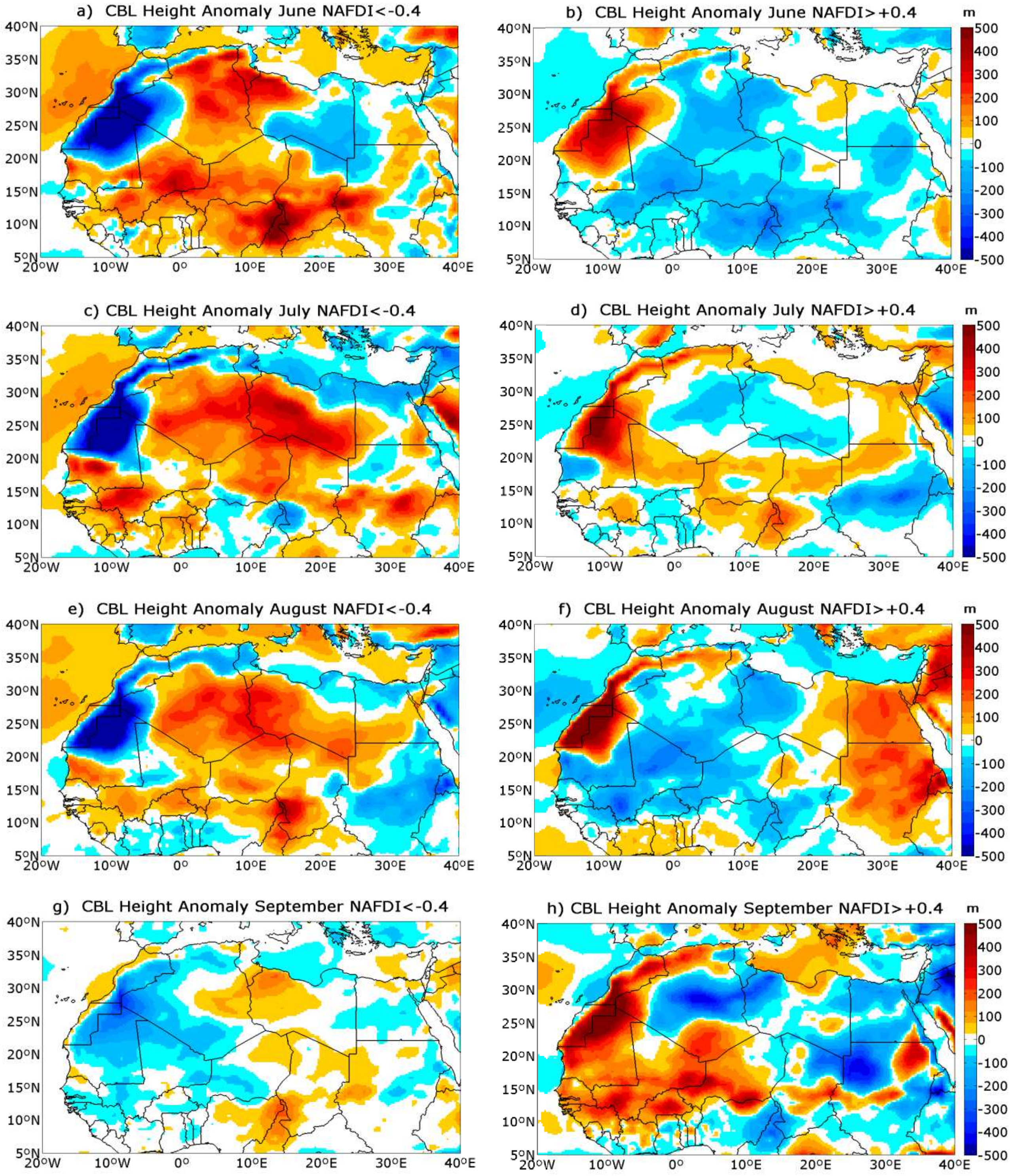
a) CBL Height Anomaly June NAFDI<-0.4

b) CBL Height Anomaly June NAFDI>+0.4

c) CBL Height Anomaly July NAFDI<-0.4

d) CBL Height Anomaly July NAFDI>+0.4

e) CBL Height Anomaly August NAFDI<-0.4

f) CBL Height Anomaly August NAFDI>+0.4

g) CBL Height Anomaly September NAFDI<-0.4

h) CBL Height Anomaly September NAFDI>+0.4

Figure S5. Monthly averages of ECMWF convective boundary layer (CBL) height (m) anomalies for summer months (June, July, August, and September) with negative (a, c, e, and g) and positive (b, d, f, and h) NAFDI phases, in the period 2003-2012.

S6. Some remarks concerning the computation of statistical confidence levels for the Pearson correlation coefficient

For the computation of statistical confidence levels for the Pearson correlation coefficient in the paper, we use tabulated values of “critical values for Pearson’s correlation coefficient” for a two-tailed (or non-directional) test. As stated in the main paper, for the spatial monthly correlation plots of the period 1980-2013 (i.e., 34 years), the critical value for having a significant Pearson´s correlation coefficient with a 95% confidence level is 0.34, when using only one month per year (e.g., August). We keep the same critical value when using more than one summer month per year, considering it as an upper bound to the real one, since there might be no null auto-correlation between the months of the same year.

To assess the level of confidence about the fact that one Pearson correlation coefficient (r_2) is significantly larger than another one (r_1) we proceed as follows (e.g., Meko, 2015): 1) apply a Fisher transformation from the variables r to z, and compute the standard error of z; 2) compute the difference D between z_2 and z_1, the standard error of such difference, and standardise the difference (i.e., compute the ratio between D and its standard error); 3) apply a one-tailed (or directional) test to the standardised D using the standard normal distribution function, to obtain the confidence level about the fact that r_2 is larger than r_1.

S6.1 Method used for daily time series with time-lag autocorrelation

Assuming that there is no time-lag autocorrelation in any of the daily time series (NAFDI, SHLLSI, WA300 and OM500), the critical value for having a significant Pearson´s correlation coefficient (R) with a 95% confidence level is 0.036 (i.e., the correlation is significant if $|R|>0.036$).

However, indeed, there is time-lag autocorrelation in the daily time series. We have used the method exposed here to establish an upper bound for the critical value of the Pearson’s correlation coefficient. In the four time series (NAFDI, SHLLSI, OM500 and WA300) the autocorrelation decreases when increasing the time-lag. The maximum time-lag (MTL) in which there is still a significant autocorrelation (larger than 0.036) is: 22 days for the NAFDI time series, 23 days for the SHLLSI time series, 7 days for the OM500 time series, and 15 days for the WA300 time series. Then, to establish an upper bound to the critical value, we consider a lower bound of the number of independent values (LBNIV) in the time series, computed as the ratio between 3060 (number of elements in each time series) and MTL. Note that this is a very conservative estimation of the lower bound. For correlations including the SHLLSI, LBNIV is 133, and the upper bound to the 95%-confidence-level critical values is 0.17. For correlations including NAFDI but not including SHLLSI, LBNIV is 139, and the upper bound to the 95%-confidence-level critical values is 0.166. However, for correlations not including the former two time series but WA300, LBNIV is 204, and the upper bound to the 95%-confidence-level critical values is 0.137.

Concerning the daily time series of Sect. 3.2.2 for the terms of the energy equation, the number of elements in the time series is: 3026 when all the stages are considered, 623 when only the "driving stage" is considered, and 630 when only the "restoring stage" is considered. To compute confidence levels for the daily correlations presented in section 3.2.2, we have applied the method described in the previous paragraph but using the pertinent number of elements instead of 3060.

S7. Details concerning the numerical computations of the energy-equation terms

In Sect. 3.2.2 we use the energy equation of the atmospheric dynamics and the NCEP/NCAR reanalysis to prove that NAFDI drives SHLLSI. In this supplement we provide some details on how the numerical computations have been carried out.

We use the NCEP/NCAR reanalysis with the highest time resolution available (6-hourly, with data at 00, 06, 12 and 18 UTC, hereafter called main hours). We denote the time resolution of the reanalysis as Δt (=0.25 days), and its spatial resolution as Δx and Δy, for the longitudinal and latitudinal direction, respectively, associated to the 2.5º NCEP/NCAR grid resolution (note that the lengths of Δx and Δy depend on latitude).

To compute the different terms of Eq. (3), we proceeded as follows. For computing the time derivative, we have used a centred difference scheme (e.g, see Morton & Mayers, 1994) with total step Δt centred at the hours 03, 09, 15, and 21 UTC, hereafter called intermediate hours (e.g., for computing the time derivative at 03 UTC, we have used the temperature at 00 and 06 UTC). For computing the horizontal advection, we have proceeded in two steps: 1) computation of the advection at the main hours using a centred difference scheme with total step $2\Delta x$ in the longitudinal direction and $2\Delta y$ in the latitudinal direction, and 2) computation of the advection at the intermediate hours as the mean of the advections corresponding to the immediately previous and posterior main hours. For computing the temperature tendency due to omega at the 925, 850, and 700 hPa levels, we have proceed in two steps: 1) computation of the pressure derivative at the main hours using a centred difference scheme that uses the potential temperature at the immediately above and below pressure levels (e.g., the levels 925 and 700 hPa for computing the vertical quasi-advection at the level 850 hPa), and 2) computation of the temperature tendency due to omega at the intermediate hours as the mean of the values corresponding to the immediately previous and posterior main hours. Note that since we are not solving a partial differential equation (the solution is already known for every time step, since it is provided by the NCEP/NCAR reanalysis), we do not need to worry about the stability of the numerical integration schemes. Finally, we have computed the diabatic heating at the intermediate hours as the residual of Eq. (3).

Once all the terms of Eq. (3) were computed at the intermediate hours (6-hourly time resolution), we proceeded as follows to compute daily values for the terms of Eq. (4). We used daily values of SHLLSI to compute its time derivative as a centred difference with total step 1 day centred at the hour 00 UTC. In this same way, the last term on the right-hand side of Eq. (4) was computed. Note that the following equation relating the numerical 6-hourly time derivatives with the daily one, holds:

$$\frac{\partial T^{n+1,n}}{\partial t} = \frac{1}{16}\left(\frac{\partial T^{n+1}}{\partial t_{15}} + 2\frac{\partial T^{n+1}}{\partial t_{9}} + 3\frac{\partial T^{n+1}}{\partial t_{3}} + 4\frac{\partial T^{n}}{\partial t_{21}} + 3\frac{\partial T^{n}}{\partial t_{15}} + 2\frac{\partial T^{n}}{\partial t_{9}} + \frac{\partial T^{n}}{\partial t_{3}}\right) \qquad (S1),$$

where the term on the left-hand side is the centred-difference time derivative between days n+1 and n, and the terms on the right-hand side are 6-hourly centred-difference time derivatives centred at the hour indicated in the sub-index corresponding to the day indicated in the super-index. Therefore, to compute *HAdv*, *Ome* and *Diab* we have proceeded in two steps: 1) computation of *HAdv* and *Ome* at the intermediate hours using Eqs. (5) and (6) and the 6-hourly terms previously computed for Eq. (3), 2) computation of the daily values centred at 00 UTC using the corresponding equation completely equivalent to (S1). In order to be consistent, to compute correlations with terms of Eq. (4), we have used SHLLSI and NAFDIDI centred at 00 UTC, as the mean of the immediately previous and posterior day.

S8. Analytical relations, equation that describes the Omega field associated to the Rossby wave in terms of the Geisler and Dickinson (1975) eigenvector, and empirical relation with the vertical shear of the zonal flow

Geisler and Dickinson (1975) obtained solutions for external Rossby modes on a beta-plane with realistic vertical wind shear, $u_0(p)$. They assume an atmosphere isothermal in the vertical direction but with a latitude-dependent temperature, $T_0(y)$. They use the log pressure coordinate $z=ln(p_r/p)$, where p_r is a reference pressure at the ground. However, for easiness of presentation here, we are going to use the pressure as vertical coordinate except for the function $\psi(z)$ that is introduced latter. They consider small perturbations to the background flow in the form (we use geopotential instead of geopotential height):

$$\Phi'(x,y,z,t) = f_0\left(\frac{p_r}{p}\right)^{1/2}\psi(z)\exp[i(kx+ly-kct)] \quad \text{(S2),}$$

where the left hand side is the perturbed geopotential, f_0 is the Coriolis parameter at a reference latitude, k is the longitudinal wavenumber, l is the latitudinal wavenumber, and kc is the Eulerian angular frequency (i.e., they perform Fourier analysis in the latitudinal and longitudinal coordinate as well as in time). In the absence of background zonal wind, the function $\psi(z)$ is equal to $(p/p_r)^{3/14}$. They introduce this form of the perturbed geopotential into the perturbed quasi-geostrophic potential vorticity equation (considering appropriate boundary conditions) and reduce the problem to an eigenvalue problem for the eigenvector $\psi(z)$ with a set of two ordinary differential equations in z, which they solve numerically.

From the perturbed geopotential height, all the perturbed variables can be obtained using the quasi-geostrophic relations (e.g., Holton, 1992). For example, this is the equation that holds for the perturbed zonal flow:

$$u'(x,y,z,t) = -il\left(\frac{p_r}{p}\right)^{1/2}\psi(z)\exp[i(kx+ly-kct)] \quad \text{(S3)}$$

Using the perturbed quasi-geostrophic energy equation (e.g., see Holton, 1992), we have obtained the following equation for the perturbed omega:

$$\omega'(x,y,z,t) = \frac{iR}{p\sigma(p)}\left[(u_0(p)k-kc)\frac{f_0}{R}\left(\frac{\psi(z)}{2}+\frac{\partial\psi(z)}{\partial z}\right)+k\psi(z)\frac{\partial T_0}{\partial y}\right]\left(\frac{p_r}{p}\right)^{1/2}\exp[i(kx+ly-kct)] \quad \text{(S4),}$$

where R is the gas constant for dry air,

$$\sigma(p) = -R\frac{T_0(y_0)}{p}\frac{d\ln\theta_0}{dp} \qquad \text{(S5)},$$

and θ_0 is the potential temperature of the unperturbed atmosphere.

In the case of no zonal velocity, $\psi(z)$ depends much less on z than in the case with vertically-sheared zonal wind (for the latter, see Figure 10 of Geisler and Dickinson, 1975, which corresponds to external Rossby modes; for the former see the curve denoted as "Barotropic" in Figure S8-1 of this Supplement). In the latter case (sheared flow), $\psi(z)$ has a relatively prominent maximum in the lower and middle troposphere (see also the curve denoted as "NAFDI Driver" in Figure S8-1). That is, the vertical shear of the zonal wind allows the free Rossby wave to have a very significant amplitude in the middle and lower troposphere. We expect from Eq. S4 that the perturbed omega at a given level will be very roughly proportional to the value of $\psi(z)$ at such level. Based on these results, we use in the paper the Omega at 500 hPa as a tracer of the capacity of the free barotropic Rossby wave to penetrate deep into the lower troposphere. We use the term "go deep in the lower troposphere" because in the real atmosphere we expect the free Rossby waves to transport longitudinally their energy along the upper troposphere (the lower troposphere has a less zonal flow, i.e., it has a significant contribution of the meridional flow that changes a lot in longitude) and that the Rossby wave is noticed more or less in the lower troposphere depending on the vertical shear of the zonal wind. In the next paragraph, we show numerically that this relation holds.

In order to test the relation between the amplitude of OM500 (defined in Section 3.4 of the paper) and the vertical shear of the background zonal wind, we have obtained NCEP daily zonal wind time series at 2.5°E and 32.5°N for the level 200 hPa (denoted as ZWB200). In some sense, the ZWB200 value is by itself representative of the mean vertical shear of the background zonal wind, due to the fact that the wind speed is much smaller near the ground than at 200 hPa (see Fig. S8-2). Since indeed we do not have the amplitude of OM500 but its instantaneous daily value, we compute the daily correlation using only days for which the absolute value of the NAFDIDI is greater than a threshold (we expect the instantaneous value of OM500 approaches the OM500 amplitude as the threshold grows). The correlation between the daily ZWB200 and OM500 time series for days in which the absolute value of the NAFDIDI is larger than 1.3, is 0.251; whereas if the NAFDI threshold is set at 2.6 (3.9) the correlation becomes 0.297 (0.335). These daily correlation values do not decrease significantly if a 15-day or 29-day running mean is applied previously to the ZWB200 time series.

Note that the Geisler and Dickinson (1975) background zonal flow does not have latitudinal dependence, and therefore does not account for the latitudinal waveguide phenomenon.To describe in a more accurate way the propagation of these Rossby waves in the real atmosphere, a much more sophisticated (and difficult) mathematical model would be necessary (not done in the literature according to our knowledge): a background zonal flow depending "strongly" in latitude and height, and depending "slightly" in longitude. The perturbation problem for such background flow would lead to an eigenvalue problem with Partial Differential Equations depending on latitude and height simultaneously, combined with a WKB method in the longitudinal direction and Fourier analysis in time.

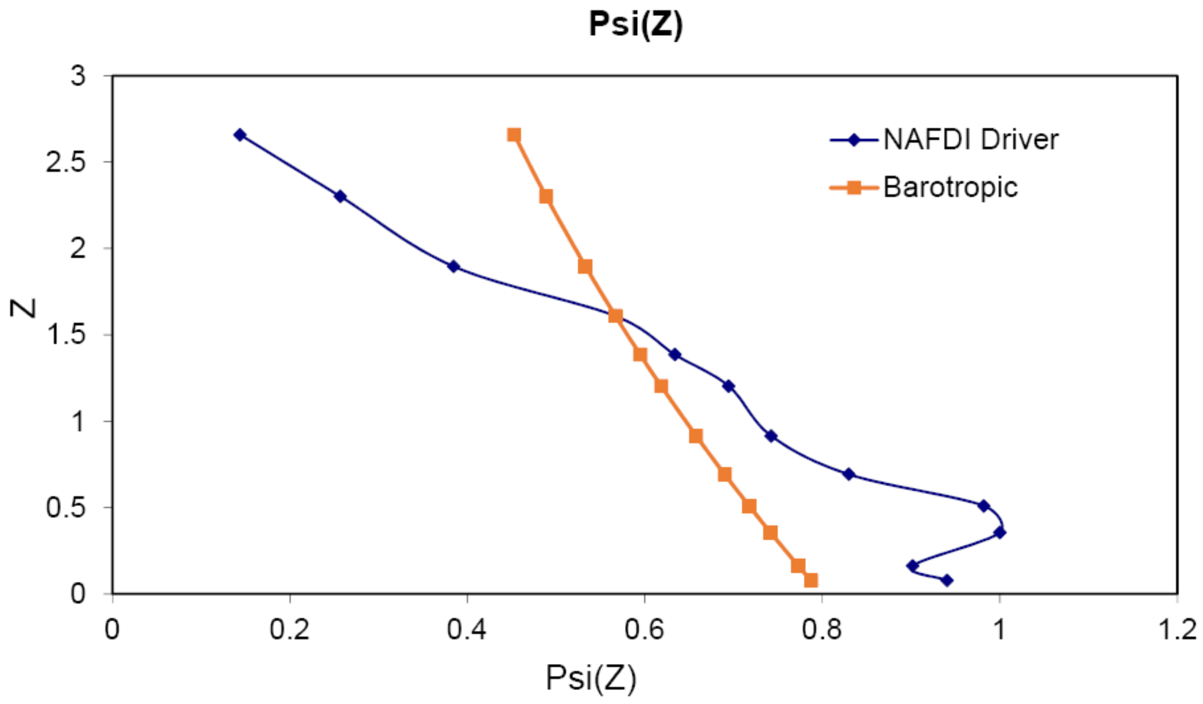

Figure S8-1. Vertical structure of the Rossby wave that drives the NAFDI variations represented using the same variables than Geisler and Dickinson (1975), for comparison (they are very similar) with the vertical structure of the external Rossby wave of Geisler and Dickinson (1975) with "effective wavenumber" 10.8 (see their Figure 10). As reference, the case with no zonal velocity (denoted "Barotropic") has been also plotted.

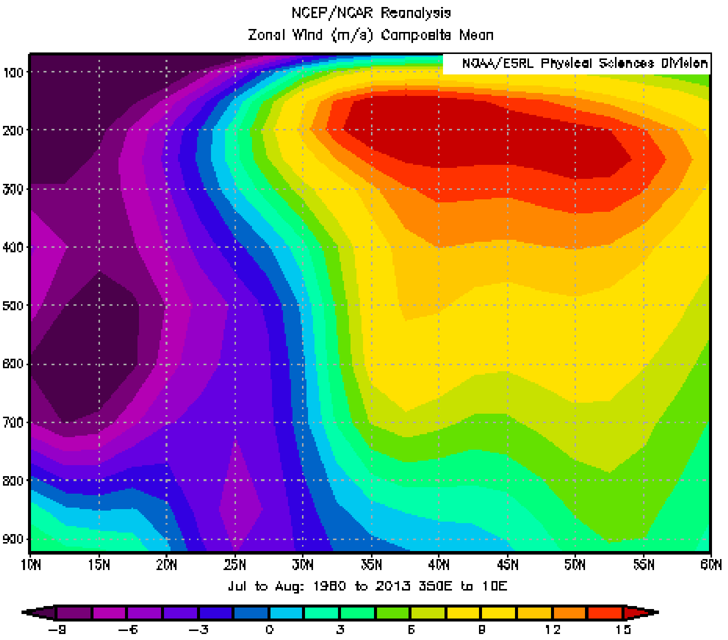

Figure S8-2. Mean zonal wind (averaged also in longitude from 10°W to 10°E) for a latitude-vertical cross-section during the period July-August 1980-2013.

S9. NCEP monthly correlation and regression maps between the monthly NAFDI and omega, for summer months in the period 1980-2013.

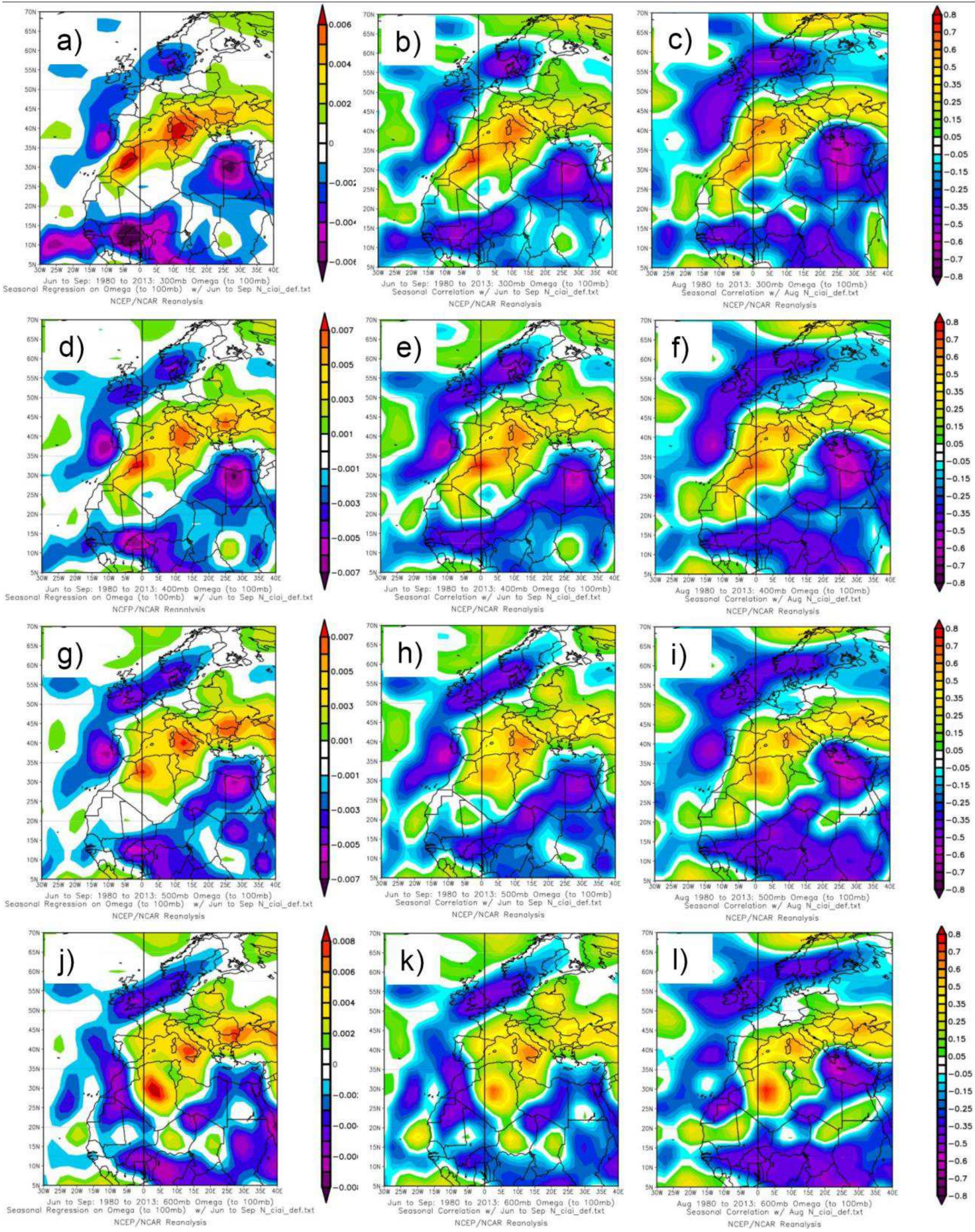

Figure S9-1. NCEP monthly regression plots (Pa/s/NAFDI) between the omega at 300, 400, 500 and 600 hPa (from top to bottom; a, d, g, j) and the monthly NAFDI for June-September of the period 1980-2013. Correlation plots between the omega at the same pressure levels and the monthly NAFDI for June-September (b, e, h, k) and for August (c, f, i, l) of the period 1980-2013. Correlations greater (in absolute value) than 0.34 are significant with a 95% confidence level.

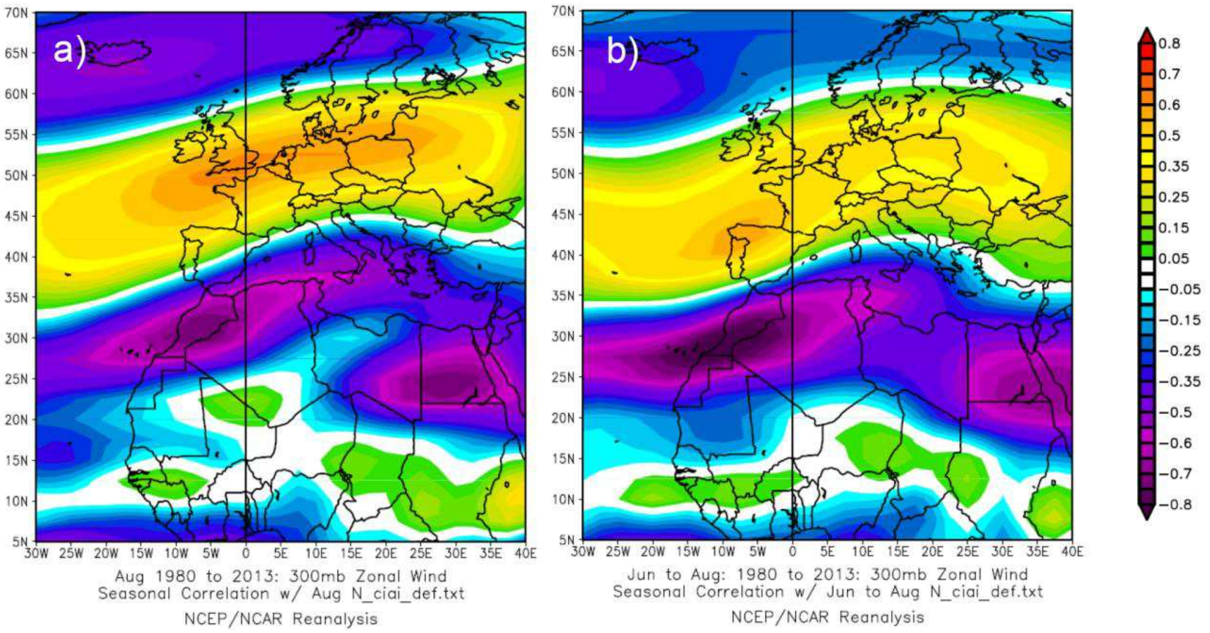

Figure S9-2. NCEP monthly correlation plots between the zonal wind at 300 hPa and the monthly NAFDI for August months (a) and for June-September (b) of the period 1980-2013. Correlations greater (in absolute value) than 0.34 are significant with a 95% confidence level.

S10. Power spectra of the time series

We have computed the power spectra of the daily NAFDIDI, SHLLSI, and LCWAOM time series for the period 20 June -17 September 1980-2013 using Fast Fourier Transform (e.g., Press et al., 1994), after padding with zeros till complete 4096 elements in each time series (i.e., the nearest larger power of 2). Then, we have reconstructed the three time series using only the Fourier components of the intermediate time-scale range (i.e., application of a band-pass filter), and computed the Pearson daily correlation between these filtered time series. The correlations are quite similar to those previously obtained for the no-filtered time series. We have also computed the Pearson correlation between the filtered OM500 and NAFDIDI time series obtaining the value 0.49, whereas the correlation is 0.43 for the no-filtered daily time series.

This rather high correlation (0.49) confirms that the influence of OM500 on NAFDI operates in the time scales of the Rossby waves.

Figure S10-1a shows the power spectra of the NAFDIDI and SHLLSI time series in the intermediate range, after applying a 5-point running mean (note that there are 273 points - discrete Fourier frequencies- in the considered range), whereas Fig. S10-1b shows the equivalent plot for the NAFDIDI and LCWAOM time series. The total power of the full spectrum for the SHLLSI, and LCWAOM time series has been normalized to that of the NAFDIDI time series, before plotting the power spectra in Fig. S10-1 for easiness in the comparison.

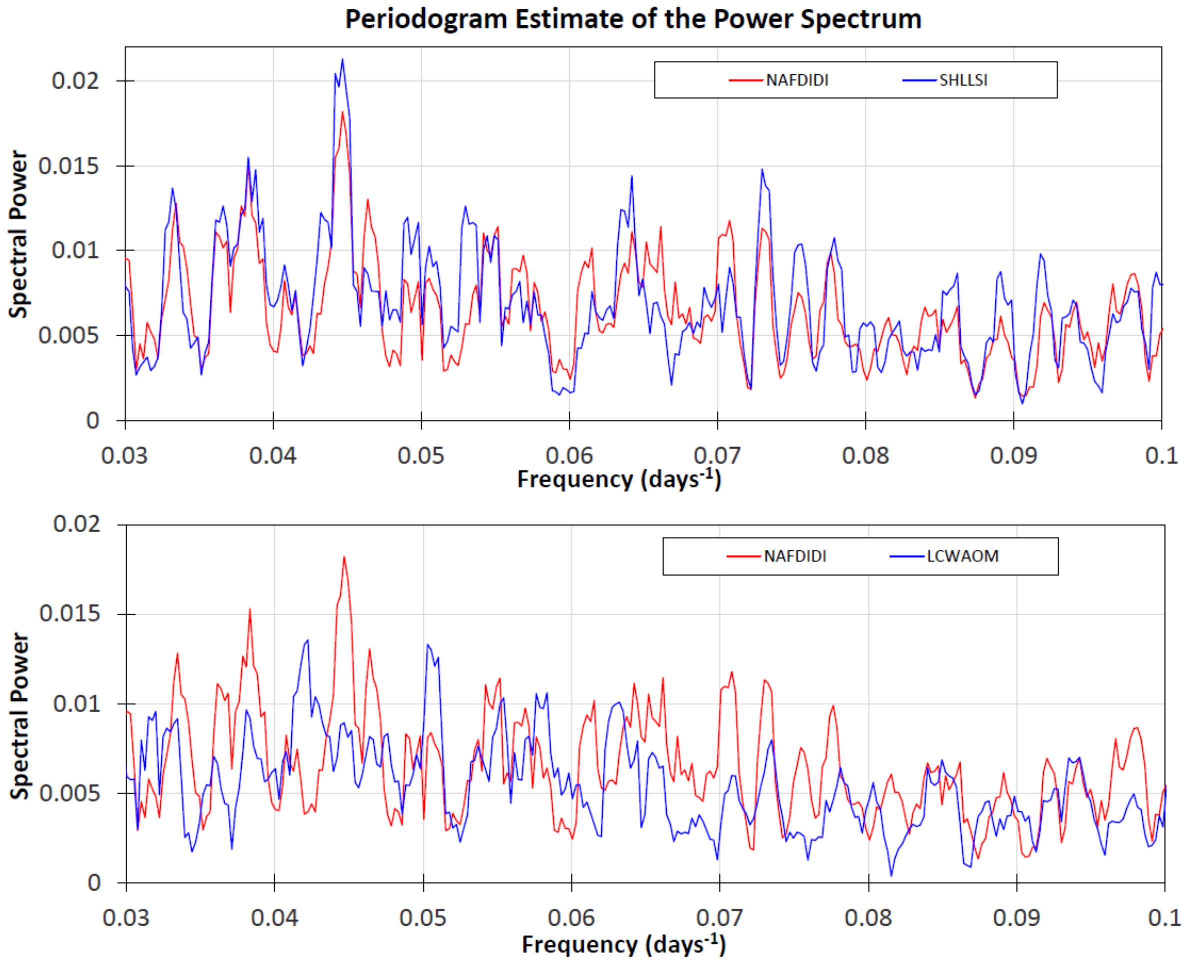

Figure S10-1. a) Upper graph: power spectra of the NAFDIDI and SHLLSI time series in the intermediate time-scale range, after applying a 5-point running mean; b) Lower graph: power spectra of the NAFDIDI and LCWAOM time series under the same conditions than in graph a).

Acknowledgements

The authors thank NCEP/NCAR Reanalysis Project at the NOAA/ESRL. All the numerical computations for Sect. 3.2.2 have been performed using the language R (R Core Team, 2016). The authors wish to thank ECMWF for providing ERA-Interim data and MACC-dust reanalysis.

References

Geisler, J. E., and Dickinson, R. E.: External Rossby modes on a beta-plane with realistic vertical wind shear, Journal of the Atmospheric Sciences, 32, 2082-2093, 1975.

Holton, J. R.: An introduction to dynamic meteorology, Third edition, International Geophysics Series, vol. 48, Academic Press, San Diego, California, 1992.

Meko, D. M., Applied Time Series Analysis, Lesson notes published on internet, GEOS 585A,Spring 2015, http://www.ltrr.arizona.edu/~dmeko/geos585a.html, 2015

Morton, K.W. and Mayers, D.F.: Numerical Solution of Partial Differential Equations, Cambridge University Press, Cambridge, 1994.

Press, W. H., Teukolsky, S. A., Vetterling, W. T., and Flannery, B. P.: Numerical Recipes in FORTRAN. The Art of Scientific Computing, Second edition reprinted with corrections, Cambridge University Press, Cambridge, 1994.

R Core Team: R: A Language and Environment for Statistical Computing, R Foundation for Statistical Computing, Vienna, Austria, https://www.R-project.org, 2016.

5. Conclusiones

Se ha cumplido el objetivo general de esta tesis de hacer una contribución científica significativa en la medida y el transporte de gases de efecto invernadero atmosféricos, monóxido de carbono y polvo sahariano, con especial énfasis en la troposfera libre del Atlántico Noreste subtropical. Los resultados presentados en esta tesis han sido previamente publicados por el doctorando en tres artículos científicos de revistas internacionales con árbitro, del primer cuartil (en índice de impacto) del campo "Ciencias Atmosféricas y Meteorología", por lo que se ha optado por presentar esta tesis como compendio de publicaciones.

Enumeración de conclusiones:

1. Se ha desarrollado un procedimiento riguroso para determinar la incertidumbre en las medidas continuas (cada 20 minutos) de CO realizadas en la estación VAG global de Izaña. Este método es aplicable a otras estaciones de la red global VAG de la OMM.

1.1 El error en las medidas ha sido calculado como incertidumbre combinada estándar. Ésta tiene cuatro componentes: 1) la incertidumbre de los gases patrón OMM interpolada sobre el rango de medida; 2) la incertidumbre que tiene en cuenta el acuerdo entre los gases patrón y la función respuesta usada; 3) la incertidumbre debida a la repetibilidad de las inyecciones de aire ambiente y su medida; y 4) la incertidumbre propagada asociada a la consistencia temporal de los parámetros de la función respuesta. Consideramos un quinto tipo de incertidumbre, que llamamos incertidumbre de representación, cuando algunos de los datos necesarios para calcular una media temporal están ausentes. Las incertidumbres de representación en las medidas in situ (continuas) son mucho menores que cuando se usan muestras semanales en matraces.

1.2 Se ha cuantificado la incertidumbre en cada una de las medidas de CO realizadas a lo largo de del periodo 2008-2011. Se ha visto una disminución significativa de la incertidumbre a partir de marzo de 2009, y se han identificado las causas de dicha disminución.

1.3 Se ha desarrollado un procedimiento para calcular la incertidumbre de las medias de CO, propagando la incertidumbre de los datos utilizados para el cálculo de dichas medias teniendo en cuenta el carácter aleatorio o sistemático (que a su vez depende de la escala temporal de la media) de cada componente de la incertidumbre.

1.4 La serie temporal de medias diarias nocturnas en Izaña para el periodo 2008-2011 ha sido analizada. La componente interanual aumenta hasta principios de 2010, y entonces decrece. La amplitud del ciclo estacional es 40.7 nmol·mol^{-1}, siendo el máximo al final del invierno y el mínimo a mitad del verano. El ciclo diurno medio por meses alcanza a mediodía un máximo de unos 5 a 6 nmol·mol^{-1} sobre el valor de fondo nocturno de la troposfera libre (excepto en diciembre que apenas llega a 4 nmol·mol^{-1}), debido al viento anabático.

1.5 Se han estudiado las diferencias entre las medias horarias obtenidas mediante medidas in situ continuas y las medias de las medidas de matraces muestreados dentro de la hora considerada (un par de matraces simultáneos cada semana). Se introduce el concepto de incertidumbre de comparación, que permite determinar cuando la diferencia es compatible o no con cero. Las diferencias medias anuales entre las medidas de matraces semanales de NOAA y las continuas in situ (de AEMET) para 2009-2011 no son significativas y están dentro de los 2 nmol·mol^{-1} de objetivo de compatibilidad entre laboratorios de VAG.

2. Se ha utilizado el modelo Oslo CTM3, que es un modelo de transporte que incluye química atmosférica, para estudiar la evolución del CH_4 durante el periodo 1970-2012.

2.1 Además, se han utilizado 18 trazadores ficticios pasivos, uno por cada sector de emisión de CH_4 considerado, emitidos continuamente y destruidos mediante decaimiento exponencial con un tiempo característico de 1 mes (el tiempo que tardan las emisiones recientes en dispersarse en la atmósfera lo suficiente para considerar que forman parte del fondo atmosférico). Los trazadores sufren transporte, pero no interaccionan químicamente. Son usados como proxy para la contribución de los diferentes sectores a las concentraciones medias mensuales de CH_4 en superficie, con el propósito de revelar sectores clave y regiones responsables de los cambios recientes del CH_4.

2.2 Se ha hecho una comparación exhaustiva de los campos de CH_4 atmosférico simulados con las medidas de estaciones de superficie para todas las regiones del planeta. La variación estacional es reproducida para la mayoría de las estaciones. El modelo también reproduce gran parte de la evolución observada del CH_4 en las escalas interanual y decadal. Las variaciones en las emisiones de los humedales son los mayores forzadores de las variaciones del CH_4 de un año a otro.

2.3 El modelo de transporte y los esquemas químicos funcionan bien, y los inventarios de emisiones usados son razonablemente buenos en su distribución temporal, espacial, sectorial, y natural versus antropogénico. Sin embargo, hay algunas discrepancias importantes en el comportamiento del modelo que cuestionan la exactitud de los datos de emisión de CH_4 en ciertas regiones y periodos. Nuestros resultados están de acuerdo con otros estudios, sugiriendo que el reciente crecimiento de las emisiones antropogénicas en Asia a partir de 2006 está sobreestimado en el inventario EDGAR v4.2 (lo simulado por nuestro modelo crece más que la realidad). Nos cuestionamos también las tendencias en las emisiones asiáticas en los años noventa y el comienzo de la década del 2000, en el inventario EDGAR v4.2.

2.4 En relación a las variaciones de las tendencias, las causas son objeto de debate. No se alcanza consenso en la contribución relativa de los sectores de emisión individuales, ni en la atribución a fuentes naturales y antropogénicas.

2.5 En nuestras simulaciones, la vida media del CH_4 decrece más de un 8% entre 1970 y 2012, debido al incremento de la capacidad de oxidación de la atmósfera. Nuestro análisis revela que los factores clave que explican esto son los cambios en: 1) la humedad específica; 2) la proporción de emisión entre NO_x y CO; 3) las emisiones de NO_x debidas a rayos; y 4) la columna total de O_3. Se ha obtenido una ecuación sencilla para predecir la vida media del CH_4 a partir de una combinación de estos parámetros.

2.6 Nuestras simulaciones muestran que tener en cuenta las variaciones en la meteorología tiene un fuerte efecto en el sumidero de CH_4 atmosférico. Esto de hecho afecta a los cambios de CH_4 interanuales y de largo plazo.

3. Se ha mostrado que NAFDI modula los flujos de salida de polvo hacia el SNA y el Mediterráneo a escala intra-estacional durante el verano, alternando entre uno y otro. Para NAFDI positivo, las anomalías positivas de AOD se observan en el Sahara occidental y el SNA, mientras que para NAFDI negativo, éstas aparecen en el Sahara central-oriental y en el Mediterráneo central-occidental.

3.1 Por primera vez, se ha demostrado que existe una estrecha relación entre la fase Oeste (Este) de la SHL y la fase positiva (negativa) del NAFDI, a escala temporal diaria, yendo el NAFDI un día adelantado respecto a la SHL.

3.2 Usando la ecuación de la energía de la dinámica atmosférica y el reanálisis NCEP/NCAR, se ha mostrado que la advección horizontal diferencial de temperatura, que es debida a la anomalía diaria de velocidad horizontal asociada a NAFDI, conduce la evolución temporal del desplazamiento longitudinal de la SHL.

3.3 El NAFDI positivo parece favorecer la emisión de polvo en el Sahara Occidental, norte de Mauritania, y Argelia central.

3.4 Se ha mostrado que las variaciones intra-estacionales del NAFDI son producidas por aquellas MLRWs que se propagan sobre el Norte de África que penetran lo suficiente en la baja troposfera.

6. Bibliografía

Allen, C.J.T.,Washington, R.: The low-level jet dust emission mechanism in the central Sahara: observations from Bordj-Badji Mokhtar during the June 2011 fennec intensive observation period, J. Geophys. Res. Atmos., 119, 2990-3015, http://dx.doi.org/10.1002/2013JD020594, 2013.

Ambrizzi, T., Hoskins, B. J., and Hsu, H. H.: Rossby-wave propagation and teleconnection patterns in the austral winter, Journal of the Atmospheric Sciences, 52, 3661-3672, 1995.

Baddoc, M.C., Strong, C.L., Murray, P.S., McTainsh, G.H.: Aeolian dust as a transport hazard, Atmospheric Environment, 71, 7–14, DOI10.1016/j.atmosenv.2013.01.042, 2013.

Bândă, N., Krol, M., van Weele, M., van Noije, T., and Röckmann, T.: Analysis of global methane changes after the 1991 Pinatubo volcanic eruption, Atmos. Chem. Phys., 13, 2267-2281, https://doi.org/10.5194/acp-13-2267-2013, 2013.

Barnaba, F., Gobbi, G.P.: Aerosol seasonal variability over the Mediterranean region and relative impact of maritime, continental and Saharan dust particles over the basin from MODIS data in the year 2001, Atmos. Chem. Phys., 4, 2367-2391, http://dx.doi.org/10.5194/acp-4-2367-2004, 2004.

Basart, S., Pérez C., Cuevas E., Baldasano J.M., Gobbi G.P.: Aerosol characterization in Northern Africa, Northeastern Atlantic, Mediterranean Basin and Middle East from direct-sun AERONET observations, Atmos. Chem. Phys., 9, 8265-8282, 2009.

Belikov, D. A., Maksyutov, S., Yaremchuk, A., Ganshin, A., Kaminski, T., Blessing, S., Sasakawa, M., Gomez-Pelaez, A. J., and Starchenko, A.: Adjoint of the global Eulerian–Lagrangian coupled atmospheric transport model (A-GELCA v1.0): development and validation, Geosci. Model Dev., 9, 749-764, doi:10.5194/gmd-9-749-2016, 2016.

Benedetti, A., Morcrette, J.-J., Boucher, O., Dethof, A., Engelen, R.J., Fisher, M., Flentjes, H., Huneeus, N., Jones, L., Kaiser, J.W., Kinne, S., Mangold, A., Razinger, M., Simmons, A.J., Suttie, M., the GEMS-AER team: Aerosol analysis and forecast in the ECMWF integrated forecast system. Part II: data assimilation, J. Geophys. Res., 114, D13205, http://dx.doi.org/10.1029/2008JD011115, 2009.

Benedetti, A., Baldasano, J.M., Basart, S., Benincasa, F., Boucher, O., Brooks, M., Chen, J.-P., Colarco, P.R., Gong, S., Huneeus, N., Jones, L., Lu, S., Menut, L., Morcrette, J.-J., Mulcahy, J., Nickovic, S., Perez, C., Reid, J.S., Sekiyama, T.T., Tanaka, T.Y., Terradellas, E., Westphal, D.L., Zhang, X.-Y., Zhou, C.-H.: Numerical prediction of dust, In: Knippertz, P., Stuut, J.-B. (Eds.), Mineral Dust - a Key Player in the Earth System, Springer, Dordrecht, pp. 230-240, 2014.

Bergamaschi, P., Houweling, S., Segers, A., Krol, M., Frankenberg, C., Scheepmaker, R. A., Dlugokencky, E., Wofsy, S. C., Kort, E. A., Sweeney, C., Schuck, T., Brenninkmeijer, C., Chen, H., Beck, V., and Gerbig, C.: Atmospheric CH4 in the first decade of the 21st century: Inverse modeling analysis using SCIAMACHY satellite retrievals and NOAA surface measurements, J. Geophys. Res.-Atmos., 118, 7350–7369, doi:10.1002/jgrd.50480, 2013.

Bousquet, P., Ciais, P., Miller, J. B., Dlugokencky, E. J., Hauglustaine, D. A., Prigent, C., Van der Werf, G. R., Peylin, P., Brunke, E. G., Carouge, C., Langenfelds, R. L., Lathiere, J., Papa, F., Ramonet, M., Schmidt, M., Steele, L. P., Tyler, S. C., and White, J.: Contribution of anthropogenic and natural sources to atmospheric methane variability, Nature, 443, 439–443, 2006.

Bousquet, P., Ringeval, B., Pison, I., Dlugokencky, E. J., Brunke, E.-G., Carouge, C., Chevallier, F., Fortems-Cheiney, A., Frankenberg, C., Hauglustaine, D. A., Krummel, P. B., Langenfelds, R. L., Ramonet, M., Schmidt, M., Steele, L. P., Szopa, S., Yver, C., Viovy, N., and Ciais, P.: Source attribution of the changes in atmospheric methane for 2006–2008, Atmos. Chem. Phys., 11, 3689–3700, doi:10.5194/acp-11-3689-2011, 2011.

Bridgham, S. D., Cadillo-Quiroz, H., Keller, J. K., and Zhuang, Q.: Methane emissions from wetlands: biogeochemical, microbial, and modeling perspectives from local to global scales, Glob. Change Biol., 19, 1325–1346, doi:10.1111/gcb.12131, 2013.

Bruhwiler, L., Dlugokencky, E., Masarie, K., Ishizawa, M., Andrews, A., Miller, J., Sweeney, C., Tans, P., and Worthy, D.: CarbonTracker-CH4: an assimilation system for estimating emissions of atmospheric methane, Atmos. Chem. Phys., 14, 8269–8293, doi:10.5194/acp-14-8269-2014, 2014.

Chauvin, F., Roehrig, R., Lafore, J.-P.: Intraseasonal variability of the Saharan heat low and its link with midlatitudes, J. Clim., 23, 2544-2561. http://dx.doi.org/10.1175/2010JCLI3093.1, 2010.

Chevallier, F., P. Ciais, T. J. Conway, T. Aalto, B. E. Anderson, P. Bousquet, E. G. Brunke, L. Ciattaglia, Y. Esaki, M. Fröhlich, A. Gomez, A. J. Gomez-Pelaez, L. Haszpra, P. B. Krummel, R. L. Langenfelds, M. Leuenberger, T. Machida, F. Maignan, H. Matsueda, J. A. Morguí, H. Mukai, T. Nakazawa, P. Peylin, M. Ramonet, L. Rivier, Y. Sawa, M. Schmidt, L. P. Steele, S. A. Vay, A. T. Vermeulen, S. Wofsy, D. Worthy: CO2 surface fluxes at grid point scale estimated from a global 21 year reanalysis of atmospheric measurements, J. Geophys. Res., 115, D21307, doi:10.1029/2010JD013887, 2010.

Chevallier, F., N. M. Deutscher, T. J. Conway, P. Ciais, L. Ciattaglia, S. Dohe, M. Fröhlich, A.J. Gomez-Pelaez, D. Griffith, F. Hase, L. Haszpra, P. Krummel, E. Kyrö, C. Labuschagne, R. Langenfeld, T. Machida, F. Maignan, H. Matsueda, I. Morino, J. Notholt, M. Ramonet, Y. Sawa, M. Schmidt, V. Sherlock, P. Steele, K. Strong, R. Sussmann, P. Wennberg, S. Wofsy, D. Worthy, D. Wunch, M. Zimnoch: Global CO2 fluxes inferred from surface air-sample measurements and from TCCON retrievals of the CO2 total column, Geophysical Research Letters, 38, L24810, doi: 10.1029/2011GL049899, 2011.

Chiapello, I., Moulin, C., Prospero, J.M.: Understanding the long-term variability of African dust transport across the Atlantic as recorded in both Barbados surface concentrations and large-scale Total Ozone Mapping Spectrometer (TOMS) optical thickness. J. Geophys. Res. 110, D18S10, http://dx.doi.org/10.1029/2004JD005132, 2005.

Ciais, P., Sabine, C., Bala, G., Bopp, L., Brovkin, V., Canadell, J., Chhabra, A., DeFries, R., Galloway, J., Heimann, M., Jones, C., Le Quéré, C., Myneni, R. B., Piao, S., and Thornton, P.: Carbon and Other Biogeochemical Cycles, in: Climate Change 2013: The Physical Science Basis. Contribution of Working Group I to the Fifth Assessment Report of the Intergovernmental Panel on Climate Change, edited by: Stocker, T. F., Qin, D., Plattner, G.-K., Tignor, M., Allen, S. K., Boschung, J., Nauels, A., Xia, Y., Bex, V., and Midgley, P. M., Cambridge University Press, Cambridge, United Kingdom and New York, NY, USA, 465–570, 2013.

Cuesta, J., Marsham, J.H., Parker, D.J., Flamant, C.: Dynamical mechanisms controlling the vertical redistribution of dust and the thermodynamic structure of the West Saharan atmospheric boundary layer during summer, Atmos. Sci. Lett., 10, 34-42, http://dx.doi.org/10.1002/asl.207, 2009.

Cuevas, E., González, Y., Rodríguez, S., Guerra, J. C., Gómez-Peláez, A. J., Alonso-Pérez, S., Bustos, J., and Milford, C.: Assessment of atmospheric processes driving ozone variations in the subtropical North Atlantic free troposphere, Atmos. Chem. Phys., 13, 1973-1998, doi: 10.5194/acp-13-1973-2013, 2013.

Cuevas, E., Camino, C., Benedetti, A., Basart, S., Terradellas, E., Baldasano, J. M., Morcrette, J. J., Marticorena, B., Goloub, P., Mortier, A., Berjón, A., Hernández, Y., Gil-Ojeda, M., and Schulz, M.: The MACC-II 2007-2008 reanalysis: atmospheric dust evaluation and characterization over northern Africa and the Middle East, Atmos. Chem. Phys., 15, 3991-4024, doi:10.5194/acp-15-3991-2015, 2015a.

Cuevas, E., Milford, C., Bustos, J. J., del Campo-Hernández, R., García, O. E., García, R. D., Gómez-Peláez, A. J., Ramos, R., Redondas, A., Reyes, E., Rodríguez, S., Romero-Campos, P. M., Schneider, M., Belmonte, J., Gil-Ojeda, M., Almansa, F., Alonso-Pérez, S., Barreto, A., González-Morales, Y., Guirado-Fuentes, C., López-Solano, C., Afonso, S., Bayo, C., Berjón, A., Bethencourt, J., Camino, C., Carreño, V., Castro, N. J., Cruz, A. M., Damas, M., De Ory-Ajamil, F., García, M. I., Fernández-de Mesa, C. M., González, Y., Hernández, C., Hernández, Y., Hernández, M. A., Hernández-Cruz, B., Jover, M., Kühl, S. O., López-Fernández, R., López-Solano, J., Peris, A., Rodríguez-Franco, J. J., Sálamo, C., Sepúlveda, E. and Sierra, M.: Izaña Atmospheric Research Center Activity Report 2012-2014. (Eds. Cuevas, E., Milford, C. and Tarasova, O.), State Meteorological Agency (AEMET), Madrid, Spain and World Meteorological Organization, Geneva, Switzerland, NIPO: 281-15-004-2, WMO/GAW Report No. 219, 2015b.

Cuevas, E., Milford, C., Bustos, J. J., del Campo-Hernández, R., García, O. E., García, R. D., Gómez-Peláez, A. J., Guirado-Fuentes, C., Marrero, C., Prats, N., Ramos, R., Redondas, A., Reyes, E., Rodríguez, S., Romero-Campos, P. M., Schneider, M., Belmonte, J., Yela, M., Almansa, F., Barreto, A., López-Solano, C., Basart, S., Terradellas, E., Afonso, S., Bayo, C., Berjón, A., Bethencourt, J., Carreño, V., Castro, N. J., Cruz, A. M., Damas, M., De Ory-Ajamil, F., García, M.I., Gómez-Trueba, V., González, Y., Hernández, C., Hernández, Y., Hernández-Cruz, B., Jover, M., León-Luís, S. F., López-Fernández, R., López-Solano, J., Rodríguez, E., Rodríguez-Franco, J. J., Rodríguez-Valido, M., Sálamo, C., Sanromá, E., Santana, D., Santo Tomás, F., Sepúlveda, E., Sierra, M. and Sosa, E.: Izaña Atmospheric Research Center Activity Report 2015-2016. (Eds. Cuevas, E., Milford, C. and Tarasova, O.), State Meteorological Agency (AEMET), Madrid, Spain and World Meteorological Organization, Geneva, Switzerland, NIPO: 014-17-012-9, WMO/GAW Report No. 236, 2017.

Dalsøren, S. B., Myhre, C. L., Myhre, G., Gomez-Pelaez, A. J., Søvde, O. A., Isaksen, I. S. A., Weiss, R. F., and Harth, C. M.: Atmospheric methane evolution the last 40 years, Atmos. Chem. Phys., 16, 3099-3126, https://doi.org/10.5194/acp-16-3099-2016, 2016.

Dlugokencky, E. J., Houweling, S., Bruhwiler, L., Masarie, K. A., Lang, P. M., Miller, J. B., and Tans, P. P.: Atmospheric methane levels off: Temporary pause or a new steady-state?, Geophys. Res. Lett., 30, 1992, doi:10.1029/2003GL018126, 2003.

Dlugokencky, E. J., R. C. Myers, P. M. Lang, K. A. Masarie, A. M. Crotwell, K. W. Thoning, B. D. Hall, J. W. Elkins, and L. P. Steele, Conversion of NOAA atmospheric dry air CH4 mole fractions to a gravimetrically prepared standard scale, J. Geophys. Res., 110, D18306, doi:10.1029/2005JD006035, 2005.

Dlugokencky, E. J., Bruhwiler, L., White, J. W. C., Emmons, L. K., Novelli, P. C., Montzka, S. A., Masarie, K. A., Lang, P. M., Crotwell, A. M., Miller, J. B., and Gatti, L. V.: Observational constraints on recent increases in the atmospheric CH4 burden, Geophys. Res. Lett., 36, L18803, doi:10.1029/2009GL039780, 2009.

Dutton, E. G. and Christy, J. R.: Solar radiative forcing at selected locations and evidence for global tropospheric cooling following the eruptions of El Chichón and Pinatubo, Geophys. Res. Lett., 19, 2313–2316, 1992.

EC-JRC/PBL: Emission Database for Global Atmospheric Research (EDGAR), release version 4.2., available at: http://edgar.jrc.ec.europa.eu (last access: February 2016), 2011.

Ehhalt, D., Prather, M., Dentener, F., Derwent, R., Dlugokencky, E., Holland, E., Isaksen, I., Katima, J., Kirchhoff, V., Matson, P., Midgley, P., and Wang, M.: Atmospheric chemistry and greenhouse gases, Chapter 4, in: Climate Change 2001: The Scientific Basis, edited by: Houghton, J. T., Ding, Y., Griggs, D. J., Noguer, M., van der Linden, P. J., Dai, X., Maskell, K., and Johnson, C. A., Cambridge University Press, Cambridge, UK, 239–287, 2001.

Engelstaedter, S. and Washington, R.: Atmospheric controls on the annual cycle of North African dust, J. Geophys. Res., 112, D17111, doi:10.1029/2006JD007195, 2007.

Engelstaedter, S., Washington, R., Mahowald, N.: Impact of changes in atmospheric conditions in modulating summer dust concentration at Barbados: a back-trajectory analysis, J. Geophys. Res., 114, D17111, http://dx.doi.org/10.1029/2008JD011180, 2009.

Escribano, J., O. Boucher, F. Chevallier, and N. Huneeus, Subregional inversion of North African dust sources, J. Geophys. Res. Atmos., 121, 8549–8566, doi:10.1002/2016JD025020, 2016.

Escudero, M., Querol, X., Ávila A., and Cuevas, E.: Origin of the exceedances of the European daily PM limit value in regional background áreas of Spain, Atmos. Environ., 41, 730–744, 2007a.

Escudero, M., Querol, X., Pey, J., Alastuey, A., Pérez, N., Ferreira, F., Alonso, S., Rodríguez, S., and Cuevas, E.: A methodology for the quantification of the net African dust load in air quality monitoring networks, Atmos. Environ., 41, 5516–5524, 2007b.

Evan, A.T., Flamant, C., Gaetani, M., Guichard, F.: The past, present and future of African dust, Nature, 531 (7595), 493-495, 2016.

Fiore, A. M., West, J. J., Horowitz, L. W., Naik, V., and Schwarzkopf, M. D.: Characterizing the tropospheric ozone response to methane emission controls and the benefits to climate and air quality, J. Geophys. Res.-Atmos., 113, D08307, doi:10.1029/2007JD009162, 2008.

Fischer, H., Nikitas, C., Parchatka, U., Zenker, T., Harris, G. W., Matuska, P., Schmitt, R., Mihelcic, D., Muesgen, P., Paetz, H.-W., Schultz, M., and Volz-Thomas, A.: Trace gas measurements during the oxidizing Capacity of the Tropospheric Atmosphere campaign 1993 at Izaña, J. Geophys. Res., 103, 13505–13518, doi:10.1029/97JD01497, 1998.

Fung, I., John, J., Lerner, J., Matthews, E., Prather, M., Steele, L. P., and Fraser, P. J.: Three-dimensional model synthesis of the global methane cycle, J. Geophys. Res., 96, 13033–13065, doi:10.1029/91JD01247, 1991.

Geisler, J.E., Dickinson, R.E.: External Rossby modes on a beta-plane with realistic vertical wind shear, J. Atmos. Sci., 32, 2082-2093, 1975.

Ghosh, A., Patra, P. K., Ishijima, K., Umezawa, T., Ito, A., Etheridge, D. M., Sugawara, S., Kawamura, K., Miller, J. B., Dlugokencky, E. J., Krummel, P. B., Fraser, P. J., Steele, L. P., Langenfelds, R. L., Trudinger, C. M., White, J. W. C., Vaughn, B., Saeki, T., Aoki, S., and Nakazawa, T.: Variations in global methane sources and sinks during 1910–2010, Atmos. Chem. Phys., 15, 2595–2612, doi:10.5194/acp-15-2595-2015, 2015.

Gillette, D.A., Passi, R.: Modeling dust emission caused by wind erosion, J. Geophys. Res., 93 D11, 14233-14242. http://dx.doi.org/10.1029/JD093iD11p14233, 1988.

Ginoux, P., Prospero, J. M., Torres, O., and Chin, M.: Long-term simulation of global dust distribution with the GOCART model: Correlation with North Atlantic Oscillation, Environ. Modell. Softw., 19, 113–128, 2004.

Ginoux, P., Prospero, J. M., Gill, T. E., Hsu, N. C., and Zhao, M.: Global-scale attribution of anthropogenic and natural dust sources and their emission rates based on MODIS Deep Blue aerosol products, Rev. Geophys., 50, RG3005, doi:10.1029/2012RG000388, 2012.

Gomez-Pelaez, A.J., “Influencia del Campo Magnético en la Evolución No Lineal de las Inestabilidades Térmicas”, Instituto de Astrofísica de Canarias: Report Interno de Investigación. Director del trabajo: Moreno-Insertis, F., doi: 10.13140/RG.2.1.2136.2724, diciembre de 1999.

Gomez-Pelaez, A.J., Moreno-Insertis, F., Thermal Instability in a Cooling and Expanding Medium Including Self-Gravity and Conduction, The Astrophysical Journal, Volume 569, Issue 2, pp. 766-779, 2002.

Gomez-Pelaez, A.J., Ramos, R., Perez-delaPuerta, J., "Methane and carbon dioxide continuous measurements at Izana GAW station (Spain)" in GAW Report (No. 168) of the "13th WMO/IAEA Meeting of Experts on Carbon Dioxide Concentration and Related Tracers Measurement Techniques (Boulder, Colorado, USA, 19-22 September 2005)", edited by J.B. Miller, World Meteorological Organization (TD No. 1359), 180-184, 2006.

Gomez-Pelaez, A.J., "A brief overview of the theory of flow along GC packed columns and some practical consequences for measuring atmospheric CH4, N2O, and SF6" in GAW Report (No. 186) of the "14th WMO/IAEA meeting of experts on carbon dioxide, other greenhouse gases, and related tracers measurement techniques (Helsinki, Finland, 10-13 September 2007)", edited by Tuomas Laurila, World Meteorological Organization (TD No. 1487), 60-64, 2009a.

Gomez-Pelaez, A.J., Ramos, R., "Installation of a new gas chromatograph at Izaña GAW station (Spain) to measure CH4, N2O, and SF6" in GAW Report (No. 186) of the "14th WMO/IAEA meeting of experts on Carbon dioxide, other greenhouse gases, and related tracers measurement techniques (Helsinki, Finland, 10-13 September 2007)", edited by Tuomas Laurila, World Meteorological Organization (TD No. 1487), 55-59, 2009b.

Gomez-Pelaez, A.J., R. Ramos, E. Cuevas, V. Gomez-Trueba, 25 years of continuous CO2 and CH4 measurements at Izaña Global GAW mountain station: annual cycles and interannual trends; Proceedings of the “Symposium on Atmospheric Chemistry and Physics at Mountain Sites (ACP Symposium 2010, June 8-10, 2010, Interlaken, Switzerland)”, 157-159, 2010.

Gomez-Pelaez, A.J., Ramos, R., "Improvements in the Carbon Dioxide and Methane Continuous Measurement Programs at Izaña Global GAW Station (Spain) during 2007-2009", in GAW report (No. 194) of the “15th WMO/IAEA Meeting of Experts on Carbon Dioxide, Other Greenhouse Gases, and Related Tracer Measurement Techniques (Jena, Germany; September 7-10, 2009)”, edited by Willi A. Brand, World Meteorological Organization (TD No. 1553), Geneva, Switzerland, 133-138, 2011.

Gomez-Pelaez, A.J., R. Ramos, V. Gomez-Trueba, R. Campo-Hernandez, E. Dlugokencky, T. Conway, "New improvements in the Izaña (Tenerife, Spain) global GAW station in-situ greenhouse gases measurement program" in GAW report (No. 206) of the "16th WMO/IAEA Meeting on Carbon Dioxide, Other Greenhouse Gases, and Related Measurement Techniques (GGMT-2011) (Wellington, New Zealand, 25-28 October 2011)", edited by Gordon Brailsford, World Meteorological Organization, 76-81, 2012.

Gomez-Pelaez, A. J., Ramos, R., Gomez-Trueba, V., Novelli, P. C., and Campo-Hernandez, R.: A statistical approach to quantify uncertainty in carbon monoxide measurements at the Izaña global GAW station: 2008–2011, Atmos. Meas. Tech., 6, 787-799, doi:10.5194/amt-6-787-2013, 2013.

Gomez-Pelaez, A. J., R. Ramos, V. Gomez-Trueba, R. Campo-Hernandez,E. Reyes-Sanchez: "Izaña Global GAW station greenhouse-gas measurement programme. Novelties and developments during October 2011-May 2013" in GAW report (No. 213) of the "17th WMO/IAEA Meeting on Carbon Dioxide, Other Greenhouse Gases, and Related Measurement Techniques (Beijing, China, June 10-14, 2013)", edited by P. Tans and C. Zellweger, World Meteorological Organization, 77-82, 2014.

Gomez-Pelaez, A.J., R. Ramos, V. Gomez-Trueba, R. Campo-Hernandez, E. Reyes-Sanchez: "GGMT-2015 Izaña station update: instrumental and processing software developments, scale updates, aircraft campaign, and plumbing design for CRDS" in GAW report (No. 229) of the "18th WMO/IAEA Meeting on Carbon Dioxide, Other Greenhouse Gases, and Related Measurement Techniques (GGMT) (La Jolla, CA, USA, 13-17 September, 2015)", edited by P. Tans and C. Zellweger, World Meteorological Organization, 125-131, 2016.

Gomez-Pelaez, A. J., Ramos, R., Cuevas, E., Gomez-Trueba, V., and Reyes, E.: Atmospheric CO2, CH4, and CO with CRDS technique at the Izaña Global GAW station: instrumental tests, developments and first measurement results, Atmos. Meas. Tech. Discuss., https://doi.org/10.5194/amt-2017-375, in review, 2017.

Goudie, A.S.: Dust storms: Recent developments, Journal of Environmental Management, 90, 89-94, 2009.

Hall, B. D., G. S. Dutton and J. W. Elkins, The NOAA nitrous oxide standard scale for atmospheric observations, Journal of Geophysical Research-Atmospheres, 112, D09305, doi:10.1029/2006JD007954, 2007.

Helgren, D.M., Prospero, J.M.: Wind velocities associated with dust deflation events in the Western Sahara, J. Clim. Appl. Meteorol., 26, 1147-1151, 1987.

Hodson, E. L., Poulter, B., Zimmermann, N. E., Prigent, C., and Kaplan, J. O.: The El Niño–Southern Oscillation and wetland methane interannual variability, Geophys. Res. Lett., 38, L08810, doi:10.1029/2011GL046861, 2011.

Holton, J.R.: An Introduction to Dynamic Meteorology, Third Edition, International Geophysics Series, vol. 48. Academic Press, San Diego, California, 1992.

Hoskins, B. J., and Ambrizzi, T.: Rossby-wave propagation on a realistic longitudinally varying flow, Journal of the Atmospheric Sciences, 50, 1661-1671, 1993.

Houweling, S., Krol, M., Bergamaschi, P., Frankenberg, C., Dlugokencky, E. J., Morino, I., Notholt, J., Sherlock, V., Wunch, D., Beck, V., Gerbig, C., Chen, H., Kort, E. A., Röckmann, T., and Aben, I.: A multi-year methane inversion using SCIAMACHY, accounting for systematic errors using TCCON measurements, Atmos. Chem. Phys., 14, 3991-4012, doi:10.5194/acp-14-3991-2014, 2014.

Hsu, H. H., and Lin, S. H.: Global teleconnections in the 250-mb streamfunction field during the northern-hemisphere winter, Monthly Weather Review, 120, 1169-1190, 1992.

Huneeus, N., Schulz, M., Balkanski, Y., Griesfeller, J., Prospero, J., Kinne, S., Bauer, S., Boucher, O., Chin, M., Dentener, F., Diehl, T., Easter, R., Fillmore, D., Ghan, S., Ginoux, P., Grini, A., Horowitz, L., Koch, D., Krol, M. C., Landing, W., Liu, X., Mahowald, N., Miller, R., Morcrette, J.-J., Myhre, G., Penner, J., Perlwitz, J., Stier, P., Takemura, T., and Zender, C. S.: Global dust model intercomparison in AeroCom phase I, Atmos. Chem. Phys., 11, 7781–7816, doi:10.5194/acp-11-7781-2011, 2011.

Huneeus, N., Boucher, O., Chevallier, F.: Atmospheric inversion of SO2 and primary aerosol emissions for the year 2010, Atmos. Chem. Phys., 13, 6555-6573, http://dx.doi.org/10.5194/acp-13-6555-2013, 2013.

Inness, A., Baier, F., Benedetti, A., Bouarar, I., Chabrillat, S., Clark, H., Clerbaux, C., Coheur, P., Engelen, R.J., Errera, Q., Flemming, J., George, M., Granier, C., Hadji-Lazaro, J., Huijnen, V., Hurtmans, D., Jones, L., Kaiser, J.W., Kapsomenakis, J., Lefever, K., Leitão, J., Razinger, M., Richter, A., Schultz, M.G., Simmons, A.J., Suttie, M., Stein, O., Thépaut, J.-N., Thouret, V., Vrekoussis, M., Zerefos, C., the MACC team: The MACC reanalysis: an 8 yr data set of atmospheric composition, Atmos.Chem. Phys., 13, 4073-4109, http://dx.doi.org/10.5194/acp-13-4073-2013, 2013.

IPCC: Annex III: Glossary [Planton, S. (ed.)]. In: Climate Change 2013: The Physical Science Basis. Contribution of Working Group I to the Fifth Assessment Report of the Intergovernmental Panel on Climate Change [Stocker, T.F., D. Qin, G.-K. Plattner, M. Tignor, S.K. Allen, J. Boschung, A. Nauels, Y. Xia, V. Bex and P.M. Midgley (eds.)]. Cambridge University Press, Cambridge, United Kingdom and New York, NY, USA, 2013a.

IPCC: Summary for Policymakers. In: Climate Change 2013: The Physical Science Basis. Contribution of Working Group I to the Fifth Assessment Report of the Intergovernmental Panel on Climate Change [Stocker, T.F., D. Qin, G.-K. Plattner, M. Tignor, S.K. Allen, J. Boschung, A. Nauels, Y. Xia, V. Bex and P.M. Midgley (eds.)]. Cambridge University Press, Cambridge, United Kingdom and New York, NY, USA, 2013b.

Isaksen, I. S. A., Gauss, M., Myhre, G.,Walter Anthony, K. M., and Ruppel, C.: Strong atmospheric chemistry feedback to climate warming from Arctic methane emissions, Global Biogeochem. Cy., 25, GB2002, doi:10.1029/2010GB003845, 2011.

Isaksen, I., Berntsen, T., Dalsøren, S., Eleftheratos, K., Orsolini, Y., Rognerud, B., Stordal, F., Søvde, O., Zerefos, C., and Holmes, C.: Atmospheric Ozone and Methane in a Changing Climate, Atmosphere, 5, 518–535, 2014.

JCGM: JCGM 100:2008, GUM 1995 with Minor Corrections, Evaluation of Measurement Data – guide to the Expression of Uncertainty in Measurement, Joint Committee for Guides in Metrology, Member organizations: BIPM, IEC, IFCC, ILAC, ISO, IUPAC, IUPAP, and OIML, 2008.

Johnson, C. E., Stevenson, D. S., Collins, W. J., and Derwent, R. G.: Interannual variability in methane growth rate simulated with a coupled Ocean-Atmosphere-Chemistry model, Geophys. Res. Lett., 29, 9-1–9-4, doi:10.1029/2002GL015269, 2002.

Joos, F., Roth, R., Fuglestvedt, J. S., Peters, G. P., Enting, I. G., von Bloh, W., Brovkin, V., Burke, E. J., Eby, M., Edwards, N. R., Friedrich, T., Frölicher, T. L., Halloran, P. R., Holden, P. B., Jones, C., Kleinen, T., Mackenzie, F. T., Matsumoto, K., Meinshausen, M., Plattner, G.-K., Reisinger, A., Segschneider, J., Shaffer, G., Steinacher, M., Strassmann, K., Tanaka, K., Timmermann, A., and Weaver, A. J.: Carbon dioxide and climate impulse response functions for the computation of greenhouse gas metrics: a multi-model analysis, Atmos. Chem. Phys., 13, 2793-2825, https://doi.org/10.5194/acp-13-2793-2013, 2013.

Kalnay, E., Kanamitsu, M., Kistler, R., Collins, W., Deaven, D., Gandin, L., Iredell, M., Saha, S., White, G., Woollen, J., Zhu, Y., Leetmaa, A., Reynolds, R., Chelliah, M., Ebisuzaki, W., Higgins, W., Janowiak, J., Mo, K.C., Ropelewski, C., Wang, J., Jenne, R., Joseph, D.: The NCEP/NCAR 40-year reanalysis project, B. Am. Meteorol. Soc., 77, 437-471, 1996.

Kaufman, Y.J., Tanré, D., Remer, L.A., Vermote, E.F., Chu, A., Holben, B.N.: Operational remote sensing of tropospheric aerosol over land from EOS moderate resolution imaging spectroradiometer, J. Geophys. Res., 102, 17-51, 1997.

Lavaysse, C., Flamant, C., Janicot, S., Parker, D.J., Lafore, J.-P., Sultan, B., Pelon, J.: Seasonal evolution of the West African heat low: a climatological perspective. Clim. Dyn. 33, 313-330, 2009.

Lavaysse, C., Flamant, C., Janicot, S.: Regional-scale convection patterns during strong and weak phases of the Saharan heat low, Atmos. Sci. Lett., 11, 255-264. http://dx.doi.org/10.1002/asl.284, 2010.

Levin, I., Veidt, C., Vaughn, B. H., Brailsford, G., Bromley, T., Heinz, R., Lowe, D., Miller, J. B., Posz, C., and White, J. W. C.: No inter-hemispheric 13CH4 trend observed, Nature, 486, E3–E4, 2012.

Lindzen, R.S.: Rossby waves with negative equivalent depths – comments on a note by G. A. Corby, Quart. J. Roy. Meteor. Soc., 94, 402-407, 1968.

Logan, J. A., Prather, M. J., Wofsy, S. C., and McElroy, M. B.: Tropospheric chemistry – a global perspective, J. Geophys. Res., 86, 7210–7254, doi:10.1029/JC086iC08p07210, 1981.

Marsham, J.H., Hobby, M., Allen, C.J.T., Banks, J.R., Bart, M., Brooks, B.J., Cavazos-Guerra, C., Engelstaedter, S., Gascoyne, M., Lima, A.R., Martins, J.V., McQuaid, J.B., O'Leary, A., Ouchene, B., Ouladichir, A., Parker, D.J., Saci, A., Salah-Ferroudj, M., Todd, M.C., Washington, R.: Meteorology and dust in the central Sahara: observations from Fennec supersite-1 during the June 2011 intensive observation period, J. Geophys. Res., 118, 4069-4089. http://dx.doi.org/10.1002/jgrd.50211, 2013.

Morcrette, J.-J., Boucher, O., Jones, L., Salmond, D., Bechtold, P., Beljaars, A., Benedetti, A., Bonet, A., Kaiser, J.W., Razinger, M., Schulz, M., Serrar, S., Simmons, A.J., Sofiev, M., Suttie, M., Tompkins, A.M., Untch, A.: Aerosol analysis and forecast in the ECMWF integrated forecast system. Part I: forward modelling, J. Geophys. Res., 114, D06206. http://dx.doi.org/10.1029/2008JD011235, 2009.

Morcrette, J.-J., Benedetti, A., Jones, L., Kaiser, J.W., Razinger, M., Suttie, M.: Prognostic Aerosols in the ECMWF IFS: MACC vs. GEMS Aerosols, vol. 659, ECMWF Tech Memo available at:

https://www.ecmwf.int/en/elibrary/11277-prognostic-aerosols-ecmwf-ifs-macc-vs-gems-aerosols (Accessed 16 June 2018), 2011.

Myhre, G., D. Shindell, F.-M. Bréon, W. Collins, J. Fuglestvedt, J. Huang, D. Koch, J.-F. Lamarque, D. Lee, B. Mendoza, T. Nakajima, A. Robock, G. Stephens, T. Takemura and H. Zhang: Anthropogenic and Natural Radiative Forcing. In: Climate Change 2013: The Physical Science Basis. Contribution of Working Group I to the Fifth Assessment Report of the Intergovernmental Panel on Climate Change [Stocker, T.F., D. Qin, G.-K. Plattner, M. Tignor, S.K. Allen, J. Boschung, A. Nauels, Y. Xia, V. Bex and P.M. Midgley (eds.)]. Cambridge University Press, Cambridge, United Kingdom and New York, NY, USA, 2013a.

Myhre, G., D. Shindell, F.-M. Bréon, W. Collins, J. Fuglestvedt, J. Huang, D. Koch, J.-F. Lamarque, D. Lee, B. Mendoza, T. Nakajima, A. Robock, G. Stephens, T. Takemura and H. Zhang: Anthropogenic and Natural Radiative Forcing Supplementary Material. In: Climate Change 2013: The Physical Science Basis. Contribution of Working Group I to the Fifth Assessment Report of the Intergovernmental Panel on Climate Change [Stocker, T.F., D. Qin, G.-K. Plattner, M. Tignor, S.K. Allen, J. Boschung, A. Nauels, Y. Xia, V. Bex and P.M. Midgley (eds.)]. Available from www.climatechange2013.org and www.ipcc.ch, 2013b.

Nakamae, K., Shiotani, M.: Interannual variability in Saharan dust over the North Atlantic Ocean and its relation to meteorological fields during Northern winter, Atmos. Res., 120, 336-346, 2013.

Neef, L., van Weele, M., and van Velthoven, P.: Optimal estimation of the present-day global methane budget, Global Biogeochem. Cy., 24, GB4024, doi:10.1029/2009GB003661, 2010.

Novelli. P.C., Elkins, J.W., and Steele, L.P., Development and evaluation of a gravimetric reference scale for measurements of atmospheric carbon monoxide, JGR, 96, 13109-13121, 1991.

Novelli, P. C., Steele, P., and Tans, P. P.: Mixing ratios of carbon monoxide in the troposphere, J. Geophys. Res., 97, 20731–20750, doi:10.1029/92JD02010, 1992.

Patra, P. K., M. Takigawa, K. Ishijima, B.-C. Choi, D. Cunnold, E. J. Dlugokencky, P. Fraser, A. J. Gomez-Pelaez, T.-Y. Goo, J.-S. Kim, P. Krummel, R. Langenfelds, F. Meinhardt, H. Mukai, S. O'Doherty, R. G. Prinn, P. Simmonds, P. Steele, Y. Tohjima, K. Tsuboi, K. Uhse, R. Weiss, D. Worthy and T. Nakazawa, Growth rate, seasonal, synoptic, diurnal variations and budget of methane in lower atmosphere, J. Meteorol. Soc. Jpn., 87(4), 635-663, 2009.

Patra, P. K., Krol, M. C., Montzka, S. A., Arnold, T., Atlas, E. L., Lintner, B. R., Stephens, B. B., Xiang, B., Elkins, J. W., 5 Fraser, P. J., Ghosh, A., Hintsa, E. J., Hurst, D. F., Ishijima, K., Krummel, P. B., Miller, B. R., Miyazaki, K., Moore, F. L., Muhle, J., O/'Doherty, S., Prinn, R. G., Steele, L. P., Takigawa, M., Wang, H. J., Weiss, R. F., Wofsy, S. C., Young, D.: Observational evidence for interhemispheric hydroxyl-radical parity, Nature, 513, 7517, 219-223, http://dx.doi.org/10.1038/nature13721, 2014.

Peixoto, J.P., Oort, A.H., Physics of climate, Springer-Verlag, New York, 1992.

Pérez, C., Nickovic, S., Baldasano, J. M., Sicard, M., Rocadenbosch, F., and Cachorro, V. E.: A long Saharan dust event over the western Mediterranean: Lidar, Sun photometer observations, and regional dust modeling, J. Geophys. Res., 111, doi:10.1029/2005JD006579, 2006.

Pison, I., Bousquet, P., Chevallier, F., Szopa, S., and Hauglustaine, D.: Multi-species inversion of CH_4, CO and H_2 emissions from surface measurements, Atmos. Chem. Phys., 9, 5281–5297, doi:10.5194/acp-9-5281-2009, 2009.

Prospero, J. M. and Carlson, T. N.: Vertical and areal distribution of Saharan dust over the western Equatorial North Atlantic Ocean, J. Geophys. Res., 77, 5255–5265, 1972.

Prospero, J.M., Ginoux, P., Torres, O., Nicholson, S., Gill, T.: Environmental characterization of global sources of atmospheric soil dust identified with the NIMBUS7 Total Ozone Mapping Spectrometer (TOMS) absorbing aerosol product, Rev. Geophys., 40 (1), 1002, http://dx.doi.org/10.1029/2000RG000095, 2002.

Prospero, J.M., Mayol-Bracero, O.: Understanding the transport and impact of African dust on the Caribbean basin. Bull. Am. Meteorol. Soc. 94, 1329-1337. BAMS-D-12-00142.1, 2013.

Prospero, J. M., Collard, F.-X., Molinié, J., and Jeannot, A.: Characterizing the annual cycle of African dust transport to the Caribbean Basin and South America and its impact on the environment and air quality, Global Biogeochem. Cycles, 29, doi:10.1002/2013GB004802, 2014.

Querol, X., Pey, J., Pandolfi, M., Alastuey, A., Cusack, M., Pérez, N., Moreno, N., Viana, M., Mihalopoulos, N., Kallos, G., and Kleanthous, S.: African dust contributions to mean ambient PM10 mass-levels across the Mediterranean basin, Atmos. Environ., 43, 4266–4277, 2009.

Ravelo-Pérez, L.M., Rodríguez, S., Galindo, L., García, M.I., Alastuey, A., López-Solano, J.: Soluble iron dust export in the high altitude Saharan Air Layer, Atmospheric Environment, 133, 49–59, 2016.

Rodríguez, S., Querol, X., Alastuey, A., Kallos, G., and Kakaliagou, O.: Saharan dust contributions to PM10 and TSP levels in Southern and Eastern Spain, Atmos. Environ., 35, 2433–2447, 2001.

Rodríguez, S., González, Y., Cuevas, E., Ramos, R., Romero, P. M., Abreu-Afonso, J., and Redondas, A.: Atmospheric nanoparticle observations in the low free troposphere during upward orographic flows at Izaña Mountain Observatory, Atmos. Chem. Phys., 9, 6319–6335, doi:10.5194/acp-9-6319-2009, 2009.

Rodríguez, S., Cuevas, E., Prospero, J. M., Alastuey, A., Querol, X., López-Solano, J., García, M. I., and Alonso-Pérez, S.: Modulation of Saharan dust export by the North African dipole, Atmos. Chem. Phys., 15, 7471-7486, doi:10.5194/acp-15-7471-2015, 2015.

Roehrig, R., Chauvin, F., Lafore, J.-P.: 10-25-Day intraseasonal variability of convection over the Sahel: a role of the Saharan heat low and midlatitudes, J. Clim., 24 (22), 5863-5878, http://dx.doi.org/10.1175/2011JCLI3960.1, 2011.

Sayer, A.M., Hsu, N.C., Bettenhausen, C., Jeong, M.-J.: Validation and uncertainty estimates for MODIS Collection 6 “Deep Blue” aerosol data, J. Geophys. Res. Atmos., 118, 7864-7872. http://dx.doi.org/10.1002/jgrd.50600, 2013.

Schepanski, K., Tegen, I., Laurent, B., Heinold, B., Macke, A.: A new Saharan dust source activation frequency map derived from MSG-SEVIRI IR-channels, Geophys. Res. Lett., 34, L18803, http://dx.doi.org/10.1029/2007GL030168, 2007.

Seinfeld, J.H., Pandis, S.N., “Atmospheric chemistry and physics. From air pollution to climate change”. John Wiley & Sons, New York, 1998.

Shirai, T., M. Ishizawa, R. Zhuravlev, A. Ganshin, D. Belikov, M. Saito, T. Oda, V. Valsala, A.J. Gomez-Pelaez, R. Langenfelds, and S. Maksyutov; A decadal inversion of CO2 using the Global Eulerian–Lagrangian Coupled Atmospheric model (GELCA): sensitivity to the ground-based observation network, Tellus B: Chemical and Physical Meteorology, Vol. 69, Iss. 1, 2017.

Solomon, S., D. Qin, M. Manning, R.B. Alley, T. Berntsen, N.L. Bindoff, Z. Chen, A. Chidthaisong, J.M. Gregory, G.C. Hegerl, M. Heimann, B. Hewitson, B.J. Hoskins, F. Joos, J. Jouzel, V. Kattsov, U. Lohmann, T. Matsuno, M. Molina, N. Nicholls, J. Overpeck, G. Raga, V. Ramaswamy, J. Ren, M. Rusticucci, R. Somerville, T.F. Stocker, P. Whetton, R.A. Wood and D. Wratt: Technical Summary. In: Climate Change 2007: The Physical Science Basis. Contribution of Working Group I to the Fourth Assessment Report of the Intergovernmental Panel on Climate Change [Solomon, S., D. Qin, M. Manning, Z. Chen, M. Marquis, K.B. Averyt, M. Tignor and H.L. Miller (eds.)]. Cambridge University Press, Cambridge, United Kingdom and New York, NY, USA, 2007.

Søvde, O. A., Prather, M. J., Isaksen, I. S. A., Berntsen, T. K., Stordal, F., Zhu, X., Holmes, C. D., and Hsu, J.: The chemical transport model Oslo CTM3, Geosci. Model Dev., 5, 1441–1469, doi:10.5194/gmd-5-1441-2012, 2012.

Stein, A.F., Draxler, R.R., Rolph, G.D., Stunder, B.J.B., Cohen, M.D., Ngan, F.: NOAA's HYSPLIT atmospheric transport and dispersion modeling system, Bull. Amer. Meteor. Soc., 96, 2059-2077, 2015.

Stocker, T.F., D. Qin, G.-K. Plattner, L.V. Alexander, S.K. Allen, N.L. Bindoff, F.-M. Bréon, J.A. Church, U. Cubasch, S. Emori, P. Forster, P. Friedlingstein, N. Gillett, J.M. Gregory, D.L. Hartmann, E. Jansen, B. Kirtman, R. Knutti, K. Krishna Kumar, P. Lemke, J. Marotzke, V. Masson-Delmotte, G.A. Meehl, I.I. Mokhov, S. Piao, V. Ramaswamy, D. Randall, M. Rhein, M. Rojas, C. Sabine, D. Shindell, L.D. Talley, D.G. Vaughan and S.-P. Xie: Technical Summary. In: Climate Change 2013: The Physical Science Basis. Contribution of Working Group I to the Fifth Assessment Report of the Intergovernmental Panel on Climate Change [Stocker, T.F., D. Qin, G.-K. Plattner, M. Tignor, S.K. Allen, J. Boschung, A. Nauels, Y. Xia, V. Bex and P.M. Midgley (eds.)]. Cambridge University Press, Cambridge, United Kingdom and New York, NY, USA, 2013.

Takemura, T., Okamoto, H., Maruyama, Y., Numaguti, A., Higurashi, A., Nakajima, T.: Global three-dimensional simulation of aerosol optical thickness distribution of various origins, J. Geophys. Res., 105, 17853-17873, http://dx.doi.org/10.1029/2000JD900265, 2000.

Tanré, D., Kaufman, Y.J., Herman, M., Mattoo, S.: Remote sensing of aerosol properties over oceans using the MODIS/EOS spectral radiances, J. Geophys. Res., 102, 16971-16988, http://dx.doi.org/10.1029/96JD03437, 1997.

Tegen, I., Fung, I.: Modeling of mineral dust transport in the atmosphere: sources, transport, and optical thickness, J. Geophys. Res, 99, 22897-22914, http://dx.doi.org/10.1029/94JD01928, 1994.

Tegen, I.: Modeling the mineral dust aerosol cycle in the climate system, Quat. Sci. Rev., 22, 1821-1834, http://dx.doi.org/10.1016/S0277-3791(03)00163-X, 2003.

Tsuruta, A., Aalto, T., Backman, L., Hakkarainen, J., van der Laan-Luijkx, I. T., Krol, M. C., Spahni, R., Houweling, S., Laine, M., Dlugokencky, E., Gomez-Pelaez, A. J., van der Schoot, M., Langenfelds, R., Ellul, R., Arduini, J., Apadula, F., Gerbig, C., Feist, D. G., Kivi, R., Yoshida, Y., and Peters, W.: Global methane emission estimates for 2000–2012 from CarbonTracker Europe-CH4 v1.0, Geosci. Model Dev., 10, 1261-1289, doi:10.5194/gmd-10-1261-2017, 2017.

Wang, W., Evan, A.T., Flamant, C., Lavaysse, C.: On the decadal scale correlation between African dust and Sahel rainfall: the role of Saharan heat low-forced winds, Sci. Adv., 1 (9), e1500646. http://dx.doi.org/10.1126/sciadv.1500646, 2015.

Warwick, N. J., Bekki, S., Law, K. S., Nisbet, E. G., and Pyle, J. A.: The impact of meteorology on the interannual growth rate of atmospheric methane, Geophys. Res. Lett., 29, 1947, doi:10.1029/2002GL015282, 2002.

WDCGG (World Data Centre for Greenhouse Gases): WMO WDCGG Data Summary, GAW Data (Volume IV-Greenhouse Gases and Other Atmospheric Gases), WDCGG No. 41, Japan Meteorological Agency in Co-operation with World Meteorological Organization, 2017.

West, J. J. and Fiore, A. M.: Management of Tropospheric Ozone by Reducing Methane Emissions, Environ. Sci. Technol., 39, 4685–4691, doi:10.1021/es048629f, 2005.

WMO: Guidelines for the Measurement of Atmospheric Carbon Monoxide, GAW Report No. 192, World Meteorological Organization, Geneva, Switzerland, 2010.

WMO: 18th WMO/IAEA Meeting on Carbon Dioxide, Other Greenhouse Gases, and Related Tracers Measurement Techniques (GGMT-2015), La Jolla, CA, USA, 13-17 September 2015, GAW report No. 229, chap. Expert group recommendations, World Meteorological Organization, Geneva, Switzerland, 1-51, 2016.

WMO: WMO Greenhouse Gas Bulletin, The state of greenhouse gases in the atmosphere based on global observations through 2016, World Meteorological Organization, Geneva, 2017.

Zellweger, C., M. Steinbacher, B. Buchmann, R. Steinbrecher: System and Performance Audit of Surface Ozone, Methane, Carbon Dioxide, Nitrous Oxide and Carbon Monoxide at the Global GAW Station Izaña, September 2013, WCC-Empa Report 13/2, http://gaw.empa.ch/audits/IZO_2013.pdf, 2015.

Zhao, C., P.P. Tans and K.W. Thoning, A high precision manometric system for absolute calibrations of CO2 in dry air. Journal of Geophysical Research, 102(D5):5885-5894, 1997.

Zhao, C. L. and P. P. Tans, Estimating uncertainty of the WMO mole fraction scale for carbon dioxide in air, Journal of Geophysical Research-Atmospheres, 111(D8), 10.1029/2005JD006003, 2006.

Anexo: Glosario de acrónimos

ACP: Atmospheric Chemistry and Physics (revista científica)

AEMET: Agencia Estatal de Meteorología (España).

AGTP: Absolute Global Temperature Potential (Potencial de cambio Absoluto de la Temperatura Global)

AMT: Atmospheric Measurement Techniques (revista científica)

AOD: Aerosol Optical Depth (Espesor Óptico de Aerosoles)

CC: Creative Commons (tipo de licencia de derechos de autor)

CCGG: Carbon Cycle and Greenhouse Gases

CCL: Central Calibration Laboratory (Laboratorio Central de Calibración)

CIAI: Centro de Investigación Atmosférica de Izaña (pertenece a AEMET)

CRDS: Cavity Ring-Down Spectroscopy (Espectroscopía por “Decaimiento” en Cavidad)

CTM: Chemical Transport Model (Modelo de Transporte Químico)

CVN: Curriculum Vitae Normalizado

DB: Deep Blue

DT: Dark Target

ECD: Detector de Captura Electrónica

ECLIPSE: Evaluating the CLimate and air quality ImPacts of Short-livEd pollutants (Inventario de Emisiones)

ECMWF: European Centre for Medium-Range Weather Forecasts (Centro Europeo de Predicción a Plazo Medio)

EDGAR: Emissions Database for Global Atmospheric Research (Inventario de Emisiones Global para la Investigación Atmosférica desarrollado por JRC y PBL).

EDP: Ecuación en Derivadas Parciales

EMPA: Swiss Federal Laboratories for Materials Science and Technology (Laboratorios Federales Suizos para Ciencia de Materiales y Tecnología)

ENSO: El Niño - Southern Oscillation

ERF: Forzamiento Radiativo Efectivo

ESRL: Earth System Research Laboratory

FECYT: Fundación Española para la Ciencia Y la Tecnología

FEDER: Fondo Europeo de Desarrollo Regional

FID: Detector de Ionización de Llama

GAW: Global Atmosphere Watch (VAG en español)

GC: Cromatografía de Gases y Cromatógrafo de Gases

GEI: Gases de Efecto Invernadero

GMD: Global Monitoring Division

GMST: Global Mean Surface Temperature (Temperatura Media Global de la Atmósfera junto a la Superficie Terrestre)

IAC: Instituto de Astrofísica de Canarias

IFS: Integrated Forecast System (Sistema de Predicción Integrado)

IPCC: Intergovernmental Panel on Climate Change

IR: Infrarrojo

JCGM: Joint Committee for Guides in Metrology

JCR: Journal Citation Reports

JJAS: junio, julio, agosto y septiembre

JRC: Joint Research Centre (Centro de Investigación Colectivo de la Comisión Europea)

LLJ: Low Level Jet (Chorro de Niveles Bajos)

MACC: Monitoring Atmospheric Composition & Climate (Monitorización de la Composición Atmosférica y del Clima)

MEI: Multivariate ENSO Index

MLRWs: MidLatitude Rossby waves (Ondas de Rossby de Latitudes Medias)

MODIS: MODerate resolution Imaging Spectrometer (Espectrómetro de Imagen de Resolución Moderada)

NAFDI: North African Dipole Intensity (Intensidad del Dipolo Norte Africano), así como su índice mensual

NAFDIDI: Índice semejante al NAFDI, pero diario en lugar de mensual

NAO: North Atlantic Oscillation (Oscilación del Atlántico Norte)

NCAR: National Centre for Atmospheric Research (Centro Nacional de Investigación Atmosférica de EE.UU.)

NCEP: National Centre for Environmental Prediction (Centro Nacional de Predicción Medioambiental de EE.UU.)

NDIR: Non-Dispersive Infrared (Analyser). Analizador Infrarrojo No Dispersivo (en español).

NMVOC: Compuestos Orgánicos Volátiles Distintos del CH_4

NOAA: National Oceanic and Atmospheric Administration (Agencia Federal de EE.UU. para los Océanos y la Atmósfera)

OAI: Observatorio Atmosférico de Izaña

OMM: Organización Meteorológica Mundial

OM500: Omega diario NCEP a 500 hPa, en Pa/s, sobre el norte de Argelia, 32.5^{o}N, 2.5^{o}E

PBL: Agencia de Evaluación del Medioambiente de Holanda.

RF: Forzamiento Radiativo

RGD: Detector de Gas por Reducción

SAG: Scientific Advisory Group (Grupo de Asesoramiento Científico)

SAL: Saharan Air Layer (Capa de Aire Sahariano)

SHL: Saharan Heat Low (Baja Térmica Sahariana)

SHLLSI: SHL Longitudinal Shift Index (Índice de Desplazamiento Longitudinal SHL)

SNA: Subtropical North Atlantic (Atlántico Norte Subtropical)

VAG: Vigilancia Atmosférica Global (programa de la OMM)

WA300: anomalía diaria de viento zonal NCEP a 300 hPa, en m/s, con el signo invertido, en el sur de Marruecos, 10^{o}W, 30^{o}N

WCC: World Calibration Centre (Centro de Calibración Mundial)

WDCGG: World Data Centre for Greenhouse Gases (Centro Mundial de Datos para Gases de Efecto Invernadero de la OMM)

WMO: World Meteorological Organization (OMM en español)

WOS: Web Of Science